UNIVERSIDAD COMPLUTENSE DE MADRID
FACULTAD DE CIENCIAS FÍSICAS

TESIS DOCTORAL

The cycle of matter in the interestellar medium: energetic processing of dust and ice

El ciclo de la materia en el medio interestellar : procesamiento energético del polvo y el hielo

MEMORIA PARA OPTAR AL GRADO DE DOCTOR

PRESENTADA POR

Rafael Martín Doménech

Director

Guillermo M. Muñoz Caro

Madrid, 2017

©Rafael Martín Doménech, 2017

UNIVERSIDAD
COMPLUTENSE
MADRID

The cycle of matter in the interstellar medium: energetic processing of dust and ice

El ciclo de la materia en el medio interestelar: procesamiento energético del polvo y el hielo

TESIS DOCTORAL

escrita por
Rafael Martín Doménech
y dirigida por
Guillermo M. Muñoz Caro

para optar al grado de Doctor en Astrofísica
ofrecido por la Facultad de Físicas de la
Universidad Complutense de Madrid.

CENTRO DE ASTROBIOLOGÍA
ASOCIADO AL NASA ASTROBIOLOGY INSTITUTE

Comité de Promoción

Director : Dr. Guillermo Manuel Muñoz Caro

Tutor: Dr. Jesús Gallego Maestro

Presidente del tribunal: Dr. David Montes Gutiérrez

Secretario del tribunal: Dr. Armando Gil de Paz

Tribunal: Dra. Barbara Michela Giuliano

Dra. María Belén Maté Naya

Dr. Miguel Ángel Satorre Aznar

Para Carmen, Mamá y Papá.

I think that the task of philosophy is not to provide answers, but to show how the way
we perceive a problem can be itself part of a problem.

Slavoj Žižek

Contents

1 Resumen 17

2 Summary 21

I Context 25

3 Introduction to the Interstellar Medium 27
3.1 Solid interstellar matter - Dust 28
3.2 Solid interstellar matter - Ice 30
3.3 Gaseous interstellar matter - Star-forming regions 35
3.4 Outlook of the thesis 36

II Methods 39

4 Methods 41
4.1 Laboratory Astrophysics 41
4.1.1 Experimental simulations in the ISAC ultra-high vacuum chamber 41
4.1.2 Additional experiments using the SICAL-X high vacuum chamber 42
4.1.3 Vacuum-ultraviolet lamp for photoprocessing of interstellar solid analogs 44
4.1.4 Infrared spectroscopy 47
4.1.5 Mass spectrometry 49
4.2 Observational Astrophysics - Radio Astronomy 54
4.2.1 Rotational spectroscopy 54
4.2.2 Single-dish observations 55
4.2.3 Interferometric observations 57

III Results - Dust 59

5 UV photoprocessing of hydrogenated amorphous carbons 61
5.1 Introduction 61

5.2 Methods . . . 63
5.2.1 SICAL-X . . . 63
5.2.2 ISAC . . . 66
5.2.3 Theoretical models . . . 66
5.3 Experimental results . . . 68
5.3.1 IR spectra of the a-C:H and a-C:D analogs . . . 69
5.3.2 QMS measurements of the outgoing H_2 or D_2 flux . . . 69
5.4 Astrophysical implications . . . 74
5.5 Conclusions . . . 77

IV Results - Ice **81**

6 CO ice accretion **83**
6.1 Introduction . . . 83
6.2 Experimental simulations . . . 84
6.2.1 IPS . . . 84
6.2.2 ISAC . . . 88
6.2.3 Summary of experimental results . . . 91
6.3 Theoretical simulations . . . 92
6.3.1 Accretion . . . 92
6.3.2 Building CO ices. . . . 93
6.3.3 Diffusion . . . 93
6.3.4 Desorption . . . 95
6.3.5 Theoretical results . . . 96
6.4 Astrophysical implications . . . 98
6.5 Conclusions . . . 102

7 Introduction to the photoprocessing of ices **105**
7.1 Photon-induced desorption processes . . . 105
7.2 Outlook of Chapters 8 - 10 . . . 107

8 UV photoprocessing of CO_2 ice **109**
8.1 Introduction . . . 109
8.2 Experimental setup . . . 110
8.3 Experimental results and discussion . . . 112
8.3.1 IR spectra of CO_2 ice during irradiation . . . 112
8.3.2 Photon-induced desorption during irradiation . . . 113
8.3.3 Temperature-programmed desorption of the irradiated CO_2 ice . . . 117
8.3.4 Photoprocessing of pure CO_2 ice: reaction scheme and photodesorption yields . . . 118
8.4 Astrophysical implications . . . 123
8.5 Conclusions . . . 124

9 UV photoprocessing of C_2H_5OH ice **129**
9.1 Introduction . . . 129
9.2 Experimental setup . . . 132

9.3 Experimental results and discussion . . . 138
  9.3.1 Photon-induced chemistry of pure C_2H_5OH ice . . . 138
  9.3.2 Photon-induced desorption from pure C_2H_5OH ice . . . 141
9.4 Astrophysical implications . . . 145

10 UV photoprocessing of H_2O:CH_4 ice 149
10.1 Introduction . . . 150
10.2 Experimental setup . . . 150
10.3 Experimental results and discussion . . . 154
  10.3.1 Photon-induced chemistry of a H_2O:CH_4 ice analog . . . 156
  10.3.2 Photon-induced desorption from a H_2O:CH_4 ice analog . 158
10.4 Astrophysical implications . . . 161
10.5 Conclusions for Chapters 9 and 10 . . . 163

11 Thermal processing of circumstellar and cometary ice analogs 169
11.1 Introduction . . . 169
11.2 Experimental setup . . . 171
11.3 Experimental results and discussion . . . 173
  11.3.1 Mixture effects on TPD of a pre-cometary ice analog . . . 173
  11.3.2 Binding energies of pure ices . . . 175
  11.3.3 Entrapment of molecules in multicomponent ices . . . 178
  11.3.4 Mixture effects on IR spectra of a pre-cometary ice analog 179
  11.3.5 Evolution of IR spectra during thermal annealing . . . 182
11.4 Astrophysical implications . . . 186
  11.4.1 Circumstellar ices . . . 188
  11.4.2 Cometary ices . . . 189
  11.4.3 The ESA-Rosetta cometary mission . . . 191
11.5 Conclusions . . . 193

V Results - Gas 197

12 Upper limits on the H_2S_2, $HS^{\cdot}_2$, and S_2 abundances toward the low-mass warm core IRAS 16293-2422 199
12.1 Introduction . . . 199
12.2 Observations . . . 201
  12.2.1 Laboratory spectroscopy of sulfur-containing molecules in the gas phase . . . 202
12.3 Results . . . 203
  12.3.1 Detection of species not containing sulfur . . . 203
  12.3.2 Non-detection of H_2S_2, $HS^{\cdot}_2$ or S_2 . . . 206
  12.3.3 Upper limits to the abundances of H_2S_2, $HS^{\cdot}_2$ and S_2 . . . 207
12.4 Discussion . . . 208
  12.4.1 Comparison with laboratory H_2S-bearing ice irradiation experiments . . . 208
  12.4.2 A chemical model of H_2S_2, $HS^{\cdot}_2$ and S_2 in IRAS16293-2422 209
12.5 Conclusions . . . 212

13 Detection of CH_3NCO toward the low mass warm core IRAS16293-2422 215
13.1 Introduction . . . 215
13.2 Observations . . . 216
13.3 Results . . . 217
13.3.1 Detection of CH_3NCO . . . 217
13.3.2 Chemically-related species: HNCO and NH_2CHO . . . 219
13.3.3 Comparison with other sources . . . 220
13.4 Conclusions . . . 221

VI Appendix 223

List of Tables

3.1 Ranges of observed abundances of the six securely identified species in interstellar ices within different environments. Adapted from Boogert et al. (2015). 33

4.1 Values used in Eq. 4.8 to derive the relation between $k^{*}_{QMS} \cdot S$ and m/z. 53

8.1 IR feature used to calculate the column density of each component (frequencies and band strengths for pure ices at 8 K). 112
8.2 Values used in Eq. 4.3 to convert integrated QMS signals to column densities of desorbed molecules. 113
8.3 Evolution of the ice and gas column densities of CO_2 and its photoproducts during UV irradiation of a pure CO_2 ice analog. 119
8.4 Initial destruction or formation cross sections of the species during UV irradiation of a pure CO_2 ice analog. 121
8.5 Evolution of the CO and O_2 photodesorption yields during UV irradiation of a pure CO_2 ice analog. 123

9.1 IR feature used to calculate the column density of selected ice components. Frequencies and band strengths for pure ices at 10 K, except for C_2H_5OH (see text). 132
9.2 Mass fragments used to monitor potentially desorbing species into the gas phase. 134
9.3 UV photoprocessing experiments of pure C_2H_5OH ices. 137
9.4 Values used in Eq. 10.2 to convert integrated QMS signals for the mass fragments into column densities of desorbing molecules. 142
9.5 Evolution of the photon-induced desorption yields during UV irradiation of a pure C_2H_5OH ice. 143

10.1 IR feature used to calculate the column density of selected ice components. Frequencies and band strengths for pure ices at 10 K. 151
10.2 Mass fragments used to monitor potentially desorbing species into the gas phase. 153
10.3 UV photoprocessing experiments of H_2O:CH_4 ice analogs. 155
10.4 Values used in Eq. 10.2 to convert integrated QMS signals in experiments 7 - 10 into column densities of desorbed molecules. 159

10.5 Evolution of the photodesorption yields during UV irradiation of a binary H_2O:$^{13}CH_4$ ice analog in exp. 9 (results were similar in experiments 7, 8, and 10). 162

11.1 IR feature used to calculate the column density of each component (frequencies and band strengths for pure ices at 8 K). 172
11.2 Composition of the ice mixture measured with FTIR spectroscopy at 8 K. For each experiment, the first row indicates the abundance (by number of molecules) in percent relative to water, while the second row shows the absolute abundance (also in percent). 173
11.3 Temperature of desorption peaks in experiments E11 (Fig. 11.1c, heating rate = 1 K/min) and E10 (Fig. 11.1b, heating rate = 2 K/min). Temperature of the ammonia desorption peak in E10 (Fig. 11.1b) is not well constrained due to the shape of the curve. Temperatures of volcano and co-desorption peaks are approximate, since they do not coincide exactly for all the species. 177
11.4 Desorption rate parameters for the five pure ices. 178
11.5 Estimation of heliocentric distance, temperature, and heating rate of comet 67P/Churyumov-Gerasimenko during its orbit, as calculated using orbital parameters provided online by the Jet Propulsion Laboratory (NASA) and equation 5. 192

12.1 Targeted transitions and observational results 204
12.2 Upper limits to the column densities and molecular abundances of H_2S_2, $HS^{\cdot}_2$, and S_2 estimated from the observations, and abundances calculated in laboratory experiments. 207
12.3 Models run for the chemistry of H_2S_2, $HS^{\cdot}_2$ and S_2 toward IRAS16293 211
12.4 Comparison of the modelled H_2S_2, $HS^{\cdot}_2$ and S_2 abundances with the upper limits derived from the observations. 212

13.1 Detected CH_3NCO unblended lines in IRAS16293 B. 217
13.2 Comparison of the CH_3NCO/HNCO and CH_3NCO/NH_2CHO ratios measured in IRAS16293 B, SgrB2(N), Orion KL and comet 67P. 220

List of Figures

3.1 *Left:* the dense cloud Barnard 68 in the Milky Way. Dense clouds are seen in silhouette against star fields (see Section 3.1). *Right:* the NGC 604 HII region in the Triangle Galaxy, seen as an emission nebula. Images are adapted from eso.org, and spacetelescope.org, respectively. . . 28

3.2 The cycle of matter in the ISM. Numbers indicate the chapters of this thesis dedicated to the study of different processes in those particular stages of the cycle (see Sect. 3.4). Picture composition made with images adapted from apod.nasa.gov provided by Gustavo A. Cruz-Díaz. . 29

3.3 The 3.4, 6.85, and 7.25 μm features corresponding to carbonaceous dust particles observed in the diffuse ISM toward the Galactic Center IRS7 line of sight (Dartois et al. 2004) are compared to the spectra of three theoretical (A, B, and C, Dartois et al. 2005) and one laboratory (a-C:H, Dartois et al. 2005) analogs (see also Fig. 3.4). Adapted from Dartois et al. (2005). 31

3.4 *Left:* Representation of three theoretical analogs of the carbonaceous dust particles observed in the diffuse ISM with different contributions from aliphatic, olefinic and aromatic substructures. *Right:* Representation of a plasma-produced a-C:H analog of the carbonaceous dust particles observed in the diffuse ISM. Adapted from Dartois et al. (2005). 31

3.5 Comparison between the ISO-SWS01 spectrum of RAFGL 7009S and a laboratory transmittance spectrum of an ice analog multiplied by the estimated continuum. Some identified molecular transitions are labeled (Dartois & d'Hendecourt 2000). 33

4.1 Schematic cartoon of the ISAC experimental setup. The Titanium - sublimation pump is no longer in use. From Cruz-Díaz (2014a). 43

4.2 Schematic representation of the main chamber in the ISAC experimental set-up. The UV spectrophotometer was not used during the experimental simulations described in this thesis. From Muñoz Caro et al. (2010). 44

4.3 Schematic representation of the SICAL-X setup. From Alata et al. (2014). 45

4.4 *Left:* Picture of the sample holder with the substrate (deposition window) at the end of the cold finger in ISAC, covered by the radiation shield. The quartz tube used as optical guide for the photons is also shown. *Right:* The region irradiated by the visible photons from the MDHL approximately coincides with the size of the substrate, and the same is expected for the VUV photons. From Cruz-Díaz et al. (2014a). . 45

4.5 Emission spectrum of the MDHL for the working conditions in ISAC (see text). From Cruz-Díaz et al. (2014b). 46

4.6 Emission spectrum of the MDHL in the 116 - 183 nm region (red) compared to the secondary UV-field expected in dense cloud interiors (black, from Gredel et al. 1989). 47

4.7 The three vibrational modes of a water molecule. From lsbu.ac.uk . . . 48

4.8 *Left*:Evolution of the m/z = 28 QMS signal corresponding to the photodesorption of CO during UV irradiation of a pure CO ice. The ion current in the y-axis corresponds, approximately, to the partial pressure (mbar) in the main chamber. Dotted lines represent the baselines used to calculate $A(28)$ in every irradiation period. Note that the y-axis is on a logarithmic scale. *Middle*: Evolution of the C=O stretching mode of CO at 2139 cm^{-1} during UV irradiation of pure CO ice. Differences in the column densities after every period of irradiation correspond to $N(CO)$ in Eq. 4.4. *Right*: Relation between $A(28)$ and $N(CO)$. The solid line is a linear fit. 52

4.9 Relation between $k^*_{QMS} \cdot S(m/z)$ and m/z. The solid line is an exponential fit. 53

4.10 Typical antenna beam pattern. From embedded.com 55

5.1 Configuration of the measurement. 65

5.2 IR transmittance spectrum of an a-C:H analog (*left panel*), and an a-C:D analog (*right panel*) deposited on an MgF$_2$ substrate.Spectra were collected at 110 K. 69

5.3 Measured m/z = 4 ion current corresponding to the outgoing D$_2$ flux during three experiments performed at ∼140 K (red solid line), ∼130 K (yellow solid line), and ∼120 K (blue solid line) on a 3.4 μm thick a-C:D analog. Irradiation starts at $t = 0$. 70

5.4 Normalized m/z = 4 ion current after background substraction (equivalent to the normalized D$_2$ flux) during three experiments performed at ∼140 K (*left panel*), ∼130 K (*middle panel*), and ∼120 K (*right panel*) on a 3.4 μm thick a-C:D analog. Black solid lines correspond to the normalized D$_2$ flux during irradiation (irradiation starts at $t = 0$), while colored solid lines correspond to 1 - normalized D$_2$ flux after irradiation (irradiation stops at $t = 0$). 71

5.5 Evolution of the normalized m/z = 4 ion current (black dots), equivalent to the normalized D_2 flux at the $x = l$ surface, during (*left panel*) and after (*middle* and *right panels*) VUV irradiation of a 2.6 μm a-C:D analog at 130 K. Theoretical models fitting the experimental data are presented (blue solid lines), along with the derived diffusion coefficient D and the 1σ associated error. The model shown in the *left panel* is described by Eq. 5.6. The *middle* and *right panels* show the models described by Equations 5.11 and 5.12, respectively. The free parameter p of the latter is an indicator of how close the model is to the one described by Eq. 5.11. The χ^2 values associated with the fits of the experimental data during and after irradiation cannot be directly compared since they are not normalized. 71
5.6 Evolution of the experimental diffusion coefficient D for the diffusion of D_2 molecules through a-C:D analogs with the temperature (black circles), along with the model described by Eq. 5.3 that best fits the experimental data (blue solid line), and the associated 3σ limits (blue dashed lines). 73
5.7 Additional diffusion coefficient D' derived for the experiments with a-C:D analogs of thickness 5.2 μm (red circles), 3.4 μm (yellow circles), 2.6 μm (green circles), 1.3 μm (blue circles), and 0.2 μm (purple circles), using the model described by Eq. 5.12. 74
5.8 Evolution of the experimental diffusion coefficient D for the diffusion of H_2 molecules through a-C:H analogs with the temperature (black circles), along with the model described by Eq. 5.3 that best fits the experimental data (blue solid line), and the associated 3σ limits (blue dashed lines). 75
5.9 Additional diffusion coefficient D' derived for the experiments with a-C:H analogs of thickness 2.2 μm (green circles), and 0.9 μm (blue circles), using the model described by Eq. 5.12. 75

6.1 Schematic representation of the Interstellar Photoprocess System, kindly provided by Y.J. Chen. 85
6.2 TPD experiment as seen by the laser interference to study the desorption of a CO ice sample (red) and the warming up of the KBr substrate alone (blank experiment, black). 86
6.3 IR measurement of the CO ice during the TPD experiment, showing the number of monolayers on the surface (1 ML=10^{15} molecules/cm^2). . 86
6.4 TPD experiment using QMS to record the gas-phase CO molecules. . . . 87
6.5 The deposition of the CO ice on top of the ASW as the temperature decreased from 80 K to 8 K was monitored by a QMS that measured the ion current due to the CO molecules in the gas phase. 89
6.6 FTIR spectroscopy in transmittance measured the number of monolayers of deposited CO. 90
6.7 TPD experiment using the QMS corresponding to the CO ice accreted during cool-down of the substrate covered with ASW. 91
6.8 Binding energies of CO molecules as function of (effective) neighbors. The points correspond to the calculations from Karssemeijer et al. 2014b. 94

6.9 Diffusion barrier to go from a initial site with energy Ei to a final site with energy Ef for the case where Ei<Ef (*left panel*), and Ei>Ef (*right panel*). 95

6.10 CO adsorption on water surface at 14 K. Each grid is taken at a time interval of 20 s. Each square is a CO molecule and the color corresponds to its binding energy in Kelvins (blue ∼1200 K, red ∼400 K). The binding energy of CO molecules on the first level of the grid is higher, because CO molecules are bound to water substrate. This figure illustrates the range of binding energies of individual CO molecules during deposition at 14 K 97

6.11 Same as 6.10 but with ice deposited on water ice surface as the temperature is decreased from 80 K. This grid shows the ice structure after depositing 10 layers. 98

6.12 Simulated TPD from Monte Carlo simulations mimicking the experiments 1 (IPS) and 2 (ISAC). 99

6.13 Binding energy of CO molecules arriving on a CO ice at T=6 K and $n_H=10^6$ cm^{-3}. The three curves show the binding energies as the coverage increases (1000, 2000 and 5000 CO molecules sent on the surface). 100

6.14 Resulting structure and binding energies of the CO ices at T=6 K and $n_H=10^6$ cm^{-3}. 100

6.15 Density temperature profile of pre-stellar cores from Keto & Caselli 2010.101

6.16 *Left:* Abundances of C^+, C, CO, O and H_2O at 10^4 years as function of extinction in our pre-stellar core model. *Right:* CO abundances derived form our model considering binding energies of CO ranging between 300K and 830 K. 102

6.17 *Left:* Abundances of C^+, C, CO, O and H_2O at 10^5 years as function of extinction in our pre-stellar core model. *Right:* CO abundances derived form our model considering binding energies of CO of ranging between 300K and 830 K. 102

8.1 Evolution of two IR bands of CO_2 during UV irradiation of a pure CO_2 ice analog. *Left*: C=O stretching mode at 2344 cm^{-1}. *Right*: degenerate bending modes at ∼658 cm^{-1} 113

8.2 Evolution of the IR bands corresponding to the photoproducts CO and CO_3 during UV irradiation of a pure CO_2 ice analog. 114

8.3 Evolution of the IR feature corresponding to the O_3 photoproduct during UV irradiation of pure CO_2 ice. 114

8.4 Photodesorption of CO, O_2, and CO_2 during UV irradiation of pure CO_2 ice. The m/z = 44 signal corresponding to CO_2 molecules is affected by contamination (see text). Ion current in the y-axis corresponds, approximately, to the partial pressure (mbar) in the main chamber. Note that the y-axis is on a logarithmic scale. 115

8.5 Signals detected by the QMS during irradiation in the main chamber of ISAC without an ice sample. The ion current in the y-axis corresponds, approximately, to the partial pressure (mbar) in the main chamber. Note that the y-axis is on a logarithmic scale. 116

8.6 Photodesorption of ^{13}CO, O_2 and $^{13}CO_2$ during UV irradiation of pure $^{13}CO_2$ ice. The ion current in the y-axis corresponds, approximately, to the partial pressure (mbar) in the main chamber. Note that the y-axis is on a logarithmic scale. 117

8.7 Temperature-programmed desorption curves of CO_2 and its photoproducts after UV irradiation of a pure CO_2 ice. The ion current in the y-axis corresponds, approximately, to the partial pressure (mbar) in the main chamber. Note that the y-axis is on a logarithmic scale. 118

8.8 Evolution of the ice and gas column densities of CO_2 and its photoproducts during UV irradiation of a pure CO_2 ice analog. O_2 (ice) column density is an estimated upper limit assuming that all remaining O atoms are locked in O_2 molecules. 120

9.1 Mass spectrum of ethanol in our setup. 133

9.2 Mass spectrum of methanol in our setup. 135

9.3 Evolution of the IR spectrum of the ice sample during UV photoprocessing in experiment 2 (see Table 9.3) conveniently split in four regions. Results were similar in experiment 1. **a)** A new feature appears at 3005 cm^{-1} (dashed line) between the O-H and C-H stretching bands of C_2H_5OH, which is attributed to the formation of CH_4. This species also displays a more intense band near 1302 cm^{-1}, shown in panel c. **b)** Formation of CO_2 and CO leads to the appearance of two C-O stretching bands at 2340 cm^{-1} and 2136 cm^{-1} (dashed lines), respectively. **c)** Dashed lines at 1715 cm^{-1}, 1349 cm^{-1}, and 1302 cm^{-1} indicate new features due to the formation of photoproducts (probably H_2CO, CH_3CHO, C_2H_6, and CH_4; see text). A broad band on the red side of the 1715 cm^{-1} peak may indicate the presence of H_2O. **d)** The intensity of the C-O stretching band of C_2H_5OH at 1048 cm^{-1} (dashed line) decreases as the ice is processed. 139

9.4 TPD curves displaying the thermal desorption of photoproducts through selected mass fragments at the end of experiment 2 (see Table 9.3) in red, compared to the blank experiment with no irradiation (black). **a)** TPD curves of the m/z=27 mass fragment, corresponding to the $C_2H_3^+$ fragment of C_2H_6. A desorption peak at $\sim$75 K (dashed line) confirms the presence of ethane in the processed ethanol ice (desorption of a pure ethane ice takes place above 60 K according to Öberg et al. 2009). **b)** TPD curves of the m/z=30 mass fragment, corresponding to the molecular ion of H_2CO. The desorption peaking at $\sim$121 K (dashed line) confirms the formation of formaldehyde during UV photoprocessing of a pure ethanol ice (see text). **c)** TPD curves of the m/z=31 mass fragment corresponding to the CH_3O^+ fragment of CH_3OH. Since no excess in the desorption is detected at $\sim$145 K compared to the blank, formation of methanol during UV photoprocessing of a pure ethanol ice is negligible. Desorption at $\sim$127 K (dashed line) is probably due to an earlier ethanol desorption triggered by less polar and more volatile components in the ice matrix that were not present in the blank experiment (mainly formaldehyde and acetaldehyde), since it is shared with the m/z=45 mass fragment (blue). **d)** TPD curves of the m/z=43 mass fragment, corresponding to the CH_3CO^+ fragment of CH_3CHO. The desorption peaking at $\sim$116 K (dashed line) confirms the formation of acetaldehyde during UV photoprocessing of a pure ethanol ice (see text). 140

9.5 Photon-induced desorption of several photoproducts during irradiation of a pure ethanol ice in experiment 2, see Table 9.3. Results were similar in experiment 1. Irradiation intervals are indicated with vertical dashed lines. Signal due to rotation of the sample holder between irradiation intervals was omitted. **a)** Phochemidesorption of formaldehyde/ethane (see text) observed with mass fragments m/z=29 and m/z=30. **b)** Photochemidesorption of ethane observed with mass fragment m/z=27. DIET photodesorption was detected for H_2O, CO and CH_4 (m/z=18, m/z=28 and m/z=15, respectively). Ion currents of different mass fragments are offset for clarity. 141

10.1 Mass spectrum of methanol in our setup. 151

10.2 Evolution of the IR spectrum of the H_2O:CH_4 ice mixture during UV photoprocessing in experiment 6, see Table 10.3. Results were similar in experiments 3 - 5. **a)** Evolution of the O-H stretching band of H_2O (broad band peaking at $\sim$3280 cm^{-1}), and the C-H stretching band of CH_4 (in the red side of the former). **b)** Formation of CO_2 and CO leads to the appearence of two C-O stretching bands at 2342 cm^{-1} and 2137 cm^{-1}, respectively (dashed lines). Negative absorbances are due to the atmospheric correction applied by the FTIR software, but the band is due to solid CO_2, as the peak position indicates. **c)** Evolution of the O-H deformation band of H_2O. The apearance of a shoulder at $\sim$1710 cm^{-1} is probably due to the formation of H_2CO. **d)** Evolution of the C-H deformation band of CH_4 at 1300 cm^{-1}. The new feature at 1016 cm^{-1} is due to the formation of methanol. 156

10.3 Evolution of the IR spectrum of the H_2O:CH_4 ice mixture during UV photoprocessing in experiment 9, see Table 10.3. Results were similar in experiments 7, 8, and 10. **a)** Formation of $^{13}CO_2$ and ^{13}CO leads to the appearence of two C-O stretching bands at 2277 cm^{-1} and 2092 cm^{-1}, respectively (dashed lines). **b)** Evolution of the O-H deformation band of H_2O. **c)** Evolution of the C-H deformation band of CH_4 at 1292 cm^{-1}. The new feature at 1000 cm^{-1} is due to the formation of methanol. . . . 157

10.4 **a)** TPD curve of the m/z=30 mass fragment, corresponding to the molecular ion of H_2CO, after irradiation in experiment 3 (red) compared to the blank (black). A desorption peak at $\sim$112 K (dashed line) confirms the formation of formaldehyde. **b)** TPD curve of the m/z=31 mass fragment, corresponding to the molecular ion of $H_2^{13}CO$, after irradiation in experiment 7 (red) compared to the blank (black). A desorption peak at $\sim$113 K (dashed line) confirms the formation of formaldehyde. . . . 157

10.5 Photon-induced desorption of formaldehyde observed with mass fragments m/z=29 and m/z=30 (*left panel*), and carbon monoxide (m/z=28 in *right panel*) during UV irradiation of a H_2O:CH_4 ice analog in experiment 5. Results were similar in exp. 3, 4, and 6. Ion currents of different mass fragments are offset for clarity. The black solid line represent an average of the corresponding ion current, shown to better evaluate the shape of the signal. Irradiation intervals are indicated with dashed vertical lines. 160

10.6 Photon-induced desorption of $H_2^{13}CO$ (m/z=30 and m/z=31 in *left panel*) and ^{13}CO (m/z=29 in *right panel*) during UV irradiation of a H_2O:$^{13}CH_4$ ice analog in experiments 10 and 7, respectively. Results were similar for experiments 8 and 9. Ion currents of different mass fragments are offset for clarity. Black solid lines represent an average of the corresponding ion currents, as shown to better evaluate the shape of the signals. Irradiation intervals are indicated with dashed vertical lines. . 160

11.1 The TPD curves of each component in experiments **a)** E1-E5 (pure ices), **b)** E10 (pre-cometary ice mixture with heating rate = 2 K/min). Desorption of a molecule with mass fragment m/z=15 at $T < 60$ K does not correspond to NH_3, since that feature is not shared with the m/z=17 fragment (not shown for clarity), and it may be due to a contaminant, **c)** E11 (pre-cometary ice mixture with heating rate = 1K/min). Temperatures of desorption peaks are indicated. Ion current in the y-axis corresponds approximately to the partial pressure (mbar) in the main chamber. Note that the y-axis is on a logarithmic scale. 176

11.2 The TPD curves of each component in experiments **a)** E6, **b)** E7, **c)** E10, **d)** E8, and **e)** E9. The concentration of CH_3OH in the mixture increases from **a)** to **e)**. Ion current in the y-axis corresponds approximately to the partial pressure (mbar) in the main chamber. Note that the y-axis is on a logarithmic scale. 180

11.3 *Black:* IR spectra of a pre-cometary ice mixture (E11) registered at 8 K. *Red:* Sum of the IR spectra of individual pure ice components (E1-E5) registered at 8 K; they were multiplied by a factor to reproduce the composition of the pre-cometary ice mixture. 181

11.4 Evolution of the C=O stretching band of CO during the warm-up of a pre-cometary ice mixture (experiment E10). 183

11.5 Evolution of the IR bands of CO_2 during the warm-up of a pre-cometary ice mixture (experiment E11). Left: C=O stretching mode at ~ 2342 cm^{-1}. Right: bending mode at ~ 655 cm^{-1}. 184

11.6 Evolution of the IR bands of H_2O during the warm-up of a pre-cometary ice mixture (experiment E10). Left: O-H stretching mode at ~ 3650 cm^{-1}. Negative absorbances are due to the atmospheric compensation applied by the spectrometer software. Right: O-H bending mode at $\sim$ 1654 cm^{-1}. 185

11.7 Evolution of the umbrella mode of NH_3 and the C-O stretching mode of CH_3OH during the warm-up of a pre-cometary ice mixture (experiment E11). 186

11.8 The C-O stretching band of CH_3OH (black) fitted with the sum of three Gaussians (red), which account for: mixed methanol (green dotted, centered at 1016 cm^{-1}), segregated methanol (purple dotted, centered at 1025 cm^{-1}), and methanol forming a type II clathrate hydrate with water molecules (blue dotted, centered at 1034 cm^{-1}). A fourth Gaussian has been used to take into account the contribution of the blue wing of the H_2O librational band (black dotted). The IR spectra correspond to a pre-cometary ice analog (E11) at a) T = 110 K, b) T = 150 K, and c) T = 160 K. The χ^2 parameter is indicated for each fit. 187

11.9 Evolution of the contribution of mixed methanol (green), segregated methanol (purple), and methanol forming a type II clathrate hydrate (blue) to the total area of the C-O stretching band of CH_3OH during warm-up of a pre-cometary ice mixture (E11), according to fit with three Gaussians of the IR band. Temperatures for which the fit was done are indicated. Figure 11.8 shows three selected fits as an example. 188

11.10 Evolution of the C-H stretching modes of CH_3OH during the warm-up of a binary mixture (experiment E9). Spectra are offset for clarity. 189
11.11 Schematic representation of thermal annealing process of ice mantles in circumstellar regions based on our experimental results for the warm-up of a pre-cometary ice mixture (H_2O:CO:CO_2:CH_3OH:NH_3 = 100:10-20:10-20:5:5). Red lines represent the temperature ranges at which the species used in our pre-cometary ice analogs desorb. Approximate positions of desorption peaks are indicated with vertical red lines. Desorption of NH_3 and CH_3OH prior to volcano desorption takes place when their abundance relative to water is above $\sim$ 3 % in the ice. Blue lines represent the temperature ranges at which structural changes in the ice occur. The top temperature scale corresponds to a heating rate of 1-2 K/min (used in experiments E10 and E11 with our pre-cometary ice mixtures and also suited to the "flash-heating" of dust grains during the periodic radial excursions considered in the fluctuating X-wind model for CAIs and chondrules formation). The bottom temperature scale corresponds to a first approximation to grains at a certain distance heated with a heating rate of 1 K/century, see text for details. 190

12.1 Spectral windows where the H_2S_2 transitions listed in Table 12.1 should be detected. Vertical dashed lines mark a central radial velocity of v_{lsr} = 3.2 km s^{-1}, assumed for IRAS16293 A (Jørgensen et al. 2011). 205
12.2 Spectral windows where the HS_2 (top panels) and S_2 (bottom panels) transitions listed in Table 12.1 should be detected. Vertical dashed lines mark a central radial velocity of v_{lsr} = 3.2 km s^{-1}, assumed for IRAS16293 A (Jørgensen et al. 2011). 206
12.3 Time-dependent evolution of abundances of selected sulfur-bearing species in IRAS16293 according to the UCL_CHEM code for models (a), (b), (c), and (d), whose most important parameters are shown in Table 12.3. Colored lines correspond to the targeted species. Black solid line is for H_2S. Black dashed and dotted lines correspond to SO and SO_2, respectively. 209

13.1 CH_3NCO unblended lines measured toward IRAS16293 B with ALMA (solid black). Transitions are shown in every panel, while their rest frequencies are reported in Table 13.1. The synthetic LTE spectrum generated by MADCUBAIJ is overplotted in red. 218
13.2 Integrated intensity maps of two representative CH_3NCO unblended lines observed toward IRAS16293 B. Black contours indicate 50% and 90% of the peak line emission, while white contours indicate 20%, and 80% of the continuum peak emission at 232 GHz. The rest frequency and E_u of the transitions are shown in every panel (see also Table 13.1). Beam sizes are shown in the bottom right corner. 219

Chapter 1

Resumen

El objetivo de esta tesis doctoral es el de profundizar en el conocimiento de ciertos procesos que tienen lugar en el medio interestelar (MI) relacionados con el procesamiento energético de granos de polvo interestelares y los mantos de hielo que los recubren, así como con la interacción entre las fases sólida y gaseosa del MI. En particular, los procesos de desorción inducida por fotones de las moléculas del hielo en las regiones frías del MI son necesarios para explicar las abundancias de ciertas especies observadas en la fase gaseosa. Se trata por tanto de un caso paradigmático de la interacción entre las dos fases del MI y su importancia está fuera de toda duda. La parte central de esta tesis (Parte IV) se centra en el estudio de estos procesos.

En astrofísica, desde hace tiempo no sólo se utilizan las observaciones astronómicas, sino que también se usan simulaciones experimentales en condiciones relevantes para la astrofísica y simulaciones teóricas para complementar la información obtenida a través de las observaciones y conseguir así un mejor entendimiento de los procesos que ocurren en el espacio en general y el MI en particular. Los resultados presentados en esta tesis han sido obtenidos combinando estas tres metodologías, aunque la astrofísica de laboratorio ha tenido un peso mayor. En las Partes III y IV se presentan diversas simulaciones experimentales llevadas a cabo con una cámara de alto vacío y otra de ultra-alto vacío. La presión en estas cámaras está un poco por encima (en el caso del alto vacío) o es directamente similar (en ultra-alto vacío) a la de las regiones más densas del MI. Además, gracias a la utilización de un criostato, se pueden alcanzar las temperaturas típicas que se observan en las regiones más templadas y frías del MI (por debajo de los 100 K, y rondando los 10 K en las partes más frías). En estas condiciones se pueden formar análogos de las partículas de polvo y hielo que se encuentran en el MI y simular cómo se procesan energéticamente (por la acción de fotones UV, en la mayoría de capítulos, aunque también se ha estudiado el procesamiento térmico). Durante estas simulaciones experimentales las muestras sólidas se monitorizan con un espectrómetro infrarrojo por transformada de Fourier (FTIR), y las moléculas que pasan a la fase gaseosa se pueden detectar con un cuadrupolo de masas (QMS). De esta manera podemos reproducir los procesos que suceden en el MI, pero en condiciones controladas dentro de un laboratorio en la Tierra, y sabiendo en cada momento cómo evolucionan la fase sólida y la fase gaseosa. En la Parte V, por otro lado, se usan observaciones astronómicas realizadas con radio telescopios (tanto con una antena única como usando radio interferómetros). Estos telescopios son capaces de detectar las líneas emitidas por las moléculas de forma espontánea en las regiones templadas y frías del MI. Tanto la astrofísica de laboratorio como la observacional se presentan en la Parte II, aunque también se han usado modelos teóricos de forma puntual para apoyar los resultados obtenidos con los experimentos o las observaciones.

Como ya se ha mencionado, los resultados se presentan en las Partes III, IV, y V, usando el ciclo evolutivo de la materia en el MI como hilo conductor.

En la Parte III (**Capítulo 5**) se presenta el estudio experimental del procesamiento por fotones UV de partículas análogas a los granos de polvo carbonáceos que se encuentran en el MI, a distintas temperaturas entre los 90 K y los 170 K. La irradiación produce la formación de moléculas de H_2 o D_2 (según qué precursor se haya utilizado para formar los análogos) que luego difunden a través de las partículas y pasan a la fase gaseosa. Este proceso está controlado por el coeficiente de difusión D, cuya dependencia con la temperatura fue el objeto de estudio, obteniéndose energías de activación para la difusión de $E_D(H_2) = 1660 \pm 110$ K y $E_D(D_2) = 2090 \pm 90$ K. Estas altas energías de activación hacen que la difusión disminuya mucho con la temperatura, por lo que es probable que los granos de polvo que se encuentran en las regiones dominadas por fotodisociación (PDRs, donde probablemente ocurre este proceso) se calienten puntualmente por el impacto de rayos cósmicos para así permitir la salida de las moléculas de H_2.

Es en la superficie de estos granos de polvo donde se forman los mantos de hielo en las regiones más frías y más densas del MI (Parte IV). El proceso de acreción de los hielos se revisa en el **Capítulo 6** combinando simulaciones experimentales y teóricas. Se demuestra que las condiciones en las que se forman los hielos de CO afectan a las energías de enlace entre las moléculas, y por tanto a la morfología de los mismos. Sin embargo, las diferencias se desvanecen cuando los hielos son calentados.

Después de esta pequeña incursión en la formación de los hielos, los **Capítulos 7 - 10** están dedicados a su procesamiento con fotones UV, prestando especial atención a los procesos de desorción inducidos por los fotones, que consituyen el núcleo de la tesis. Tres tipos de hielo distintos se irradiaron a una temperatura de 8 K. En el **Capítulo 8** se estudia la irradiación de un hielo puro de CO_2. Gracias a la combinación del espectrómetro IR (que observa la composicin del hielo) y el cuadrupolo de masas (que monitoriza el gas) se pudo obtener una cuantificación completa de los procesos fotoquímicos (formación de CO, CO_3, O_2, y O_3) y de fotodesorción (de CO, O_2, y en menor medida CO_2). En los **Capítulos 9 y 10** se usaron un hielo puro de etanol, y una mezcla binaria rica en agua con moléculas de metano más realista. El objetivo de estos experimentos era explorar la posible formación (a temperaturas muy bajas an torno a 8 K) y la consiguiente desorción de moléculas de metanol y otras especies relacionadas. La formación de metanol no se observó durante los experimentos de irradiación del hielo de etanol, pero sí la de otros productos (H_2CO, CH_3CHO, H_2O, CH_4, C_2H_6, CO, y CO_2). La química de la mezcla H_2:CH_4 fue más simple: sólo se observó la formación de H_2CO, CO y CO_2, además de la de metanol, que sí se produjo en esta serie de experimentos aunque no se detectó su fotodesorción. Una de las principales conclusiones de esta tesis es que la fotodesorción de los fotoproductos puede seguir dos patrones distintos a medida que aumenta el tiempo de irradiación. Algunos fotoproductos fotodesorben directamente después de su formación en la superficie de los hielos (siempre que se formen con la suficiente energía cinética como para romper los enlaces intermoleculares), como el H_2CO formado durante la irradiación de la mezcla H_2:CH_4. A este proceso se le ha denominado fotoquimidesorción, y está asociado a una fotodesorción que se mantiene constante para cualquier tiempo de irradiación. Otros productos, en cambio, pueden fotodesorber más tarde gracias a la transferencia de energía por parte de otra molécula distinta que se encuentre bajo la superficie del hielo y que haya absorbido un fotón previamente. Si la fotodesorción ocurre a través de este mecanismo indirecto, las moléculas de un fotoproducto determinado se pueden acumular en el hielo antes de fotodesorber, lo cual lleva a un aumento de la cantidad de moléculas que fotodesorben con el tiempo de irradiación. Esto le ocurre, por ejemplo, a las moléculas de CO que se forman al irradiar los hielos de CO, C_2H_5OH y H_2O:CH_4. Los distintos mecanismos de fotodesorción están presentados en el **Capítulo 7**.

En el **Capítulo 11** se estudia, por otro lado, el procesamiento térmico de un análogo de hielo más astrofísico: una mezcla rica en agua formada por un total de 5 componentes. Durante los experimentos se observaron picos de desorción térmica para todos los componentes a temperaturas muy similares a las que se miden cuando se calientan los hielos puros. Al mismo tiempo, una parte de las moléculas se queda atrapada en la estructura del hielo, y desorbe posteriormente en tres etapas: co-desorbiendo con metanol (esta co-desorción no estaba documentada), desorbiendo justo después del cambio de fase de agua amorfa a agua cristalina cúbica, y co-desorbiendo finalmente con el agua.

Por último, en la Parte V se presentan osbervaciones realizadas con el radio telescopio APEX 12-m, y el interferómetro ALMA para intentar detectar diversas especies en una región de formación estelar: el hot corino IRAS16293-2422. En el **Capítulo 12** no se pudo confirmar la presencia de H_2S_2, $HS_2^{\cdot}$, y S_2 (se piensa que pueden formarse en los mantos de hielo y después desorber), pero se dan límites superiores a sus abundancias ($\leq 8.1\times10^{-9}$, $\leq 1.1\times10^{-8}$, y $\leq 2.9\times10^{-7}$, respectivamente). Las simulaciones teóricas llevadas a cabo con el modelo químico UCLCHEM indican que estas especies podrían formarse efectivamente en los mantos de hielo, pero que las reacciones químicas en la fase gas una vez desorben podrían disminuir sus abundancias hasta límites indetectables. Por otro lado, en el **Capítulo 13** se presenta la primera detección de CH_3NCO (una molécula con interés prebiótico) en los alrededores de una protoestrella de tipo solar, con una abundancia de $(1.4\pm0.1)\times10^{-10}$.

Chapter 2

Summary

The aim of this PhD thesis is to expand our knowledge of particular processes taking place in the interstellar medium (ISM). These processes are related in one way or another to the energetic processing of the interstellar dust grains and the ice mantles on top of them, and to the interplay between the solid and the gaseous phases of the ISM. In particular, photon-induced desorption processes of ice molecules in cold regions of the ISM are needed to explain the observed gas-phase abundances of several species. It is therefore a paradigmatic case of the interaction between the two phases of the ISM, and its importance is nowadays beyond any doubt. The core of this thesis (Part IV) is devoted to the study of such processes.

Astrophysics is no longer about observations only. Both experimental simulations under astrophysically relevant conditions, and theoretical models are used to complement the observations and get a better understanding of the processes that are taking place in space and the ISM in particular. The results presented in this thesis have been obtained using a combination of these three methodologies, although more attention is paid to laboratory astrophysics. Parts III (Chapter 5 and IV (Chapters 6 - 11) deal with experimental simulations carried out in a high-vacuum (HV) and an ultra-high-vacuum (UHV) chambers. These chambers have base pressures slightly over (in the case of the HV) or similar (UHV) to those found in the densest regions of the ISM. A closed-cycle helium cryostat is used in both cases to reach the temperatures typically found in the cold and warm ISM (below 100 K, and as low as 10 K in the densest and coldest regions). Under these conditions, dust or ice analogs can be grown onto a substrate in order to simulate the energetic processing (photoprocessing in most chapters, but also thermal processing) of the solid component of the ISM. During these experimental simulations, the solid sample is monitored with a Fourier transform infrared (FTIR) spectrometer, while the molecules desorbing from the solid samples to the gas-phase are detected with a quadrupole mass spectrometer (QMS). This way, we can reproduce some processes that occur in space, but under controlled conditions in the laboratory, and obtain information of both the solid and the gaseous phases. Part V makes use of astronomical observations performed with radio telescopes (either with a single-dish or with an interferometer). Radio telescopes are able to detect the spectral lines spontaneously emitted by the molecules in the cold and warm regions of the ISM. Detecting these spectral lines allow us not only to confirm the presence of different species in the ISM (more than 180 molecules have been detected to date in the ISM) but also to extract the physical conditions of the different regions in which they are detected. In this thesis, we have used radio telescopes to look for species that are thought to be formed in the ice and subsequently desorb to the gas-phase (Chapter 12), and also species of unclear origin, that could be formed in the solid or the gas phase (Chapter 13). Laboratory and observational astrophysics are presented in Part II. Theoretical models have been occasionally used to support both the experimental and observational results.

As mentioned above, the results of this thesis are presented in Parts III, IV, and V. The common line of the thesis is the cycle of matter in the interstellar medium.

Part III (**Chapter 5**) presents the experimental study of the UV photoprocessing of carbonaceous dust grain analogs at temperatures between 90 K and 170 K, that leads to the formation of H_2 and D_2 molecules (depending on the precursor used for the formation of the analogs), which subsequently diffuse out to the gas phase. The diffusion is ruled by the diffusion coefficient D, and its temperature dependence was studied, obtaining an activation energy of $E_D(H_2) = 1660 \pm 110$ K and $E_D(D_2) = 2090 \pm 90$ K. Due to the strong decrease of the diffusion coefficient at low temperatures (because of the high activation energy), transient dust heating by cosmic rays needs to be invoked for the release of the photo-produced H_2 molecules in cold PDR regions, where destruction of the aliphatic component in hydrogenated amorphous carbons most probably takes place.

The surface of these dust grains is where the accretion of ice mantles takes place in the coldest and densest regions of the ISM (Part IV). The accretion process is briefly revised in **Chapter 6**, by combining experimental and theoretical simulations. We found that the conditions at which the freeze-out of CO molecules takes place determines the binding energies, and therefore, the morphology of the resulting ice layer. However, these differences in the ice structure are vanished when the ices are thermally processed.

After this incursion on the formation of the ice mantles, **Chapters 7 - 10** are devoted to their UV photoprocessing, with special attention to the photon-induced desorption processes that make up the core of this thesis. Three different ice samples were irradiated at 8 K. In **Chapter 8**, a pure CO_2 ice was irradiated. By combining the FTIR and the QMS (calibration of the latter has been also included in the thesis), a complete quantification of the photochemistry (formation of CO, CO_3, O_2, and O_3) and the photodesorption (of CO, O_2, and CO_2 to a lesser extent) processes was presented. In **Chapters 9 and 10**, a pure C_2H_5OH ice and a more realistic water rich-binary mixture with methane were used, respectively. The aim of these experiments was to explore the *in situ* formation (at temperatures as low as 8 K) and subsequent photodesorption of methanol and other related species. Methanol was not formed during irradiation of a pure C_2H_5OH ice, but formation of other species (H_2CO, CH_3CHO, H_2O, CH_4, C_2H_6, CO, and CO_2) was observed. The chemistry of the H_2O:CH_4 ice mixture was simpler, and only formation of H_2CO, CO, and CO_2 was reported, in addition to CH_3OH, that was detected in the ice during that series of experiments but did not photodesorb. One of the main conclusions of this thesis is that those photoproducts observed to photodesorb followed one out of two different patterns during the irradiation time. Some photoproducts desorbed directly after their formation on the surface of the ice if they were formed with enough excess energy allowing breakage of the intermolecular bonds (photochemidesorption), leading to a constant photodesorption yield with fluence[1]. This was the case, for example, of H_2CO photodesorbing from a H_2O:CH_4 ice mixture. Other photoproducts desorbed later via energy transfer after the absorption of a photon by a different molecule in the sub-surface of the ice. When this indirect photodesorption takes place, photoproduct molecules can accumulate in the ice before their photodesorption, leading to an increasing photodesorption yield with fluence. For example, CO molecules produced during the irradiation of the CO_2, C_2H_5OH, and H_2O:CH_4 ice samples followed this photodesorption mechanisms. A brief review of the different photodesorption mechanisms is provided in **Chapter 7**.

---

[1] Fluence = UV flux × irradiation time.

The thermal processing of an astrophysical, water-rich ice analog with five components is studied in **Chapter 11**. A thermal desorption peak was observed for every component at temperatures near the desorption temperatures of the corresponding pure ices. At the same time, a fraction of the molecules remained trapped in the ice structure and desorbed at higher temperatures in three steps: i) co-desorbing with methanol (this co-desorption was not reported in the literature), ii) desorbing during reorganization of the ice structure from amorphopus to cubic crystalline water ice (the so-called "volcano" desorption), and iii) co-desorbing with the water molecules.

Finally, Part V presents the observations of the hot corino IRAS16293-2422 with the APEX 12-m radio telescope and the ALMA interferometer that were used to search for different species. In **Chapter 12**, the presence of H_2S_2, $HS_2^{\cdot}$, and S_2 (thought to be formed by UV photoprocessing of H_2S-containing ices and subsequently desorbed) could not be confirmed, but stringent upper limits to their abundances were calculated ($\leq 8.1\times10^{-9}$, $\leq 1.1\times10^{-8}$, and $\leq 2.9\times10^{-7}$, respectively). Theoretical simulations with the UCLCHEM chemical model show that these species could be indeed formed in the processed ices, but after desorption, the subsequent gas-phase chemical reactions could lower their abundances to undetectable levels. On the other hand, the first detection of CH_3NCO (a molecule with prebiotic interest) in a solar-type protostar is reported in **Chapter 13**, with an observed abundance of $(1.4\pm0.1)\times10^{-10}$.

Part I
Context

Chapter 3

Introduction to the Interstellar Medium

In our Galaxy (and also in other galaxies in the Universe) the space between the stars is not empty. Instead, the so-called Interstellar Medium (ISM)[1], that contains **ordinary matter** (i.e., baryonic matter), mostly in *gaseous* form (atoms, molecules, protons, electrons, and heavier ions). Charged particles travelling with relativistic velocities are known as **cosmic rays**. A small fraction of this matter is in the form of solid particles (*dust grains* that can be covered by *ice mantles* in the colder regions). Interstellar matter (presented in more detail in the next sections) only represents 10 - 15 % of the total mass in our Galaxy. Solid particles account for an even lower percentage, but play an important role as it will be shown throughout this thesis. In addition, **magnetic fields** permeate the ISM, but they are not treated in this thesis.

The ISM is a very heterogeneous medium that comprises various environments exposed to different conditions. Attending to the gas-phase component (the solid particles tend to follow the gas distribution), they can be classified in dense or diffuse ISM, according to their density (above or below $\sim 10^4$ particles cm^{-3}, respectively); and cold ($\sim$ 10 - 100 K), warm ($\sim 10^4$ K) or hot (up to 10^6 K) ISM according to their temperature. Alternatively, the regions in the ISM can be classified attending to the form taken by the most abundant element in the Universe, hydrogen, leading to molecular, atomic neutral, and atomic ionized regions (McKee & Ostriker 1977). Nevertheless, the density, temperature, and form taken by hydrogen are intimately related, leading to only a handful of different regions that can be observed in the ISM (in a simplified vision).

Roughly half of the interstellar mass is found in interstellar clouds of three types. Dense clouds or molecular clouds with typical densities of 10^4 - 10^6 particles cm^{-3}, and temperatures down to 10 K are composed mainly of molecular hydrogen. They represent $\sim$20% of the interstellar mass, but only $\sim$1% of the interstellar volume. Diffuse clouds or cold neutral medium present lower densities and slightly higher (but still cold) temperatures around 100 K, and contain hydrogen in atomic neutral form.
Translucent clouds represent the transition between these two regions. In global, these clouds take up for only $\sim$2 % of the interstellar space.

The other half of the interstellar mass fills the remaining $\sim$98 % of the space, where three different regions can be distinguished. The warm neutral medium is similar to the diffuse clouds, but with much higher temperatures. The warm ionized medium can be found in the surroundings of massive and hot stars that emit energetic photons able to ionize the hydrogen atoms, leading to the HII regions made of H^+ cations. Finally, the hot ionized medium, probably generated by supernova explosions, fills up to $\sim$20 % of the interstellar space (Ferrière 1998).

The interstellar matter present in everyone of these regions completes a particular

---

[1] A very interesting review of the different components of the ISM can be found in Ferrière (2001).

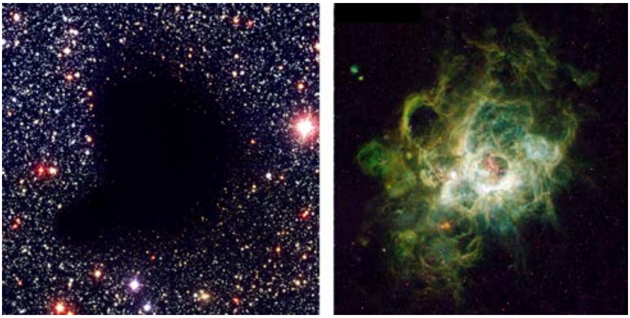

Figure 3.1. *Left: the dense cloud Barnard 68 in the Milky Way. Dense clouds are seen in silhouette against star fields (see Section 3.1). Right: the NGC 604 HII region in the Triangle Galaxy, seen as an emission nebula. Images are adapted from eso.org, and spacetelescope.org, respectively.*

lifecycle in which the stars are the cornerstones (see Fig. 3.2). Very roughly, the death of the stars feeds the ISM with ordinary matter (both solid and gas) through the stellar mass loss and supernovae explosions, that eventually constitutes the diffuse clouds. Some parts of the diffuse clouds collapse forming translucent clouds, where the atomic hydrogen is fully converted into molecular hydrogen, and finally the dense clouds as the temperature drops and the density increases. Inside dense clouds, the interstellar ultraviolet (UV) radiation field is screened and temperatures are very low, allowing the accretion of ice mantles on the surface of dust grains. In the interior of these clumpy molecular clouds, the densest cores collapse due to the gravitational forces, leading to the formation of a protostar and a protoplanetary disk, that evolve to form a new stellar system where the central star is surrounded by planets, asteroids, comets, and other bodies. Finally, the death of the star closes the cycle, returning a fraction of the matter to the ISM.

More details on the ordinary matter of the ISM and its lifecycle is given in Sections 3.1 - 3.3.

3.1 Solid interstellar matter - Dust

Interstellar dust particles are thought to form in the dense outflows of late-type, Asymptotic Giant Branch (AGB) stars (see, e.g., Chiar et a. 1998) and be subsequently ejected into the ISM. If the stars are oxygen-rich, most carbon atoms form CO molecules, and the remaining oxygen reacts with silicium and other metals [2] to form dust grains. When the stars are carbon rich, all oxygen atoms are locked up in the CO molecules, and it is the remaining carbon that leads to the formation of the dust particles. Dust particles in the ISM thus include minerals (silicates and oxides) and carbonaceous matter of various types, and present sizes ranging from a few nm to a few μm (Mathis et al. 1977, Kim et al. 1994), following a power-law distribution (i.e., the number of small grains is larger; Zubko et al. 2004).

---

[2] In the jargon of astrophysics, a metal is any element heavier than helium.

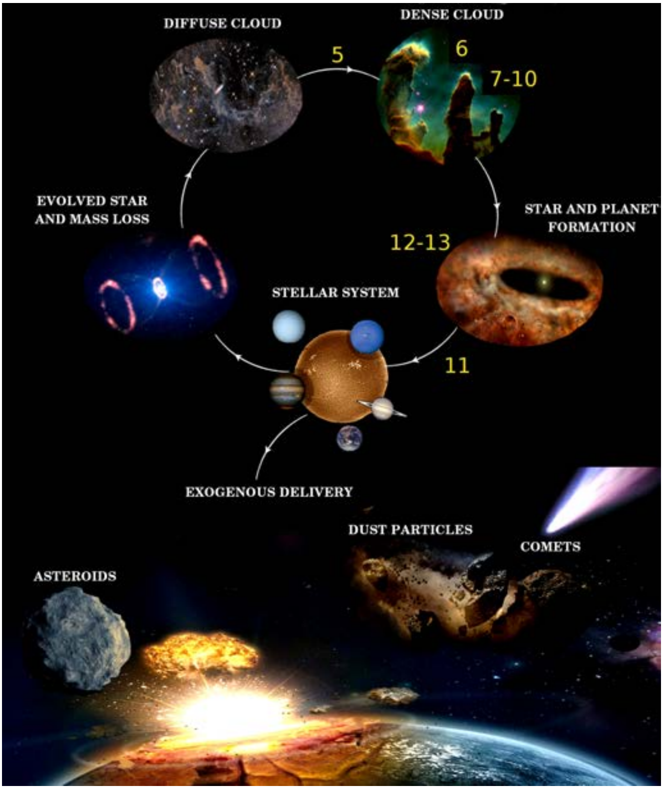
DIFFUSE CLOUD
DENSE CLOUD
5
6
7-10
EVOLVED STAR AND MASS LOSS
STAR AND PLANET FORMATION
12-13
STELLAR SYSTEM
11
EXOGENOUS DELIVERY
DUST PARTICLES
COMETS
ASTEROIDS

Figure 3.2. *The cycle of matter in the ISM. Numbers indicate the chapters of this thesis dedicated to the study of different processes in those particular stages of the cycle (see Sect. 3.4). Picture composition made with images adapted from apod.nasa.gov provided by Gustavo A. Cruz-Díaz.*

Interstellar dust grains from both populations interact with the light emitted by the stars in a given line of sight leading to its absorption and scattering. In fact, in the dense ISM the density of dust grains is high enough to extinct all visible light coming from the background stars, and dense clouds are thus seen in silhouette against field stars as dark clouds (see left panel of Fig. 3.1). Dust grains in the ISM also emit their own light, mainly due to the thermal emission of circumstellar dust grains, peaking in the infrared (IR) region of the spectrum.

Silicate dust particles are detected by IR spectroscopy[3] toward different regions of the ISM. In particular, silicate bands corresponding to the Si-O stretching and the O-Si-O deformation modes are observed at $\sim$10 and $\sim$18 μm, respectively, in both emission and absorption (see, e.g., Jäger et al. 1998, and Bowey & Adamson 2002).

---

[3] see Chapter 4, Sect. 4.1.4 for more information on IR spectroscopy

In the diffuse ISM, carbonaceous solids[4] are also observed through both emission and absorption bands in the mid-IR region of the spectrum.

The so-called aromatic infrared bands (AIBs) are a group of emission bands ubiquitously observed at 3.3, 6.2, 7.7, 8.6, and 11.3 μm, often associated with the infrared fluorescence of polycyclic aromatic hydrocarbons (PAHs; Leger & Puget 1984, Allamadola et al. 1985) upon absorption of ultraviolet (UV) photons, although this assignment is in dispute (see, e.g., Pino et al. 2008, Tsuge et al. 2014). The observed AIBs spectral variabilities have been classified in three main types (named A, B, and C), reflecting the evolution of the carriers in the environment (Peeters et al. 2002, van Diedenhoven et al. 2004), which would account for 4-5% of the total cosmic carbon abundance (Draine & Li 2007).

The 3.4 μm absorption band observed toward several lines of sight (Soifer et al. 1976, McFadzean et al. 1989, Adamson et al. 1990, Sandford et al. 1991, Pendleton et al. 1994, Bridger et al. 1994, Imanishi 2000a, Imanishi 2000b, Spoon et al. 2004, Dartois & Muñoz Caro 2007) has been assigned to hydrogenated amorphous carbons (a-C:Hs or HACs), that harbor 5-30% of the cosmic carbon, depending on the assumed carrier (see, e.g., Sandford et al. 1991). The 3.4 μm ($\sim$2900 cm^{-1}) feature arises from the contribution of the symmetric and asymmetric C-H stretching modes of the methyl (-CH_3) and methylene (-CH_2-) groups, but it is not observed, though, in the dense ISM, probably due to dehydrogenation (this is further studied in Chapter 5). The corresponding bending modes are also observed at 7.25 μm ($\sim$1380 cm^{-1}), and 6.85 μm ($\sim$1460 cm^{-1}), respectively. These bands are accompanied by a broad absorption between 6.0 and 6.4 μm attributed to aromatic and olefinic C=C stretching modes, although the carrier is predominantly aliphatic (Dartois & Muñoz Caro 2007).

Several theoretical and laboratory analogs have been proposed to fit these observed IR features with different contributions from aliphatic, olefinic and aromatic substructures (see Schnaiter et al. 1998, Lee & Wdowiak 1993, Furton et al. 1999, Mennella et al. 1999, Mennella et al. 2003, Dartois et al. 2005, Godard & Dartois 2010, Godard et al. 2011, and Fig. 3.3).

In Chapter 5, plasma-produced a-C:H analogs (see Godard & Dartois 2010, Godard et al. 2011, Fig. 3.4 right panel, and Chapter 4, Sect. 4.1.2) are used to simulate in the laboratory the dehydrogenation caused by UV photoprocessing of carbonaceous dust particles in the ISM.

Finally, during the star formation process in the interior of dense clouds, the dust grains in the protoplanetary disks coagulate into larger and larger particles, forming planetesimals, asteroids, comets (in the outer and colder disk where grains are still covered by ice mantles), and planets.

3.2 Solid interstellar matter - Ice

As explained above, dense molecular clouds have typical densities of 10^4-10^6 particles cm^{-3} and temperatures down to 10 K in their interiors. These low temperatures are reached thanks to the screening from the interstellar ultraviolet (UV) radiation field provided by the gas and dust particles (see the previous section) at the edge of the cloud,

---

[4] Information on the carbonaceous dust particles is partially adapted from the Introduction in Martín-Doménech et al. 2016.

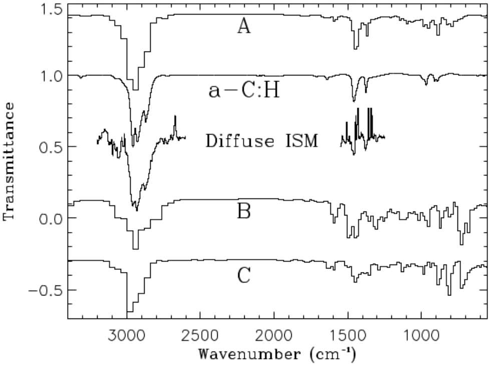

Figure 3.3. *The 3.4, 6.85, and 7.25 μm features corresponding to carbonaceous dust particles observed in the diffuse ISM toward the Galactic Center IRS7 line of sight (Dartois et al. 2004) are compared to the spectra of three theoretical (A, B, and C, Dartois et al. 2005) and one laboratory (a-C:H, Dartois et al. 2005) analogs (see also Fig. 3.4). Adapted from Dartois et al. (2005).*

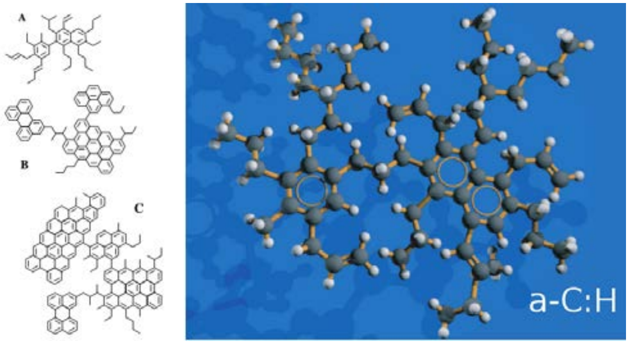

Figure 3.4. *Left: Representation of three theoretical analogs of the carbonaceous dust particles observed in the diffuse ISM with different contributions from aliphatic, olefinic and aromatic substructures. Right: Representation of a plasma-produced a-C:H analog of the carbonaceous dust particles observed in the diffuse ISM. Adapted from Dartois et al. (2005).*

present in a high enough density to absorb most of the radiation. Under these conditions, gas molecules are able to condense onto the surface of the dust grains, forming ice mantles. The size of interstellar dust grains ranges from a few nm to a few μm (see previous section), and they are covered by a $\sim$0.01 μm ice mantle in dense cloud interiors (Zubko et al. 2004). The canonical ice thickness of $\sim$0.01 μm is equivalent to $\sim$40 monolayers (ML). A monolayer has an average thickness of one molecule and, for crystalline water ice, this corresponds to an ice column density of 10^{15} molecules cm^{-2}.

The presence of ices in the ISM was first proposed by Lindblad (1935), and confirmed forty years later (Gillet & Forrest 1973) by means of an absorption feature at $\sim 3\ \mu$m (which corresponds to water ice) in the spectrum measured toward the line of sight of the Becklin-Neugebauer (BN) infrared source in Orion.

Shortly after their detection, it became evident that ice mantles were common in dense clouds (e.g. Merrill et al. 1976; Willner et al. 1982). Indeed, if the sticking probability of the molecules is close to 1, which is the case of most species under dense cloud conditions, all gas-phase molecules (except maybe H_2) should condense as ice mantles within the lifetime of a molecular cloud ($10^9/n_H$ years; Willacy & Millar 1998).

Ices are present not only in the interior of dense, quiescent clouds, but in a wide range of environments inside and outside the solar system. As explained in the previous section, the dust grains (covered by ice mantles) in the densest cores are incorporated into the star formation process, and ice mantles can be detected also in the envelopes of high- and low-mass protostars, in protoplanetary disks, and in comets once the stellar system is formed (please note that the circumstellar ices could be (at least partially) destroyed and subsequently reformed in the protoplanetary disks; Mumma & Charnley 2011, and references therein).

Ice mantles composition Interstellar ice compositions are revealed through their IR features, usually in absorption using an IR source situated in (an embedded protostellar source, probing circumstellar ices) or behind (a background star, probing ices in quiescent cores) the dense clouds. The observed features can be compared to IR spectra of ice analogs obtained in the laboratory under astrophysically relevant conditions in order to identify ice constituents (e.g., Fig. 3.5), and the abundance of the different components can be also calculated from their IR features (see Chapter 4 Sect. 4.1.4 for more information). Cometary ices, on the other hand, are usually observed indirectly through the gas-phase molecules that form the coma of the comets after their thermal desorption. Recently, the gas chromatograph − mass spectrometer COSAC (Cometary Sampling and Composition) on board the Philae lander of the Rosetta mission analyzed the material ejected from the surface of the comet 67P/Churyumov-Gerasimenko shortly after its landing Goesmann et al. 2015. The presence of sixteen molecules was proposed, including H_2O, CO, CH_4, and other thirteen more complex organic species such as isocyanic acid (HNCO), formamide (NH_2CHO), or methyl isocyanate (CH_3NCO, see also Chapter 13).

The ice composition vary greatly across the different environments in which ice mantles are detected, but also within objects of the same type (see Table 3.1 for the range of abundances measured in each environment)[5]. Water is the primary component of these ice mantles. The following most abundant species are CO and CO_2, with an average abundance of ∼20% relative to water. The presence of CH_3OH, NH_3, and CH_4 has also been confirmed, with an abundance relative to water around 5%. For these six species, more than one infrared absorption band have been observed. Interstellar ice mantles are probably composed by more species, but their presence could not be confirmed to date since only one absorption (at most) band has been detected, and their assignment is not clear. This is the case of H_2CO, OCS, or C_2H_5OH, among others (Boogert et al. 2015, and references therein).

---

[5] In Chapter 11, an average composition is assumed for the more realistic astrophysical ice analogs.

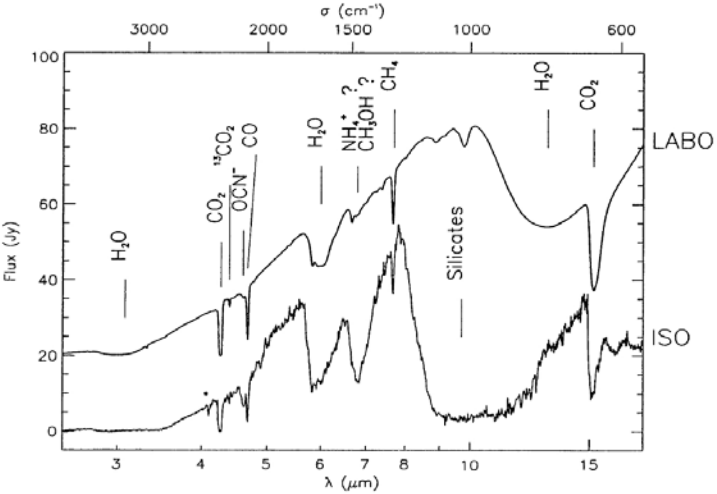

Figure 3.5. *Comparison between the ISO-SWS01 spectrum of RAFGL 7009S and a laboratory transmittance spectrum of an ice analog multiplied by the estimated continuum. Some identified molecular transitions are labeled (Dartois & d'Hendecourt 2000).*

Table 3.1. *Ranges of observed abundances of the six securely identified species in interstellar ices within different environments. Adapted from Boogert et al. (2015).*

	X_{H_2O} (%)			
Species	Quiescent dense clouds	High-mass protostars	Low-mass protostars	Comets
H_2O	100	100	100	100
CO	9 - 67	3 - 26	<3 - 85	0.4 - 30
CO_2	14 - 43	11 - 27	12 - 50	4 - 30
CH_3OH	<1 - 12	<3 - 31	<1 - 25	0.2 - 7
NH_3	<7	~7	3 - 10	0.2 - 1.4
CH_4	<3	1 - 3	1 - 11	0.4-1.6

Accretion of ices According to the observations (the ice composition and structure affect the observed IR features), ice mantles are thought to form on the surface of dust grains following a two-phase process that results in the bi-layered ice structure that is generally accepted nowadays (see, e.g., Boogert et al. 2015).

Early at the onset of the diffuse cloud collapse that leads to the formation of molecular clouds, when the H/H_2 ratio is still large, the accreting gas is atomic H- and O-rich and hydrogenation (H atom addition) reactions on the surface of dust grains dominate. This leads to the formation of a polar ice layer where H_2O is expected to be the major constituent, accompanied by NH_3, CH_4, and the polar component of CO_2 (see Chapter 8 for more information), which are observed to be intimately mixed with water.

As the cloud collapse progresses, formation of H_2 continues, and the H/H_2 ratio keeps decreasing, leading to the subsequent accretion of a non-polar (or slightly polar) layer mainly composed of CO, the polar component of CO_2, and CH_3OH (the profile of the CO IR feature indicates that it is not mixed with water, but with methanol; Cuppen et al. 2011). In particular, the accretion of CO molecules is further studied in Chapter 6.

Evolution of ices Ice mantles in the interior of dense clouds can be energetically processed by both UV photons and cosmic rays.

The interstellar UV-radiation field is about 10^8 photons cm^{-2} s^{-1} at the outer edge of a dense cloud (Mathis et al. 1983). However, as it was explained above, cloud interiors where dust grains are covered by ice mantles are protected from this interstellar UV-field. There is, however, a secondary UV-field produced in the interior of the clouds by cosmic rays that do penetrate a dense cloud without being substantially absorbed. Cosmic rays ionize H_2 molecules, and those secondary electrons can excite other H_2 molecules (as well as atomic H), that subsequently emit mainly Lyman and Werner recombination bands, thus producing this secondary UV-field of about 10^4 photons cm^{-2} s^{-1} (Cecci-Pestellini & Aiello 1992; Shen et al. 2004) that is able to induce photochemical reactions and photodesorption processes. The photon-induced desorption of ice molecules in cold interstellar regions where thermal desorption is inhibited has been invoked to account for the gas-phase abundances of different species when gas-phase-only chemical models are not able to explain them (this is the case, for example, of methanol in cold cores and photodissociation dominated regions, see, e.g., Guzmán et al. 2013). The importance of these processes is therefore beyond all doubts, and more information on the UV photoprocessing of ice mantles is provided in Chapter 7. Experimental simulations have been carried out over the past decade, and new experiments on this issue make up an important fraction of the results presented in this thesis (Chapters 8 - 10).

Cosmic rays that do not contribute to the secondary UV-field may also induce chemical reactions and non-thermal desorption processes. Moreover, their ability to penetrate ice mantles allow them to interact with the dust grains themselves (e.g., inducing hydrogenation of carbonaceus material; Mennella et al. 2003).

When a dense core collapses to form a star, grain agglomeration takes place in cold circumstellar regions leading to cluster particles composed of sub-micron grains (Steinacker et al. 2015). At the same time, the protostar heats its environment, and thermal processing must be taken into account as well. The main effect of thermal processing is the sublimation of ice mantles[6]. The warm-up of both gas and dust grains in the envelope by the central protostar generates a temperature gradient as a function of radius at any time, resulting in chemical segregation in these regions (Jiménez-Serra et al. 2012). Indeed, models predict that thermal desorption of ices governs the gas-phase chemistry during star formation (e.g. Viti et al. 2004).

The remaining ice mantles in protoplanetary disks can be incorporated in comets and other minor bodies (see, e.g., Greenberg & Hage 1990) that are also exposed to energetic processing.

---

[6] In addition, if radicals and reactive neutral species are present in the ices, warm-up will overcome certain reaction barriers, leading to the formation of new species.

In particular, when a comet passes within r $\sim$ 3 AU of the Sun during its orbit, volatiles in the ice begin to sublime, forming an expanding atmosphere of gas and dust called the coma.

Comets are believed to come from two main reservoirs. The Oort Cloud is considered to be the source of long-period comets (P>200 yr; Stern 2003). Gravitational perturbations caused by giant planets or passing stars may eject them from the Oort Cloud, reducing their perihelion. On the other hand, the Kuiper Belt is regarded as the source of short-period comets (P<200 yr; Levison & Duncan 1997). According to tentative estimates, the Solar System is populated by 10^{10-12} comets. Since the perihelion of their orbits range typically from 0.05 AU to 7 AU, the sample of known comets ($\sim$ 1300) constitutes only a negligible fraction and is strongly biased by observational selection.

The evolution of comets may be divided into three stages: (1) formation and early thermal evolution, (2) dynamical evolution, and (3) late thermal evolution (Prialnik et al. 2008). Comets evolve during many solar passages, but, due to both their small masses and long orbital periods, they have undergone less evolution than other members of the solar system, and are thought to contain the most pristine matter of the solar nebula.

The thermal processing of circumstellar (and cometary) ice mantles is studied in Chapter 11.

3.3 Gaseous interstellar matter - Star-forming regions

While Parts III and IV in this thesis (Chapters 5 - 11) deal with the solid interstellar matter (presented in Sections 3.1 and 3.2) and, in particular, with the experimental simulations of several processes undergone by this component of the ISM; Part V is devoted to the observational study of the gaseous component of the interstellar matter. Specifically, observations with radio telescopes toward the hot corino IRAS16293-2422 are used in Chapters 12 and 13.

As previously explained, when a dense core inside a clumpy molecular cloud collapses due to the gravitational forces, the star-formation process begins. The collapse of the dense core takes place in two phases: a cold phase when the core is still optically thin, and a warm-up phase, that begins when the core becomes optically thick and its temperature starts to increase. This collapse leads to the formation of a young stellar object (YSO). YSOs are classified in class 0 - III according to their evolutionary state, and are generally composed by the central forming star (or protostar), surrounded by a circumstellar envelope that eventually includes an accretion disk. Class *O* YSOs are the youngest ones, and they are formed by the central protostar embedded in a (still) dense envelope. This envelope gets warmer as it is closer to the central protostar. The region of the circumstellar envelope where the temperature is high enough to induce thermal desorption of the ice mantles on top of the dust grains present in the envelope is known as hot core (for high-mass YSOs or MYSOS) or hot corinos (for low-mass YSOs or LYSOs).

Hot cores and hot corinos are therefore compact regions around protostars, characterized by densities even higher than the characteristic densities of the parent molecular clouds (n $\geq$$10^6$ cm^{-3}) and temperatures warmer than those of the parental cloud (T$\geq$100 K). Hot cores/corinos are surrounded by a lukewarm and a colder envelope in the collapsing core, obscuring the central protostar. These regions are characterized by a very rich chemistry that is the result of the thermal desorption of the ice mantles and the subsequent gas-phase chemical reactions, making them perfect candidates for the search of new species formed either in the ice mantles (Chapter 12) or in the gas phase (Chapter 13).

3.4 Outlook of the thesis

Part I of this thesis has been dedicated to introduce the Context of this research work. The Results, shown in Parts III - V, represent insights in particular processes that the interstellar matter undergoes during its lifecycle. These processes have been studied by means of the Methods available in astrophysics nowadays: observational, laboratory, and theoretical astrophysics. The first two are briefly described in Part II. Theoretical models have been occasionally used, and they are described in the corresponding chapters.

Part III (Chapter 5) is devoted to the study of the energetic processing of dust particles in intermediate regions like the translucent clouds (evolutionary placed between diffuse and dense clouds).

During the formation of the dense clouds, ice mantles (Part IV) are accreted on top of dust grains. This process is studied in Chapter 6. Once the ice mantles are formed, they are also energetically processed inside dense clouds, leading to several effects including photodesorption of ice molecules. In particular, UV photoprocessing of ices is studied in Chapters 8, 9 (pure ices), and 10 (a more realistic water-rich binary ice), with special attention to the afore-mentioned photon-induced desorption processes. An introduction to this subject is provided in a separate Chapter (7).

Later during the star formation, dust grains in the circumstellar envelope are heated by the central protostar, and the ice mantles on top of them are evaporated[7]. Even in the Solar System, cometary ices desorb as the comet approaches the Sun during its orbit, leading to the formation of the coma. The thermal processing of circumstellar and cometary ices is studied in Chapter 11.

In particular, the molecules desorbed from circumstellar ices at the early stages of the star-formation process form the so-called hot cores and hot corinos around high-mass and low-mass protostars, respectively. Observations of a hot corino are used in the final two Chapters (12 and 13, Part V).

References

Adamson, A. J., Whittet, D. C. B., & Duley, W. W. 1990, MNRAS, 243, 400
Adel, M. E., Amir, O., Kalish, R., & Feldman, L. C. 1989, J. Appl. Phys., 66, 3248
Allamandola, L. J., Tielens, A. G. G. M., & Bakrer, J. R. 1985, ApJ, 290, L25
Tsuge, M., Bahou, M., Wu, Y.-J., Allamandola, L., & Lee, Y.-P. 2016, ApJ, 825, 2, id.96
Boogert, A. C. A., Gerakines, P. A., & Whittet, D. C. B. 2015, ARA&A, 53, 541
Bowey, J.E., & Adamson, A.J. 2002, MNRAS, 334, 1, 94
Bridger, A., Wright, G. S., & Geballe, T. R., 1994, in Infrared Astronomy with Arrays: The Next Generation, ed. I. S. McLean, Astrophysics and Space Science Library, 190, 537

---

[7] In astrophysics, evaporation or desorption are used as synonymous of sublimation.

Cecchi-Pestellini, C. & Aiello, S. 1992, MNRAS, 258, 125
Cuppen, H.M., Penteado, E.M., Isokoski, K., et al. 2011, MNRAS, 417, 2809
Dartois, E., D'Hendecourt, L. 2000, ESA-SP, 456, 71
Dartois, E., Muñoz Caro, G. M., Deboffle, D., & D'Hendecourt, L. 2004, A&A, 423, L33
Dartois, E., Muñoz Caro, G. M., Deboffle, D., Montagnac, G., & D'Hendecourt, L. 2005, A&A, 432, 895
Dartois, E., & Muñoz Caro, G. M. 2007, A&A, 476, 1235
Draine, B. T., & Li, A. 2007, ApJ, 657, 810
Imanishi, M. 2000a, MNRAS, 313, 165
Imanishi, M. 2000b, MNRAS, 319, 331
Ferrière, K.M. 1998, ApJ, 503, 700
Ferrière, K.M. 2001, RvMP, 73, 4, 1031
Furton, D. G., Laiho, J. W., & Witt, A. N. 1999, ApJ, 526, 752
Gillett, F.C. & Forrest, W.J. 1973, ApJ, 179, 483
Godard, M., & Dartois, E. 2010, A&A, 519, A39
Godard, M., Féraud, G., Chabot, M., et al. 2010, A&A, 529, A146
Goesmann, F., Rosenbauer, H., Bredehöft, J.H., et al. 2015, Science, 346, 6247, id.0689
Greenberg, J.M., Hage, J.I. 1990, ApJ, 361, 260
Guzmán, V. V., Goicoechea, J. R., Pety, J., et al. 2013, A&A, 560, A73
Jäger, C., Molster, F.J., Dorschner, J., et al. 1998, A&A, 339, 904
Jiménez-Serra, I., Zhang, Q., Viti, S., Martín-Pintado, J., & de Wit, W.-J. 2012, ApJ, 753, 34
Kim, S.H., Martin, P.G., & Hendry, P.D. 1994, 422, 164
Lee, W., & Wdowiak, T. J. 1993, ApJ, 417, L49
Leger, A., & Puget, J. L. 1984, A&A, 137, L5
Levison, H.F. & Duncan, M.J. 1997, Icarus, 127, 13
Lindblad, B. 1935, Nature, 135, 133
Mathis, J.S., Mezger, P.G., & Panagia, N. 1983, A&A. 128, 212
Mathis, J.S., Rumpl, W., & Nordsieck, K.H. 1977, ApJ, 217, 425
Martín-Doménech, R., Dartois, E., & Muñoz Caro, G.M. 2016, A&A, 591, A107
McFadzean, A. D., Whittet, D. C. B., Bode, M. F., Adamson, A. J., & Longmore, A. J. 1989, MNRAS, 241, 873
McKee, C.F. & Ostriker, J.P. 1977, ApJ, 218, 148
Mennella, V., Baratta, G. A., Esposito, A., Ferini, G., & Pendleton, Y. J. 2003, ApJ, 587, 727
Mennella, V., Brucato, J. R., Colangeli, L., & Palumbo, P. 1999, ApJ, 524, L171
Merrill, K.M., Russell, R.W., & Soifer, B.T. 1976, ApJ, 207, 763
Peeters, E., Hony, S., van Kerckhoven, C., et al. 2002, A&A, 390, 1089
Pendleton, Y. J., Sandford, S. A., Allamandola, L. J., Tielens, A. G. G. M., & Sellgren, K. 1994, ApJ, 437, 683
Pino, T., Dartoir, E., Cao, A.-T., et al. 2008, A&A, 490, 665
Prialnik, D., Sarid, G., Rosenberg, E.D., & Merk, R. 2008, Space Sci. Rev., 138, 147
Sandford, S. A., Allamandola, L. J., Tielens, A. G. G. M., et al. 1991, ApJ, 371, 607
Schnaiter, M., Mutschke, H., Dorschner, J., Henning, T., & Salama, F. 1998, ApJ, 498, 486
Shen, C. J., Greenberg, J. M., Schutte, W. A., & van Dishoeck, E. F. 2004, A&A, 415, 203
Soifer, B. T., Russel, R. W., & Merrill, K. M., 1976, ApJ, 207, L83
Spoon, H. W. W., Armus, L., Cami, J., et al. 2004, ApJS, 154, 184

Steinacker, J., Andersen, M., Thi, W.-F., et al. 2015, A&A, 582, A70
Stern, S.A. 2003, Nature, 424, 639
van Diedenhoven, B., Peeters, E., van Kerckhoven, C., et al. 2004, ApJ, 611, 928
Viti, S., Collings, M.P., Dever, J.W., & McCoustra, M.R.S. 2004, MNRAS, 354, 1141
Willacy, K. & Millar, T.J. 1998, MNRAS, 298, 562
Willner, S.P., Gillett, F.C., Herter, T.L., et al. 1982, ApJ, 253, 174
Zubko, V., Dwek, E., & Arendt, R.G. 2004, ApJSS, 152, 211

Part II
Methods

Chapter 4

Methods

4.1 Laboratory Astrophysics

4.1.1 Experimental simulations in the ISAC ultra-high vacuum chamber

The astrophysical processes studied in Chapters 5 - 11 were experimentally simulated under realistic conditions using the InterStellar Astrochemistry Chamber (ISAC) setup, located at the Centro de Astrobiología near Madrid, Spain.

ISAC is an ultra-high vacuum (UHV) chamber with a base pressure of about 4 x 10^{-11} mbar, which corresponds to a density of 10^6 cm^{-3}, similar to that found in dense cloud interiors (Muñoz Caro et al. 2010).

The setup has a vertical configuration (see Fig. 4.1), actually consisting in two chambers: the main chamber, where the experimental simulations take place, and a smaller prechamber placed on top of the main chamber and separated by a manual, hydraulic VAT valve. The prechamber is used to introduce or extract samples with no need to break the ultra-high vacuum in the main chamber. The pumping system of the prechamber is independent from that of the main chamber, reaching a pressure of about 10^{-9} mbar, and supporting the pumping system of the main chamber when the VAT valve is open. It counts with a turbomolecular pump (TMP, pumping capacity of 220 l s^{-1}) backed up by a rotary pump. The ultra-high vacuum in the main chamber is achieved thanks to the combination of a TMP with a pumping capacity of 550 l s^{-1} backed up by a second TMP and a rotary pump (in addition to the pumping system connected to the pre-chamber). A Non-Evaporable Getter pump (NEG) is also connected to the main chamber, and a Bayard-Alpert pressuremeter measures pressures down to the 10^{-11} mbar range.

Interstellar solid analogs are placed on a substrate (usually a 13 mm diameter infrared transparent KBr or MgF_2 window) in the sample holder at the tip of the cold finger connected to a closed-cycle-He cryostat, reaching a temperature as low as $\sim$8 K, similar to that found in dense cloud interiors. The sample holder is covered by a radiation shield for thermal isolation, and is mounted on a tube that can be rotated by 180°. This structure can be vertically translated to the prechamber as a whole (see above). The radiation shield has two holes of $\sim$ 2.5 $\times$ 3.5 cm size to allow UV irradiation of the samples with photons emitted by a Microwave Discharged Hydrogen-flow Lamp (MDHL, see Sect. 4.1.3) for the simulation of the UV photoprocessing. In addition, samples can be warmed up by a tunable heater located close to the sample up to $\sim$400 K to simulate thermal processing. A silicon diode temperature sensor and a LakeShore Model 331 temperature controller are used to monitor and control the sample temperature at every moment, reaching a sensitivity of about 0.1 K.

During the experimental simulations, the solid analogs are characterized and monitored by a Bruker Vertex 70 Fourier Transform Infrared (FTIR) spectrometer in transmittance (see Sect. 4.1.4). Rotation of the sample holder by 90° with respect to the position for the UV irradiation is required for FTIR spectroscopy of the sample during the photoprocessing experimental simulations (Chapters 5 and 8 - 10, see Fig. 4.2).

The molecules desorbing from the sample to the gas phase can be detected by a Pfeiffer Prisma quadrupole mass spectrometer (QMS) (see Sect. 4.1.5), which is situated $\sim$ 17 cm apart from the sample (see Fig. 4.2).

Samples used in Chapters 6 - 11 consisted in ice analogs prepared *in situ* by gas deposition onto the substrate from an independent gas-line system. The gas-line system is pumped by a rotatory pump, reaching a base pressure of $\sim 1 \times 10^{-2}$mbar, and allows the preparation of a complex gas mixture under controlled conditions using electrical valves to control the entrance of the individual components, and working dynamically at a total pressure below 1 mbar, thus ensuring laminar flow conditions. This setup allows to work with up to two vapors, usually H_2O or CH_3OH (and even C_2H_5OH) in our experiments, and two gas components, commonly CO, CO_2, or CH_4. The resultant gas mixture (with up to four components) is introduced into the main chamber through a capilar tube. The abundance of the four components in the gas mixture (and therefore in the ice mantle grown later on the substrate) is monitored with another QMS (Pfeiffer Prisma of mass spectral range 1–100 amu with a Faraday detector) connected to the gas line. One more gas component can be introduced through a second capilar, usually used for corrosive gases like NH_3. The abundance of this component relative to the rest of the mixture is controlled by means of its partial pressure in the main chamber. When the desired composition of the gas mixture is obtained, the deposition tubes are opened through a leak valve and the gas enters the main chamber, accreting onto the substrate window at 7 - 8 K and forming the ice analog with up to five components.

Particular information on the different experimental simulations performed are provided in the corresponding chapters.

4.1.2 Additional experiments using the SICAL-X high vacuum chamber

Most of the experimental simulations described in Chapter 5 aimed to study the dehydrogenation caused by UV photoprocessing of hydrogenated amorphous carbon analogs (see also Chapter 3, Sect. 3.1) were performed using the SICAL-X setup at the IAS (Institute
d'Astrophysique Spatial) in Orsay, France, during a three-month internship in 2015.

The SICAL-X setup (see, e.g., Alata et al. 2014, and Fig. 4.3 in this Chapter) consists in a high-vacuum (HV) chamber with a base pressure of about 2×10^{-8} mbar. At this pressure, residual H_2 inside the chamber is not negligible. Therefore, deuterated amorphous carbon (a-C:D) analogs were preferentially used over hydrogenated amorphous carbon (a-C:H) analogs to study the dehydrogenation by energetic processing of this material (see Chapter 5). Nevertheless, the latter analogs were used for the complementary experimental simulations performed at the ISAC setup (see Sect. 4.1.1).

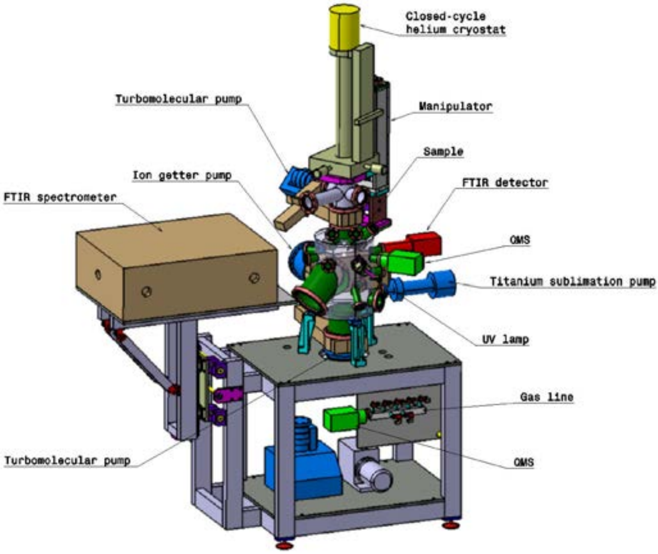
Closed-cycle helium cryostat
Turbomolecular pump
Manipulator
Sample
Ion getter pump
FTIR detector
FTIR spectrometer
QMS
Titanium sublimation pump
UV lamp
Gas line
Turbomolecular pump
QMS

Figure 4.1. *Schematic cartoon of the ISAC experimental setup. The Titanium - sublimation pump is no longer in use. From Cruz-Díaz (2014a).*

The high-vacuum inside the SICAL-X chamber is achieved thanks to two turbomolecular pumps and one rotatory pump connected in series. The rotatory pump alone reaches a pressure of only $\sim10^{-3}$ mbar, which is lowered to 10^{-6} - 10^{-7} mbar thanks to the action of a small turbomolecular pump, and finally to the base pressure on the order of 10^{-8} mbar when the Pfeiffer 2000l/s hybrid turbomolecular pump is activated. In addtion, an ionic pump is directly connected to the chamber by a guillotine valve (not shown in Fig. 4.3).

The samples, that in the case of the experiments described in Chapter 5 are plasma-produced a-C:D analogs on a MgF_2 substrate, can be cooled down to $\sim$10 K by a closed-cycle helium cryostat (SRDK series, CRYOCOOLER F-50 series Compressor Unit). The temperature of the sample can be adjusted with a resistive-type heater element, and is monitored with a thermocouple reaching a sensitivity of 0.1 K. In addition, samples can be irradiated with VUV photons emitted by a MDHL (see Chapter 4, Sect. 4.1.3) to study their UV photoprocessing.

A Bruker Vertex FTIR spectrometer in transmittance (see also Sect. 4.1.4) is used to monitor the evolution of the samples during the experimental simulations.

A Quadera 200 QMS (see also Sect. 4.1.5) located at $\sim$10 cm from the samples is used to detect the molecules coming from the samples to the gas phase (D_2 in the case of the experiments described in Chapter 5). More details on the experimental setup and protocol are provided in Chapter 5, Sect. 5.2.

Both the a-C:H and the a-C:D analogs studied in Chapter 5 were prepared by a

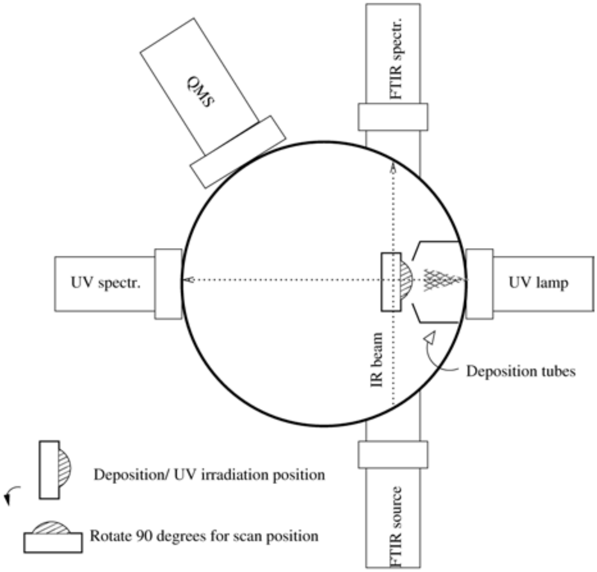
QMS
FTIR spectr.
UV spectr.
UV lamp
IR beam
Deposition tubes
Deposition/ UV irradiation position
Rotate 90 degrees for scan position
FTIR source

Figure 4.2. *Schematic representation of the main chamber in the ISAC experimental set-up. The UV spectrophotometer was not used during the experimental simulations described in this thesis. From Muñoz Caro et al. (2010).*

plasma-enhanced vapor chemical deposition (PECVD) method (Godard & Dartois 2010, Godard et al. 2011), using the SICAL-P setup, and CH_4 and CD_4 as gas precursors, respectively.

The SICAL-P setup is a vacuum chamber with a base pressure on the order of 10^{-2} mbar achieved thanks to a rotatory pump, in which a microwave-induced plasma is created. Radicals and ions of the low pressure plasma produced by radiofrequency (RF) at 2.45 GHz were deposited on a substrate (a MgF_2 window in the case of the experiments in Chapter 5) located at a fixed distance of a few centimetres from the plasma. The precursor pressure was kept at $\sim$1 mbar in the SICAL-P vacuum chamber, and the power applied to the plasma was set to 100 W for all samples. Consequently, structure of all plasma-produced analogs was expected to be similar. Deposition time ranged from a few seconds to half an hour, leading to a wide range of sample thicknesses. Hydrogenated and deuterated samples were subsequently transferred to the ISAC (see Sect. 4.1.1) or the SICAL-X setup, respectively.

4.1.3 Vacuum-ultraviolet lamp for photoprocessing of interstellar solid analogs

For the simulation of the UV photoprocessing, interstellar solid analogs are irradiated with UV photons from a F-type Microwave-Discharged Hydrogen-flow lamp (MDHL) from Opthos Instruments. Molecular hydrogen flows through the lamp from a hydro-

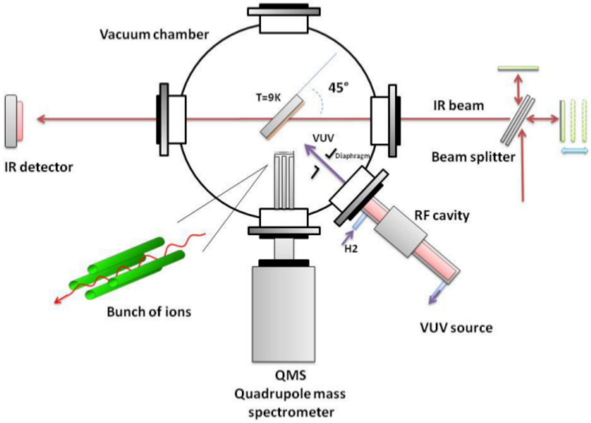
Vacuum chamber
T=9K
45°
IR beam
IR detector
VUV
Diaphragm
Beam splitter
RF cavity
H2
Bunch of ions
VUV source
QMS
Quadrupole mass
spectrometer

Figure 4.3. *Schematic representation of the SICAL-X setup. From Alata et al. (2014).*

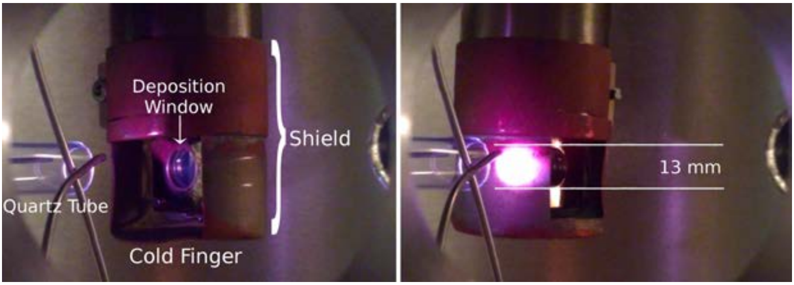
Deposition
Window
Shield
Quartz Tube
Cold Finger
13 mm

Figure 4.4. *Left: Picture of the sample holder with the substrate (deposition window) at the end of the cold finger in ISAC, covered by the radiation shield. The quartz tube used as optical guide for the photons is also shown. Right: The region irradiated by the visible photons from the MDHL approximately coincides with the size of the substrate, and the same is expected for the VUV photons. From Cruz-Díaz et al. (2014a).*

gen bottle with a working pressure of 0.40 ± 0.02 mbar thanks to the action of a rotatory pump. Inside the Evenson cavity of the lamp, a low pressure plasma is produced by a microwave generator with an applied power of 100 W, while the cavity is refrigerated with air. A MgF_2 window is used as the interface between the lamp and the chamber interior, and a cylindrical quartz tube of 10 mm diameter located between the MgF_2 window and the sample holder is used as an optical guide for the vacuum ultraviolet (VUV) photons. The spot size of the irradiated region approximately coincides with the size of the substrate (see Fig. 4.4).

This source has a VUV flux of $\approx 2 \times 10^{14}$ photons cm^{-2} s^{-1} at the sample position, as measured by $CO_2 \rightarrow CO$ actinometry (Muñoz Caro et al. 2010). Its emission spec-

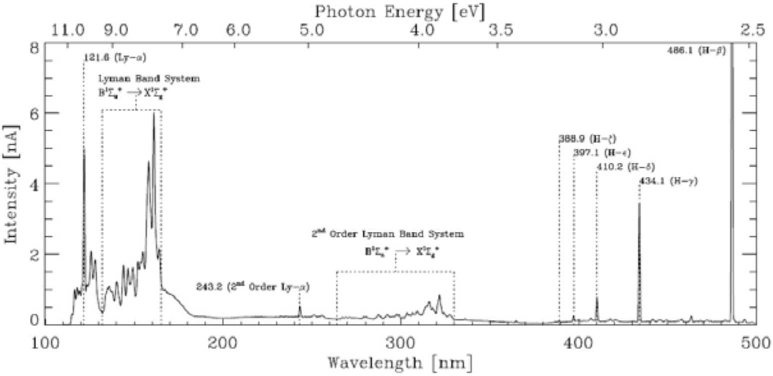

Figure 4.5. *Emission spectrum of the MDHL for the working conditions in ISAC (see text). From Cruz-Díaz et al. (2014b).*

trum depends on the working conditions, and it has been previously characterized by Chen et al. (2010), Chen et al. (2014). The emission spectrum in the 110 - 500 nm region is shown in Fig. 4.5 for the conditions used in the experimental simulations described in this thesis. Most of the emission falls at wavelengths $\leq$183 nm. In addition, the MgF_2 window used as interface between the lamp and the chamber leads to a cutoff in the emission at $\sim$116 nm. The majority of the photons are emitted at the molecular hydrogen bands centered at 157.8 and 160.8 nm, while a small fraction ($\sim$6 %) is emitted at the Ly-α wavelength (121.6 nm). The mean photon energy in the 116 - 183 nm (10.68 - 6.77 eV) range is 8.6 eV. The spectrum of the MDHL is similar to the secondary UV field of dense cloud interiors calculated by Gredel et al. (1989) (see Fig. 4.6) and also to the diffuse interstellar UV field (Jenniskens et al. 1993, Muñoz Caro & Schutte 2003), as well as to the far-UV field of emission/reflection nebulae (France et al. 2005). More information can be found in Cruz-Díaz et al. (2014b), where a description of the VUV spectrophotometer used in the ISAC setup to monitor the VUV flux of the lamp is provided.

UV irradiation of the samples in the SICAL-X setup is also performed using a MDHL similar to that attached to the ISAC setup, whose Evenson cavity is coupled to the same radiofrequency microwave generator described in Sect. 4.1.2 for the SICAL-P setup. In the SICAL-X setup, the VUV-photon flux at the sample position is 2.7 × 10^{14} photons cm^{-2} s^{-1}, measured by actinometry using a polyethylene film with a thickness of 15μm (Alata et al. 2014), and the mean photon energy is also 8.6 eV (the hydrogen pressure in both lamps was set to 0.7 mbar in the lamp during the experiments described in Chapter 5). In addition, in this setup a 20 mm diameter metallic shutter is placed 5 cm away in front of the substrate to prevent the VUV photons from reaching the sample when necessary, without turning off the lamp and changing the conditions inside the chamber during the experiments (blank conditions).

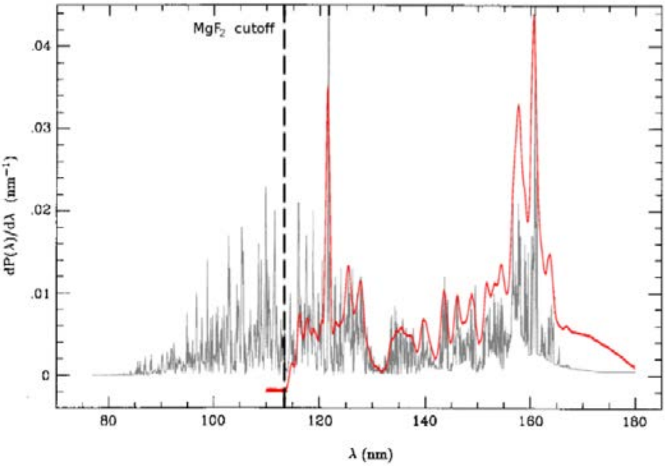

Figure 4.6. *Emission spectrum of the MDHL in the 116 - 183 nm region (red) compared to the secondary UV-field expected in dense cloud interiors (black, from Gredel et al. 1989).*

4.1.4 Infrared spectroscopy

Infrared spectroscopy is a powerful tool in the study of interstellar dust and ice particles. Telescope observations of the infrared (IR) light absorbed (and also emitted) by these particles have allowed astrophysicists not only to detect them, but also to reveal their composition by comparing the data from the observations to the IR spectra of dust and ice analogs collected in the laboratory under astrophysically relevant conditions (see also Chapter 3).

Absorbed photons in the IR region of the spectrum ($\sim$ 1 - 500 μm, or 10000 - 20 cm^{-1}) are able to induce transitions between vibrational levels of the same electronic state. The vibration of a single molecule can be decomposed into a number [1] of simple vibrational movements known as vibrational modes. Vibrational modes are named according to how the atoms in the molecule move with respect to each other (see Fig. 4.7), leading to stretching, bending, or librational modes, for example. A quantum number is assigned to every vibrational mode[2], and every combination of the values taken by these quantum numbers corresponds to a different vibrational level (for example, the ground vibrational state of a molecule has all the quantum numbers equal to zero). A transition between two vibrational levels is thus understood, in a first approximation, as the excitation of one vibrational mode [3] (or a combination of several vibrational modes at the same time). The required energy to produce the transition corresponds to the vibrational frequency of the mode(s) involved.

---

[1] 3N-6 for non-linear molecules or 3N-5 for linear molecules, where N is the number of atoms of the molecule.

[2] There are, therefore, 3N-6 or 3N-5 vibrational quantum numbers that characterize the vibration of a molecule.

[3] i.e., an increase of its quantum number.

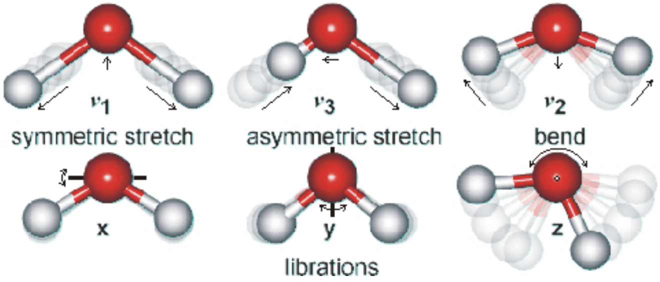

Figure 4.7. *The three vibrational modes of a water molecule. From lsbu.ac.uk*

The frequency, and therefore, the IR band position, of the vibrational modes are shifted in the solid phase relative to the gas phase, thus allowing distinction between solid and gas phase molecules. In addition, rotational transitions are supressed for molecules in the solid phase, while those in the gas phase usually undergo ro-vibrational transitions.

During the experimental simulations described in this thesis, the solid analogs were characterized and monitored by a Bruker Vertex 70 Fourier Transform Infrared (FTIR) spectrometer in transmittance, equipped with a deuterated triglycine sulfate detector (DTGS) working in the 7500 - 370 cm^{-1} ($\sim$ 1.3 - 27 μm, near and mid-IR) spectral range. Another DTGS detector working in the 600-30 cm^{-1} spectral range ($\sim$ 16 - 330 μm, far IR) can be also used in the ISAC setup. Both in the ISAC and the SICAL-X setups, the infrared beam goes across the main chamber through two ZnSe windows (for mid-IR spectroscopy) or diamond (suitable for far-IR spectroscopy, but it also allows mid-IR spectroscopy).

Instead of scanning the solid samples with monochromatic infrared photons with different wavelengths until the complete infrared spectrum is collected, the FTIR spectrometer uses a beam containing photons with different wavelengths at the same time, and measures how much of the light is absorbed. By changing the wavelengths contained in the IR beam, an interferogram is obtained. The Fourier transform of the interferogram is the infrared spectrum of the solid sample.

Column densities of the different components in the ice analogs were calculated from the IR spectra using the formula

$$N = \frac{1}{A} \int_{band} \tau_{\nu} \, d\nu, \tag{4.1}$$

where N is the column density of the species in molecules cm^{-2}, τ_{ν} the optical depth of the absorption band, and A the band strength in cm molecule^{-1}, as derived from laboratory experiments. The same values measured for pure ices are usually adopted in ice mixtures, which introduce an uncertainty of about 20-30% (d'Hendecourt & Allamandola 1986).

The ice structure and the environment of the molecules can also alter the band profiles and the band strength values. For example, in the case of H_2S ice, the band strength of the stretching S-H vibrational mode at $\sim$ 2543 cm^{-1} changes from 2$\times$10^{-17}

cm molecule^{-1} at $\sim$ 10 K to 2.9$\times$10^{-17} cm molecule^{-1} at 70 - 80 K, due to the crystallization of the ice (Jiménez-Escobar & Muñoz Caro 2011). More information can be found in Chapter 11 for astrophysical ice analogs.

4.1.5 Mass spectrometry

During the experimental simulations described in this thesis, the molecules desorbing from the solid samples to the gas phase were detected by mass spectrometry. Mass spectrometers are generally composed by three different components: the ion source that ionizes the molecules prior to their analysis, the mass analyzers that separate the ions according to their m/z ratio, and the actual detector.

In the ISAC and SICAL-X setups, a quadrupole mass spectrometer (QMS) was used. These QMSs use an electron ionization source, so once they reach the QMS, the gas-phase molecules are ionized by low energy ($\sim$ 70 eV) electron bombardment (electrons are produced by a heated filament and subsequently accelerated), forming the molecular ion. The fraction of ions formed in the QMS depends on the electron-impact ionization cross section of the species. On average, one ion is produced for every 1000 molecules entering the source. The excess energy deposited on the molecular ion leads to its fragmentation. This way, for every species, different mass fragments can be detected by the QMS, leading to a characteristic mass spectrum.

Once the fragments are produced, they are separated according to their m/z ratio by a quadrupolar mass analyzer operated at unit resolution. These analyzers are made of four rods that generate a variable electric field in which certain ions have a stable pathway, being able to reach the detector, while other ions do not. This way, by changing the electic field, different fragments with different m/z ratios can be separated.

Finally, the ions are detected by a secondary-emission multiplier (SEM) detector, producing an ion current that is proportional to the number of molecules reaching the QMS. To convert the signal measured by the QMS into a column density of desorbed molecules during photoprocessing of the solid samples, we performed additional experiments with the same setup to calibrate our QMS (see below).

The species potentially desorbing into the gas phase during the experimental simulations were preferably monitored through their main mass fragment (the most abundant one), which does not always coincide with the molecular ion. In some cases the main mass fragment of a given species was common to a mass fragment of another species, and another fragment was chosen to avoid interferences between different molecules. The mass fragments selected for every species are detailed in the corresponding chapters.

Calibration of a Quadrupole Mass Spectrometer

[4] The integrated ion current measured by a Quadrupole Mass Spectrometer (QMS) corresponding to a mass fragment m/z of the molecules of a given species desorbed during

---

[4] This section is adapted from the Appendix A in Martín-Doménech et al. (2015).

ice irradiation experiments[5] is proportional to the total number of molecules desorbed, and it can be calculated as follows:

$$A(m/z) = k_{QMS} \cdot \sigma^{+}(mol) \cdot N(mol) \cdot I_F(z) \cdot F_F(m) \cdot S(m/z), \tag{4.2}$$

where $A(m/z)$ is the integrated area below the QMS signal of a given mass fragment m/z during photon-induced desorption, k_{QMS} is the proportionality constant, $\sigma^{+}(mol)$ the ionization cross section for the first ionization of the species of interest and the incident electron energy of the mass spectrometer, $N(mol)$ the total number of desorbed molecules in column density units, $I_F(z)$ the ionization factor, that is, the fraction of ionized molecules with charge z, $F_F(m)$ the fragmentation factor, that is, the fraction of molecules of the isotopolog of interest leading to a fragment of mass m in the mass spectrometer, and $S(m/z)$ the sensitivity of the QMS to the mass fragment (m/z) (see Tanarro et al. 2007, and references therein).

The measured ion current depends on the ionization cross section of the species ($\sigma^{+}(mol)$), since only ionized molecules produce a signal in the QMS.

The product $I_F(z) \cdot F_F(m)$ represents the fraction of desorbed molecules that leads to the monitored mass fragment m/z once they are ionized in the QMS.

The sensitivity $S(m/z)$ must be calibrated for every mass spectrometer.

On the other hand, k_{QMS} depends not only on the mass spectrometer, but on the configuration of the experimental setup, and, in particular, on the fraction of desorbed molecules that reach the QMS. This fraction in turn depends on the pumping speed for the different molecules. The pumping speed depends on the molecular mass and, to a lesser extent, on the molecular structure (Kaiser et al. 1995). In Chapter 8 we have assumed as a first approximation that this speed is the same for all the molecules, so that k_{QMS} does not depend on the species. The same assumption has been used in previous works (see Fayolle et al. 2013, Fillion et al. 2014, and references therein). The error introduced as a result is very low compared to other sources of errors (~5%). Nevertheless, in Chapters 9 and 10 the different pumping speeds are taken into account.

Both k_{QMS} and, to a lesser extent, $S(m/z)$ are subject to variations in the behavior of the QMS with time. Therefore, calibration of the QMS must be done periodically, since the parameters may change with time. Calibration of these two factors for our QMS is described below. The derived parameters in this section are valid for the experimental simulations in Chapter 8. The correct values for the experiments in Chapters 9 and 10 are presented in the corresponding chapters.

Calibration of proportionality constant k_{QMS}

CO ice irradiation experiments under UHV conditions can be used as a reference to calibrate the QMS signal, since the interface between the UV source and the chamber where the ice sample is located is, usually, a MgF_2 window with a cutoff at ~114 nm (10.87 eV), that is, below the dissociation energy of CO molecules (11.09 eV, Cruz-Díaz et al. (2014b),

---

[5] During ice irradiation experiments, only molecules from the irradiated ice are able to photodesorb, since the UV spot size is comparable to the sample surface (see Fig. 4.4. On the other hand, during thermal processing experiments, molecules from other parts of the system may desorb at the same time than the ice sample molecules (more information is provided in Chapter 6), making the quantification of thermal desorption rates using the QMS data not possible.

Chen et al. (2014)). Therefore, in the CO ice experiments UV irradiation mainly leads to photodesorption. Equation 4.2 can be rewritten as follows:

$$A(m/z) = k_{CO} \cdot \frac{\sigma^+(mol)}{\sigma^+(CO)} \cdot N(mol) \cdot \frac{I_F(z)}{I_F(CO^+)} \cdot \frac{F_F(m)}{F_F(28)} \cdot \frac{S(m/z)}{S(28)}, \tag{4.3}$$

where k_{CO} is

$$k_{CO} = \frac{A(28)}{N(CO)} = k_{QMS} \cdot \sigma^+(CO) \cdot I_F(CO^+) \cdot F_F(28) \cdot S(28). \tag{4.4}$$

Finally, the total number of photon-induced desorbed molecules can be thus calculated as[6]:

$$N(mol) = \frac{A(m/z)}{k_{CO}} \cdot \frac{\sigma^+(CO)}{\sigma^+(mol)} \cdot \frac{I_F(CO^+)}{I_F(z)} \cdot \frac{F_F(28)}{F_F(m)} \cdot \frac{S(28)}{S(m/z)}. \tag{4.5}$$

These equations assume that the pumping speed in the ISAC setup is the same for all molecules, so that k_{QMS} does not depend on the species. Formally, constant k_{QMS} in equation 4.4 corresponds to the pumping speed of CO molecules. Therefore, $N(mol)$ calculated with equation 4.5 would be only valid if the pumping speed of a specific species is the same as for CO. Taking the different pumping speeds into account, the real number of photon-induced desorbed molecules would be

$$N^{real}(mol) = N^{calc}(mol) \cdot S_{rel}(mol), \tag{4.6}$$

with $N^{calc}(mol)$ the column density calculated with eq. 4.5, and $S_{rel}(mol)$ the relative pumping speed with respect to the CO molecules. This equation has been used in Chapters 9 and 10, where more information about $S_{rel}(mol)$ is provided.

In any case, the problem of calibrating k_{QMS} can be replaced by the problem of calculating k_{CO}.

To derive k_{CO} for our experimental setup, we performed UV-irradiation experiments of a pure CO ice made by deposition of CO (gas, Praxair 99.998%), using the protocol described in Chapters 8 - 10. Since in the case of solid CO photon-induced chemistry accounts for only ~5% of the absorbed photons (Muñoz Caro et al. 2010), the area below the m/z=28 signal detected with the QMS ($A(28)$ in Eq. 4.4; left panel of Fig. 4.8) practically corresponds to the loss of CO molecules in the ice ($N(CO)$ in Eq. 4.4), measured with the FTIR spectrometer (middle panel of Fig. 4.8). The relation between $A(28)$ and $N(CO)$ (right panel of Fig. 4.8) gives k_{CO} = 1.32 x 10^{-10} A min ML^{-1}, with 1 ML defined as 10^{15} molecules cm^{-2}. This value is good for our setup by the time the experiments were performed.

---

[6] A small rise in the signal of several mass fragments was detected every time the UV lamp was switched on. This effect has been previously reported in other works (see, e.g., Loeffler et al. 2005), but it was not reproducible and difficult to quantify. It may be due to a microwave leaking from the UV lamp to the QMS (Chen, private communication). When comparable to the rise produced by photon-induced desorption of molecules from the ice during some of the experiments, calculated desorbed column densities were considered upper limits.

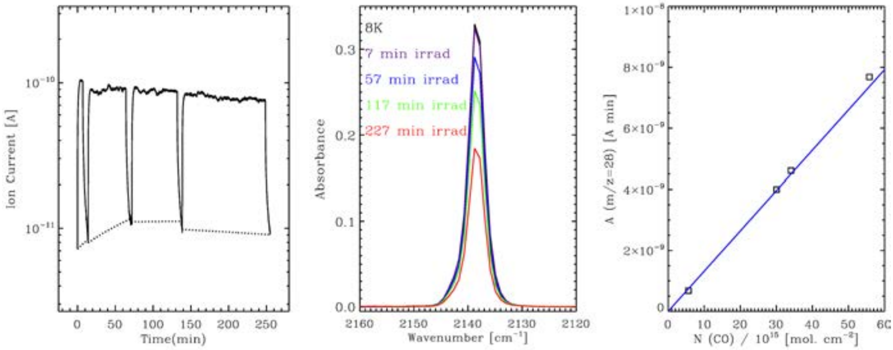

Figure 4.8. *Left:Evolution of the $m/z = 28$ QMS signal corresponding to the photodesorption of CO during UV irradiation of a pure CO ice. The ion current in the y-axis corresponds, approximately, to the partial pressure (mbar) in the main chamber. Dotted lines represent the baselines used to calculate $A(28)$ in every irradiation period. Note that the y-axis is on a logarithmic scale. Middle: Evolution of the C=O stretching mode of CO at 2139 cm^{-1} during UV irradiation of pure CO ice. Differences in the column densities after every period of irradiation correspond to $N(CO)$ in Eq. 4.4. Right: Relation between $A(28)$ and $N(CO)$. The solid line is a linear fit.*

Calibration of the QMS sensitivity $S(m/z)$

The experimental protocol used to obtain $S(m/z)$ was slightly different from the one described in Sect. 4.1.5. The QMS ion current ($I(m/z)$), corresponding to a mass fragment m/z of the molecules of a given species present in the chamber at a given time, is proportional to the pressure measured for that species (P_{mol}), and can be calculated with an equation similar to Eq. 4.2, but with a different constant of proportionality:

$$I(m/z) = k^*_{QMS} \cdot \sigma^+(mol) \cdot P(mol) \cdot Is_F(m) \cdot I_F(z) \cdot F_F(m) \cdot S(m/z). \qquad (4.7)$$

In this case, the Bayard-Alpert ionization gauge (model IoniVac IM540) used as pressuremeter in ISAC does not discriminate between different isotopologs of the same species, and $P(mol)$ (once corrected for the gas correction factors provided by the gauge manufacturer) account for all of them. Therefore, an isotopic factor ($Is_F(m)$) must be introduced to take into account only the isotopolog of mass m that is being measured by the QMS.

Since Eq. 4.3 uses the relative sensitivity of the QMS between any mass fragment and the mass fragment m/z=28, it is not necessary to obtain the absolute sensitivity of the mass spectrometer. Instead we worked with

$$k^*_{QMS} \cdot S(m/z) = \frac{I(m/z)}{\sigma^+(mol) \cdot P(mol) \cdot Is_F(m) \cdot I_F(z) \cdot F_F(m)} \qquad (4.8)$$

for every mass fragment, since the ratio $S(m/z)/S(28)$ is the same as the ratio $k^*_{QMS} \cdot S(m/z)/k^*_{QMS} \cdot S(28)$, assuming that k^*_{QMS} is the same for all the species and does not depend on the pumping speed. That assumption is correct since k^*_{QMS} is related to

Table 4.1. *Values used in Eq. 4.8 to derive the relation between* $k^*_{QMS} \cdot S$ *and* m/z.

Factor	He	Ne	Ar
$\sigma^+(mol)$ $(\AA^2)^a$	0.296	0.475	2.520
$I_F(z)^a$	1	1	0.948
$Is_F(m)^b$	1.000	0.905	0.996

[a] From Rejoub et al. (2002).

[b] From de Laeter et al. (2003).

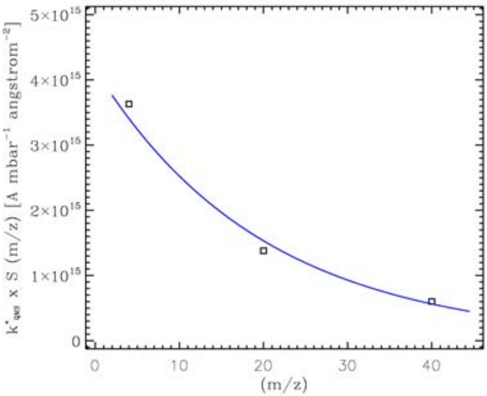

Figure 4.9. *Relation between* $k^*_{QMS} \cdot S(m/z)$ *and* m/z. *The solid line is an exponential fit.*

the actual pressure in the chamber, which is kept constant in these experiments, thus compensating for the different pumping speeds of the noble gases.

To derive a relation between $k^*_{QMS} \cdot S$ and m/z that could be used for mass fragments of any species, we introduced three noble gases into the ISAC chamber: He (gas, Air Liquide 99.999%), Ne (gas, Air Liquide 99.995%), and Ar (gas, Praxair 99.997%) at different pressures. For every gas, the ratio between the QMS signal ($I(m/z)$) and the pressure of the gas ($P(mol)$) was corrected for the factors in Eq. 4.8 (Table 4.1, except for the fragmentation factor, since noble gas atoms do not produce any fragments in the mass spectrometer), leading to a value of $k^*_{QMS} \cdot S(m/z)$ for three different m/z values (m/z=4 for He, m/z=20 for Ne, and m/z=40 for Ar). These values are plotted in Fig. 4.9. An exponential fit leads to a sensitivity curve

$$k^*_{QMS} \cdot S(m/z) = 4.16 \times 10^{15} \cdot e^{-(m/z)/20.02} \tag{4.9}$$

in A mbar^{-1} $\AA^{-2}$.

Please note that calibration of the QMS must be done periodically, since the parameters may change with time. The values presented in this Chapter are only valid for the experimental simulations in Chapter 8. Values to be used in Chapters 9 and 10 are presented in the corresponding chapters.

4.2 Observational Astrophysics - Radio Astronomy

Infrared (vibrational) spectroscopy (Sect. 4.1.4) is a powerful tool to study the interstellar solid particles, and it was widely used during the experimental simulations described in Chapters 5 - 11. Gas-phase molecules in the ISM, on the other hand, are usually observed thanks to the rotational spectroscopy, and in particular, to the spectral lines emitted in the sub-mm - radio region of the spectrum ($\sim$ 0.5 mm[7] - 10 m, or 600 GHz - 30 MHz) that can be detected by radio telescopes on Earth. A brief introduction to the rotational spectroscopy of molecules is provided in Sect. 4.2.1. In Sect. 4.2.2, some concepts regarding the operation of radio telescopes used in Chapter 12 are revised. Finally, some fundaments of interferometry are introduced in Sect. 4.2.3.

4.2.1 Rotational spectroscopy

At the typical temperatures of the cold and warm ISM regions, transitions to excited rotational levels (of the ground vibrational state, in most cases) are allowed. The subsequent decay to a lower rotational level leads to the spontaneous emission of a photon of a given frequency in the sub-mm - radio region of the spectrum.

In general, a given rotational level i with energy E_i (usually expressed in K), which may be degenerated in g_i levels of equal energy, is characterized by three quantum numbers: J, the main rotational quantum number, corresponds to the total rotational angular momentum of the molecule, while K_a and K_c (which can take values ranging from -J to +J) are the projections of J onto two of the three principal inertial axes. For symmetric top molecules, K_a = K_c = K. Additional quantum numbers may be needed in some particular cases. The difference between the energy of the upper and lower rotational levels involved in a given transition (E_u and E_l, respectively) corresponds to the frequency of the photon emitted.

The intensity[8] of photons of a given frequency (i.e., corresponding to a given transition between levels u and l) emitted by the gas-phase molecules of a given source in the ISM depends not only on the population of the upper energy level (N_u[9], in molecules cm^{-2}), but also on the probability of the transition (A_{ul}, known as Einstein coefficient, and expressed in s^{-1}), since the transitions are spontaneous.

When the gas-phase molecules of an interstellar region are in local thermodynamical equilibrium (LTE), the rotational levels are populated following a Boltzmann law (see, e.g., Goldsmith & Langer 1999):

$$N = \frac{N_i \cdot Q(T)}{g_i} \cdot e^{\frac{E_i}{T}}, \tag{4.10}$$

where N is the total column density of a particular species; N_i, E_i, and g_i are the population, energy, and degeneracy of level i, respectively; $Q(T)$ the partition function of the species, that determines how the different levels are populated at a given temperature; and T the excitation (or rotational) temperature, that corresponds to the kinetic temperature of the gas.

In radio astronomy, the emitted intensity at a given frequency (I_ν) is usually expressed in units of T_B (brightness temperature, in K), even when the molecules in the

---

[7] 500 μm or 20 cm^{-1}.

[8] Emited energy per unit time per unit area per unit frequency per unit solid angle.

[9] N_u takes into account all the g_u degenerate levels with energy E_u.

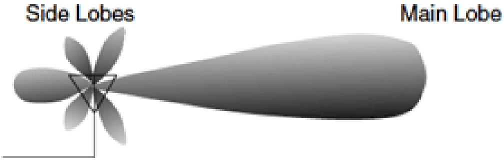

Figure 4.10. *Typical antenna beam pattern. From embedded.com*

interstellar regions do not emit photons as black bodies [10]. The integration of the intensity over a delta function in solid angle leads to the emitted flux density (F_ν), usually expressed in Jy (1 Jy = 10^{-26} W m^{-2} Hz^{-1}):

$$F_\nu = \int_{4\pi} I_\nu d\Omega. \tag{4.11}$$

4.2.2 Single-dish observations

The molecular rotational emission lines can be collected by radio telescopes (also known as dishes), which are technically antennas.

The sensitivity of an antenna depends on the direction of the incoming photons, following a particular antenna beam pattern (or power pattern, P_n; see Fig. 4.10). Two angles (θ and ϕ) can be used to express this dependence, and the antenna beam pattern is normalized to 1 in the (θ=0, ϕ=0) position ($P_n(0,0)=1$). The antenna beam solid angle (Ω_A) is the integration of the antenna power pattern over the entire sphere:

$$\Omega_A = \int_{4\pi} P_n(\theta, \phi) d\Omega. \tag{4.12}$$

As it is shown in Fig. 4.10, most of the photons are collected in the so-called main lobe or main beam (mb) of the antenna. The integration of the antenna beam pattern over the main beam is the main beam solid angle (Ω_{mb}):

$$\Omega_{mb} = \int_{mainbeam} P_n(\theta, \phi) d\Omega. \tag{4.13}$$

The angular resolution of the radio telescope depends on the main beam size, and corresponds to the half power beamwidth of the main beam, which is on the order of λ/D, being D the diameter of the antenna. The ratio between the main beam and the antenna solid angle is the main beam efficiency (θ_{mb}):

$$\eta_{mb} = \frac{\Omega_{mb}}{\Omega_A}. \tag{4.14}$$

---

[10] The emission spectrum of a black body depends only on its temperature, according to the Planck law: $I_\nu \equiv B_\nu^{BB}(\mathrm{T}_B) = \frac{2\cdot h\cdot\nu^3}{c^2\cdot(exp(h\nu/k_B T_B)-1)}$, where h is the Planck constant, k_B the Boltzmann constant and c the speed of light. At low frequencies the Rayleigh-Jeans approximation can be used, leading to: $B_\nu^{BB}(\mathrm{T}_B) \approx \frac{2\cdot\nu^2\cdot k_B T_B}{c^2}$

Actually, both the interstellar source brightness temperature ($T_B(\theta,\phi)$), and the antenna power pattern ($P_n(\theta,\phi)$) depend on the angular position. The convolution of the brightness temperature of a source and the antenna beam pattern leads to the measured antenna temperature (T_A):

$$T_A = \frac{1}{\Omega_A} \int_{4\pi} T_B(\theta, \phi) P_n(\theta, \phi) d\Omega, \tag{4.15}$$

which is the antenna convolution equation.

In the sub-mm region, the atmosphere is not completely transparent (the atmospheric transmission is not 1). Therefore, the antenna temperature measured by the radio telescope (T_A) on the Earth must be corrected from the atmospheric attenuation (leading to T^*_A).

Usually, observations are expressed in T_{mb} units (main beam temperature), assuming that all the photons have been collected by the main beam. The main beam temperature is related to the measured antenna temperature through the main beam efficiency:

$$T_{mb} = \frac{T^*_A}{\eta_{mb}}. \tag{4.16}$$

In addition, when the source size is smaller than the antenna beam size the intensity measured by the telescope is diluted with respect to the intensity emitted by the source, and it must be corrected using the beam filling factor (Maret et al. 2011):

$$\eta = \frac{\theta^2_{source} + \theta^2_{beam}}{\theta^2_{source}}. \tag{4.17}$$

The photons collected by the antenna are subsequently analyzed (selected upon their frequency) by the receivers of the radio telescope, also known as frontends.

In general, heterodyne receivers (see, e.g., Vassilev et al. 2008) are used as frontends when molecular emission lines detection is intended. In that case, the radio telescope detects signals instead of directly photons. The observed signal, with a range of frequencies ν typically on the order of 100 GHz, is mixed with the signal produced by a tunable local oscillator ν_{LO}, whose frequency is of the same order, producing a signal with a much lower frequency ($\nu - \nu_{LO}$, on the order of 1 GHz), that can be more easily handled by any electronic equipment. The receiver selects those observed frequencies ν that fulfill the condition $|\nu - \nu_{LO}|$=ν_{IF}, whith ν_{IF} usually ranging from 4 GHz to 8 GHz (depending on the bandwidth of the receiver). Therefore, two ranges of frequencies are selected: the upper sideband (USB), where $\nu - \nu_{LO}$=ν_{IF}; and the lower sideband (LSB), where $\nu_{LO} - \nu$= ν_{IF}. Since the range of ν_{IF} is fixed for any receiver, the frequency of the local oscillator ν_{LO} is selected in every observation depending on the frequencies of interest. Single sideband receivers (SSB) are able to work with only one of the sidebands, and the other is filtered out. Dual sideband receivers (DSB), on the other hand, can work with both sidebands at the same time, thus doubling the observed bandwidth.

The selected signal is amplified before reaching the detector (also known as the backend of the radio telescope), where the autocorrelator transforms the signal into energy, and is finally measured.

4.2.3 Interferometric observations

[11] As stated in the previous section, the angular resolution of a single antenna is on the order of λ/D. Since the wavelengths of the sub-mm - radio region of the spectrum are rather high, the spatial resolution achieved in radio astronomy is much worse than that of the optical telescopes (for example) and, in general, interstellar sources are not spatially resolved with single antennas, but observed as point-like sources. However, a much better spatial resolution can be achieved using radio interferometers [12].

Radio interferometers consist of an array of antennas distributed over a large ($\sim$km^2) surface on the Earth, that are used to observe a particular source at the same time. The signals observed with two different telescopes of the array can be correlated, generating an interference pattern as a function of the delay with which the same wave front emitted by the interstellar source is observed by either telescopes.

Mathematically, this interference pattern is the Fourier transform for the given delay of the source intensity distribution in the plane of the sky ($I(x, y)$) (see eq. 4.18), and contains information about the spatial distribution of the source. Two connected telescopes in the array are separated by a baseline vector (**B**, as seen from the source point of view) that represents a different point in the so-called (u,v) plane[13] at every moment (that is, a different delay). The Fourier transform of the source intensity distribution for a given delay is the visibility of the source for a particular (u,v) point ($V(u, v)$):

$$V(u,v) = e^{ik\mathbf{Bs}} \int\int I(x,y) e^{2\pi i(ux+vy)} dxdy, \tag{4.18}$$

where **s** is the unit vector in the direction of the source and **B**·**s** represents the delay.

A visibility is therefore a complex quantity with

- phase: $e^{ik\mathbf{Bs}}$
- amplitude: $\int\int I(x,y) e^{2\pi i(ux+vy)} dxdy$

By observing with different baselines (different couples of telescopes in the array) during a span of time, more visibilities corresponding to different (u,v) points are measured, and more spatial information is collected.

The Fourier transform of all the observed visibilities should recover the image of the source:

$$I(x,y) = \int\int V(u,v) e^{2\pi i(ux+vy)} dudv^{14}, \tag{4.19}$$

if $V(u, v)$ was measured for every point in the (u,v) plane. This process is called *imaging*.

However, the resulting image is actually convolved with the dirty beam, i.e., the Fourier transform of the sampling function ($S(u, v)$) that is 1 in the parts of the (u,v) plane sampled during the observations, and 0 elsewhere. This is called the dirty image:

---

[11] This section is based on the notes of the European Radio Interferometry School ERIS 2015.

[12] An exhaustive description of interferometric techniques is way beyond the scope of this thesis. Only a gentle introduction is provided in this section.

[13] The (u,v) plane contains the coordinates of the infinite possible baseline vectors.

[14] Taking into account only the amplitude of the visibilities for simplification purposes.

$$I_D(x,y) = \int\int V(u,v)S(u,v)e^{2\pi i(ux+vy)}dudv. \tag{4.20}$$

This happens because of the lack of spatial information due to a finite sampling of the (u,v) plane when observing during a finite span of time with a finite number of baselines. By making several assumptions, additional information can be supplied, and a clean image can be obtained. The simplest case is to assume that the sky consists of a finite number of point sources (this is the Hogbom *clean* algorithm), but a wealthy ammount of different *clean* algorithms with different approximations are used.

References

Alata, I., Cruz-Díaz, G. A., Muñoz Caro, G. M., & Dartois, E. 2014, A&A, 569, A119

Chen, Y.-J., Chu, C.-C, Lin, Y.-C. et al. 2010, Advances in Geosciences, 25, 259

Chen, Y.-J., Chuang, K.-J, Muñoz Caro, G. M., et al. 2014, ApJ, 781, 15

Cruz-Díaz, G. A. 2014, PhD Thesis

Cruz-Díaz, G. A., Muñoz Caro, G. M., Chen, Y.-J., & Yih, T.-S. 2014, A&A, 562, A119

d'Hendecourt, L. B.,& Allamandola, L. J. 1986, A&AS, 64, 453

Fayolle, E. C., Bertin, M., Romanzin, C., et al. 2013, A&A, 556, A122

Fillion, J.-H., Fayolle, E., Michaut, X., et al. 2014, Faraday Discuss., 168, 533

France, K., Andersson, B.-G., McCandliss, S. R., & Feldman, P. D. 2005, ApJ, 682, 750

Godard, M., & Dartois, E. 2010, A&A, 519, A39

Godard, M., Féraud, G., Chabot, M., et al. 2010, A&A, 529, A146

Goldsmith, P.F., & Langer, W.D. 1999, ApJ, 517, 209

Gredel, R., Lepp, S., Dalgarno, A., & Herbst, E. 1989, ApJ, 347, 289

Jenniskens, P., Baratta, G. A., Kouchi, A., et al. 1993, A&A, 273, 583

Jiménez-Escobar, A. & Muñoz Caro, G.M. 2011, A&A, 536, A91

Kaiser, R. I., Jansen, P., Petersen, K., & Roessler, K. 1995, Rev. Sci. Instrum. 66, 5226

de Laeter, J. R., Böhlke. J. R., De Bievre, P., et al. 2003, Pure and Applied Chemistry, 75, 685

Loeffler, M. J., Baratta, G. A., Palumbo, M. E., Strazzulla, G., & Baragiola, R. A. 2005, A&A, 435, 587

Maret, S., Hily-Blant, P., Pety, J., Bardeau, S., & Reynier, E. 2011, A&A, 526, A47

Martín-Doménech, R., Manzano-Santamaría, J., Muñoz Caro, G. M., et al. 2015, A&A, 584, A14

Muñoz Caro, G. M., Jiménez-Escobar, A., Martín-Gago, J.Á. et al. 2010, A&A, 522, A108

Muñoz Caro, G. M., & Schutte, W. A. 2003, A&A, 412, 121

Rejoub, R., Lindsay, B. G., & Stebbings, R. F. 2002, Phys. Rev. A, 65, 042713

Tanarro, I., Herrero, V. J., Islyaikin, A. M., et al. 2007, J. Phys. Chem. A, 111, 9003

Vassilev, V., Meledin, D., Lapkin, I., et al. 2008, A&A, 490, 1157

Part III

Results - Dust

Chapter 5

UV photoprocessing of hydrogenated amorphous carbons

Adapted from *Vacuum ultraviolet photolysis of hydrogenated amorphous carbons. III. Diffusion of photo-produced H_2 as a function of the temperature*. Martín-Doménech, R., Dartois, E., & Muñoz Caro, G.M. 2016, A&A, 591, A107 [1].

Abstract

Hydrogenated amorphous carbon (a-C:H) has been proposed as one of the carbonaceous solids detected in the interstellar medium. Energetic processing of the a-C:H particles leads to the dissociation of the C-H bonds and the formation of hydrogen molecules and small hydrocarbons. Photo-produced H_2 molecules in the bulk of the dust particles can diffuse out to the gas phase and contribute to the total H_2 abundance.

We have simulated this process in the laboratory with plasma-produced a-C:H and a-C:D analogs under astrophysically relevant conditions to investigate the dependence of the diffusion as a function of the temperature.

Experimental simulations were performed in a high-vacuum chamber, with complementary experiments carried out in an ultra-high-vacuum chamber. Plasma-produced a-C:H analogs were UV-irradiated using a microwave-discharged hydrogen flow lamp. Molecules diffusing to the gas-phase were detected by a quadrupole mass spectrometer, providing a measurement of the outgoing H_2 or D_2 flux. By comparing the experimental measurements with the expected flux from a one-dimensional diffusion model, a diffusion coefficient D could be derived for experiments carried out at different temperatures.

Dependence on the diffusion coefficient D with the temperature followed an Arrhenius-type equation. The activation energy for the diffusion process was estimated (E_D(H$_2$) = 1660 $\pm$ 110 K, E_D(D$_2$) = 2090 $\pm$ 90 K), as well as the pre-exponential factor (D_0(H$_2$) = $0.0007^{+0.0013}_{-0.0004}$ cm^2 s^{-1}, D_0(D$_2$) = $0.0045^{+0.005}_{-0.0023}$ cm^2 s^{-1}).

The strong decrease of the diffusion coefficient at low dust particle temperatures exponentially increases the diffusion times in astrophysical environments. Therefore, transient dust heating by cosmic rays needs to be invoked for the release of the photo-produced H_2 molecules in cold PDR regions, where destruction of the aliphatic component in hydrogenated amorphous carbons most probably takes place.

5.1 Introduction

As stated in Chapter 3, Sect. 3.1, dust particles in the interstellar medium (ISM) include minerals (silicates and oxides) and carbonaceous matter of various types. In particular, the absorption band observed at 3.4 μm toward several lines of sight (Soifer et al. 1976, Wickramasinghe & Allen 1980, McFadzean et al. 1989, Adamson et al. 1990, Sandford et al. 1991, Pendleton et al. 1994, Bridger et al. 1994, Imanishi 2000a, Imanishi 2000b, Spoon et al. 2004, Dartois & Muñoz Caro 2007) has been assigned to hydrogenated amorphous carbons (a-C:Hs or HACs). Several laboratory analogs have been proposed to fit these observed IR features (Schnaiter et al. 1998, Lee & Wdowiak 1993, Furton et al. 1999, Mennella et al. 1999, Mennella et al. 2003, Dartois et al. 2005, Godard & Dartois 2010, Godard et al. 2011). In this Chapter, we focus on plasma-produced a-C:H analogs (see Godard & Dartois 2010, Godard et al. 2011, and Chapter 4, Sect.4.1.2).

---

[1] In particular, Sections 5.1 and 5.2 have been shortened with respect to the paper version, since part of the information is presented in Chapters 3 and 4.

Interestingly, this feature is not observed in the dense ISM. Previous laboratory simulations on the energetic processing of HAC analogs under astrophysically relevant conditions have shown a decrease of their hydrogen content and, therefore, of the aliphatic C-H spectral features (see, e.g., Mennella et al. 2003, Godard et al. 2011, Alata et al. 2014, Alata et al. 2015, and references therein). In the diffuse ISM, the energetic processing is driven by the interaction of the hydrogenated amorphous carbon particles with ultraviolet (UV) photons (dehydrogenation by cosmic rays is negligible in these regions, see Mennella et al. 2003) while destruction by cosmic rays (directly, or indirectly through the generated secondary UV field) dominates in the dense ISM. The presence of atomic hydrogen allows re-hydrogenation in the diffuse ISM. However, this process is inhibited in the dense ISM, possibly leading to a more aromatic carbonaceous solid (amorphous carbons or a-Cs) if not fully destroyed at earlier times. The destruction/transformation of the aliphatic C-H component most probably takes place in intermediate regions such as translucent clouds or photo-dominated regions, where dehydrogenation by both UV photons and cosmic rays is still active while hydrogen is in molecular form, thus not allowing re-hydrogenation (Godard et al. 2011).

Hydrogen atoms resulting from the rupture of C-H bonds recombine to form H_2 molecules. Molecular hydrogen subsequently diffuses to the surface and is lost from the a-C:H (Wild & Koidl 1987, Möller & Scherzer 1987, Adel et al. 1989, Marée et al. 1996, Godard et al. 2011, Alata et al. 2014). This process thus constitutes an alternative pathway for H_2 formation within the bulk of the hydrogenated amorphous carbon particles in the ISM, in addition to the previously studied formation on the surface of interstellar solids from physisorbed and/or chemisorbed H atoms (see, e.g., Pirronello et al. 1997, Katz et al. 1999, Habart et al. 2005, Cazaux et al. 2011, Gavilán et al. 2012). Although molecular hydrogen is the main product resulting from the photolysis of a-C:H analogs, small hydrocarbons with up to four carbon atoms are also detected (Alata et al. 2014, Alata et al. 2015). Production of these small hydrocarbons in the bulk of carbonaceous solids is proposed as an additional source that may account for the abundance of these species in some regions where pure gas-phase models face difficulties in predicting them (Pety et al. 2005, Alata et al. 2015).

In this work, we have investigated the diffusion of molecular hydrogen through the plasma-produced hydrogenated amorphous carbon analogs under astrophysically relevant conditions. Deuterated analogs have been preferently used to avoid confusion with background H_2 during the first experiments. We have focused on the variation of the diffusion coefficient as a function of the temperature and, in particular, we have estimated D_0 and E_D for the diffusion of H_2 (D_2) molecules through the a-C:H (a-C:D) analogs. The Chapter is organized as follows: Section 5.2 describes the experimental setup and the theoretical models used to evaluate the diffusion coefficient from the experiments. Section 5.3 presents the experimental results, while their astrophysical implications are discussed in Sect. 5.4. Finally, conclusions are summarized in Sect. 5.5.

5.2 Methods

5.2.1 SICAL-X

The majority of the experiments were carried out using the SICAL-X setup described in previous papers (see, e.g., Alata et al. 2014) and in Chapter 4, Sect. 4.1.2 at the IAS (Institut
d'Astrophysique Spatiale).

As mentioned in the aforementioned Chapter, deuterated amorphous carbon analogs were preferentially used to study the diffusion of in situ photoproduced D_2 within this material. The a-C:D analogs produced in a different setup (SICAL-P) on a MgF_2 substrate were introduced in the chamber and cooled down to the working temperature thanks to the combination of a closed-cycle helium cryostat and a resistive-type heater. The sample temperature was monitored with a thermocouple, reaching a sensitivity of 0.1 K.

Solid samples were monitored with a Bruker Vertex 80v Fourier transform infrared (FTIR) spectrometer. Spectra were collected at a resolution of 1 cm^{-1}, covering the spectral region between 7500 and $\sim$1500 cm^{-1} (due to the low transmittance of the MgF_2 substrate below $\sim$1500 cm^{-1}). The analogs thicknesses l were estimated from the interference pattern (or fringes) in the IR spectra, using the formula

$$l = 1/(2 \cdot n \cdot \Delta\sigma \cdot cos(\alpha_{IR})), \tag{5.1}$$

where n is the refractive index of the analogs, estimated to be 1.7 ± 0.2, $\Delta\sigma$ the fringe spacing, and α_{IR} the angle of incidence of the IR beam with the sample normal (45° in SICAL-X).

To study the diffusion of D_2 molecules through the a-C:D analogs, samples were irradiated with vacuum-ultraviolet (VUV) photons from a Microwave-Discharged Hydrogen-flow Lamp (MDHL, see Chapter 4, Sect. 4.1.3), leading to the dissociation of C-D bonds and the formation of D_2 in the analogs. Photochemical properties of a-C:H and a-C:D analogs are expected to be similar (see Alata et al. 2014). UV photons reached the surface of the analogs directly in contact with the MgF_2 substrate, and the photoproduced D_2 molecules diffused through the samples to the opposite surface, subsequently passing into the gas phase (see Fig. 5.1). The mean penetration depth for the VUV photons in the a-C:D analogs was approximately 80 nm as measured with VUV-dedicated experiments (Gavilán et al. 2016). Since the plasma-produced analogs had a thickness of around 1 μm, the region affected by the VUV photons was negligible compared to the total thickness of the sample, which remained almost unaltered. The surface of the a-C:D analogs was around 1 cm^2, much larger than the thickness of the samples. Therefore, only diffusion in the direction orthogonal to the substrate was considered.

The initial D_2 concentration throughout the a-C:D analogs was zero. Photo-production of D_2 at the irradiated a-C:D surface in contact with the MgF_2 substrate established a constant D_2 flux entering the samples, since the IR spectra of the analogs did not change after UV irradiation. Deuterium molecules that were subsequently diffused through the samples eventually reached the opposite surface, where they inmediately passed into the gas-phase. Deuterium concentration at the sample surface in contact with the gas phase was thus negligible during the experiments.

D_2 molecules in the gas phase were detected by a Quadera 200 quadrupole mass spectrometer (QMS) located at ∼10 cm from the samples. A heated filament in the QMS produced a stable current of energetic electrons (∼70 eV), which ionized the D_2 molecules by electron bombardment. Ions were subsequently detected by a secondary-emission multiplier (SEM) detector. The ion current corresponding to the $m/z = 4$ mass fragment provided a measure of the D_2 flux through the surface of the a-C:D analogs in contact with the gas phase, considering the background level as zero flux. Therefore, upon onset of the VUV irradiation, D_2 concentration throughout the a-C:D analogs, as well as the measured outgoing flux of D_2 molecules, increased to a steady-state value (see Alata et al. 2014). Once the steady state was reached, the shutter was placed in front of the sample, blocking the VUV photons and stopping the D_2 production, thus eliminating the entering D_2 flux at the sample surface in contact with the substrate. As a consequence, the measured $m/z = 4$ ion current (i.e., the outgoing D_2 flux) decreased back to the background value.

The evolution of the measured D_2 flux with time during irradiation of the sample (flux increasing to a steady-state value), and after irradiation (when D_2 formation is stopped and the $m/z = 4$ ion current decreases from the steady-state back to the background value) depends on the diffusion coefficient D of the D_2 molecules through the a-C:D analogs. The diffusion coefficient can thus be estimated from the one-dimensional diffusion models that provide outgoing flux values that best fit the measured ion currents during the experiment (see Sect. 5.2.3).

Since the deuterium molecules were produced in situ in the a-C:D analogs during irradiation of the samples, we could not a priori disentangle the different steps taking place in the process: rupture of the C-D bonds, diffusion of the D atoms and recombination of two D atoms or direct neighbor D-abstraction from a C-D bond to form D_2 molecules, and the diffusion process itself. Therefore, the derived diffusion coefficients should be seen, in principle, as so-called apparent coefficients, describing the convolution of all these steps. However, D_2 molecules passing into the gas phase were detected very early on, once UV irradiation was established, subsequently increasing the observed flux with time (see Figures 5.3, 5.4, and left panel of Fig. 5.5, in Sect. 5.3 where the experimental results are presented). This means that all processes prior to the diffusion of molecules were probably taking place in a much shorter timescale than the diffusion itself, which could be considered the limiting step. In particular, Fig. 5.4 in Sect. 5.3 shows the symmetry between the measured $m/z = 4$ ion current during irradiation (increasing curve) and the decreasing signal observed once the UV beam was blocked after reaching the steady-state (when the diffusion equilibrium is achieved and the film is full of D_2). This shows that the measurement is dominated by the diffusion step with respect to the molecule formation timescale. Otherwise, if D_2 formation was the limiting step, we would expect to observe a delay and asymmetry in the $m/z = 4$ signal for the increasing curve owing to the D_2 formation limiting steps at the beginning, compared to the decreasing curve, when the beam is off and the bulk of the film is full of of previously formed D_2 molecules. Other measured behaviors supported the fact that the D_2 formation steps occurred at much shorter timescales than the diffusion step for the film thicknesses used and at the temperatures we performed the experiments, as explained below.

The diffusion coefficient D of a diffusing species through a given material is tem-

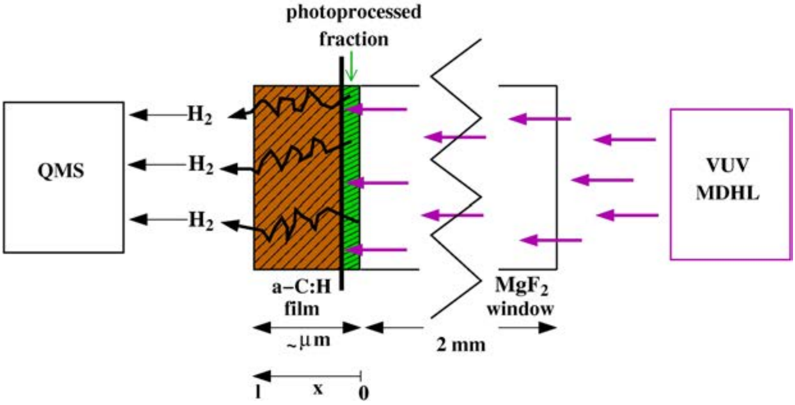

Figure 5.1. *Configuration of the measurement.*

perature dependent. Therefore, consecutive experiments following the above explained protocol were carried out with the same sample at different temperatures, allowing the evaluation of the diffusion coefficient as a function of the temperature. After every experiment, the a-C:D analogs were warmed up to 250 K with a heating rate of 5 K/min, to evacuate the eventual remaining deuterium from the sample, and set the D_2 concentration back to zero before performing the experiment at a different temperature.

According to Equation 5.3 (see Sect. 5.2.3), the diffusion coefficient increases with increasing temperature. Therefore, the diffusion time decreases with increasing temperature for a given sample thickness. At the same time, diffusion of deuterium through thicker samples takes longer, since molecules have to go through a longer distance to reach the analog surface in contact with the gas phase. A set of a-C:D analogs with different thicknesses were used to study diffusion in a wide range of temperatures while keeping the duration of the experiments within reasonable limits. In this way, diffusion at low temperatures (95 K - 140 K) was preferentially probed with thinner samples (0.2 μm - 2.6 μm), since diffusion times were shorter despite the lower diffusion coefficient; while diffusion at high temperatures (110 K - 170 K) was studied with thicker analogs (3.4 μm - 5.2 μm). When thinner films were irradiated at the same temperature (i.e., the diffusion length was short and bulk diffusion timescale was rapid), the molecular D_2 release was observed immediately after turning the UV lamp on, and stopped immediately after switching it off, with no delay that would otherwise indicate a longtime scale limiting the D_2 formation step (meaning with timescales of the order of seconds, which was the QMS scanning time). These test measurements did not allow us to measure the bulk diffusion and are thus not shown in Sect. 5.3. In addition, the diffusion timescales changed with the thickness according to what was expected for different films at the same temperature (see above), whereas the production rate of D_2 on one side was confined to the same small thickness ($\sim$80 nm, as explained above) for all films, supporting the fact that diffusion was the limiting step.

5.2.2 ISAC

Complementary experiments were carried out with a-C:H analogs (also produced in the SICAL-P setup on MgF_2 substrates, see Chapter. 4.1.2) using the ISAC setup (Muñoz Caro et al. 2010, see also Chapter 4, Sect. 4.1.1). The ISAC setup consists in an ultra-high-vacuum (UHV) chamber with a base pressure of about 4×10^{-11} mbar, three orders of magnitude lower than that of the SICAL-X setup (see Sect. 5.2.1), thus enabling us to work with H_2 instead of D_2; and to evaluate the diffusion coefficient D of H_2 molecules through hydrogenated amorphous carbon analogs as a function of the temperature, Since H_2 molecules are smaller than D_2 molecules, diffusion coefficient of the former is expected to be higher than that of the latter at a given temperature. However, dependence of the diffusion coefficient of H_2 through the a-C:H analogs as a function of the temperature is expected to be similar to that of the diffusion coefficient of D_2 through a-C:D analogs, leading to similar E_D values.

The a-C:H analogs were introduced in the chamber and cooled down to the working temperature, also using a closed-cycle helium cryostat and a resistive-type heater. The temperature was controlled thanks to a silicon-diode sensor and a LakeShore Model 331 controller, reaching a sensitivity of 0.1 K. As in the SICAL-X setup, solid samples were monitored with a Bruker Vertex 70 FTIR spectrometer. Spectra were collected with a spectral resolution of 2 cm^{-1}, covering the range between 6000 and $\sim$1500 cm^{-1}. The angle of incidence of the IR beam with the sample normal was 0° in this setup.

Diffusion of H_2 molecules through the a-C:H analogs were studied using the experimental protocol described in Sect. 5.2.1, and the vacuum-ultraviolet lamp described in Chapter 4, Sect. 4.1.3.

A Pfeiffer Prisma QMS with a Channeltron detector (see also Chapter 4, Sect. 4.1.5 located at $\sim$17 cm apart from the sample was used to detect the H_2 molecules in the gas phase, which were also ionized by electron bombardment with energetic ($\sim$70 eV) electrons. The ion current of the m/z = 2 mass fragment provided a measure of the outgoing H_2 flux. No shutter was present in the ISAC setup, and we had to turn off the lamp after the steady state was reached to stop the production of H_2 molecules. Subsequent changes in the background m/z = 2 ion current were taken into account.

5.2.3 Theoretical models

Produced H_2 in the bulk of the a-C:H particles diffuses to the surface and is subsequently released from the solid. Diffusion of H_2 in a particular direction inside the HAC material can be described by the Fick's first law:

$$F(x,t) = -D \cdot \frac{\partial C(x,t)}{\partial x}, \tag{5.2}$$

where $F(x,t)$ is the rate of transfer of H_2 molecules through unit area of HAC section (i.e., the H_2 flux), in cm^{-2} s^{-1}, D is the diffusion coefficient of molecular hydrogen in the hydrogenated amorphous carbon material, in cm^2 s^{-1}, and $\frac{\partial C(x,t)}{\partial x}$ is the concentration gradient of H_2 molecules in the particular direction x, in cm^{-4}. The negative sign indicates that diffusion takes place in the direction of decreasing concentration. The diffusion coefficient D usually depends on the diffusing species, the material through which it is diffusing, and the temperature. The dependence of D with the temperature generally follows an Arrhenius-type equation:

$$D = D_0 \cdot e^{\frac{-E_D}{T}}, \tag{5.3}$$

where the pre-exponential factor D_0 is the diffusion at infinite temperature, in cm^2 s^{-1}, E_D is the activation energy for the diffusion process in K, and T the temperature in K.

As mentioned in Sect. 5.2.1, the diffusion coefficient D can be estimated from one dimensional diffusion models that provides outgoing flux values that best fit the measured H_2 or D_2 ion currents during the experiments. Diffusion models are particular solutions of the fundamental differential equation of diffusion, which is also known as the Fick's second law:

$$\frac{\partial C(x,t)}{\partial t} = D \cdot \frac{\partial^2 C(x,t)}{\partial x^2}. \tag{5.4}$$

This equation results from combining Equation 5.2 with a mass balance equation applied to a differential element of volume of the material through which diffusion is being studied.

Particular solutions of Equation 5.4 depend on the initial and surface conditions, leading to a series of diffusion models. Concentration of H_2 or D_2 in our samples during UV-irradiation (i.e., when a constant flux F_i is established at the irradiated surface ($x = 0$) of a sample of thickness l, the initial H_2 or D_2 concentration is zero throughout the sample, and concentration at $x = l$ is $C(l,t) = 0$ at all times) is modelled by the following equation (Early 1978):

$$\begin{aligned} C(x,t) = \frac{F_i}{D}(l-x) - \frac{8F_i l}{\pi^2 D} \times \sum_{n=0}^{\infty} \frac{(-1)^n}{(2n+1)^2} \cdot exp[-\frac{(2n+1)^2\pi^2 Dt}{4l^2}] \\ \cdot sin\frac{(2n+1)\pi(l-x)}{2l}. \end{aligned} \tag{5.5}$$

Using Eq. 5.2 at $x = l$, the outgoing flux measured by the QMS, according to this model, can be calculated from Equation 5.5:

$$F(l,t) = 1 - \frac{4}{\pi} \times \sum_{n=0}^{\infty} \frac{(-1)^n}{(2n+1)} \cdot exp[-\frac{(2n+1)^2\pi^2 Dt}{4l^2}], \tag{5.6}$$

normalized to the steady-state value of the outgoing flux ($F(l,\infty) = 1$).

On the other hand, concentration of H_2 or D_2 in the amorphous carbon analogs after UV-irradiation (i.e., when no flux is introduced at the surface $x = 0$ of a sample of thickness l, the initial H_2 or D_2 concentration is C_0 at $x = 0$, and concentration at $x = l$ is $C(l,t) = 0$ at all times) is modelled by the following equation (Carslaw & Jaeger 1959):

$$\begin{aligned} C(x,t) = \frac{8C_0}{\pi^2} \times \sum_{n=0}^{\infty} \frac{1}{(2n+1)^2} \cdot exp[-\frac{(2n+1)^2\pi^2 Dt}{4l^2}] \\ \cdot cos\frac{(2n+1)\pi x}{2l}. \end{aligned} \tag{5.7}$$

According to this model, the outgoing flux measured by the QMS can be derived from Equation 5.7 using Equation 5.2 at $x = l$:

$$F(l,t) = \frac{4}{\pi} \times \sum_{n=0}^{\infty} \frac{(-1)^n}{(2n+1)} \cdot exp[-\frac{(2n+1)^2\pi^2 Dt}{4l^2}], \tag{5.8}$$

normalized to the initial (steady-state) value ($F(l,0) = 1$). We note that Eq. 5.6 = 1 - Eq. 5.8. As shown in Fig. 5.4, evolution of the H_2 or D_2 ion current after irradiation is symmetric with respect to the rise of the signal during irradiation.

In our case, evolution of the m/z = 2 and m/z = 4 ion currents during the experiments was found to be better described by adding a second term in Equations 5.6 and 5.8, introducing an additional diffusion coefficient D'. This led to

$$\begin{aligned} F(l,t) = 1 - p \cdot \frac{4}{\pi} \times \sum_{n=0}^{\infty} \frac{(-1)^n}{(2n+1)} \cdot exp[-\frac{(2n+1)^2\pi^2 Dt}{4l^2}] \\ +(1-p) \cdot \frac{4}{\pi} \times \sum_{n=0}^{\infty} \frac{(-1)^n}{(2n+1)} \cdot exp[-\frac{(2n+1)^2\pi^2 D' \cdot t}{4l^2}], \end{aligned} \tag{5.9}$$

and

$$\begin{aligned} F(l,t) = p \cdot \frac{4}{\pi} \times \sum_{n=0}^{\infty} \frac{(-1)^n}{(2n+1)} \cdot exp[-\frac{(2n+1)^2\pi^2 Dt}{4l^2}] \\ +(1-p) \cdot \frac{4}{\pi} \times \sum_{n=0}^{\infty} \frac{(-1)^n}{(2n+1)} \cdot exp[-\frac{(2n+1)^2\pi^2 D't}{4l^2}], \end{aligned} \tag{5.10}$$

respectively, where p is a free parameter varying between 0.5 and 1, indicative of how close our modified model is to the models described with Equations 5.6 and 5.8. In this work, we refer to the diffusion coefficient D when the opposite is not specified. The physical meaning of the additional diffusion coefficient D' was studied independently in Sects. 5.3.2 and 5.3.2.

5.3 Experimental results

Two different a-C:H analogs with thicknesses 0.9 μm and 2.2 μm were produced under the same conditions in the SICAL-P setup and subsequently studied in the ISAC setup. Diffusion experiments were carried out at 85 K, 95 K, 105 K, and 110 K for the former sample, and at 95 K, 105 K, 110 K, and 120 K for the latter (thinner samples allow the study of diffusion at lower temperatures, since diffusion of molecules through these samples takes less time even though the diffusion coefficient is lower, see Sect. 5.2.1). In the case of the a-C:D analogs, up to five samples with thicknesses 0.2 μm, 1.3 μm, 2.6 μm, 3.4 μm, and 5.2 μm were studied in the SICAL-X setup. Experiments were performed at a wide range of temperatures (from 95 K to 170 K). As explained in Sect. 5.2.2, diffusion coefficients for the D_2 molecules in the a-C:D analogs are lower than those of the H_2 molecules through the a-C:H analogs at the same temperature. Therefore, to keep the duration of the experiments within reasonable limits, experiments with deuterated analogs were carried out at slightly higher temperatures than those performed with hydrogenated analogs of similar thickness.

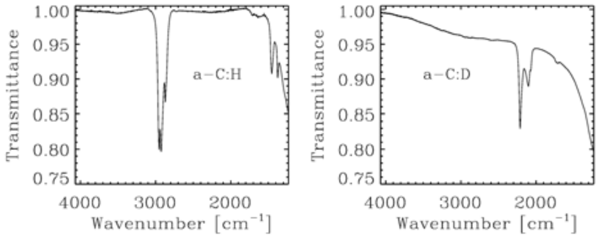

Figure 5.2. *IR transmittance spectrum of an a-C:H analog (left panel), and an a-C:D analog (right panel) deposited on an MgF_2 substrate.Spectra were collected at 110 K.*

5.3.1 IR spectra of the a-C:H and a-C:D analogs

Figure 5.2 shows the mid-IR transmittance spectra of an a-C:H analog (left panel, l = 2.2 μm), and an a-C:D analog (right panel, l = 2.6 μm), collected at 110 K, between 4000 cm^{-1} and 1300 cm^{-1}. Transmittance of the MgF_2 substrate starts decreasing strongly below 1500 cm^{-1}.

As explained in Chapter 3, Sect. 3.1, the asymmetric C-H stretching modes corresponding to methyl (-CH_3) and methylene (-CH_2-) groups led to two absorption peaks at 2955 cm^{-1} and 2925 cm^{-1}, respectively, in the left panel of Fig. 5.2. The symmetric stretching modes at 2873 cm^{-1} and 2857 cm^{-1}, respectively, are blended, which leads to one absorption peak in the red side of the 3.4 μm absorption band. The corresponding bending modes are observed at 1460 cm^{-1} and 1380 cm^{-1} for the methylene and methyl groups, respectively. Absorption at $\sim$1600 cm^{-1} is assigned to the C=C stretching mode, which corresponds to the olefinic fraction of the analog.

The same modes are shifted to lower frequencies in the a-C:D analogs. The assymetric stretching modes, located at 2220 cm^{-1} and 2200 cm^{-1}, are blended in the right panel of Fig. 5.2, as well as the symmetric modes at 2073 cm^{-1} and 2100 cm^{-1}. The corresponding bending modes are also shifted to lower frequencies, where the absorption of the MgF_2 substrate prevents their detection.

Since only a small fraction of the analogs were photoprocessed during the experiments (see Sect. 5.2.1), IR spectra did not change after UV irradiation, which is a condition to the hypothesis of a constant flux at $x = 0$.

5.3.2 QMS measurements of the outgoing H_2 or D_2 flux

As previously explained, the measured ion current of the mass fragments m/z = 2 and m/z = 4 above the background level provided a measure of the outgoing H_2 and D_2 fluxes through the $x = l$ surface of the hydrogenated and deuterated amorphous carbon analogs, respectively, during the experiments.

Figure 5.3 shows the m/z = 4 ion current measured during three experiments performed at three different temperatures with a 3.4 μm thick a-C:D analog, as an example. After onset of the UV irradiation at $t = 0$, the outgoing flux of the photo-produced D_2 molecules increased rapidly at first, and then more slowly, until the steady state was reached. Diffusion times depended on the diffusion coefficient D. At higher temper-

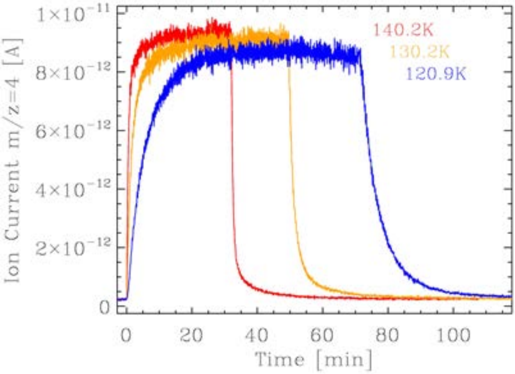

Figure 5.3. *Measured m/z = 4 ion current corresponding to the outgoing D_2 flux during three experiments performed at* ∼*140 K (red solid line),* ∼*130 K (yellow solid line), and* ∼*120 K (blue solid line) on a 3.4 μm thick a-C:D analog. Irradiation starts at $t = 0$.*

atures, a higher D value led to a faster diffusion, and therefore, to a faster increase of the m/z = 4 ion current, while diffusion at lower temperatures was slower. The ion current value at the steady state depends not only on the diffusion coefficient (which in turn depends on the temperature), but also on the VUV photon flux reaching the sample, which may change slightly from one experiment to another. Parallel experiments with different VUV photon fluxes were carried out to check that the derived value of the diffusion coefficient at a given temperature did not vary with the value of the UV flux. Once the steady state was reached, the shutter was placed in front of the sample, preventing the VUV photons from reaching the analog, and thus stopping the D_2 production. The m/z = 4 ion current then decreased back to the background value, again rapidly at first and more slowly later. As for the increase of the outgoing D_2 flux, decay time also depended on the diffusion coefficient. As expected from Equations 5.6 and 5.8, once the background level was subtracted, the normalized ion current (which is equivalent to the normalized D_2 flux) during irradiation was equal to unity minus the normalized ion current during decay of the D_2 flux (see Fig. 5.4 as an example).

Evolution of the normalized ion current (i.e., normalized H_2 or D_2 flux through the analog surface $x = l$) during and after irradiation is modeled by Equations 5.6 and 5.8, respectively. The value of D, which best fits the measured ion currents during the experiments, would be the diffusion coefficient of H_2 (D_2) molecules through the a-C:H (a-C:D) analogs at a given temperature. Evolution of the diffusion coefficient with the temperature is described by Eq. 5.3.

Most of the experiments were carried out with a-C:D analogs in the SICAL-X setup. Derived D values for the D_2 molecules at different temperatures enabled us to calculate the pre-exponential factor D_0 and the activation energy E_D for the diffusion of D_2 through the deuterated analogs. Results are presented in Sect. 5.3.2. Complementary experiments were performed with two a-C:H analogs in the ISAC setup. Calculated D_0 and E_D values are presented in Sect. 5.3.2. E_D was expected to be similar in both cases.

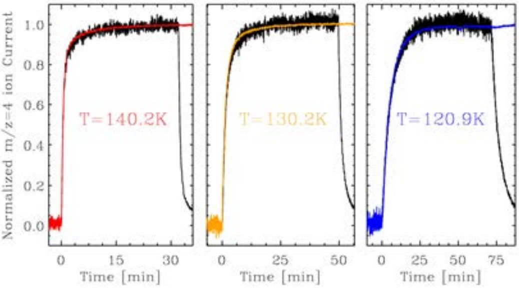

Figure 5.4. *Normalized m/z = 4 ion current after background substraction (equivalent to the normalized D_2 flux) during three experiments performed at ∼140 K (left panel), ∼130 K (middle panel), and ∼120 K (right panel) on a 3.4 μm thick a-C:D analog. Black solid lines correspond to the normalized D_2 flux during irradiation (irradiation starts at $t = 0$), while colored solid lines correspond to 1 - normalized D_2 flux after irradiation (irradiation stops at $t = 0$).*

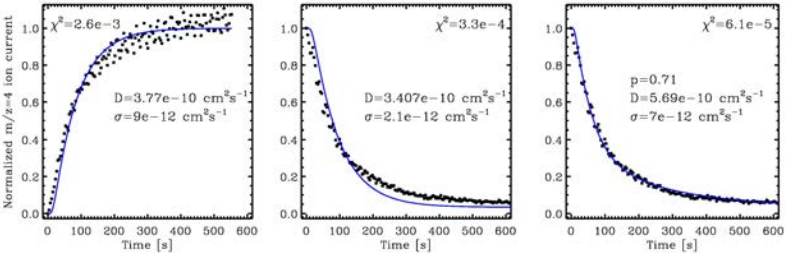

Figure 5.5. *Evolution of the normalized m/z = 4 ion current (black dots), equivalent to the normalized D_2 flux at the $x = l$ surface, during (left panel) and after (middle and right panels) VUV irradiation of a 2.6 μm a-C:D analog at 130 K. Theoretical models fitting the experimental data are presented (blue solid lines), along with the derived diffusion coefficient D and the 1σ associated error. The model shown in the left panel is described by Eq. 5.6. The middle and right panels show the models described by Equations 5.11 and 5.12, respectively. The free parameter p of the latter is an indicator of how close the model is to the one described by Eq. 5.11. The χ^2 values associated with the fits of the experimental data during and after irradiation cannot be directly compared since they are not normalized.*

Modeling of the D_2 diffusion through a-C:D analogs

As explained above, we estimated for every experiment a diffusion coefficient D for the diffusion of D_2 molecules through the a-C:D analogs at a given temperature by fitting the models described with Equations 5.6 and 5.8 to the experimental evolution of the normalized m/z = 4 ion current during and after the irradiation of the sample, respectively, with the linfit procedure programmed with the IDL programming language. This procedure finds the free parameter D which minimizes the χ^2 parameter.

Left panel of Fig. 5.5 shows the evolution of the normalized m/z = 4 ion current, i.e., the normalized outgoing D_2 flux, during irradiation of a 2.6 μm a-C:D analog at 130 K, along with the model described by Eq. 5.6 that best fits the experimental results. The diffusion coefficient derived for that experiment is also shown in the figure. This value is the same within 10% to the diffusion coefficient derived from the decay of the normalized outgoing D_2 flux in the same experiment (middle panel of Fig. 5.5). In this case, instead of subtracting the background level of the m/z = 4 ion current, we included it as a free parameter b in Eq. 5.8:

$$F(l,t) = (1-b)\cdot\frac{4}{\pi}\times\sum_{n=0}^{\infty}\frac{(-1)^n}{(2n+1)}\cdot exp[-\frac{(2n+1)^2\pi^2 Dt}{4l^2}] + b. \tag{5.11}$$

We note that χ^2 values in the left and middle panels of Fig. 5.5 cannot be directly compared since they are not normalized. However, since there is a larger dispersion in the experimental data collected at the steady state than in the background level, we consider the diffusion coefficient derived from the decay curves more accurate, and they have thus been used preferently.

As explained in Sect. 5.2.3, experimental data were better described by a modified model including a second term with an additional diffusion coefficient D'. Adding a second term to Eq. 5.11 results in

$$\begin{aligned} F(l,t) =& p\cdot\frac{4}{\pi}\times\sum_{n=0}^{\infty}\frac{(-1)^n}{(2n+1)}\cdot exp[-\frac{(2n+1)^2\pi^2 Dt}{4l^2}] \\ &+(1-p-b)\cdot\frac{4}{\pi}\times\sum_{n=0}^{\infty}\frac{(-1)^n}{(2n+1)}\cdot exp[-\frac{(2n+1)^2\pi^2 D't}{4l^2}] \\ &+b, \end{aligned} \tag{5.12}$$

which reduced the χ^2 value of the fit (see right panel of Fig. 5.5). Estimated diffusion coefficients D with the modified model were of the same order as those found with the model described by Eq. 5.11. Values of the free parameter p usually varied between ~0.7 and ~0.9. The physical meaning of the D' diffusion coefficient was studied independently (see below).

The estimated 1σ errors presented in Fig. 5.5 for the diffusion coefficient D are model-dominated. We note that diffusion coefficients derived with different experiments at the same temperature can vary up to a factor ~6 (see Fig. 5.6). This was taken into account for the D_0 and E_D estimation.

A total of 19 experiments at temperatures between 95 K and 170 K were carried out with five a-C:D analogs. The diffusion coefficient at intermediate (120 K - 140 K) temperatures was probed with most of the analogs, while D value at low (high) temperatures was probed only with thin (thick) analogs. As explained in Sect. 5.1, dependence of the diffusion coefficient D with the temperature follows an Arrhenius-type equation. Equation 5.3 changes into a line by applying natural logarithm to both sides of the equation

$$ln[D] = ln[D_0] - E_D\cdot\frac{1}{T}, \tag{5.13}$$

where the slope E_D corresponds to the activation energy of the diffusion process. Fitting Eq. 5.13 to the derived diffusion coefficients D from the experiments with the

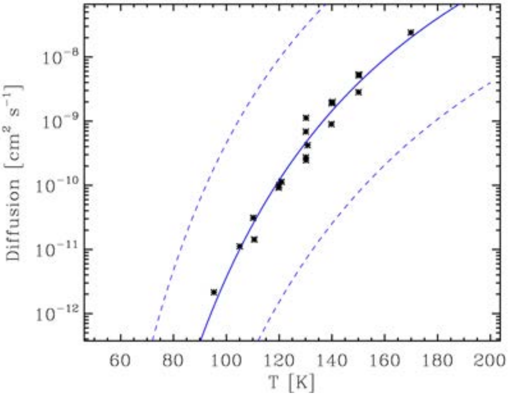

Figure 5.6. *Evolution of the experimental diffusion coefficient D for the diffusion of* D_2 *molecules through a-C:D analogs with the temperature (black circles), along with the model described by Eq. 5.3 that best fits the experimental data (blue solid line), and the associated* 3σ *limits (blue dashed lines).*

linfit procedure programmed with the IDL programming language led to an activation energy of $E_D = 2090 \pm 90$ K for the diffusion of D_2 molecules through the a-C:D analogs, and $D_0 = 0.0045^{+0.0050}_{-0.0023}$ cm^2 s^{-1} for the pre-exponential factor. This activation energy falls in the same range as that found in Falconneche et al. (2001) for the diffusion of rare gases and small molecules through carbonaceous polymer materials. Figure 5.6 shows the evolution of the experimental and modeled diffusion coefficient with the temperature, along with the associated 3σ limits.

On the other hand, the additional diffusion coefficient D' introduced to improve the model did not depend on the temperature, but on the thickness of the analogs, as seen in Fig. 5.7. The second term in Equations 5.9 and 5.10 could be an artifact that accounts for the differences between the model described by Equations 5.6 and 5.8, and the real process taking place during the experiments. For example, the entering D_2 flux established during irradiation is assumed to enter the sample at the surface $x = 0$ with infinitesimal thickness, while in the real process a finite (yet negligible) thickness of the sample is processed by the VUV photons. In which case, the diffusion coefficient D' would have no physical meaning. Alternatively, this second term could account for a parallel diffusion process taking place along with the "main" studied diffusion represented by the coefficient D. In that case, the diffusion coefficient D' would describe this parallel diffusion, which could be taking place, for example, through the pores or cracks of the samples. Since D' increases with the analogs' thickness (see Fig. 5.7), pores or cracks should be larger in thicker plasma-produced analogs.

Modelling of the H_2 diffusion through a-C:H analogs

A total of seven complementary experiments were carried out with 2 a-C:H analogs, at temperatures between 85 K and 120 K. The modified model described by Eq. 5.12 was

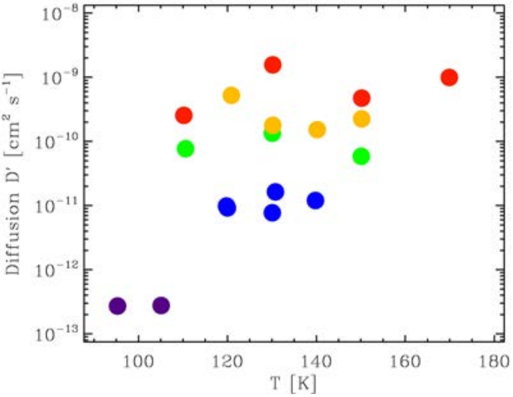

Figure 5.7. *Additional diffusion coefficient D' derived for the experiments with a-C:D analogs of thickness 5.2 μm (red circles), 3.4 μm (yellow circles), 2.6 μm (green circles), 1.3 μm (blue circles), and 0.2 μm (purple circles), using the model described by Eq. 5.12.*

also used to fit the normalized m/z = 2 ion current measured during the experiments. Estimated diffusion coefficients D for the diffusion of H_2 molecules through the a-C:H analogs were found to be approximately one order of magnitude higher than those of D_2 molecules through a-C:D analogs measured at the same temperatures. However, dependence of the diffusion coefficient with temperature was similar in both cases. The estimated activation energy and diffusion at infinite temperature were E_D = 1660 ± 110 K, and $D_0 = 0.0007^{+0.0013}_{-0.0004}$ cm^2 s^{-1}, respectively (see Fig. 5.8). The errors could be slightly larger due to the assumptions made for the m/z = 2 background level changes when switching the VUV lamp on and off, since the metallic shutter used to block the VUV photons in the SICAL-X setup after irradiation was not available in the ISAC setup. The additional diffusion coefficient in Eq. 5.12 followed the same behavior as in Sect. 5.3.2, as shown in Fig. 5.9, with averaged values for similar thicknesses higher by a factor of ∼2.

5.4 Astrophysical implications

The mobility and desorption of H_2 and D_2 on water ice, mineral, or graphite surfaces are high (see, e.g., Amiaud et al. 2015, Acharyya 2014, Vidali & Li 2010, Fillion et al. 2009, Haas et al. 2009, and references therein), with typical activation energies of only a few hundreds of K. This ensures the rapid molecular hydrogen desorption in high dust grain temperature regions, such as some PDRs, but at the same time it constitutes an issue when trying to explain the formation of H_2 molecules by the surface recombination of H atoms, since they may not stay physisorbed for long enough on the surface to recombine. Alternatively to these formation paths, a-C:Hs are energetically processed in the ISM, leading to the destruction of the aliphatic C-H component (which is not detected in dense regions), and the formation of hydrogen molecules. Recent models help in explaining the H_2 formation at such apparent high temperatures,

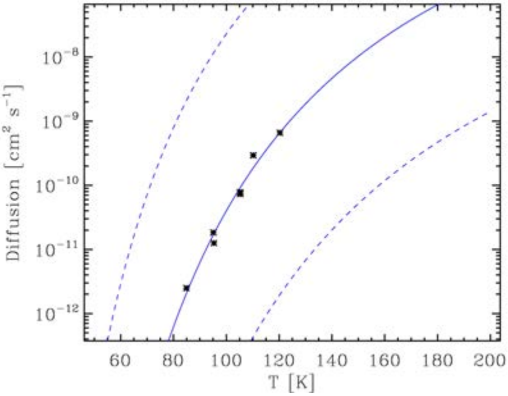

Figure 5.8. *Evolution of the experimental diffusion coefficient D for the diffusion of* H_2 *molecules through a-C:H analogs with the temperature (black circles), along with the model described by Eq. 5.3 that best fits the experimental data (blue solid line), and the associated* 3σ *limits (blue dashed lines).*

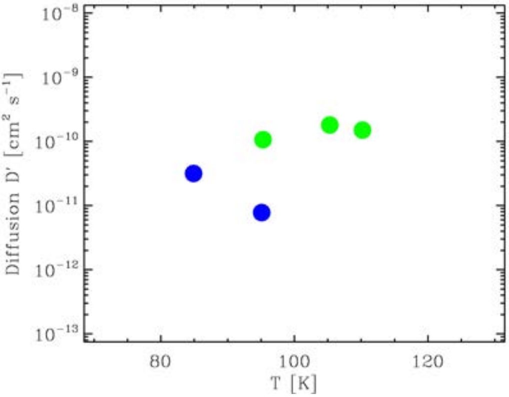

Figure 5.9. *Additional diffusion coefficient* D' *derived for the experiments with a-C:H analogs of thickness 2.2* μm *(green circles), and 0.9* μm *(blue circles), using the model described by Eq. 5.12.*

because of the time fraction spent by small grains at low temperature between transient heating events (Bron et al. 2016). The subsequently formed hydrogen molecules diffuse out of the carbonaceous particles and contribute to the total H_2 abundance in the ISM (Alata et al. 2014).

In the diffuse ISM, re-hydrogenation of the amorphous carbon particles by atomic H equilibrates the destruction of the aliphatic C-H component by UV photons (mainly) and cosmic rays. In the dense ISM, re-hydrogenation is much less efficient. However, the interstellar UV field cannot penetrate dense clouds, and destruction only by cosmic rays (directly or indirectly through the generated secondary UV field) cannot account for the disappearance of the 3.4 μm absorption band. Godard et al. (2011) state that this dehydrogenation should therefore take place in intermediate regions such as translucent clouds or PDRs.

In this scenario, when H_2 molecules are produced in the bulk by photolytic reactions, they diffuse out slowly outward of the grains contrary to the production and immediate release of H_2 that are formed on the surface of interstellar solids. Surface Eley-Rideal or LangmuirHinshelwood mechanism (see, e.g., Roser et al. 2003, Hornekaer et al. 2003, Islam et al. 2007, Vidali et al. 2007, Latimer et al. 2008, Cazaux et al. 2008, Mennella 2008, Vidali et al. 2009, Lemaire et al. 2010, Sizun et al. 2010, Vidali 2013, Hama & Watanabe 2013, Bron et al. 2014, Amiaud et al. 2015) led to the H_2 molecule desorption with debated amounts of internal excitation energy. By contrast, the diffusion process in the bulk allows the molecules to thermalize during their escape path toward the surface. One thus expects no high vibrational level excitation for these molecules contrary to the possible hydrogen surface recombination processes.

Formation of hydrogen molecules and subsequent diffusion in the bulk of the a-C:H particles also enables us to thermalize the ortho-to-para (OPR) ratio to the dust temperature, which is lower than the gas temperature in PDRs. For dust temperatures of 55-70 K typical of a warm PDR such as the Orion Bar nebula (see, e.g., Guzmán et al. 2011, and references therein), an OPR of $\sim$1 is expected. Observed OPR values in PDRs are indeed around 1, lower than the value of $\sim$3 expected from the excitation temperature of the H_2 rotational lines (Fuente et al. 1999, Habart et al. 2003, Habart et al. 2011). Alternatively, Bron et al. (2016) propose the ortho-to-para conversion of physisorbed H_2 molecules on dust grain surfaces to explain these low OPR values. This process is only efficient on cold dust grains and, therefore, dust temperature fluctuations need to be invoked in that case.

Diffusion of H_2 through the a-C:H particles is characterized by the diffusion coefficient D, which depends on the dust temperature according to Eq. 5.3. With the D_0 and E_D values estimated in Sect. 5.3.2 we can extrapolate D values to the temperature of a PDR region, and obtain a typical decay-time constant for the release of the hydrogen molecules from the a-C:Hs in space. Interstellar a-C:Hs can be approximated to a slab of thickness $2r$, r being the typical radius of a carbonaceous dust particle. If the a-C:H is initially filled with a concentration C_0 of H_2 molecules, and the molecules are released to the gas phase through the surfaces $x = -r$ and $x = r$ maintained at zero concentration, then the average hydrogen concentration in the slab at time t is given by

$$C_{av}(t) = \frac{4C_0}{\pi^2} \times \sum_{n=0}^{\infty} \frac{1}{(2n+1)^2} \cdot exp[-\frac{(2n+1)^2\pi^2 Dt}{4r^2}], \tag{5.14}$$

according to Carslaw & Jaeger (1978). We define the decay-time constant τ as the time interval needed for the average hydrogen concentration in the slab to be 10% of the initial value (i.e., $\frac{C_{av}(\tau)}{C_0} = 0.1$). Adopting a typical $\sim$0.1 μm grain radius, we calculated τ for two different temperatures: 30 K, representative of a cold PDR such as the Horsehead nebula; and 55 K, the lower limit of a warmer PDR such as the Orion Bar nebula (see, e.g., Guzmán et al. 2011, and references therein). While at 55 K calculated τ_{55} is about 19 years, at 30 K τ_{30} would be about 1.1×10^{15} years, since the diffusion coefficient depends strongly on the temperature. If we instead adopt half the typical radius for a dust grain ($r \sim 0.05$ μm), decay times are reduced to a quarter (see Eq. 5.14), leading to $\tau_{55} \sim 5$ years and $\tau_{30} \sim 3 \times 10^{14}$ years. The latter decay-time is way longer than the typical dynamical time of a PDR (see, e.g., Goldsmith et al. 2007, Glover & Mac Low 2007).

To decrease the desorption time of the photo-produced hydrogen molecules in the coldest interstellar regions, several solutions can be invoked. On one hand, transient heating episodes of the a-C:H particles by, for example, cosmic rays could increase the dust temperature (and therefore the diffusion of the H_2 molecules), thus reducing significantly the release time. On the other hand, the presence of open channels in the grains, or a higher surface-to-volume ratio than that of the compact films used in the laboratory simulations could also assist the hydrogen release from the a-C:H particles.

5.5 Conclusions

We have explored the diffusion of photo-produced H_2 (D_2) molecules through a-C:H (a-C:D) analogs. Hydrogenated amorphous carbon particles (which harbor between 5% and 30% of the total C cosmic abundance) are energetically processed in the ISM, leading to the loss of the aliphatic C-H component and the formation of hydrogen molecules that diffuse out of the particles, contributing to the total H_2 abundance. This constitutes an alternative additional formation pathway to the hydrogen surface recombination process that allows the hydrogen molecules to thermalize to the dust temperature before passing into the gas phase, leading to no high vibrational level excitation, and to OPR values similar to those observed in PDRs.

We have simulated this process in the laboratory using plasma-produced a-C:H and a-C:D analogs. The surface of the analogs in contact with the substrate was irradiated by VUV photons under astrophysically relevant conditions. Photo-produced H_2 and D_2 molecules subsequently diffused through the analogs, eventually reaching the opposite surface, and passing into the gas phase. Molecules released from the analogs were detected by a QMS. The measured m/z = 2 and m/z = 4 ion current corresponded to the outgoing H_2 or D_2 flux, respectively, which was compared to the expected flux from the diffusion model that best fitted the experimental measurements, enabling us to derive a diffusion coefficient that described the diffusion process. A modified diffusion model with two different diffusion coefficients, D and D' was used. The diffusion coefficient D described the diffusion of the molecules through the HAC material, which depended on the temperature of the analogs, following an Arrhenius-type equation. Experiments at several temperatures were carried out, estimating a diffusion coefficient D for every experiment. This allowed us to derive an activation energy E_D of the diffusion process. Estimated E_D was 1660 ± 110 K for the diffusion of H_2 through the a-C:H analogs, and 2090 ± 90 K for the diffusion of D_2 through the a-C:D analogs. The pre-exponential factors were also derived ($D_0(H_2) = 0.0007^{+0.0013}_{-0.0004}$ cm^2 s^{-1}, and $D_0(D_2) = 0.0045^{+0.005}_{-0.0023}$ cm^2 s^{-1}). The additional diffusion coefficient D' did not depend on the temperature, but on the thickness of the analogs. This coefficient could trace the differences between the model and the real process taking place in the laboratory, or, alternatively, it could be accounting for a parallel diffusion process taking place, for example, through the pores or cracks of the analogs.

Using these experimental values, we extrapolated the diffusion coefficient D to two different temperatures representative of PDR regions, where the destruction of the C-H bonds and formation of H_2 molecules is expected to take place. A typical decay-time constant τ was calculated characterizing the release of the H_2 molecules from the a-C:H particles. Transient heating episodes of the dust particles or other alternative solutions need to be invoked for the release of the hydrogen molecules in cold regions where the typical diffusion times exceed the dynamical time of these regions.

Acknowledgements

This research has been financed by the ANR and French INSU-CNRS program Physique et Chimie du Milieu Interstellaire (PCMI), and by the Spanish MINECO under projects AYA-2011-29375 and AYA2014-60585-P. R.M.D. benefited from a FPI grant from Spanish MINECO. The authors acknowledge funding support from the PICS (Projet International de Coopration Scientifique) between the CNRS and CSIC which consolidated this French and Spanish teams' cooperation. We also thank the anonymous reviewer for constructive remarks

References

Acharyya, K. 2014, MNRAS, 443, 1301
Adamson, A. J., Whittet, D. C. B., & Duley, W. W. 1990, MNRAS, 243, 400
Adel, M. E., Amir, O., Kalish, R., & Feldman, L. C. 1989, J. Appl. Phys., 66, 3248
Alata, I., Cruz-Díaz, G. A., Muñoz Caro, G. M., & Dartois, E. 2014, A&A, 569, A119
Alata, I., Jallat, A., Gavilan, L., et al. 2015, A&A, 584, A123
Allamandola, L. J., Tielens, A. G. G. M., & Bakrer, J. R. 1985, ApJ, 290, L25
Amiaud, L., Fillion, J.-H., Dulieu, F., Momeni, A., & Lemaire, J.-L. 2015, Physical Chemistry Chemical Physics (Incorporating Faraday Transactions), 17, 30148
Bridger, A., Wright, G. S., & Geballe, T. R., 1994, in Infrared Astronomy with Arrays: The Next Generation, ed. I. S. McLean, Astrophysics and Space Science Library, 190, 537
Bron, E., Le Bourlot, J., & Le Petit, F. 2014, A&A, 569, A100
Bron, E., Le Petit, F., & Le Bourlot, J. 2016,A&A, 588, A27
Carslaw, H. S., & Jaeger, J. C. 1959, in Conduction of Heat in Solids, Oxford Univ. Press
Cazaux, S., Caselli, P., Cobut, V., & Le Bourlot, J. 2008, A&A, 483, 495
Cazaux, S., Morisset, S., Spaans, M., & Allouche, A. 2011, A&A, 535, A27
Cruz-Díaz, G. A., Muñoz Caro, G. M., Chen, Y.-J., & Yih, T.-S. 2014, A&A, 562, A119
Dartois, E., Muñoz Caro, G. M., Deboffle, D., Montagnac, G., & D'Hendecourt, L. 2005, A&A, 432, 895
Dartois, E., & Muñoz Caro, G. M. 2007, A&A, 476, 1235
Draine, B. T., & Li, A. 2007, ApJ, 657, 810
Early, J. G. 1978, Acta Metall., 26, 1215
Falconnèche, B., Martin, J., & Klopffer, M.H. 2001, Oil & Gas Science and Technology, 56, 271
Fillion, J.-H., Amiaud, L., Congiu, E., et al. 2009, Physical Chemistry Chemical Physics (Incorporating Faraday Transactions), 11, 4396

Fuente, A., Martín-Pintado, J., Rodríguez-Fernández, N. J., et al. 1999, ApJ, 518, L45

Furton, D. G., Laiho, J. W., & witt, A. N. 1999, ApJ, 526, 752

Gavilan, L., Alata, I., Le, K. C., et al. 2016, A&A, 586, A106

Gavilan, L., Lemaire, J. L., & Vidali, G. 2012, MNRAS, 424, 2961

Glover, S. C. O., & Mac Low, M. 2007, A&A, 463, 635

Godard, M., & Dartois, E. 2010, A&A, 519, A39

Godard, M., Féraud, G., Chabot, M., et al. 2010, A&A, 529, A146

Goldsmith, P. F., Li, D., & Krčo, M. 2007, ApJ, 654, 273

Guzman, V. V., Pety, J., Goicoechea, J. R., Gerin, M., & Roueff, E. 2011, A&A, 534, A49

Haas, O.-E., Simon, J. M., & Kjelstrup, S. 2009, J. Phys. Chem. C, 113, 20281

Habart, E., Abergel, A., Boulanger, F., et al. 2011, A&A, 527, A122

Habart, E., Boulanger, F., Verstraete, L., et al. 2003, A&A, 397, 623

Habart, E., Walsmley, M., Verstraete, L., et al. 2005, Space, Sci. Rev., 119, 71

Hama, T., & Watanabe, N. 2013, Chem. Rev., 113, 8783

Hornekaer, L., Baurichter, A., Petrunin, V. V., Field, D., & Luntz, A. C. 2003, Science, 302, 1943

Imanishi, M. 2000a, MNRAS, 313, 165

Imanishi, M. 2000b, MNRAS, 319, 331

Islam, F., Latimer, E. R., & Price, S. D. 2007, J. Chem. Phys., 127, 064701

Katz, N., Furman, I., Biham, O., Pirronello, V., & Vidali, G. 1999, ApJ, 522, 305

Latimer, E. R., Islam, F., & Price, S. D. 2008, Chemical Physics Letters, 455, 174

Lee, W., & Wdowiak, T. J. 1993, ApJ, 417, L49

Leger, A., & Puget, J. L. 1984, A&A, 137, L5

Lemaire, J. L., Vidali, G., Baouche, S., et al. 2010, ApJ, 725, L516

Marée, C., Vredenberg, A., & Habraken, F. 1996, Mater. Chem. Phys., 46, 198

McFadzean, A. D., Whittet, D. C. B., Bode, M. F., Adamson, A. J., & Longmore, A. J. 1989, MNRAS, 241, 873

Mennella, V., ApJ, 684, L25

Mennella, V., Baratta, G. A., Esposito, A., Ferini, G., & Pendleton, Y. J. 2003, ApJ, 587, 727

Mennella, V., Brucato, J. R., Colangeli, L., & Palumbo, P. 1999, ApJ, 524, L171

Möller, W., & Scherzer, B. M. U. 1987, Appl. Phys. Lett. 50, 1870

Muñoz Caro, G. M., Jiménez-Escobar, A., Martín-Gago, J.Á. et al. 2010, A&A, 522, A108

Peeters, E., Hony, S., van Kerckhoven, C., et al. 2002, A&A, 390, 1089

Pendleton, Y. J., Sandford, S. A., Allamandola, L. J., Tielens, A. G. G. M., & Sellgren, K. 1994, ApJ, 437, 683

Pety, J., Teyssier, D., Fossé, D., et al. 2005, A&A, 435, 885

Pirronello, V., Liu, C., Shen, L., & Vidali, G. 1997, ApJ, 475, L69

Roser, J. E., Swords, S., Vidali, G., Manico, G., & Pirronello, V. 2003, ApJ, 596, L55

Sandford, S. A., Allamandola, L. J., Tielens, A. G. G. M., et al. 1991, ApJ, 371, 607

Schnaiter, M., Mutschke, H., Dorschner, J., Henning, T., & Salama, F. 1998, ApJ, 498, 486

Sizun, M., Bachellerie, D., Aguillon, F., & Sidis, V. 2010, Chemical Physics Letters, 498, 32

Soifer, B. T., Russel, R. W., & Merrill, K. M., 1976, ApJ, 207, L83

Spoon, H. W. W., Armus, L., Cami, J., et al. 2004, ApJS, 154, 184

van Diedenhoven, B., Peeters, E., van Kerckhoven, C., et al. 2004, ApJ, 611, 928

Vidali, G. 2013, Chem. Rev., 113, 8752

Vidali, G., & Li, L. 2010, Journal of Physics Condensed Matter, 22, 304012
Vidali, G., & Li, L. Roser, J. E., & Badman, R. 2009, Adv. Space Res., 43, 1291
Vidali, G., Pirronello, V., Li, L., et al. 2010, J. Chem. Phys. A, 111, 12611
Wickramasinghe, D. T., & Allen, D.A. 1980, Nature, 287, 518
Wild, C. & Koidl, P. 1987, Appl. Phys. Let., 51, 1506

Part IV

Results - Ice

Chapter 6

CO ice accretion

Adapted from *CO depletion: a microscopic perspective*. Cazaux, S., Martín-Doménech, R., Chen, Y.J., & Muñoz Caro, G.M. 2017, submitted to ApJ.

Abstract

In the regions where stars form (dense cloud interiors), the density and temperature conditions can cause gas to freeze-out onto dust grains forming ice mantles, which influences the chemical composition of the cloud. The aim of this Chapter is to understand in detail the depletion (and subsequent desorption) of CO on (from) interstellar dust grains.

Two experimental setups were used for this purpose. The experimental simulations for the deposition of CO ices were performed under two different conditions, while the subsequent thermal desorption of the CO molecules was carried out under the same conditions in both cases. In parallel, Kinetic Monte Carlo simulations were used to mimic the experimental conditions and determine the fate of each CO molecule in the experiments.

We show that the calculated binding energies of the CO molecules in the ice depend on the conditions at which they are deposited, leading to the formation of CO ices with different structures. However, during the warm-up phase, CO molecules in the ices re-arrange and these differences vanish, as shown by both the experimental and the theoretical simulations.

Applied to astrophysical conditions, in a pre-stellar core CO molecules can be bound in the ice with energies ranging from 180 K to 950 K. Because of this wide range of binding energies, the depletion of CO as a function of A_V is much less important than initially thought. The weakly bound molecules, because easily released into the gas phase through desorption, change the balance between accretion and desorption, and therefore result in a larger abundance of CO at high extinctions. In addition, the CO molecules weakly bound to the ices will also be more mobile, and this could increase the reactivity within interstellar ices.

6.1 Introduction

In the last decades, observing facilities have significantly increased in sensitivity allowing to study in detail the chemical composition of many places of our Universe. Molecules and atoms are powerful indicators of the gas characteristics of a medium and are used to derive detailed properties of astrophysical objects.

In particular, observations of star forming environments have rapidly been confronted with the impossibility to explain the abundances of some species with gas-phase reactions only. In regions where stars forms, about 1% of the mass is constituted by small dust particles ranging in size from few tens of Å to a few micrometer (see Chapter 3, Sect. 3.1). However small and inconspicuous these dust grains seem, they interact with the gas phase and can dramatically alter its composition. In the first phases of star formation, dense clouds present some overly dense regions, called pre-stellar cores, which are the precursors of the stars. To reproduce the observations of dense clouds, about 90% of CO molecules should leave the gas phase, on average along the line of sight, and over 99% of them must deplete in the core nucleus (Caselli et al. 1999). This is due to CO freeze-out onto dust particles, which then form thick icy mantles (e.g. Ossenkopf & Henning 1994, Pontoppidan et al. 2008; see also Chapter 3.2).

When a protostar forms and heats its surroundings, a rich molecular chemistry is triggered driven by thermal desorption of the ice mantles (Cazaux et al. 2003). This chemically rich phase is called hot core/hot corino (for high/low mass protostars, see Chapter 3, Sect. 3.3) and it is characterized by an abundant organic inventory (water and organics such as H_2CO and CH_3OH (Schöier et al. 2002), c omplex O- and N-bearing molecules such as formic acid and acetaldehyde (Cazaux et al. 2003)).

In order to explain these observations, the understanding of CO interaction with dust surfaces is unavoidable. In this study we followed experimentally the formation of CO ices at different conditions. For this purpose, we used two experiments focusing on two different accretion processes: 1) accretion onto a substrate at a constant temperature of 14 K [1], and 2) accretion at a decreasing temperature from 80 to 8 K. After accretion, the temperature of the substrate was increased and CO molecules desorbed and were detected in the gas phase. This is called a temperature programmed desorption (TPD) experiment. The present study aims at understanding whether TPD experiments can be sensitive to the different accretion processes. The experimental results are supported by theoretical calculations taking into account the microphysics occurring in the ices. Our results are then exported to astrophysical conditions.

This Chapter is articulated as follow. In Section 6.2 the two experiments performed in this study are described as well as their results. In Section 6.3, the theoretical model and assumptions are described and used to reproduce the experimental results. Finally, in Section 6.4 the model is extended to pre-stellar cores in order to reproduce the CO depletion observed in these objects.

6.2 Experimental simulations

Deposition and warming up of CO ices have been studied experimentally in two different setups and under two different conditions in the case of the deposition phase of the experiment, in order to address whether the deposition conditions influence the desorption of the CO ices. The two setups are described in the following sections, as well as the experimental results.

6.2.1 IPS

Part of the experimental simulations (in particular, CO ice accretion at a constant temperature of 14 K and subsequent TPD, experiment 1) were performed using the Interstellar Photoprocess System (IPS) described in Chen et al. (2014). Here we only provide a brief description of IPS [2].

A schematic representation of IPS is shown in Figure 6.1. IPS is an ultra-high-vacuum (UHV) chamber with a base pressure of 1.3×10^{-10} mbar. The substrate for

---

[1] In this sense, the experiment 1 performed in this study is similar to that described in Fayolle et al. (2016) where CO is deposited at 15K, but our aim here is to focus on how accretion is subsequently seen in the TPD phase of the experiment. Moreover, a laser reflective interference system is used in experiment 1 in order to monitor the solid phase, in addition to IR spectroscopy.

[2] IPS is similar to the ISAC setup described in Chapter 4, Sect. 4.1.1.

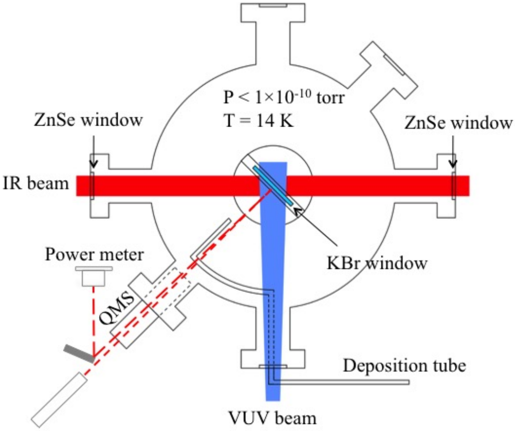

Figure 6.1. *Schematic representation of the Interstellar Photoprocess System, kindly provided by Y.J. Chen.*

interstellar solid analogs is located at the sample holder, placed on the tip of a cold finger from a closed-cycle helium cryostat (CTI-M350), which reaches temperatures as low as 14 K. Two silicon diodes are used to monitor the temperature of both the substrate and the cold finger, with an accuracy of 0.1 K. Gas mixtures (or in the case of the experimental simulations described in this chapter, pure gases) are prepared in an independent gas-line system, and subsequently allowed to enter the UHV chamber through a capillary tube, condensing onto the substrate (usually a KBr window) and forming the interstellar ice analogs *in situ*. During the experimental simulations, a Fourier Transform Infrared (FTIR, ABB FTLA-2000-104) spectrometer equipped with a mercury-cadmium-telluride (MCT) detector monitors the solid sample. The spectrometer is connected to the IPS system through a small cylindrical UHV chamber, in order to avoid water vapour and carbon dioxide contamination. The ice sample position is at 45 deg from the IR beam (see Fig. 6.1) and, therefore, the thickness experienced by the IR beam (effective ice thickness) is larger than the actual ice thickness by a factor of $\sqrt{2}$. This is taken into account during the experimental simulations. A Quadrupole Mass Spectrometer (QMS) covering the range of 1 - 200 amu with 0.5 amu resolution, provides monitoring of the introduced gas during the deposition, and measures the presence of desorbing molecules in the gas phase during the warm-up phase.

In addition, a laser reflective interference system (not included in the ISAC setup) counts with a He-Ne laser (λ = 632.8 nm), and a power meter (Newport M835) calibrated for measuring the reflected intensity of the laser at 632.8 nm (power $<$ 5 mW). The He-Ne laser reaches the solid sample with an incident angle of 2 degrees with respect to the normal, and the reflective light is subsequently directed by a mirror to the power meter (see Fig. 6.1). The reflected intensity of the laser oscillates between constructive and destructive interference, leading to a sinusoidal pattern. This interference pattern was monitored during both a blank experiment (warming up of a KBr substrate alone) and the TPD of a CO ice deposited onto a KBr substrate at 14 K. During the blank

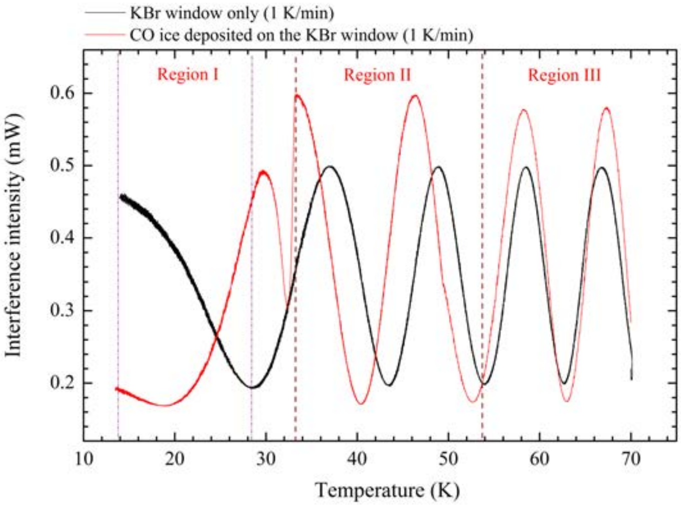

Figure 6.2. *TPD experiment as seen by the laser interference to study the desorption of a CO ice sample (red) and the warming up of the KBr substrate alone (blank experiment, black).*

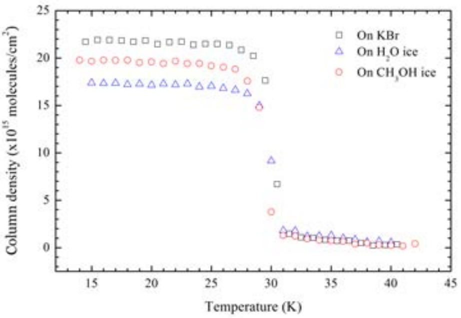

Figure 6.3. *IR measurement of the CO ice during the TPD experiment, showing the number of monolayers on the surface (1 ML=10^{15} molecules/cm^2).*

experiment, the sinusoidal interference pattern responded to the (constructive and destructive) interference between the light reflected from the front KBr surface and the rear KBr surface. When the KBr window is held at a specific temperature, its thickness is constant and does not cause any variation of light interference, but this changes during the warm up, leading to a variation in the sinusoidal pattern. On the other hand, during

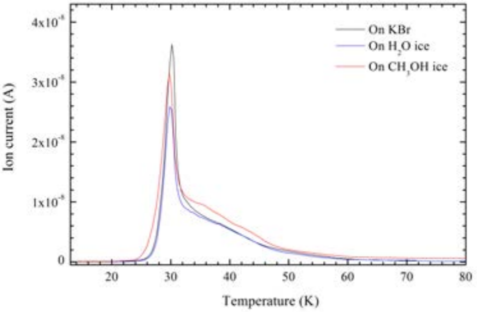

Figure 6.4. *TPD experiment using QMS to record the gas-phase CO molecules.*

the TPD of the deposited CO ice, the pattern responded to the interference between the light reflected from the ice surface and the KBr window. The thickness variation of the KBr window during the blank experiment, or the ice sample during the TPD experiment can be estimated, in principle, as:

$$\Delta d = \frac{\lambda_0 \, m}{2n\sqrt{1 - \frac{sin\theta^2}{n^2}}} \tag{6.1}$$

where Δd is the KBr substrate or ice sample thickness variation, λ_0 is the wavelength of He-Ne laser, n is the refractive index of the KBr or the ice, θ is the He-Ne laser incident angle, and m is number of interference periods (Brunetto et al. 2008).

Results The results corresponding to the blank experiment (warming up of a KBr substrate alone) and the TPD of a CO ice deposited onto a KBr substrate at a constant temperature of 14 K using laser interference to study the subsequent desorption of the CO ice are shown in Fig. 6.2. In both experiments the sample temperature was increased from 14 K to 70 K at an identical rate of 1 K/min by turning off the cryostat. The interference pattern as a function of the temperature during TPD of the CO ice is shown in red, and compared to the blank experiment in black. The variation of the sinusoidal pattern during the TPD experiment is due to the thickness variation of both the KBr substrate and the CO ice. Therefore, the laser interference pattern cannot be used to estimate the thickness variation of the CO ice alone because it is difficult to determine the contributed weights from the ice sample and the substrate to this effect. However, the differences in the variation of this sinusoidal pattern during the TPD of the CO ice with respect to the blank experiment allow us to determine if some CO is retained on the KBr surface, and if its thickness considerably changes.

Between 13 K and 28.5 K, the measurements indicate that no important changes of the ice thickness are observed for temperatures prior to CO desorption (region I), since the variation of the sinusoidal pattern is similar to that of the blank experiment. Around 30K, a fast decrease and a subsequent increase of the laser intensity (red line) is observed due to the sublimation of CO molecules and the subsequent thickness variation. For temperatures higher than 32 K, in region II, the phase of the red line (CO ice) is delayed compared to the black line (blank experiment). This could imply that some residual CO is still present on the surface. In region III, above 54 K, the phases of the red line (CO ice) and black line (KBr substrate) become the same, which suggests that CO is no longer present on the surface.

The decrease of the CO ice column density was simultaneously monitored from integration of the IR band at ~2139 cm^{-1} during the TPD experiment, and is reported in Fig. 6.3. Column densities were calculated from the IR spectra using the formula

$$N = \frac{1}{A}\int_{band} \tau_\nu d\nu \tag{6.2}$$

where N is the column density in molecules cm^2, τ_ν the optical depth of the absorption band, and A the band strength in cm $\mathrm{molecule}^{-1}$ (1.1×10^{-17} for the CO band, Jiang et al. 1975).

The IR measurements support the idea that approximately 1 monolayer (1ML = 10^{15} molecules cm^{-2}) of CO remains on the surface at temperatures above ~30 K (region II in Fig. 6.2).

The desorbing CO molecules into the gas phase were detected by the QMS, which complemented the laser interference and IR spectroscopy study of the solid sample. The TPD measurements are reported in Fig. 6.4.

CO deposition was studied on three different types of surfaces, namely: the aforementioned bare KBr substrate (this experiment is represented in black in Figures 6.3 and 6.4), water ice previously deposited at 80 K with a rate of 0.1 ML/s (blue), and methanol ice deposited at the same temperature with a rate of 0.07 ML/s (red). Results are very similar in the three cases. CO ices stay adsorbed on the substrate until ~ 30 K. At this temperature, the CO molecules that constitute the bulk of the ice desorb into the gas phase and are detected by the QMS, leading to the desorption peak in Fig. 6.4. From ~30 K to ~50 K, the TPD measurements from the QMS show a slow decrease of the signal. This, along with the IR and laser interference measurements (only shown for the TPD of CO ice deposited onto the KBr substrate in Fig. 6.2), suggests that around 1 ML of CO is still present on the different surfaces until ~54 K, as expected from previous experiments (see, e.g., Noble et al. 2011).

The slow decrease in intensity of the TPD signal inferred from the QMS data collected during the three experiments suggests that CO molecules are strongly bound to the different surfaces, with binding energies ranging between ~1000 K and 1600 K. The binding energies of the molecules can be directly estimated from the desorption temperature by using a thumb rule as described in page 72 from Attard & Barnes 1998, where E_{bin} (in K)=30 × $\mathrm{T}des$ (in K).

6.2.2 ISAC

Additional experiments were performed using the InterStellar Astrochemistry Chamber (ISAC) (see Muñoz Caro et al. 2010 and Chapter 4, Sect. 4.1.1) under conditions tht differ to that reproduced in the IPS setup.

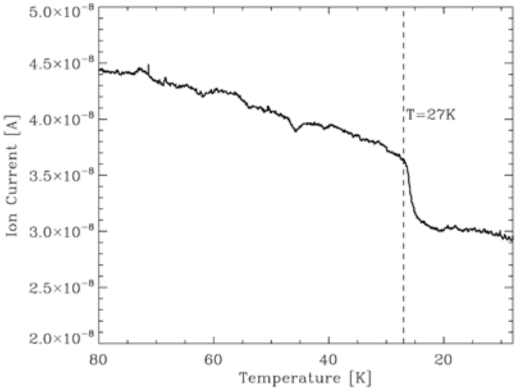

Figure 6.5. *The deposition of the CO ice on top of the ASW as the temperature decreased from 80 K to 8 K was monitored by a QMS that measured the ion current due to the CO molecules in the gas phase.*

Since the experimental results in Sect. 6.2.1 were very similar for the three studied surfaces, only accretion of CO molecules on top of a previously deposited water ice (the most astrophysical scenario, see Chapter 3, Sect. 3.2) was studied in this case. The chemical components used in experiment 2 were thus H_2O (liquid, triply distilled), and CO (gas) The evolution of the solid sample was monitored by transmittance FTIR spectroscopy, with a spectral resolution of 2 cm^{-1}.

A total of 33.6 ML of amoprphous solid water (ASW) were first deposited onto a KBr substrate at 80 K with a rate of 6.3 ML/min. Then, CO gas was admitted in the chamber, and the temperature of the substrate was gradually decreased from 80 K to 8 K at a constant rate of 0.5 K/min, thanks to the combination of the closed-cycle helium cryostat, the tunable heater, the silicon diode temperature sensor and the LakeShore Model 331 temperature controller (see Chapter 4, Sect. 4.1.1). Therefore, accretion of the CO ice on top of ASW took place at different conditions than those used in experiment 1 (decreasing substrate temperature *versus* fixed substrate temperature). Once the CO ice was deposited, the substrate was warmed up at a rate of 0.5 K/min by turning off the cryostat, leading to the desorption of the CO molecules that were subsequently detected by the QMS (TPD).

Results Figure 6.5 (left panel), shows the CO in the gas phase as measured by the QMS while the temperature of the substrate was cooled down from 80 K to 8 K at a rate of 0.5 K/min. The slow decrease of the ion current between 80 and 27 K is not actually due to CO deposition, but to the temperature decreasing in the cold head, cold finger and radiation shield of the cryostat. When gas molecules collide with these cold parts, they lose their kinetic energy (E = 3/2KT) and slow down their velocity. In this situation the number density of gas molecules does not really decrease, but the probability of them reaching the pressure detector or the QMS becomes lower, thus leading to the observed decrease. On the other hand, the drastic decrease observed at 27 K is due to

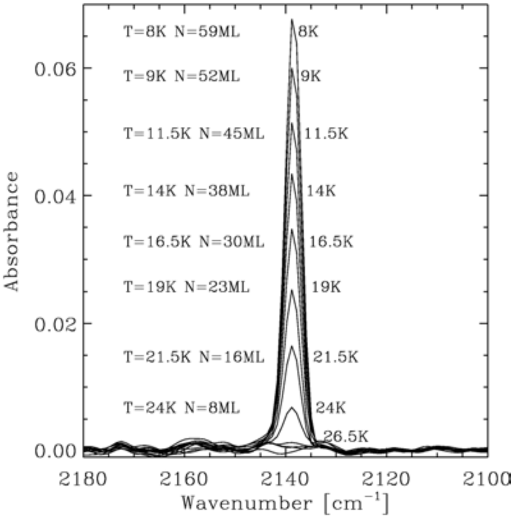

Figure 6.6. *FTIR spectroscopy in transmittance measured the number of monolayers of deposited CO.*

the accretion of CO molecules on the substrate. Both statements are confirmed by IR spectroscopy, as shown in Figure 6.6. The CO IR band at ~2139 cm^{-1} was not observed at temperatures higher than 26.5 K. This means that only 1 ML of CO (which is the sensitivity of our FTIR spectrometer) could have been accreted on top of the ASW before that temperature was reached. However, once the temperature decreases below 27 K, the solid CO IR feature is observed, increasing its intensity at a constant rate, which corresponds to an accretion rate of 1.4ML/min. This feature does not present any shoulder at ~2152 cm^{-1}, typical of CO molecules interacting with dangling OH bonds (see, e.g., Collings et al. 2003, Martín-Doménech et al. 2014). Therefore, CO diffusion into the ASW structure does not take place in our experiment, at least to a significant extent. This is due to the lower porosity of the water ice deposited at 80 K compared to that deposited at lower temperatures (see, e.g., Bossa et al. 2012). The shoulder may not be observed either in astronomical spectra (see, e.g., Cuppen et al. 2011). This would support the bi-layered structure scenario for the interstellar ice mantles presented in Chapter 3, Sect. 3.2, in which CO and H_2O molecules are not intimately mixed.

Once the substrate reached a temperature of 8 K, the cryostad was turned off, and the temperature increased at a rate of 0.5 K/min (TPD). The desorbing CO molecules were detected by the QMS (see Fig. 6.7). While an important peak can be seen at 30 K, corresponding to the desorption of the bulk of the CO molecules, an extended shoulder ranges from 30 K to ~60 K, and corresponding to the desoprtion in the sub-monolayer regime (Noble et al. 2011).

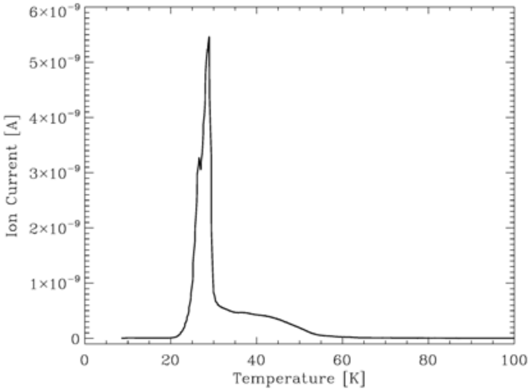

Figure 6.7. *TPD experiment using the QMS corresponding to the CO ice accreted during cool-down of the substrate covered with ASW.*

6.2.3 Summary of experimental results

The two experiments differed in the CO ice deposition temperature (fixed at 14 K *versus* decreasing temperature from 80 K to 8 K), as well as in the deposition rates (7.3 ML/min *versus* 1.4 ML/min).

Deposition of CO with decreasing surface temperature in the ISAC setup shows that CO accretes on the surface from 27 K. At this temperature, the drop in the CO ion current, due to the important accretion on the substrate, reflects the multilayer regime, where the temperature is low enough so that CO can be bound to CO ice. This suggests that CO molecules deposited at 27 K are able to find binding sites on the CO ice with binding energies of the order of 800 K.

In addtion, the two experiments show that deposition at the two different conditions mentioned above result in identical TPD curves, in which CO desorbs at ~30 K in the multilayer regime, while the sub-monolayer regime desorbs between 30 K and 60 K (see also Noble et al. 2011). The QMS measurements were confirmed by IR spectroscopy and reflective laser interference of the solid sample in the case of experiment 1 performed with the ISP setup. TPD curves are also very similar when the CO ice is accreted on different surfaces, as shown is Fig. 6.4.

A desorption peak at around 50 K attributed to monolayer desorption has been reported in previous experimental studies (see, e.g., Collings et al. 2004) but was not observed in the TPD curves shown in Sections 6.2.1 and 6.2.2. When the TPD is performed with a heater located close to the sample, a temperature gradient is created from the sample to other parts of the cryostat. In this scenario, desorption of CO molecules adsorbed on surfaces different from the substrate can take place when the temperature of the substrate is higher than the temperature of this surface, leading to a desorption peak in the TPD curve that is actually an artifact. When the TPD is performed by turning off the cryostat, as in this study, the temperature of the system increases in a more homogenous way, and the second desorption peak is no longer detected. Instead, a long tail in the curve is observed due to the sub-monolayer regime desorption previously reported in Noble et al. (2011).

6.3 Theoretical simulations

We used a step-by-step Monte Carlo simulation to follow the formation of CO ices through deposition and the subsequent desorption into the gas phase.

Our model is described in Cazaux et al. 2016. CO molecules originating from the gas phase arrive at a random time and location and follow a random path within the ice. The arrival time depends on the rate at which gas species collide with the surface (Section 6.3.1). The molecules arriving on the surface can be bound to the substrate and to other CO molecules through van der Waals interactions. The binding energy of each CO molecule depends on its number of neighbors, as described in Section 6.3.2. Our theoretical approach to estimate binding energies is similar to the one in Cuppen et al. (2007), but here we had to determine how the binding energy of a single CO molecule increases with the number of CO neighbors around in order to reproduce the experimental results. Depending on its binding energy, the CO molecules diffuse on the surface/in the CO ices. The diffusion is described in Section 6.3.3. During warm-up, the CO molecules can evaporate from the substrate/ices (Section 6.3.4). The number of molecules desorbing as a function of the temperature correspond to the experimental QMS measurements.

6.3.1 Accretion

In our model, we defined the surface as a grid with a size of 20×20 sites[3]. CO molecules from the gas-phase arrive on the grid and can be bound to the substrate (that we choose as water substrate to mimic the experiments in Sect. 6.2) and/or to previously adsorbed CO molecules through van der Waals interactions. The accretion rate (in s^{-1}) depends on the density of the molecules, their velocity, and the cross section of the surface, and can be calculated as:

$$R_{acc} = n_{\rm CO} v_{\rm CO} \sigma S, \tag{6.3}$$

where $v_{\rm CO} = \sqrt{8kT_{\rm gas}/(\pi m_{\rm CO})} \sim 2.74 \times 10^4 \sqrt{\frac{T_{gas}}{100}}$ cm s^{-1} is the thermal velocity, S the sticking coefficient (that we consider to be unity in this study). The cross section of the surface, σ, directly scales with the size of the grid we use for the simulations, which is 20×20 sites in our calculations. Since the distance between two sites is 3 Å, the density of sites is what is typically assumed, i.e. $\sim$(3 Å)$^{-1}$ $\sim 10^{15}$cm^{-2}. The cross section scales with the size of the grid considered in our calculations, as $\sigma \sim (3\times 10^{-8} \times 20)^2$cm^2=3.6 10^{-13} cm^2.

The deposition rate is therefore: $R_{acc} = 9.8\ 10^{-9}$ $n_{\rm CO}$ s^{-1}, for $T_{\rm gas}$=300 K. In order to mimic experimental conditions with deposition rates of 7.8 ML/min $\sim$ 52 molecules/s and 1.4 ML/min $\sim$ 10 molecules/s, we set the density of CO molecules in the gas in cm^{-3} as being $n_{\rm CO}$= 3×10^9 cm^{-3} and $n_{\rm CO}$=6×10^8 cm^{-3} respectively

---

[3] The size of the grid was chosen so the column density of one layer in the theoretical simulations corresponds to the column density of one monolayer in the experimental simulations (10^{15} molecules cm^{-2}).

6.3.2 Building CO ices.

The desorption of a CO molecule on top of a water ice surface is observed between 30-50 K, which corresponds to binding energies ranging between 900 and 1500 (He et al. 2016, Martín-Doménech et al. 2014, Noble et al. 2011)for the CO molecules bound to the water surface. To account for the fact that the water ice substrate is not homogeneous, we describe the initial surface of water ice with a random distribution of binding energies for the CO molecules on top of it, centered around 1200 K with a dispersion of 180 K as shown in Noble et al. 2011.

If the CO molecules are not bound to the water surface, but start to pile up, the binding energies of CO molecules, due in this case to CO-CO interactions, increase with the number of surrounding CO neighbors. The lowest interaction between two CO neighbors molecules is around 16 meV (185 K, Karssemeijer & Cuppen 2014a). In a multilayer regime, the binding energy of a CO molecule is about 830 K (Luna et al. 2014, Noble et al. 2011, Muñoz Caro et al. 2010, Pontoppidan 2006, Acharyya et al. 2007, Collings et al. 2003).
The binding energy as function of coverage of CO on ASW water ice has been previously reported by Karssemeijer et al. (2014). At low coverages, the binding energy of CO molecules bound to the water surface is $\sim$ 125 meV (1450 K), while for high coverages the water surface becomes completely covered by CO molecules and the binding energy between CO molecules becomes $\sim$ 75 meV (870 K; TPD desorption temperature of 29 K, Table 3 from Martín-Doménech et al. 2014).

Therefore, in order to estimate the binding energy of CO molecules as function of the number of CO neighbors, we use a simple approximation that is shown in Fig. 6.8. The points show the interaction of a CO molecule with one single CO molecule, which is about 185 K and becomes of 860 K in the multilayer regime, which corresponds to 1 (CO adsorbed one CO molecule) to 3 direct neighbors (CO embedded on a top layer with 1 neighbor underneath and 2 neighbors around). By using a fit through these points we mimic a saturation for a high number of neighbors and can calculate the binding energy of a CO molecule as function of its number of CO neighbors nn:

$$E_{CO} = -3360 * (nn + 1)^{-2} + 1040 \tag{6.4}$$

In our calculations, we compute the binding energy by considering an effective number of neighbors nn, that scales with the distance between the neighbor CO$_n$ and the CO molecule. In that sense, one neighbor would contribute as +1/(r$_{CO-CO_n}$)^6 depending on the CO-CO$_n$ distance, to account for the fact that van der Waals interactions depend on distance as 1/r^6. For direct neighbors, this distance is 1, while for neighbors on the sides this distance is $\sqrt{2}$ and for the neighbors located in a corner the distance is $\sqrt{3}$.

6.3.3 Diffusion

A recent study on the diffusion of CO on hexagonal water ice surface shows that diffusion barriers are of the order of 50 meV (Karssemeijer & Cuppen 2014a), which represent only $\sim 30\%$ of the the binding energy. In our model, we define the diffusion rates refered to the binding energy, thus depending on the number of neighbors interacting with the CO molecules, that we call nn in the above section.

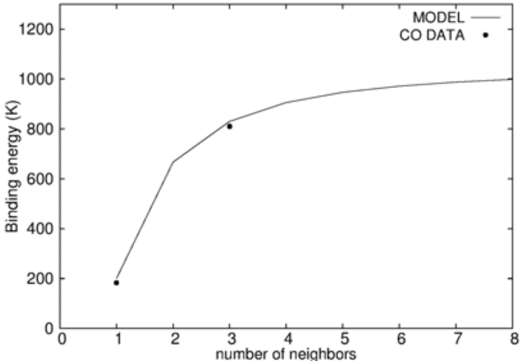

Figure 6.8. *Binding energies of CO molecules as function of (effective) neighbors. The points correspond to the calculations from Karssemeijer et al. 2014b.*

For a position (i,j,k), of a CO molecule in the grid, being k the number layer in which a CO molecule is, we calculate the associated binding energy Ei and identify the possible sites where the molecule can diffuse to as i±1; j±1; k±1. The final binding energy Ef is calculated as function of the neighbors present around this site. The diffusion rate, from an initial site with an energy Ei to a final site with an energy Ef, is illustrated in Fig.6.9.

The barrier to go from Ei to Ef is defined as follows if Ei≤Ef (Fig.6.9, left panel):

$$Ed = \alpha \times min(Ei, Ef), \qquad if Ei < Ef \tag{6.5}$$

If Ei>Ef, on the other hand, the barrier becomes (Fig.6.9; right panel)

$$Ed = \alpha \times min(Ei, Ef) + \Delta E, \qquad if Ei > Ef \tag{6.6}$$

with ΔE = max(Ei,Ef)-min(Ei,Ef).

By defining the barriers in such a manner, we do take into account microscopic reversability in this study (Cuppen et al. 2013). The barriers to move from one place to another should be identical to the reverse barrier. The diffusion barriers scale with the binding energies with a parameter α.

We consider the activation energy for diffusion to be 70% of the binding energy (α = 0.7) [4]. This value is higher than the 30% derived for CO on water ice from Karssemeijer et al. (2014) and from the value derived experimentally for water-on-water diffusion (Collings et al. 2003). However, the CO-on-CO diffusion has not been determined, and recent studies highlight the large differences between bulk and surface diffusion (Ghesquiere et al. 2015). In addtion, the transition from amorphous to α-crystalline CO ice was observed by Kouchi et al. 1990 at 23 ±1 K. CO molecules can therefore diffuse and re-arrange in the ices at temperatures of ~20 K, which suggests that the diffusion barriers should be around 600 K. This represents ~70% of the binding energy of CO on CO (830 K). Therefore, in this study we use diffusion barriers of 70% of the binding energies.

---

[4] This value is chosen *ad hoc* so that the theoretical simulations correctly reproduce the experiments, and it is justified below.

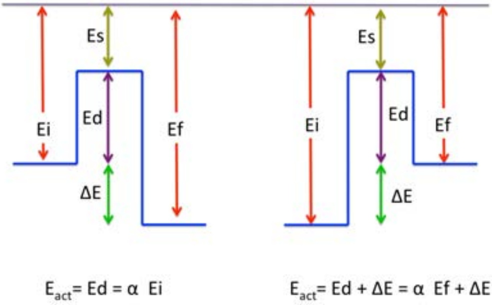

Figure 6.9. *Diffusion barrier to go from a initial site with energy Ei to a final site with energy Ef for the case where Ei<Ef (left panel), and Ei>Ef (right panel).*

The diffusion rate, in s^{-1}, for a CO molecule can be thus written as:

$$R_{diff} = 4 \times \sqrt{\frac{Ei - Es}{Ef - Es}} \times \nu \exp\left(-\frac{E_{act}}{T}\right), \tag{6.7}$$

where ν is the vibrational frequency of a CO molecule in its site (that we consider as 10^{12} s^{-1}), T is the temperature of the substrate (water ice or CO ice) and Es is the energy of the saddle point, which is Es=(1-α)× min(Ei,Ef). This formula differs from typical thermal hopping because the energy of the initial and final sites are not identical (Cazaux & Tielens 2004).

6.3.4 Desorption

The CO molecules present on the surface can return into the gas phase during warm up. The desorption rate depends on the binding energy of the molecules with the surface/ice. As previously mentioned, the binding energy of a CO molecule depends on its number of neighbors, or wether the molecule is directly bound to the surface. The binding energy Ei of the desorbing CO molecule sets the desorption rate as:

$$R_{evap}(X) = \nu \exp\left(-\frac{Ei}{T}\right), \tag{6.8}$$

where ν is the oscillation factor of the CO molecule on the surface, which is typically ν=10^{12} s^{-1}, and T the temperature of the substrate.

6.3.5 Theoretical results

Deposition

As explained in Sect. 6.3.1, we performed theoretical simulations for the two different deposition rates used in experiments 1 (7.8 ML/min for CO deposited at 14 K) and 2 (1.4 ML/min for CO deposited from 80 K with decreasing temperatures of 0.5 K/min down to 8 K).

In experiment 1 (Sect. 6.2.1), CO molecules were deposited at 14 K on different types of surfaces. In our theoretical simulations, we focused on the adsorption of CO on water ice, which is the most realistic scenario. We used a grid of 20 $\times$ 20 sites, admited CO molecules on the surface, and followed the build up of the CO ice at 14 K. The growth of the CO ice with time is shown in Fig. 6.10, where the grid is shown for time intervals of 20 seconds (with a deposition rate of 7.8 ML/min).

Each CO molecule is represented by a box in the figure, whose color represents the binding energy of each of these molecules. These binding energies shows a wide range from 500 K (a CO molecule with 2 neighbors) to $\sim$1200 K (a CO molecule on the water substrate). The build up of the CO layers thus takes place in a disordered way, showing many empty spaces, and therefore weakly bound CO molecules (because of the missing neighbors). This is due to the fact that the deposition temperature is low enough for the CO molecules to be weakly bound and yet not to evaporate, without the need to diffuse to a high binding energy site. The CO molecules arriving on the surface to a site with very low binding energies ($\sim$ 200 K), have low diffusion barriers (see Sect. 6.3.3) and can diffuse to a site where the binding energy is high enough to settle in that site.

In experiment 2, the CO molecules are deposited onto the ASW as the temperature of the substrate is decreased from 80 K to 10 K.

In this case, the CO ices are build up layer by layer as the temperature goes down. The first molecules are adsorbed on the water surface at temperatures $\sim$44 K, and 1 monolayer is formed at 32 K. We note that the deposition of only 1 monolayer could not be observed by the FTIR spectrometer during the experimental simulations described in Section 6.2.2 due to the sensitivity of the instrument. This first monolayer has no empty sites, since every CO molecule must diffuse on the water surface to find the sites with binding energies high enough so that the CO molecule can stay on the surface. The second layer of CO is built on top of previously deposited CO at 27 K, and it is also very well organized without any holes. The drop in the gas-phase CO at 27 K implies (Fig. 6.6) that the temperature was low enough to allow the adsorption of CO on the first layer of CO. For these temperatures, the multilayer regime is reached and CO from the gas phase disappear while CO can be seen on the surface.

As a result, this ice is much more ordered than the ice grown at low temperatures. The ice structure after deposition in the second experiment is shown in Fig. 6.11.

Therefore, the deposition temperature sets the structure and binding energies of the CO molecules in the ice.

Desorption

In both experiments, the ices obtained after deposition were heated to higher temperatures and the desorption was measured.

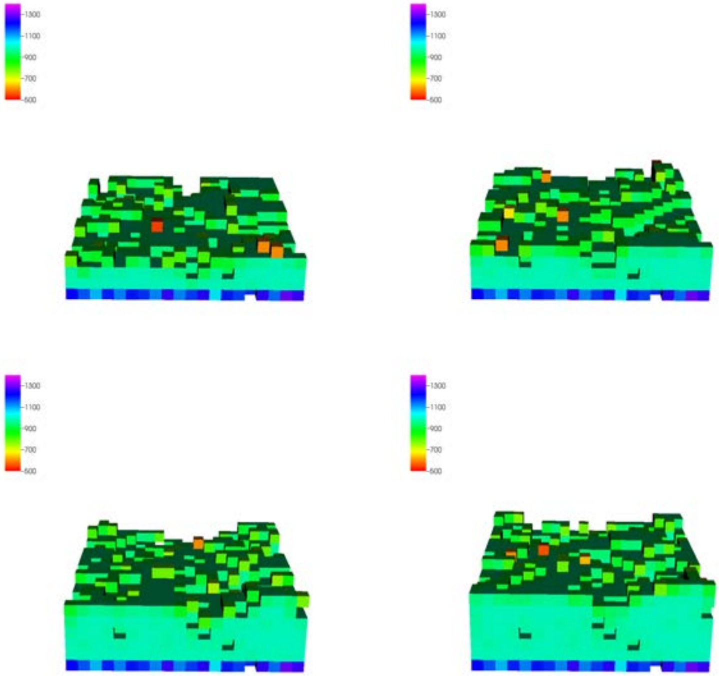

Figure 6.10. *CO adsorption on water surface at 14 K. Each grid is taken at a time interval of 20 s. Each square is a CO molecule and the color corresponds to its binding energy in Kelvins (blue ∼1200 K, red ∼400 K). The binding energy of CO molecules on the first level of the grid is higher, because CO molecules are bound to water substrate. This figure illustrates the range of binding energies of individual CO molecules during deposition at 14 K*

To mimic experiment 1, we performed simulations where CO molecules are deposited at low temperatures (14 K, see Sect. 6.3.5). The resulting ices presented a disordered structure where most of the CO molecules were weakly bound and many holes are present. To simulate the warming up of the ices, we used conditions similar to the ones met in the experiments so that the ices deposited at 14 K were heated to higher temperatures with a rate of 1 K/min. The resulting TPD is reported in Fig. 6.12. Our simulations can reproduce the multilayer peak located at 30 K as well as the monolayer contribution, extending until 50 K.

To mimic the second experiment, we performed simulations with the ices deposited at high temperatures, which show no presence of holes in the structure. The temperature of the substrate was heated at a rate of 0.5 K/min, from 8 K until 80 K. The TPD obtained with these ices is also shown in Fig. 6.12. Our simulations show that while ices

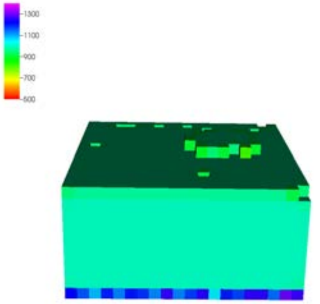

Figure 6.11. *Same as 6.10 but with ice deposited on water ice surface as the temperature is decreased from 80 K. This grid shows the ice structure after depositing 10 layers.*

grown at low or high temperatures present different structures, the TPD measurements are very similar, in agreement with the experimental TPD results displayed in Fig. 6.4 and 6.7.

These results imply that the CO molecules in the theoretical ices reproducing experiment 1 must get re-organized as the temperature increases, forming layers with much less holes, in order to explain the similar TPD obtained for both experiments in the theoretical and experimental simulations [5]. Therefore, TPD measurements do wash away the initial differences on the structure of the ices, and only allow to measure the binding energies of the ices once these are well organized.

6.4 Astrophysical implications

As explained in the Introduction, an important CO depletion has been measured in starless cores (Bergin et al. 2002). Evidence of depletions by factor of ∼4-15 (∼75-94% of CO missing from the gas phase) in many of these cores was found (Bacmann et al. 2002). However, by observing CO isotopologues, a higher CO depletion of up to ∼100 and ∼1000 in the center of the B68 and L1544 dense clouds, respectively, has been measured (≥99% of CO missing from the gas phase; Caselli et al. 1999, Bergin et al. 2002).

The most common explanation is that CO is frozen on dust grains at high densities and low temperatures. However, in order to match the observed remaining gas-phase CO abundance, Keto & Caselli 2010 found that the desorption rate due to cosmic ray strikes (Hasegawa & Herbst 1993) should be increased by a factor of 30. At this rate, desorption and depletion have equal time-scales at a density of about 10^4

---

[5] However, this re-arrangement/change in the CO binding energies seen in the theoretical simulations does not have a counterpart in our IR and/or laser interference measurements monitoring the solid samples during the experiment 1. Muñoz Caro et al. 2016 reported no changes in the IR and the vacuum-UV absorption spectra during warm-up of pure CO ices, while changes are observed for ices deposited at temperatures higher than 20 K.

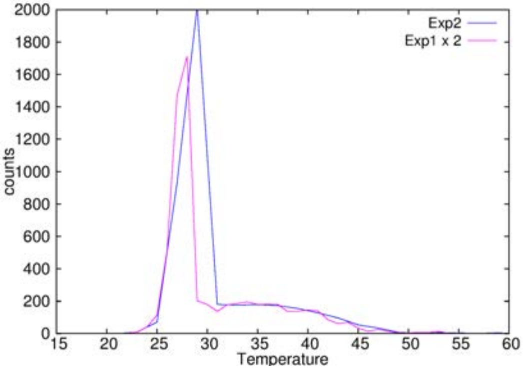

Figure 6.12. *Simulated TPD from Monte Carlo simulations mimicking the experiments 1 (IPS) and 2 (ISAC).*

cm^{-3}, typical of dense clouds. There are other non-thermal processes in addition to direct cosmic ray strikes that cause desorption and could increase the gas-phase abundance of CO. These processes are impulsive spot heating on grains by cosmic rays (Ivlev et al. 2015); cosmic ray induced radical diffusion (Reboussin et al. 2014) or cosmic ray induced explosive chemical desorption (Shen et al. 2004); chemical desorption (Dulieu et al. 2013); formation of H_2 (Takahashi & Williams 2000) and non canonical explosions (Rawlings et al. 2013); and photodesorption with UV photons (Öberg et al. 2007, Öberg et al. 2009, Fayolle et al. 2011, Muñoz Caro et al. 2010).

In order to understand which processes allow to keep the required fraction of the depleted CO in the gas phase of the ISM, we first compute the binding energies of the CO molecules arriving on the surface of an interstellar CO ice with our Monte Carlo simulations.

As a first approximation, we calculate the binding energies of CO molecules as they arrive on CO ices in dense core conditions ($T_{\rm dust}$=6 K and n_H=10^6). We here therefore consider only CO in multilayer regime (not directly bound to the dust grain surface, but to other CO molecules). These energies are reported in Fig. 6.13. The binding energies of the newly arrived CO molecules range between 184 K to 1000 K. An important fraction of the molecules have low binding energies, ranging between 200 and 600 K, while another fraction have binding energies between 700 and 1000 K. The distribution in energies shows many peaks because the binding energy is defined by the number of direct neighbors, which makes a discrete distribution in energy. The different curves show the number of CO molecules sent on the surface, i.e., 1000, 2000 and 5000 which correspond to 2.5, 5 and 12.5 layers for a 20×20 grid size. The resulting structure and binding energies of CO molecules in the ices, after moving and being relocalized on the surface is shown in Fig. 6.14. The CO ices deposited in conditions typical of pre-stellar cores show a wide range of binding energies and a very disordered structure, similar to that calculated for the CO ices in experiment 1 (see Sect. 6.3.5).

In order to address how this range of CO binding energies influence the freeze out of

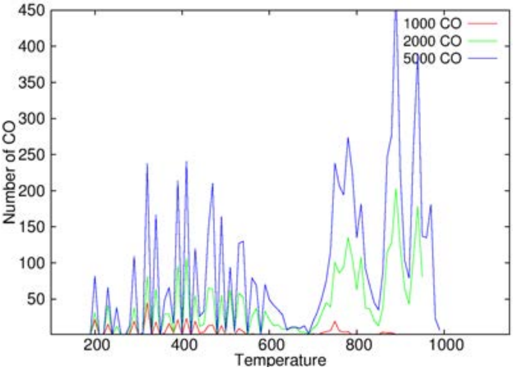

Figure 6.13. *Binding energy of CO molecules arriving on a CO ice at T=6 K and* n_H*=10*^{6} *cm*$^{-3}$*. The three curves show the binding energies as the coverage increases (1000, 2000 and 5000 CO molecules sent on the surface).*

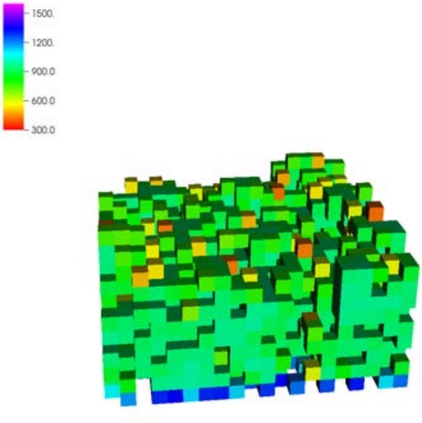

Figure 6.14. *Resulting structure and binding energies of the CO ices at T=6 K and* n_H*=10*^{6} *cm*$^{-3}$*.*

CO molecules from the gas phase, we used a time dependent gas-grain model to follow the abundances of species in the gas, as well as in the ices in a pre-stellar core.

We used a three-phase chemical model that combines gas-phase chemistry with surface and bulk chemistry. The grain surface chemistry model (surface + bulk) takes into account the different binding energies of the species on bare or icy surfaces and includes desorption, reactions, photodissociation, and thermal and photodesorption processes, which transform surface species either into other surface species or into gas-

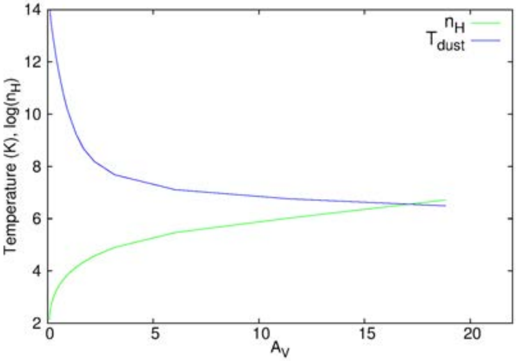

Figure 6.15. *Density temperature profile of pre-stellar cores from Keto & Caselli 2010.*

phase species, as in Cazaux et al. (2016). Note that in this study, we only consider CO freeze out on the dust surface, but do not allow surface reactions with CO as a first approximation. In addition, our model does not take into account neither the diffusion of molecules from bulk to surface nor from surface to bulk. In this sense, when the coverage has reached one layer, the accreted molecules become bulk species with higher binding energies and lower diffusion rates (because the diffusion depends on the binding energy). The surface chemistry model is described in Cazaux et al. (2016), while the gas-phase chemical model is adopted from the KIDA database (Wakelam et al. 2012). The model starts with atomic conditions (in particular, n_H=10^4 cm^{-3}, A_V=5, and T_{dust}=17 K), and molecular cloud conditions are obtained when steady state is reached. The input parameters to mimic the temperature and density profile of a pre-stellar core in the interior of the parental molecular cloud are taken from Keto & Caselli 2010 and shown in Fig. 6.15.

The C^+, C, CO, O and H_2O abundances in the gas phase as a function of extinction are reported in Fig. 6.16 (left panel) for a lifetime of 10^4 years. Our results show that if we consider a binding energy of CO typical of CO on CO ices $\sim$ 830 K, then the CO depletion at extinctions of A_V $\sim$ 20 can reach 5 orders of magnitude (0.001% of CO in the gas phase, that is, 99.999% of CO frozen-out in the ice and missing from the gas phase). However, as the binding energy of weakly bound CO is considered, such as 400 K (green), 350 K (blue) and 300 K (pink), as shown in Fig. 6.16 (right panel), the depletion is strongly decreased and CO in the gas phase becomes 0.1%, 10% and 100%, respectively.

Therefore considering the weakly bound CO molecules can completely change the depletion of CO at high A_V. As the cloud evolves and reaches 10^5 years, C^+, C, CO, O and H_2O abundances also evolve as shown in Fig. 6.17 (left panel). For typical binding energies of CO with CO ($\sim$ 830 K), the depletion is more pronounced from extinctions of A_V $\sim$2. When the weakly bound CO molecules are also considered, as shown in Fig. 6.17 (right panel), differences from the depletion of CO can be already seen for binding energies of 400 K (green). This is due to the fact that the abundances of CO are set by the accretion versus desorption processes. In this case, the CO bound at low

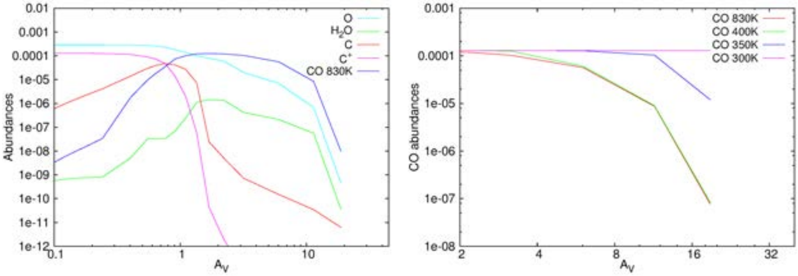

Figure 6.16. *Left: Abundances of* C^{+}*, C, CO, O and* H_2O *at* 10^4 *years as function of extinction in our pre-stellar core model. Right: CO abundances derived form our model considering binding energies of CO ranging between 300K and 830 K.*

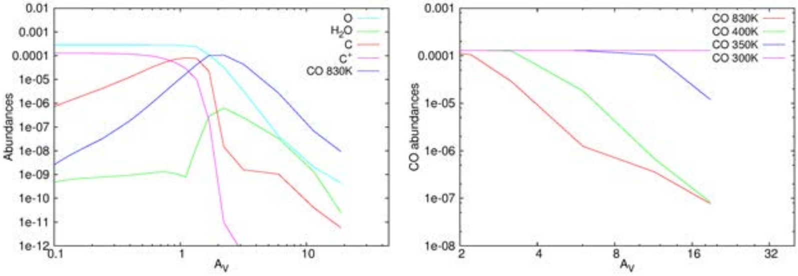

Figure 6.17. *Left: Abundances of* C^{+}*, C, CO, O and* H_2O *at* 10^5 *years as function of extinction in our pre-stellar core model. Right: CO abundances derived form our model considering binding energies of CO of ranging between 300K and 830 K.*

energies will be earlier in equilibrium, which implies that the abundances of CO in the gas phase for bindings of CO of 300 and 350 K do not change between 10^4 and 10^5 years. However, for CO molecules more strongly bound to the surface, the equilibrium is not reached yet at 400 K and 830 K and depletion is still increasing.

6.5 Conclusions

We have shown experimentally that CO ices deposited under different conditions (low temperatures $\sim$ 14 K *versus* decreasing temperatures from $\sim$ 80 K to 8 K) show identical TPD spectra. This implies that individual CO molecules are bound with the same binding energy when CO ices are being warmed up and desorbed into the gas phase. However, the TPD experiments do not allow to quantify the binding energies of individual CO molecules during their deposition (prior to their desorption).

In this work we have tried to quantify the binding energy of CO molecules upon deposition using theoretical simulations, and shown that the deposition conditions (flux and temperature) set the binding energy, and that CO molecules can have a very wide range of binding energies when accreted at low temperatures. However, during the warming up of the CO ices, the CO molecules re-organize in the most stable configuration, leading to higher binding energies, which result in identical TPD spectra regardless of the initial conditions of deposition, as expected from the experimental simulations. In this sense, TPD measurements do not allow to determine the binding energy of molecules during deposition, but allow to derive the binding energy of molecules after re-organization.

In environments where stars are forming, the temperature can be so low that weakly bound molecules do not need to re-organize and stay weakly bound to dust grains (i.e., with low binding energies). This can have an impact on the gas phase composition of the environment, but also on the chemistry occurring onto dust which could be more efficient as weakly bound species are more mobile. In pre-stellar cores, CO molecules are seen to be depleted as the medium becomes denser and cooler. While this is attributed to the freeze out of CO molecules from the gas phase, actual models overestimate the freezing of CO on dust. In this work we have shown that considering both weekly and strongly bound molecules in the CO ices changes the CO depletion in pre-stellar cores and results in a less severe depletion.

Acknowledgements

S. C. is supported by the Netherlands Organization for Scientific Research (NWO; VIDI project 639.042.017) and by the European Research Council (ERC; project PALs 320620). This work was supported by the MOST grants MOST 103-2112-M-008-025-MY3 (Y.J.C.), and by the Spanish MINECO under projects AYA-2011-29375 and AYA2014-60585-P. R.M.D. benefited from a FPI grant from Spanish MINECO. .

References

Acharyya, K., Fuchs, G. W., Fraser, H. J., van Dishoeck, E. F., & Linnartz, H. 2007, A&A, 466, 1005

Attard & Barnes. 1998, Surfaces, Vol. Oxford chemistry primers (Oxford University Press)

Bacmann, A., Lefloch, B., Ceccarelli, C., et al. 2002, A&A, 389, L6

Bergin, E. A., Alves, J., Huard, T., & Lada, C. J. 2002, ApJL, 570, L101

Brunetto, R., Caniglia, G., Baratta, G. A., & Palumbo, M. E. 2008, ApJ, 686, 1480

Bossa, J.-B., Isokoski, K., de Valois, M.S., & Linnart, H. 2012, A&A, 545, A82

Caselli, P., Walmsley, C. M., Tafalla, M., Dore, L., & Myers, P. C. 1999, ApJL, 523, L165

Cazaux, S., Minissale, M., Dulieu, F., & Hocuk, S. 2016, A&A, 585, A55

Cazaux, S. & Tielens, A. G. G. M. 2004, ApJ, 604, 222

Cazaux, S., Tielens, A. G. G. M., Ceccarelli, C., et al. 2003, ApJL, 593, L51

Chen, Y.-J., Chuang, K.-J., Muñoz Caro, G. M., et al. 2014, ApJ, 781, 15

Collings, M. P., Dever, J. W., Fraser, H. J., McCoustra, M. R. S., & Williams, D. A. 2003, ApJ, 583, 1058

Cuppen, H. M. & Herbst, E. 2007, ApJ, 668, 294

Cuppen, H.M., Penteado, E.M., Isokoski, K., van der Marel, M., & Linnartz, H. 2011, MNRAS, 417, 2809

Cuppen, H. M., Karssemeijer, L. J., & Lamberts, T. 2013, Chemical Reviews, 113, 8840
Collings, M.P., Anderson, M.A., Chen, R., et al. 2004, MNRAS, 354, 1133
Dulieu, F., Congiu, E., Noble, J., et al. 2013, Scientific Reports, 3
Fayolle, E. C., Balfe, J., Loomis, R., et al. 2016, ApJL, 816, L28
Fayolle, E. C., Bertin, M., Romanzin, C., et al. 2011, ApJL, 739, L36
Ghesquiere, P., Mineva, T., Talbi, D., et al. 2015, Phys. Chem. Chem. Phys., 17, 11455
Hagen, W. & Tielens, A. G. G. M. 1981, J. Chem. Phys., 75, 4198
Hasegawa, T. I. & Herbst, E. 1993, MNRAS, 263, 589
He, J., Acharyya, K., & Vidali, G. 2016, ApJ, 825, 89
Ivlev, A. V., Padovani, M., Galli, D., & Caselli, P. 2015, ApJ, 812, 135
Jiang, G. J., Person, W. B., & Brown, K. G. 1975, J. Chem. Phys., 62, 1201
Karssemeijer, L. J. & Cuppen, H. M. 2014, A&A, 569, A107
Karssemeijer, L. J., Ioppolo, S., van Hemert, M. C., et al. 2014, ApJ, 781, 16
Keto, E. & Caselli, P. 2010, MNRAS, 402, 1625
Lauck, T., Karssemeijer, L., Shulenberger, K., et al. 2015, ApJ, 801, 118
Luna, R., Satorre, M. Á., Santonja, C., & Domingo, M. 2014, A&A, 566, A27
Martín-Doménech, R., Muñoz Caro, G. M., Bueno, J., & Goesmann, F. 2014, A&A, 564, A8
Muñoz Caro, G. M., Chen, Y.-J., Aparicio, S., et al. 2016, A&A, 589, A19
Muñoz Caro, G. M., Jiménez-Escobar, A., Martín-Gago, J. Á., et al. 2010, A&A, 522, A108
Noble, J. A., Dulieu, F., Congiu, E., & Fraser, H. J. 2011, ApJ, 735, 121
Öberg, K. I., Fuchs, G. W., Awad, Z., et al. 2007, ApJL, 662, L23
Öberg, K. I., Garrod, R. T., van Dishoeck, E. F., & Linnartz, H. 2009, A&A, 504, 891
Ossenkopf, V. & Henning, T. 1994, A&A, 291, 943
Pontoppidan, K. M. 2006, A&A, 453, L47
Pontoppidan, K. M., Blake, G. A., van Dishoeck, E. F., et al. 2008, ApJ, 684, 1323
Rawlings, J. M. C., Williams, D. A., Viti, S., Cecchi-Pestellini, C., & Duley, W. W. 2013, MNRAS, 430, 264
Reboussin, L., Wakelam, V., Guilloteau, S., & Hersant, F. 2014, MNRAS, 440, 3557
Schöier, F. L., Jørgensen, J. K., van Dishoeck, E. F., & Blake, G. A. 2002, A&A, 390, 1001
Shen, C. J., Greenberg, J. M., Schutte, W. A., & van Dishoeck, E. F. 2004, A&A, 415, 203
Takahashi, J. & Williams, D. A. 2000, MNRAS, 314, 273
Wakelam, V., Herbst, E., Loison, J.-C., et al. 2012, ApJ Suppl., 199, 21

Chapter 7

Introduction to the photoprocessing of ices

Molecules in the ice mantles can be energetically processed. In the coldest regions (i.e., dense clouds), thermal processing is inhibited, and interaction with photons and cosmic rays plays the most important role. In particular, photoprocessing of ices in molecular clouds is possible thanks to the secondary ultraviolet (UV) field that is generated by the interaction of cosmic rays with H_2 molecules that are present in the gas phase (Cecchi-Pestellini & Aiello 1992, Shen et al. 2004). Ice mantles in circumstellar environments can be also irradiated by the central stellar object.

UV photons can induce photochemistry and desorption of ice molecules.

Photochemistry is initiated by photolysis of absorbing molecules and subsequent recombination of radicals, directly or by diffusion in the ice upon warm-up. UV-induced chemistry has been proposed as a possible formation pathway for species of diverse complexity, enriching the chemical composition of the ice mantles. An interesting review on this subject has recently been published (Öberg 2016).

UV-photon-induced desorption is one of the proposed nonthermal desorption mechanisms necessary to explain the presence of molecules in the gas phase at temperatures well below their desorption temperature (e.g., Willacy & Langer 2000, Bergin et al. 2001). Other nonthermal desorption processes are cosmic ray induced desorption (either by sputtering (Dartois et al. 2015), impulsive spot heating (Ivlev et al. 2015), cosmic ray induced radical diffusion (Reboussin et al. 2014) or cosmic ray induced explosive chemical desorption (Shen et al. 2004)); and chemical desorption (Dulieu et al. 2013, including formation of H_2 (Takahashi & Williams 2000) and non canonical explosions (Rawlings et al. 2013)), but they have not been studied in this thesis.

7.1 Photon-induced desorption processes

Ultraviolet photons can induce desorption of ice molecules through two different main mechanisms. We can distinguish between **direct photodesorption** when the molecule that absorbs the UV photon subsequently desorbs (or at least a fragment of the molecule does); and **photodesorption via energy transfer** when the molecule that absorbs the photon does not photodesorb, but the absorbed energy is transferred or redistributed to a different molecule that finally desorbs.

Direct photodesorption

A molecule on the surface of an ice mantle can absorb a UV photon and subsequently desorb, in case it is not photodissociated. For example, van Hemert et al. (2015) recently proposed this mechanism based on molecular dynamics simulations for the photodesorption of CO molecules from a pure CO ice. However, this process has been proven to be inefficient, and its contribution may be negligible when other mechanisms are available, since the amount of UV photons absorbed by the ice surface is proportionally lower than the one absorbed by several monolayers (5±1 in the case of pure CO ice; see, e.g., Muñoz Caro et al. 2010) below the surface that could lead to photodesorption via energy transfer (see below). Experimental evidences of this can be found, e.g., in Muñoz Caro et al. (2010), and Bertin et al. (2012, 2013) for the case of CO and N_2 photodesorption.

If the surface molecule that absorbs the photon dissociates, the excited photofragment could also desorb directly after its formation thanks to the excess energy provided by the photon, provided that this photofragment is formed with enough kinetic energy (see, e.g., Fayolle et al. 2013, Fillion et al. 2014, Bertin et al. 2016).

Alternatively, the photofragment may recombine with another fragment or a molecule on the surface of the ice, leading to a new molecule that can desorb inmediately after its formation thanks to the excess energy of the forming photofragments and/or the exothermicity of the recombination reaction (see, e.g., Fillion et al. 2014).

In this sense, this mechanism is similar to the chemical desorption previously mentioned, but the chemical reaction (dissociation or recombination) that triggers the desorption of the products is induced in this case by the absorption of a UV photon (it is therefore a photochemical reaction). For this reason, this mechanism is referred to as photochemical desorption or photochemidesorption in Martín-Doménech et al. (2015, 2016) and Cruz-Díaz et al. (2016); and in Chapters 8 - 10 in this thesis.

Photochemidesorption should be always present (provided that dissociation of the ice molecules takes place upon UV absorption), but it may be difficult to detect during the experimental simulations depending on the incident UV flux, the UHV conditions, and the sensibility of the gas-phase detector. Even though photochemidesorption could be negligible when other photodesorption mechanisms are available, certain photoproducts in certain environments are not able to photodesorb via energy transfer and can only photochemidesorb. The photochemidesorption of photofragments or photoproducts only takes one step after the UV photon absorption, since they desorb directly after their formation, without the need of absorbing an additional UV photon. This leads to a *constant photodesorption yield of photoproducts with fluence*, as it is shown in Chapters 9 and 10.

Photodesorption via energy transfer

When the absorption of a UV photon takes place below the surface of the ice without photodissociation of the absorbing molecule, it leads to its electronic excitation. Then, the electronic excitation energy can be redistributed to the neighboring molecules, eventually providing sufficient energy to the surface molecules to break intermolecular bonds and be ejected into the gas phase (Rakhovskaia et al. 1995, Öberg et al. 2007, Muñoz Caro et al. 2010, Fayolle et al. 2011, Fayolle et al. 2013, Bertin et al. 2012, Bertin et al. 2013, Fillion et al. 2014). This is usually known as desorption induced by electronic transitions or DIET [1]. Therefore, in addition to the intermolecular bond strengths on the ice surface, this process depends on both the composition and the UV absorption spectra of the subsurface ice layers. This dependence can be readily observed during irradiation experiments using monochromatic light with variable wavelength (see, e.g., Fayolle et al. 2011 for the case of pure CO ice), while this interpretation is more difficult when a continuum emission source (such as the MDHL described in Chapter 4, Sect. 4.1.3) is used, since several effects may contribute simultaneously[2].

---

[1] This process is called kick-out photodesorption in van Hemert et al. (2015). However, it must not be confused with the kick-out photodesorption explained in this Chapter.

In this case, the desorbing molecules may or may not belong to the same species that the molecules absorbing the UV photons. When they belong to different species, this mechanism is sometimes referred to as indirect DIET or photon-induced co-desorption, but in general no distinctions are made.

If the molecule that absorbs the photon dissociates, the excess energy can still be transferred or redistributed by the resulting excited photofragment to a surface molecule, leading to its photodesorption, although in this case the amount of transferred energy diminishes.

In addition, the photofragment can also recombine with another fragment or a molecule forming a photoproduct, which can transfer the excess energy provided by the UV photon, along with the exothermicity of the recombination reaction, to a surface molecule leading to a photodesorption event. In both cases, these processes can be seen as contributions to the DIET photodesorption (see, e.g., Fillion et al. 2014).

When the photofragment is a hot/fast atom (e.g., an H atom) actually moving through the ice and transferring its momentum to a surface molecule, the photodesorption process is known as kick-out photodesorption (see, e.g., Andersson et al. 2008).

When photoproducts desorb via energy transfer through any of the mechanisms explained above, their photodesorption takes two steps instead of only one, in contrast to the photochemidesorption process. First, the photoproduct is formed in the ice upon absorption of one (or more than one) photon. Then, the energy coming from a second UV photon absorbed below the surface of the ice can be transferred to a photoproduct molecule near the surface, inducing its photodesorption. Since this photodesorption in two steps allow accumulation of photoproduct molecules before their desorption, it leads to an *increasing photodesorption yield of photoproducts with fluence*, as it is shown in Chapters 8 - 10 [3].

7.2 Outlook of Chapters 8 - 10

Photodesorption of pure ices made of species whose presence in interstellar ice mantles is already confirmed has extensively been studied:

- Photodesorption from a pure H_2O ice is studied in Cruz-Díaz et al. (2017, *submitted*).
- Photodesorption from a pure CO ice is the most studied case (see, e.g., Muñoz Caro et al. 2010, Fayolle et al. 2011, Bertin et al. 2012, Bertin et al. 2013).

---

[2] In contrast, the short irradiation times typical of the experiments using a monochromatic source lead to low UV fluences, and neglegible formation of photoproducts (e.g., CO_2 when a pure CO ice is irradiated), thus making the study of the effect of photoproduct formation in the photodesorption process, as well as the evolution of the photodesorption yields of both the original ice components and the newly formed photoproducts with fluence, much more difficult.

[3] If a previously formed photoproduct molecule absorbs the UV photon itself and subsequently desorbs, this direct photodesorption could also lead to an increasing photodesorption yield. However, the contribution of this photodesorption mechanism is negligible, as explained above.

- Photodesorption from a pure CO_2 ice was studied in (e.g.) Fillion et al. (2014) and is revisited in Chapter 8.
- Photodesorption from a pure CH_3OH ice has recently been discussed in Bertin et al. (2016), and Cruz-Díaz et al. (2016).
- Photodesorption-dedicated studies of pure NH_3 and CH_4 ices remain to be published.

On the other hand, photodesorption from a pure C_2H_5OH ice (which is a candidate to be present in interstellar ice mantles) is studied in Chapter 9.

In addition, photodesorption from a more realistic water-rich binary mixture composed by H_2O and CH_4 is studied in Chapter 10.

References

Andersson, S., & van Dishoeck, E. F. 2008, A&A, 491, 907
Bergin, E. A., Ciardi, D. R., Lada, C. J., et al. 2001, ApJ, 557, 209
Bertin, M., Fayolle, E. C., Romanzin, C., et al. 2012, PCCP, 14, 9929
Bertin, M., Fayolle, E. C., Romanzin, C., et al. 2012, ApJ, 779, 120
Bertin, M., Romanzin, C., Doronin, M., et al. 2016, ApJL, 817, 2, L12
Boogert, A. C. A., Gerakines, P. A., & Whittet, D. C. B. 2015, ARA&A, 53, 541
Cecchi-Pestellini, C. & Aiello, S. 1992, MNRAS, 258, 125
Cruz-Díaz, G.A., Martín-Doménech, R., Moreno-Atahonero, E., Muñoz Caro, G.M., & Chen, Y.-J. 2017, ApJ, *submitted*
Cruz-Díaz, G. A., Martín-Doménech, R., Muñoz Caro, G. M., & Chen, Y.-J. 2016, A&A, 592, A68
Dartois, E., Augé, B., Boduch, P., et al. 2015, A&A, 576, A125
Dulieu, F., Congiu, E., Noble, J., et al. 2013, Scientific Reports, 3
Fayolle, E. C., Bertin, M., Romanzin, C., et al. 2011, ApJL, 739, L36
Fayolle, E. C., Bertin, M., Romanzin, C., et al. 2013, A&A, 556, A122
Fillion, J.-H., Fayolle, E., Michaut, X., et al. 2014, Faraday Discuss., 168, 533
Ivlev, A. V., Padovani, M., Galli, D., & Caselli, P. 2015, ApJ, 812, 135
Muñoz Caro, G. M., Jiménez-Escobar, A., Martín-Gago, J.Á. et al. 2010, A&A, 522, A108
Öberg, K. I. 2016, Chem. Rev. 2016, 116(17), 9631
Öberg, K. I., Fuchs, G. W., Awad, Z., et al. 2007, ApJ, 662, L23
Rakhovskaia, O., Wiethoff, P., & Feulner, P. 1995, NIM B, 101, 169
Rawlings, J. M. C., Williams, D. A., Viti, S., Cecchi-Pestellini, C., & Duley, W. W. 2013, MNRAS, 430, 264
Reboussin, L., Wakelam, V., Guilloteau, S., & Hersant, F. 2014, MNRAS, 440, 3557
Shen, C. J., Greenberg, J. M., Schutte, W. A., & van Dishoeck, E. F. 2004, A&A, 415, 203
Takahashi, J. & Williams, D. A. 2000, MNRAS, 314, 273
Willacy, K., & Langer, W. D. 2000, ApJ, 544, 903

Chapter 8

UV photoprocessing of CO_2 ice

Adapted from *UV photoprocessing of CO_2 ice: A complete quantification of photochemistry and photon-induced desorption processes*, Martín-Doménech, R., Manzano-Santamaría, J., Muñoz Caro, G.M., Cruz-Díaz, G.A., Chen, Y.-J., Herrero, V.J., & Tanarro, I. 2015, A&A, 584, A14 [1].

Abstract

Ice mantles that formed on top of dust grains are photoprocessed by the secondary ultraviolet (UV) field in cold and dense molecular clouds. UV photons induce photochemistry and desorption of ice molecules. Experimental simulations dedicated to ice analogs under astrophysically relevant conditions are needed to understand these processes.

In this chapter we present UV-irradiation experiments of a pure CO_2 ice analog. Calibration of the quadrupole mass spectrometer (QMS) allowed us to quantify the photodesorption of molecules to the gas phase. This information was added to the data provided by the Fourier transform infrared spectrometer (FTIR) on the solid phase to obtain a complete quantitative study of the UV photoprocessing of an ice analog.

Experimental simulations were performed in an ultra-high vacuum chamber. Ice samples were deposited onto an infrared transparent window at 8K and were subsequently irradiated with a microwave-discharged hydrogen flow lamp. After irradiation, ice samples were warmed up until complete sublimation was attained.

Photolysis of CO_2 molecules initiates a network of photon-induced chemical reactions leading to the formation of CO, CO_3, O_2, and O_3. During irradiation, photon-induced desorption of CO and, to a lesser extent, O_2 and CO_2 took place through a process called indirect desorption induced by electronic transitions (DIET), with maximum photodesorption yields (Y_{pd}) of $\sim$1.2 x 10^{-2} molecules incident photon^{-1}, $\sim$9.3 x 10^{-4} molecules incident photon^{-1}, and $\sim$1.1 x 10^{-4} molecules incident photon^{-1}, respectively.

Calibration of mass spectrometers allows a direct quantification of photodesorption yields instead of the indirect values that were obtained from infrared spectra in most previous works. Supplementary information provided by infrared spectroscopy leads to a complete quantification, and therefore a better understanding, of the processes taking place in UV-irradiated ice mantles.

8.1 Introduction

A series of experimental studies have been carried out in the past decades to better understand the photoprocessing of cosmic ice mantles. These studies help understanding astronomical observations of both the solid and gaseous phases of the ISM, and their results are also incorporated into theoretical models of dense clouds and star-forming regions. Despite being the simplest case, experimental simulations on UV photoprocessing of pure ice analogs provide the most fundamental information about the processes triggered by UV photons on ice mantles. They are a necessary step before attempting the simulation of processes in ice mixtures made of various molecular components. Gerakines et al. (1996) presented a study of UV irradiation of nine pure ice analogs of astrophysical interest. Photoprocessing of pure CO ice has been widely studied, since it is one of the most abundant species found in ice mantles. The interface between the UV source and the chamber where the ice sample is located is, usually, a MgF_2 window with a cutoff at ∼114 nm (10.87 eV), that is, below the dissociation energy of CO molecules (11.09 eV, Cruz-Díaz et al. 2014a, Chen et al. 2014). Therefore, in these experiments UV irradiation mainly leads to photodesorption (see, e.g., Öberg et al. 2007, Muñoz Caro et al. 2010, Fayolle et al. 2011, Bertin et al. 2012, Chen et al. 2014). In the past years, photoprocessing of other pure ices made of CO_2, H_2O, CH_3OH, O_2, or N_2 has been studied (see, e.g., Westley et al. 1995, Öberg et al. 2009a, Öberg et al. 2009b, Bahr & Baragiola 2012, Fayolle et al. 2013, Yuan & Yates 2013, Fillion et al. 2014, Yuan & Yates 2014, Zhen & Linnartz 2014, Cruz-Díaz et al. 2016).

---

[1] The information on the photodesorption processes present in the Introduction of the published version of the paper has been moved to Chapter 7. The Appendix A where the calibration of the QMS was described has been also moved to Chapter 4.

Previous works failed in providing a complete quantitative study of the relative contribution of photodestruction, photoproduction, and photon-induced desorption taking place in irradiated ice analogs, since a quantification of the desorbing molecules in the gas phase is necessary. These molecules are often measured by a quadrupole mass spectrometer (QMS) in addition to the quantification of the solid phase molecules, which usually is performed by infrared spectroscopy. This is not strictly required for the irradiation experiments of pure CO ice, since photodesorption is the main effect (only ∼5% of the absorbed UV photons lead to photoproducts, Muñoz Caro et al. 2010), and can be thus quantified using infrared spectroscopy alone.

In this work, we have used the outcome of our Fourier transform infrared (FTIR) spectrometer and the QMS in previous CO irradiation experiments as a reference for the calibration of the measured QMS ion current of other species. A similar approach has recently been used by Fayolle et al. 2013, Fillion et al. 2014, Zhen & Linnartz 2014 to quantify photon-induced desorption from UV-irradiated pure O_2, N_2, and CO_2 ices, linking the QMS signal of desorbed molecules to the data recorded by reflection absorption infrared spectroscopy and quadrupole mass spectrometry of previous pure CO ice irradiation experiments. Using our calibrated QMS and a transmittance-FTIR spectrometer, we have performed a complete quantitative study of the UV-irradiation experiment of a pure CO_2 ice analog. We describe this in Sect. 8.2. The QMS calibration method for ice irradiation experiments is explained in Chapter 4, Sect. 4.1.5. The experimental results are presented in Sect. 8.3, while the astrophysical implications are discussed in Sect. 8.4. The conclusions are summarized in Sect. 8.5.

8.2 Experimental setup

The UV-irradiation experiments presented in this work have been performed using the InterStellar Astrochemistry Chamber (ISAC) at the Centro de Astrobiología (see Muñoz Caro et al. 2010 and Chapter 4, Sect. 4.1.1). The ISAC setup is an ultra-high vacuum (UHV) chamber with a base pressure about 4 x 10^{-11} mbar, similar to that found in dense cloud interiors. Ice samples were grown by deposition of CO_2 (gas, Praxair 99.996%), introduced in the chamber at a pressure of 1 x 10^{-6} mbar during 30 s onto a

KBr window at 8 K, achieved by means of a closed-cycle helium cryostat. This led to an ice thickness of $\sim$ 200 x 10^{15} CO_2 molecules cm^{-2}. Additional experiments with $^{13}CO_2$ (gas, Cambridge Isotope Laboratories 99.0%) introduced into the chamber at a pressure of 8.6 x 10^{-6} mbar during 1 - 2 min (leading to an ice thickness of $\sim$ 180 - 320 x 10^{15} CO_2 molecules cm^{-2}) were performed to rule out contamination effects.

Deposited ice analogs were subsequently UV irradiated using an F-type microwave-discharged hydrogen flow lamp (MDHL), from Opthos Instruments, with a MgF_2 window used as interface between the lamp and the chamber. This source has a vacuum ultraviolet (VUV) flux of $\approx 2 \times 10^{14}$ photons cm^{-2} s^{-1} at the sample position (measured by $CO_2 \rightarrow CO$ actinometry, Muñoz Caro et al. 2010). The spot size of the region irradiated by the lamp coincides with the size of the window substrate. Characterization of the MDHL spectrum has been studied by Chen et al. (2010, 2014), and it is similar to the calculated secondary UV field by Gredel et al. (1989). More information can be found in Cruz-Díaz et al. (2014), where a description of the VUV spectrophotometer used in our setup to monitor the VUV flux of the hydrogen lamp during ice irradiation is provided, and in Chapter 4, Sect. 4.1.3.

After irradiation, ice samples were warmed up to room temperature with a heating rate of 1 K min^{-1} using a LakeShore Model 331 temperature controller until complete sublimation was attained, simulating thermal processing of the ice in warm circumstellar regions. A silicon diode temperature sensor was used to measure the sample temperature at any time, reaching a sensitivity of about 0.1 K.

The evolution of the ice after successive irradiations and during the warm-up was monitored by in situ FTIR transmittance spectroscopy, using a Bruker Vertex 70 spectrometer equipped with a deuterated triglycine sulfate detector (DTGS). The IR spectra were collected after ice deposition at 8 K, after every period of UV irradiation, or every five minutes during warm-up, with a spectral resolution of 2 cm^{-1}. Column densities of each species in the ice were calculated from the IR spectra using the formula

$$N = \frac{1}{A} \int_{band} \tau_\nu \, d\nu, \tag{8.1}$$

where N is the column density of the species in molecules cm^{-2}, τ_ν the optical depth of the absorption band, and A the band strength in cm molecule^{-1}, as derived from laboratory experiments (Table 11.1). The band strength of the 2044 cm^{-1} IR feature corresponding to CO_3 was calculated in this work, assuming that all remaining C atoms not locked in CO_2 or CO molecules after the first five minutes of irradiation were forming CO_3, since no other carbon-bearing photoproducts were detected during the experiments. The other band strengths in Table 11.1 were measured for pure ices made of one molecular component. The same values are usually adopted in ice mixtures, which introduce an uncertainty of about 20-30% (d'Hendecourt & Allamandola 1986).

Molecules desorbing to the gas phase during irradiation or during the warm-up were detected using a Pfeiffer Prisma quadrupole mass spectrometer (QMS) of mass spectral range from 1 to 200 amu equiped with a Channeltron detector. The QMS ionizes gas-phase molecules with $\sim$ 70 eV electron bombardment. All the species were monitored through its main mass fragment: m/z=44 (CO_2), m/z=45 ($^{13}CO_2$), m/z=28 (CO, with a small contribution of CO_2 fragmentation into CO^+ of, approximately, 10% of the m/z=44 signal), m/z=29 (^{13}CO), m/z=60 (CO_3), m/z=61 ($^{13}CO_3$), m/z=32 (O_2), and m/z=48 (O_3).

Table 8.1. *IR feature used to calculate the column density of each component (frequencies and band strengths for pure ices at 8 K).*

Molecule	Frequency (cm^{-1})	Band strength (cm $molec^{-1}$)
CO_2	2344	7.6×10^{-17} [a]
$^{13}CO_2$	2283	7.8×10^{-17} [b]
CO	2141	1.1×10^{-17} [c]
^{13}CO	2092	1.3×10^{-17} [b]
CO_3	2044	1.5×10^{-17} [d]
O_3	1042	1.4×10^{-17} [e]

[a] From Yamada & Person 1964. [b] From Gerakines et al. 1995. [c] From Jiang et al. 1975. [d] This work. [e] From Smith et al. 1985

To convert the signal measured by the QMS into a column density of desorbed molecules during irradiation, we performed additional experiments with the same setup to calibrate our QMS. These experiments are described in Chapter 4, Sect. 4.1.5.

8.3 Experimental results and discussion

8.3.1 IR spectra of CO_2 ice during irradiation

As explained in Sect. 8.2, the solid sample was monitored by IR spectroscopy during the irradiation of the pure CO_2 ice. The C=O stretching band of CO_2 at 2344 cm^{-1} is the dominant IR feature, although its intensity decreases during UV irradiation of the ice (see left panel of Fig. 8.1) along with the bands corresponding to combination modes at 3708 cm^{-1} and 3600 cm^{-1} (not shown) and the bending mode at $\sim$658 cm^{-1} (right panel of Fig. 8.1).

At the same time, three features appear due to the formation of new species upon photochemistry induced by the UV photons. The C=O stretching band of CO at 2141 cm^{-1} rapidly increases after irradiation is initiated, as was reported by Gerakines et al. (1996), reaching its maximum intensity after 60 minutes of irradiation (Fig. 8.2). A similar behavior is found for the band peaking at 1042 cm^{-1}, which corresponds to O_3 (Fig. 8.3).

The band peaking at 2044 cm^{-1} is assigned to CO_3 (Fig. 8.2; Gerakines et al. 1996, Öberg et al. 2009b). Unlike CO and O_3, this species reaches its maximum abundance during the first five minutes of irradiation, which correspond to a fluence of 6 x 10^{16} photons/cm^2, similar to the value found by Öberg et al. 2009b, and then it decreases gradually as the fluence increases. The presence of these photoproducts in the ice leads to the loss of the double-peak structure of the degenerate bending modes of CO_2 (see right panel of Fig. 8.1), as has previously been reported for carbon dioxide in multi-component ice analogs (Sandford & Allamandola 1990, Martín-Doménech et al. 2014). Similarly, the shoulder of the C=O stretching band of CO_2 peaking at $\sim$2328 cm^{-1} corresponding to pure and amorphous CO_2 ice gradually decreases during irradiation (Escribano et al. 2013).

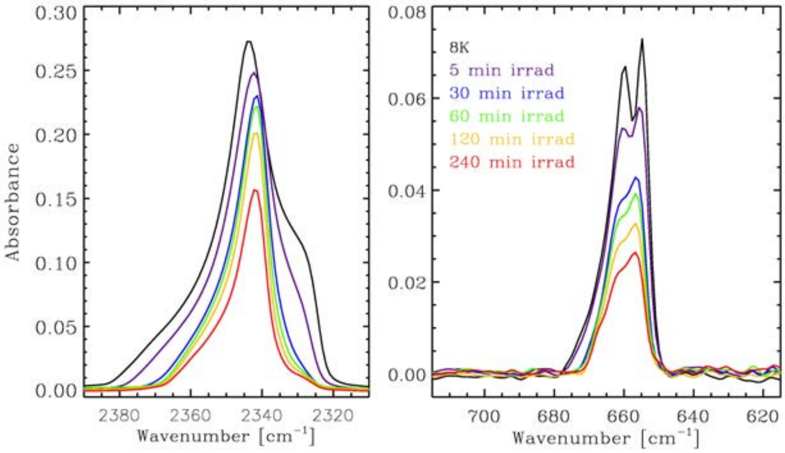

Figure 8.1. *Evolution of two IR bands of CO_2 during UV irradiation of a pure CO_2 ice analog. Left: C=O stretching mode at 2344 cm^{-1}. Right: degenerate bending modes at ∼658 cm^{-1}*

Table 8.2. *Values used in Eq. 4.3 to convert integrated QMS signals to column densities of desorbed molecules.*

Factor	$^{13}CO_2$	CO	O_2
$\sigma^+(mol)$ (Å^2)^a	3.521^b	2.516	2.441
$I_F(z)$	1^c	1^c	1^c
$F_F(m)^d$	0.794^b	0.949	0.898
$k^*_{QMS} \cdot S(m/z)$ (A mbar^{-1} Å^{-2})^e	4.62 x 10^{14}	1.03 x 10^{15}	8.41 x 10^{14}

[a] Extracted from the online database of the National Institute of Standard and Technologies (NIST).
[b] We have used the value corresponding to $^{12}CO_2$ as an approximation.
This introduces an uncertainty of about 2% in the case of the fragmentation factor, according to previous measurements.
[c] A value of 1 has been taken, assuming that no double ionization of the molecules takes place.
[d] Extracted from the mass spectra library of the QMS software.
[e] This work (see Chapter 4, Sect. 4.1.5).

8.3.2 Photon-induced desorption during irradiation

The desorbing molecules were detected in the gas phase by the QMS during irradiation. Figure 8.4 shows the signal of the main mass fragments of all the species mentioned in Sect. 8.3.1, including m/z = 32, which corresponds to O_2. This molecule was not detected in the IR spectra since it is infrared inactive due to the lack of an electric dipole moment. The integrated QMS ion currents have been converted into the column density values shown in Table 8.3 and Fig. 8.8 using Eq. 4.3, the values in Table 8.2, and the k_{CO} value found in Chapter 4, Sect. 4.1.5.

As reported by Bahr et al. (2012) and Fillion et al. (2014), the CO product displays the

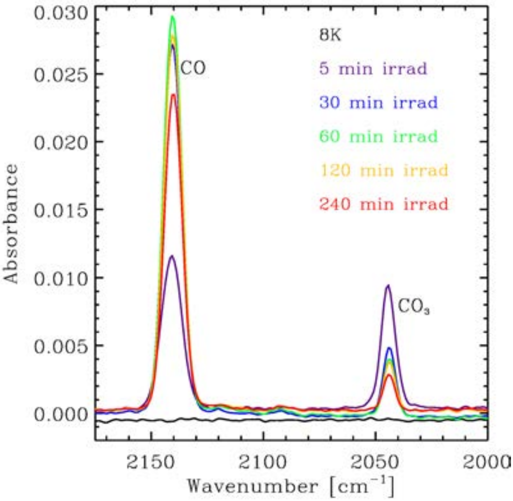

Figure 8.2. *Evolution of the IR bands corresponding to the photoproducts CO and CO_3 during UV irradiation of a pure CO_2 ice analog.*

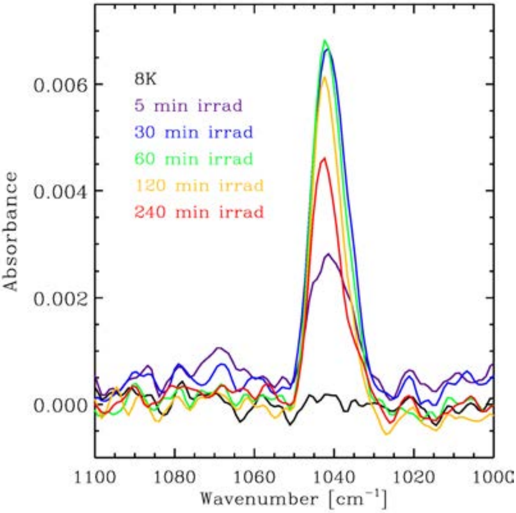

Figure 8.3. *Evolution of the IR feature corresponding to the O_3 photoproduct during UV irradiation of pure CO_2 ice.*

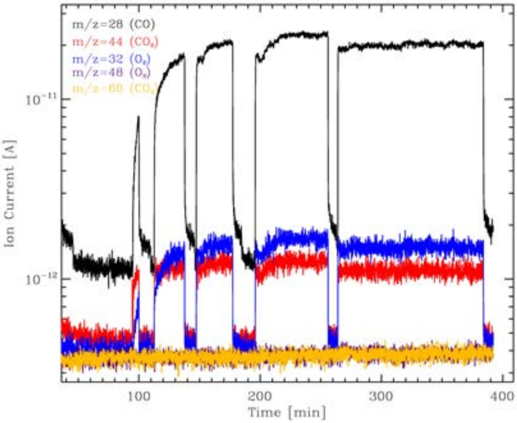

Figure 8.4. *Photodesorption of CO, O_2, and CO_2 during UV irradiation of pure CO_2 ice. The m/z = 44 signal corresponding to CO_2 molecules is affected by contamination (see text). Ion current in the y-axis corresponds, approximately, to the partial pressure (mbar) in the main chamber. Note that the y-axis is on a logarithmic scale.*

highest desorption in CO_2 ice irradiation experiments. The photon-induced desorption of O_2 leads to a signal increase over the background level that is about four to five times lower than that of the CO in every irradiation period, which is only slightly lower than the relative increase of the O_2 signal observed by Bahr et al. (2012). The increase of the m/z = 44 signal during irradiation is affected by contamination, since a similar rise is detected even when no sample is irradiated in the main chamber (see Fig. 8.5). This is not the case for O_2, which is not detected in Fig. 8.5. Contamination problems are also reported in Loeffler et al. (2005), with a higher impact since in that work a high vacuum chamber is used instead of a UHV chamber. Irradiation of a $^{13}CO_2$ ice allowed us to rule out the contamination signal and detect the carbon dioxide desorbing from the ice. Figure 8.6 shows that the amount of $^{13}CO_2$ molecules desorbing during irradiation is even lower than the one corresponding to O_2 (see Sect. 8.3.4). Therefore, photon-induced desorption of CO_2 is negligible, as reported in Bahr et al. (2012), in contrast to what was previously claimed in Öberg et al. (2009b). No desorption of CO_3 and O_3 was detected during irradiation. Photon-induced desorption of these species was not observed in previous works irradiating pure ices (e.g., Bahr & Baragiola 2012, Zhen & Linnartz 2014).

The QMS ion current measured during the various CO_2 ice irradiation intervals due to the photon-induced desorption of CO and O_2 in Fig. 8.4 increases progressively with the fluence up to a constant value after approximately 60 minutes of irradiation, which coincides with the irradiation time in which the maximum abundance of CO in the ice is reached. This means that the molecules of both species that formed and accumulated in the bulk of the ice are taking part in the desorption process as the top ice layers are gradually removed by the UV photons. Photon-induced desorption is thus taking place

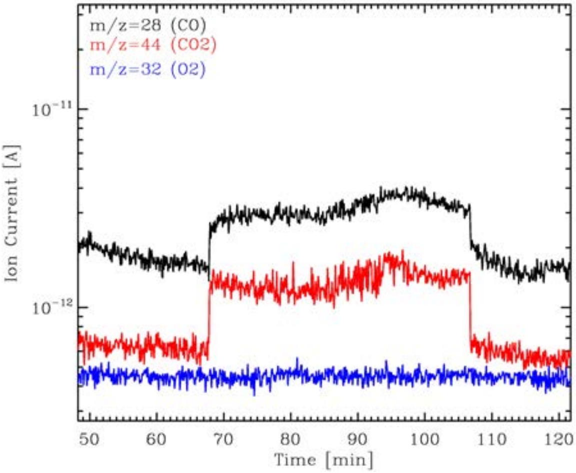

Figure 8.5. *Signals detected by the QMS during irradiation in the main chamber of ISAC without an ice sample. The ion current in the* y*-axis corresponds, approximately, to the partial pressure (mbar) in the main chamber. Note that the* y*-axis is on a logarithmic scale.*

through the DIET mechanism [2], and photochemidesorption, if taking place, has a negligible effect (see Chapter 7 for more information on the photodesorption mechanisms). If photon-induced desorption were taking place through the photochemical mechanism alone, only molecules newly formed in the surface of the ice would be desorbing. The number of desorbing molecules would then be either constant or, alternatively, it would decrease with continuing irradiation, since there would be fewer CO_2 molecules available in the ice surface to lead to photoproducts (see also Cruz-Díaz et al. 2016 and Chapter 7). Moreover, as explained in Sect. 3, photon-induced desorption of both species has already been observed in pure CO and O_2 ice irradiation experiments, respectively[3]. In the case of CO[4], photochemidesorption does not apply[5], and photon-induced desorption takes place through the DIET mechanism. Fillion et al. (2014, and references therein) have reported that the contribution of photochemical desorption relative to photodesorption is about $\sim$10%[6].

On the other hand, photodesorption of CO_2 was expected to increase with the abundance of CO in the ice [7] according to the experiments performed by Fillion et al. (2014) with a monochromatic UV source. However, evolution of the m/z = 44 and m/z = 45

---

[2] Or through any mechanism in two steps involving energy transfer to the previously photoproduced molecules (see Chapter 7).

[3] Please note that the photochemidesorption mechanism could be available in pure ices where photodissociation takes place upon absorption of UV photons

[4] Pure CO ice.

[5] Since there is no photodissociation.

[6] In the case of photodesorption of CO_2 during irradiation of a pure CO_2 ice.

[7] This could happen in case photodesorption of CO_2 took place via energy transfer from CO molecules. Even in that case, an increase in the abundance of CO molecules means a decrease in the abundance of CO_2

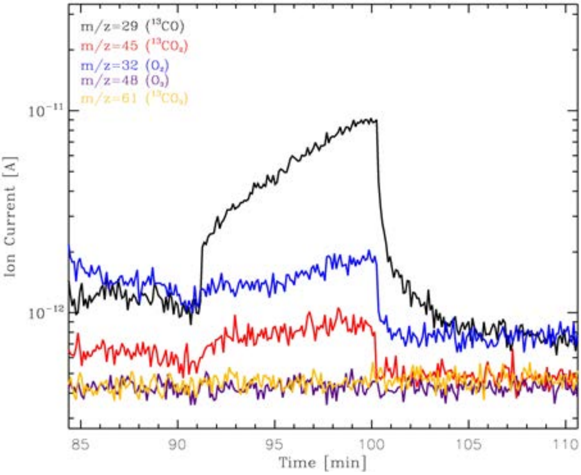

Figure 8.6. *Photodesorption of ^{13}CO, O_2 and $^{13}CO_2$ during UV irradiation of pure $^{13}CO_2$ ice. The ion current in the y-axis corresponds, approximately, to the partial pressure (mbar) in the main chamber. Note that the y-axis is on a logarithmic scale.*

signals in Figs. 8.4 and 8.6 shows that the increase is not significant in our experiments.

8.3.3 Temperature-programmed desorption of the irradiated CO_2 ice

After photoprocessing, the ice sample was warmed up with a heating rate of 1 K/min, leading to thermal desorption of all the observed species. Figure 8.7 shows the temperature-programmed desorption curves of CO_2 and the four photoproducts detected during irradiation.

CO and O_2 present desorption peaks at 36 K and 30 K, respectively. While the desorption peak temperature of O_2 is similar to that of a pure O_2 ice (Acharyya et al. 2007), CO is desorbing at a slightly higher temperature than for pure ice (Muñoz Caro et al. 2010, Martín-Doménech et al. 2014). Both species show a broad peak at ∼50 K, which was also detected in Bahr et al. (2012). O_3 presents a desorption peak at ∼67 K, which is a temperature value similar to that reported in Bahr et al. (2012). Finally, entrapped molecules of the three species co-desorb with CO_2 at 87 K, which corresponds to the desorption peak temperature of a pure CO_2 ice (see, e.g., Martín-Doménech et al. 2014). Thermal desorption of CO_3 is not detected during warm up, probably because of its low abundance at the end of the experiment (see Table 8.3), leading to a QMS signal below our sensitivity limit, as it was the case in Bahr et al. (2012). An additional problem may be the fragmentation pattern of the CO_3 ionized molecules, which could not be found in the literature. If m/z=44 (shared with CO_2) were the main mass fragment instead of

---

molecules. Therefore, the photodesorption yield of CO_2 does not necessarily have to increase with the abundance of CO.

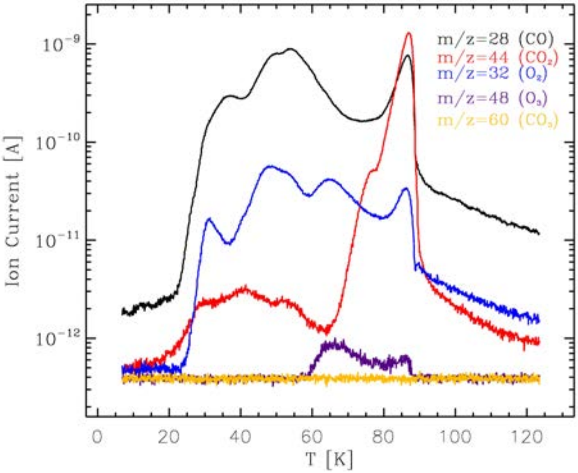

Figure 8.7. *Temperature-programmed desorption curves of CO_2 and its photoproducts after UV irradiation of a pure CO_2 ice. The ion current in the y-axis corresponds, approximately, to the partial pressure (mbar) in the main chamber. Note that the y-axis is on a logarithmic scale.*

m/z=60 (which is plausible since it is an unstable molecule), detection of CO_3 would be more difficult.

8.3.4 Photoprocessing of pure CO_2 ice: reaction scheme and photodesorption yields

Evolution of the species

Table 8.3 and Fig. 8.8 show the evolution of all the species involved in the photoprocessing of a pure CO_2 ice analog in both the solid and gaseous phases. Since photon-induced desorption of CO_2 is negligible (see Sect. 8.3.2), we have assumed that $N_{gas}(CO_2) = 0$.

After the first five minutes of irradiation (corresponding to a fluence of 6 x 10^{16} photons/cm^2), the total number of C and O atoms relative to the initial values in the deposited ice does not remain constant, with a discrepancy up to 25% once the irradiation is completed in the case of C. This is probably because of the uncertainties in the quantification of the column densities in the ice (see Sect. 8.2), which can be of about 20-30%. In a follow-up paper, the presence of C and O atoms in the ice or in the gas phase after desorption (not quantified here) is studied in more depth, giving an alternative explanation to this issue (Chen et al. 2017). A fraction of O atoms is locked in the ice in the form of O_2 molecules, which cannot be detected by IR spectroscopy. We have estimated an upper limit to the column density of O_2 in the ice assuming that all remaining O atoms are contained in O_2 molecules.

An initial destruction or formation cross section $\sigma_{des/form}$ is calculated independently for every species in Table 8.3, fitting their column densities before equilibrium is

Table 8.3. *Evolution of the ice and gas column densities of CO_2 and its photoproducts during UV irradiation of a pure CO_2 ice analog.*

Fluence (photons cm^{-2})	N$_{ice}$(CO$_2$)^a	N$_{ice}$(CO)	N$_{gas}$(CO)	N$_{total}$(CO)	N$_{ice}$(CO$_3$)	N$_{ice}$(O$_2$)^b	N$_{gas}$(O$_2$)	N$_{ice}$(O$_3$)
				(10^{15} molecules cm^{-2})				
0.00	200.3	0.0	0.0	0.0	0.0	0.0	0.0	0.0
6.0 x 10^{16}	159.7	27.9	0.2	28.1	12.1	0.0	0.0	5.8
3.6 x 10^{17}	110.3	62.0	2.6	64.6	7.4	28.9	0.2	11.6
7.2 x 10^{17}	99.0	67.6	6.62	74.2	5.3	37.5	0.5	12.3
1.4 x 10^{18}	87.9	58.9	15.7	74.7	3.7	53.8	1.3	10.7
2.9 x 10^{18}	67.7	47.1	32.3	79.4	2.8	75.6	2.5	7.8

[a] We have assume that N$_{gas}$(CO$_2$) = 0 as a first approximation (see text). [b] Estimated upper limit (see text).

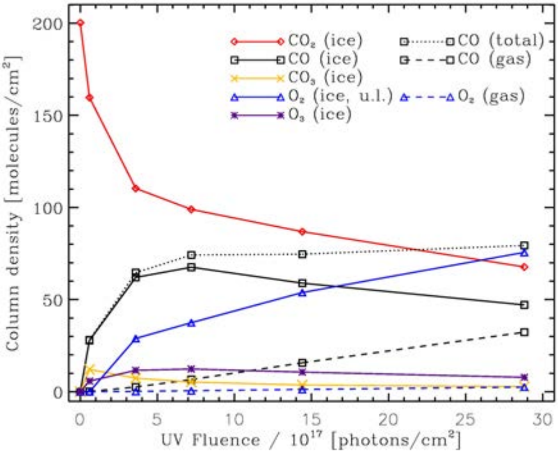

Figure 8.8. *Evolution of the ice and gas column densities of CO_2 and its photoproducts during UV irradiation of a pure CO_2 ice analog. O_2 (ice) column density is an estimated upper limit assuming that all remaining O atoms are locked in O_2 molecules.*

reached to an equation of the form

$$N = N_\infty[1 + \frac{N_0 - N_\infty}{N_\infty} e^{-\sigma_{des} Fluence}], \tag{8.2}$$

or, alternatively,

$$N = N_{max}[1 - e^{-\sigma_{form} Fluence}] \tag{8.3}$$

for the species that are either destroyed or formed during photoprocessing of the CO_2 ice, respectively. These equations are adapted from Loeffler et al. (2005). While N_0 and N_{max} are fixed by the experimental data, N_∞ was a free parameter of the fit. Since CO_3 is readily formed during the first irradiation period and is then subsequently destroyed, Eq. 8.2 was used in that case. Calculated cross sections are shown in Table 8.4. These values should be regarded as apparent initial cross sections [8] for the destruction or formation of every species. The values estimated for CO_2 and CO are more than one order of magnitude higher than those reported in Gerakines et al. (1996) for the same experiment, but the ratio between the two is similar. This is probably due to an overestimation of their photon flux, as suggested in Loeffler et al. (2005). At the same time, the value found for the destruction cross section of CO_2 is on the same order as the one reported in Loeffler et al. (2005) for the destruction of this molecule in a pure CO ice

---

[8] We have used only one destruction or formation cross section $\sigma_{des/form}$ for each species, instead of one for each reaction as in Loeffler et al. (2005). In addition, we have fitted the column densities before equilibrium was reached (the three first values in Table 8.3). For this reason, cross sections in this work should be regarded as apparent and initial cross sections.

Table 8.4. *Initial destruction or formation cross sections of the species during UV irradiation of a pure CO_2 ice analog.*

Species	$\sigma_{des/form}$ (cm^2)^a
CO_2	9.5×10^{-18}
CO	5.71×10^{-18}
CO_3	3.1×10^{-18}
O_2	$1.1 \times 10^{-18\ b}$
O_3	1.0×10^{-17}

[a] Uncertainties of 20-30% are expected due to the uncertainty in the measurement of the column densities in the ice. [b] Upper limit (see text).

irradiation experiment, calculated with a more complex model that includes the simultaneous fit of the CO and CO_2 column densities at high fluences. A deeper study of the reaction rates would require the assigment of a kinetic constant k_i to every reaction in Sect. 8.3.4 and the simultaneous fit of the column densities of the five species, which is beyond the scope of this work.

Reaction scheme

Ultraviolet photons dissociate CO_2 molecules through the reaction

$$CO_2 + h\nu \rightarrow CO + O. \tag{8.4}$$

Carbon monoxide is thus the primary product of photoprocessing of pure CO_2 ice. Its final total abundance after a UV fluence of 2.9 x 10^{18} photons/cm^2 is ~40% of the initial CO_2 column density. This value is four times higher than the one reported in Öberg et al. (2009b) for the photoprocessing of a thinner CO_2 ice and a fluence about four times lower, and it is slightly higher than that found in Gerakines et al. (1996) with a similar fluence but a higher initial column density. In our case, with an initial CO_2 column density of 200.3 ML, 12.6% of the incident photons are absorbed in the ice (for an average VUV-absorption cross section of 0.67 x 10^{-18} cm^{-2}, Cruz-Díaz et al. 2014b), leading to ~0.000125 absorbed photons molecule^{-1} s^{-1}.

O atoms formed by the reaction in Eq. 8.4 can easily react with nearby CO_2 molecules to produce CO_3 as a secondary product,

$$O + CO_2 \rightarrow CO_3. \tag{8.5}$$

However, these molecules can be photodissociated, thus reforming CO_2 and O atoms:

$$CO_3 + h\nu \rightarrow CO_2 + O. \tag{8.6}$$

As the fluence increases, photodissociation dominates formation, and the CO_3 abundance drops to ~1% of the initial CO_2. This value is lower than the one in erakines et al. (1996), but agrees well with the low abundances in more recent works performed in UHV conditions (Öberg et al. 2009b, Bahr & Baragiola 2012).

Alternatively, O atoms can react with the photodissociation products of other CO_2 molecules,

$$O + CO + CO_2 \rightarrow 2CO_2 \tag{8.7}$$

(Bahr & Baragiola 2012)

$$O + O \rightarrow O_2. \tag{8.8}$$

As irradiation proceeds, reactions 8.6 and 8.7 compete with reaction 8.4, decreasing the net CO_2 photodissociation rate to ~10 ML/hr.

In an analogous way, reaction 8.7 competes with CO formation in reaction 8.4. Equilibrium is reached after a UV fluence of 7.2 x 10^{17} photons/cm^2, at this stage the total number of CO molecules remains almost constant. However, after equilibrium is reached, the column density of CO in the ice decreases due to the contribution of photodesorption, which proceeds at a constant rate of ~8 ML/hr. Finally, ~40% of the produced CO has photodesorbed to the gas phase.

The O_2 molecules formed in the ice by reaction 8.8 can either photodissociate,

$$O_2 + h\nu \rightarrow O + O \tag{8.9}$$

(E_{dis} = 5.1eV for gas phase molecules, Okabe 1978), or further react with free O atoms to form O_3,

$$O + O_2 \rightarrow O_3. \tag{8.10}$$

Ozone molecules can be destroyed by the photodissociation reaction,

$$O_3 + h\nu \rightarrow O_2 + O, \tag{8.11}$$

leading to a drop in its column density after about one hour of irradiation. Its final abundance is ~4% of the initial CO_2 column density, which is slightly lower than the value reported in Gerakines et al. (1996).

Photodesorption yields

Photodesorption yields (Y_{pd}) of CO and O_2 reach constant values after ~ 60 minutes of irradiation (see Table 8.5), with Y_{pd} (CO) ~1.2 x 10^{-2} molecules incident photon^{-1}, and Y_{pd} (O_2) ~9.3 x 10^{-4} molecules incident photon^{-1}. The value found in this work for Y_{pd}(CO), measured directly from the quantification of the CO molecules detected by the QMS is about ten times higher than the one reported in Öberg et al. (2009b) for the sum of all the photodesorption products, which was measured indirectly from the loss of ice molecules using reflection absorption infrared spectroscopy (RAIRS). This photodesorption yield is about five times lower than the one reported in Muñoz Caro et al. 2010, Chen et al. 2014 for pure CO ice irradiation experiments. The photodesorption yield of O_2 in this work is ~50% higher than the one reported in Zhen & Linnartz 2014 for VUV irradiation of a pure O_2 ice with broad Lyα light. Photodesorption yield of CO_2 has only been measured for the $^{13}CO_2$ ice irradiation experiments and remains constant with fluence. We have found a value of Y_{pd} ($^{13}CO_2$) ~1.1 x 10^{-4} molecules incident

Table 8.5. *Evolution of the CO and O_2 photodesorption yields during UV irradiation of a pure CO_2 ice analog.*

Irradiation time (min)	Fluence (photons cm^{-2})	Y_{pd} (CO)^a 10^{-2} ($\frac{\text{molecules}}{\text{incident photon}}$)	Y_{pd} (O_2)^a 10^{-4} ($\frac{\text{molecules}}{\text{incident photon}}$)
5	6.0 x 10^{16}	0.3	1.7
30	3.6 x 10^{17}	0.8	6.7
60	7.2 x 10^{17}	1.1	9.2
120	1.4 x 10^{18}	1.3	10.0
240	2.9 x 10^{18}	1.2	8.9

[a] Averaged for each irradiation period. We assume uncertainties of about 30-40%, mostly due to the uncertainty in the ionization cross sections (15% according to Majeed & Strickland 1997) and in the measurement of the UV flux.

photon^{-1}, on the same order of magnitude as the photodesorption yields reported in Fillion et al. (2014) for monochromatic UV irradiation with similar photon energy. Photodesorption yield of ^{13}CO is virtually the same as in the case of ^{12}CO, and we expect a similar behavior for carbon dioxide.

8.4 Astrophysical implications

As mentioned in Chapter 3, Sect. 3.2, CO_2 is, along with CO, one of the most abundant species found in the water-rich ice mantles covering dust grains. Solid CO_2 is consistently detected in a variety of environments. Its average abundance relative to water is ~18% in quiescent molecular clouds where ice mantles are formed (Whittet et al. 2007), and ~17% in high-mass protostellar envelopes (Gerakines et al. 1999). However, this abundance is much higher in circumstellar ices around low-mass protostars (32%, Pontoppidan et al. 2008), suggesting that there is a new formation route to CO_2 that is activated in these regions. Formation of solid CO_2 is not fully understood yet, but a gas-phase pathway is ruled out since models predict CO_2 abundances much lower than observed (Bergin et al. 1995). The two most likely formation pathways are UV photoprocessing of H_2O:CO ices (d'Hendecourt et al. 1986) and cosmic-ray irradiation of pure CO ices (e.g., Jamieson et al. 2006). Approximately two thirds of the observed solid CO_2 is found in a water-rich environment, while one third is detected in a CO environment. Pure and crystalline CO_2 ice, such as the one used in our experimental simulations, is also observed (Escribano et al. 2013). It may be formed by segregation from the water-rich environment or through evaporation of the CO from the CO:CO_2 component (Pontoppidan et al. 2008).

CO_2 ice in space can be energetically processed. In particular, UV photoprocessing in dense cloud interiors is possible thanks to the secondary UV field mentioned in Sect. 8.1. Assuming a flux value of 10^4 photons cm^{-2} s^{-1}, ice mantles experience a fluence of 3.2 x 10^{17} photons cm^{-2} in the expected lifetime of a molecular cloud (Shen et al. 2004). This fluence is similar to that experienced for the pure CO_2 ice after 30 minutes of irradiation in our experiments.

During our experimental simulations, the estimated photon-induced desorption rate of CO_2 was $\sim$1.1 x 10^{-4} molecules per incident VUV photon, which only accounts for the desorption of 3.5 x 10^{13} molecules cm^{-2} during the cloud lifetime. This agrees well with observations, since CO_2 is completely frozen, except in very hot or shocked regions (Bergin et al. 1995, Boonman et al. 2003, Nomura & Millar 2004, Lahuis et al. 2007).

Only 4% of the CO formed from photolysis of CO_2 molecules photodesorbed after a fluence of 3.6 x 10^{17} photons cm^{-2}, although this value increased as irradiation took place in our experiments, up to 75% for a total fluence of 2.88 x 10^{18} photons cm^{-2}. Therefore, we do not expect that CO formed from CO_2 represents a significant contribution to the gas-phase CO observed in molecular clouds. Instead, photodesorption of pure CO ice has been found to be more efficient by a factor of 5 (Muñoz Caro et al. 2010, Chen et al. 2014).

The column density of CO_3 after 30 minutes of irradiation represented only 3.6% of the initial CO_2. Moreover, we did not observe photon-induced or thermal desorption of this species during our experiments. The abundance of CO_3 in the ISM is thus expected to be very low; this species was indeed never observed. Finally, photodesorption of O_2 was very low in our experimental simulations, a rate of 9.3 x 10^{-4} molecules per incident photon was estimated, while photon-induced desorption of O_3 was not observed at all. Therefore, these two species would be more likely observed in warm regions where they can be thermally desorbed from the ice mantles. Molecular oxygen has recently been detected in a warm region of the Orion molecular cloud using Herschel observations (Goldsmith et al. 2011).

8.5 Conclusions

We have revisited the UV photoprocessing of a pure CO_2 ice analog.

IR spectroscopy in transmittance allowed us to monitor the solid sample during irradiation. Three photoproducts were detected: CO, CO_3, and O_3, with final column densities of approximately 40%, 1%, and 4% relative to the initial CO_2 after a total UV fluence of 2.88 x 10^{18} photons cm^{-2}. If we limit UV irradiation to a fluence similar to that experienced by the ice mantles in dense cloud interiors ($\sim$3 x 10^{17} photons cm^{-2} for a flux of 2 x 10^{14} photons cm^{-2} s^{-1} after a cloud lifetime of 10^6 yr, Shen et al. 2004, and references therein), the final column density of CO is slightly lower (32%), while those of CO_3 and O_3 are higher (4% and 6%, respectively). A fourth photoproduct, the homonuclear O_2 with no permanent dipole moment, is IR inactive and could not be detected by the FTIR spectrometer. We have estimated an upper limit to its ice abundance of 38% relative to the initial CO_2 for a fluence of 2.88 x 10^{18} photons cm^{-2}, or 14% after a fluence similar to the above astrophysical scenario.

A chemical network leading to these four photoproducts was presented in Sect. 8.3.4.

We used a calibration method for quadrupole mass spectrometers that allowed us to quantify the photodesorbing molecules detected directly in the gas phase during ice irradiation, leading to an estimation of the fraction of photoproducts in the ice that were photodesorbed. Photodesorption of CO and, to a lesser extent, O_2 and CO_2 was observed in the CO_2 ice irradiation experiment, with photodesorption yields of Y_{pd} (CO) $\sim$1.2 x 10^{-2} molecules incident photon^{-1}, Y_{pd} (O_2) $\sim$9.3 x 10^{-4} molecules incident photon^{-1}, and $\sim$1.1 x 10^{-4} molecules incident photon^{-1}, respectively. Photon-induced desorption took place mainly through the DIET mechanism[9], since the QMS signal produced by CO and O_2 desorbed molecules gradually increases until the maximum column density of CO is reached as a result of the participation of accumulated molecules in the bulk of the ice.

These findings have important implications for the release of ice molecules into the gas phase in cold regions where thermal desorption is inhibited. Certain molecules, like CO_2 in this paper, are efficiently photodissociated and their photodesorption is negligible, while photon-induced desorption of their photoproducts is observed, driven either by the DIET mechanism (as in this work) or by photochemidesorption (see Cruz-Díaz et al. 2015, Martín-Doménech et al. 2016).

The photodesorption yields found in this work are not high enough to represent a significant contribution to the presence of these species in the gas phase of quiescent molecular clouds, since only 4% of the formed CO, and a negligible amount of CO_2 and O_2 have photodesorbed after a UV fluence similar to the one that ice mantles experience during the mean lifetime of these regions. Therefore, the observed gaseous CO in molecular clouds may come from a different origin than CO_2 photolysis, while gaseous CO_2, O_2 , and O_3 are more likely present in warm regions of circumstellar environments where these species can be thermally desorbed. Finally, based on our experimental evidence, CO_3 production may be too low to be observed in the gas phase.

Acknowledgements

This research was financed by the Spanish MINECO under project AYA2011-29375. R.M.D. benefited from a FPI grant from Spanish MINECO. V.J.H. and I.T. acknowledge financial support from Spanish MINECO under project FIS2013-48087-C2-1-P.

References

Acharyya, K., Fuchs, G. W., Fraser, H. J., van Dishoeck, E. F., & Linnartz, H. 2007, A&A, 466, 1005

Agarwal, V. K., Schutte, W. A., Greenberg, J. M., et al. 1985, Origins of Life and evolution of the Biosphere, 16, 21

Allamandola, L. J., Sandford, S. A., & Valero, G. J. 1988, Icarus, 76, 225

Andersson, S., & van Dishoeck, E. F. 2008, A&A, 491, 907

Arasa , C., van Hermet, M. C., van Dishoeck, E. F., & Kroes, G. J. 2013, JPCA, 117, 7064

Bahr, D. A. & Baragiola, R. A. 2012, ApJ, 761, 36

Bergin, E. A., Ciardi, D. R., Lada, C. J., et al. 2001, ApJ, 557, 209

Bergin, E. A., Langer, W. D., & Goldsmith, P. F. 1995, ApJ, 441, 222

Bernstein, M. P., Sandford, S. A., Allamandola, L. J., Chang, S., & Scharberg, M. A. 1995, ApJ, 454, 327

Bernstein, M. P., Dworkin, J. P., Sandford, S. A., Cooper, G. W., & Allamandola, L. J. 2002, Nature, 416, 401

Bertin, M., Fayolle, E. C., Romanzin, C., et al. 2012, PCCP, 14, 9929

Bertin, M., Fayolle, E. C., Romanzin, C., et al. 2012, ApJ, 779, 120

---

[9] Or at least through a mechanism in two steps involving energy transfer to the previously photoproduced molecules (see Chapter 7).

Boonman, A. M. S., van Dishoeck, E. F., Lahuis, F., & Doty, S. D. 2003, A&A, 399, 1063

Briggs, R., Ertem, G., Ferris, J. P., et al. 1992, Origins of Life and evolution of the Biosphere, 22, 287

Cecchi-Pestellini, C. & Aiello, S. 1992, MNRAS, 258, 125

Chen, Y.-J., Chu, C.-C, Lin, Y.-C. et al. 2010, Advances in Geosciences, 25, 259

Chen, Y.-J., Chuang, K.-J, Muñoz Caro, G. M., et al. 2014, ApJ, 781, 15

Chen, Y.-J., Chuang, K.-J, Muñoz Caro, G. M., et al. in preparation

Cruz-Díaz, G. A., Martín-Doménech, R., Muñoz Caro, G. M., & Chen, Y.-J. 2016, A&A, 592, A68

Cruz-Díaz, G. A., Muñoz Caro, G. M., Chen, Y.-J., & Yih, T.-S. 2014a, A&A, 562, A119

Cruz-Díaz, G. A., Muñoz Caro, G. M., Chen, Y.-J., & Yih, T.-S. 2014b, A&A, 562, A120

d'Hendecourt, L. B.,& Allamandola, L. J. 1986, A&AS, 64, 453

d'Hendecourt, L. B., Allamandola, L. J., Grim, R. J. A., & Greenberg, J. M. 1986, A&A, 158, 119

Escribano, R. M., Muñoz Caro, G. M., Cruz-Díaz, G. A.,, Rodríguez-Lazcano, Y., & Maté, B. 2013, PNAS, 110, A32

Fayolle, E. C., Bertin, M., Romanzin, C., et al. 2011, ApJL, 739, L36

Fayolle, E. C., Bertin, M., Romanzin, C., et al. 2013, A&A, 556, A122

Fillion, J.-H., Fayolle, E., Michaut, X., et al. 2014, Faraday Discuss., 168, 533

Gerakines, P. A., Schutte, W. A., Greenberg, J. M., & van Dishoeck, E. F. 1995, A&A, 296, 810

Gerakines, P. A., Schutte, W. A., & Ehrenfreund, P. 1996, A&A, 312, 289

Gerakines, P. A., Whittet, D. C. B., Ehrenfreund, P. A., et al. 1999, ApJ, 522, 357

Gerakines, P. A., Moore, M. H., & Hudson, R.L. 2001, J. Geophys. Res. -Planets, 106 (E12), 33381

Gerakines, P. A., Moore, M. H., & Hudson, R.L. 2004, Icarus, 170, 202

Goldsmith, P. F., Liseau, R., Bell, T. A., et al. 2011, ApJ, 737, A96

Gredel, R., Lepp, S., Dalgarno, A., & Herbst, E. 1989, ApJ, 347, 289

Herbst, E., & van Dishoeck, E. F. 2009, Annu. Rev. Astron. Astrophys., 47, 427

van Hemert, M. C., Takahashi, J., & van Dishoeck, E. F. 2015, A&A, in preparation

Jamieson, C. S., Mebel, A. M., & Kaiser, R. I. 2006, ApJS, 163, 184

Jiang, G. J., Person, W. B., & Brown, K. G. 1975, J. Chem. Phys., 62, 1201

de Laeter, J. R., Böhlke. J. R., De Bievre, P., et al. 2003, Pure and Applied Chemistry, 75, 685

Lahuis, F., van Dishoeck, E. F., Blake, G. A., et al. 2007, ApJ, 665, 492

Loeffler, M. J., Baratta, G. A., Palumbo, M. E., Strazzulla, G., & Baragiola, R. A. 2005, A&A, 435, 587

Majeed, T. & Strickland, D. J. 1997, J. Phys. Chem. Ref. Data, 26, 2, 335

Martín-Doménech, R., Muñoz Caro, G. M., Bueno, J., & Goesmann, F. A&A, 2014, 564, A8

Martín-Doménech, R., Muñoz Caro, G. M., & Cruz-Díaz, G.A. A&A, 2016, 589, A107

Meierhenrich, U. J., Muñoz Caro, G. M., Schutte, W. A., et al. 2005, Chem. Eur. J., 11, 4895

Moore, M. H., Hudson, R. L., & Gerakines, P. A. 2001, Spectrochimica Acta Part A, 57, 843

Mumma, M. J., & Charnley, S.B., 2011, Annu. Rev. Astron. Astrophys., 49, 471

Muñoz Caro, G. M., Meierhenrich, U. J., Schutte, W. A., et al. 2002, Nature, 416, 403

Muñoz Caro, G. M., Meierhenrich, U. J., Schutte, W. A., Thiemann, W. H. P., & Greenberg, J. M. 2004, A&A, 413, 209
Muñoz Caro, G. M., Ruiterkamp, R., Schutte, W. A., Greenberg, J. M., & Mennella, V. 2001, A&A, 367, 347
Muñoz Caro, G. M., & Schutte, W. A. 2003, A&A, 412, 121
Muñoz Caro, G. M., & Dartois, E. 2009, A&A, 494, 109
Muñoz Caro, G. M., Jiménez-Escobar, A., Martín-Gago, J.Á. et al. 2010, A&A, 522, A108
Nomura, H., & Millar, T. J. 2004, A&A, 414, 909
Nuevo, M., Meierhenrich, U. J., Muñoz Caro, G. M., et al. 2006, A&A, 457, 741
Öberg, K. I., Fuchs, G. W., Awad, Z., et al. 2007, ApJ, 662, L23
Öberg, K. I., Garrod, R. T., van Dishoeck, E. F., & Linnartz, H. 2009a, A&A, 504, 891
Öberg, K. I., van Dishoeck, E. F., & Linnartz, H. 2009b, A&A, 496, 281
Öberg, K. I., van Dishoeck, E. F., Linnartz, H., & Andersson, S. 2010, ApJ, 718, 832
Okabe, H. 1978. Photochemistry of small molecules, ed. John Wiley & Sons, New York.
Pontoppidan, K. M., Boogert, A. C. A., Fraser, H. J., et al. 2008, ApJ, 678, 1005
Rakhovskaia, O., Wiethoff, P., & Feulner, P. 1995, NIM B, 101, 169
Rejoub, R., Lindsay, B. G., & Stebbings, R. F. 2002, Phys. Rev. A, 65, 042713
Sandford, S. A. & Allamandola, L. J. 1990, ApJ, 355, 357
Shen, C. J., Greenberg, J. M., Schutte, W. A., & van Dishoeck, E. F. 2004, A&A, 415, 203
Smith, M. A. H., Rinsland, C. P., Fridovich, B., & Rao, K. N. 1985, in Molecular Spectroscopy-Modern research, Vol. III, ed. K.N.Rao (Academic Press, London), 111
Tanarro, I., Herrero, V. J., Islyaikin, A. M., et al. 2007, J. Phys. Chem. A, 111, 9003
Westley, M. S., Baragiola, R. A., Johnson, R. E., & Baratta, G. A. 1995, Nature, 373, 405
Willacy, K., & Langer, W. D. 2000, ApJ, 544, 903
Whittet, D. C. B., Shenoy, S. S., Bergin, E. A., et al. 2007, ApJ, 655, 332
Yamada, H., & Person, W. B. 1964, J. Chem. Phys., 41, 2478
Yuan, C. & Yates, Jr., J. T. 2013, J. Chem. Phys., 138, 154303
Yuan, C. & Yates, Jr., J. T. 2014, ApJ, 780, 8
Zhen, J., & Linnartz, H. 2014, MNRAS, 437, 3190

Chapter 9

UV photoprocessing of C_2H_5OH ice

Adapted from *Study of the photon-induced formation and subsequent desorption of CH_3OH and H_2CO in interstellar ice analogs*, Martín-Doménech, R., Muñoz Caro, G.M., & Cruz-Díaz, G.A. 2016, 589, A107 [1]

Abstract

Methanol and formaldehyde are two simple organic molecules that are ubiquitously detected in the interstellar medium, in both the solid and gaseous phases. An origin in the solid phase and a subsequent nonthermal desorption into the gas phase is often invoked to explain their abundances in some of the environments where they are found. Experimental simulations under astrophysically relevant conditions have been carried out in the past four decades in order to find a suitable mechanism for that process. In particular, photodesorption from pure methanol ice (and presumably from pure formaldehyde ice) has been found to be negligible in previous works [2], probably because both molecules are very readily dissociated by vacuum-UV photons.

In Chapters 9 and 10 we explore the *in situ* formation and subsequent photon-induced desorption of these species, studying the UV photoprocessing of pure ethanol ice (Chapter 9), and a more realistic binary H_2O:CH_4 ice analog (Chapter 10).

Experimental simulations were performed in an ultra-high vacuum chamber. Pure ethanol ice samples deposited onto an infrared transparent window at 8 K were UV-irradiated using a microwave-discharged hydrogen flow lamp. Evidence of photochemical production of these two species and subsequent UV-photon-induced desorption into the gas phase were searched for by means of a Fourier transform infrared spectrometer and a quadrupole mass spectrometer, respectively. After irradiation, ice samples were warmed up to room temperature until complete sublimation was attained for detection of volatile products.

Photochemical production of H_2CO was observed during photoprocessing of a pure C_2H_5OH ice. Formation of formaldehyde accounted for $\leq$45% conversion of the initial ethanol ice. Photochemidesorption of formaldehyde, i.e., photon-induced formation on the ice surface and inmediate desorption, was observed with a yield of $\sim$6 x 10^{-5} ($\frac{\text{molecules}}{\text{incident photon}}$).

Photoprocessing of the ice samples lead to formation of other species. Some of them were also found to desorb upon UV irradiation.

9.1 Introduction

More than 180 molecules have been detected to date in the interstellar medium (ISM). Simple organic molecules (hydrogenated species with just one carbon atom and another heavy element) are proposed as precursors of more complex organic species with prebiotic interest.

---

[1] This paper has been splitted in Chapters 9 and 10. Therefore, some parts of the Abstract, Introduction, Experimental, and Astrophysical implications sections are common to both chapters. The information on the photodesorption processes present in the Introduction of the published version of the paper has been moved to Chapter 7.

[2] Bertin et al. (2016, and 2017 *in prep.*) have found a photodesorption yield for methanol and formaldehyde on the order of 10^{-5} - 10^{-4} ($\frac{\text{molecules}}{\text{incident photon}}$) from a pure CH_3OH and H_2CO ice, respectively.

Two of the most studied simple organic molecules are CH_3OH and H_2CO. These species are found in a variety of interstellar environments, such as molecular clouds and hot cores, and in comets inside our solar system, with abundances relative to H_2 ranging from 10^{-6} to 10^{-9} (see, e.g., Sutton et al. 1995, Wootten et al. 1996, Ceccarelli et al. 2000, Ehrenfreund et al. 2002, Maret et al. 2004, Smith et al. 2004, Young et al. 2004, Araya et al. 2007, Leurini et al. 2010, Bergman et al. 2011, Guzmán et al. 2011, 2013).

The origin of CH_3OH and H_2CO is, however, not yet fully understood. Pure gas-phase chemical models cannot always reproduce their observed abundances (Garrod et al. 2006, Geppert et al. 2006, Guzmán et al. 2011, Guzmán et al. 2013), and solid-phase chemistry, either on the surface of dust grains or in the ice mantles that accrete on top of them, must therefore play a role in their formation.

Methanol is present in the solid and gaseous phases of the ISM. Solid CH_3OH has been detected in interstellar ice in dense cores with an abundance of 5 % - 12 % relative to water (Boogert et al. 2011) and also in the cold envelopes around high and low-mass protostars with abundances ranging from 1% up to 30% relative to water (Dartois et al. 1999, Gibb et al. 2000, Gibb et al. 2004, Boogert et al. 2008,Pontoppidan et al. 2008, Bottinelli et al. 2010). Its abundance in solar system comets is lower (0.2 % - 7 %, Mumma & Charnley 2011, and references therein).

Gas-phase CH_3OH has been detected in dense cores and photodissociation - dominated regions (PDRs) with a typical abundance of $\sim10^{-9}$ relative to H_2 (e.g., Bergman et al. 2011, Guzmán et al. 2011, 2013). This abundance is usually higher in hot cores ($\sim10^{-7}$, Öberg et al. 2014, and references therein). In dense cores and PDRs where thermal desorption is inhibited, gas-phase models fail to reproduce the abundance of CH_3OH. Therefore, formation of this species in the solid phase and subsequently non-thermal desorption into the gas phase needs to be invoked (Guzmán et al. 2011, 2013, and references therein).

It has been proposed that CH_3OH is formed by successive addition of H atoms to CO molecules on the surface of dust grains (Tielens & Whittet 1997, Watanabe & Kouchi 2002, Fuchs et al. 2009) or, alternatively, in the bulk of water-rich ices (e.g., Watanabe et al. 2003). However, Hiraoka et al. (2002, 2005) have claimed that this formation pathway cannot be the major source of methanol in the ISM, since the reaction rates are too slow. Watanabe et al. (2007) acknowledge that the contribution of photolysis mechanisms (see below) could not be negligible in molecular clouds. Therefore, energetic processing of CO molecules in a water-ice matrix without directly involving any addition of H atoms has been proposed as an alternative source of CH_3OH. For example, photolysis of H_2O:CO ice analogs (Schutte et al. 1996), proton bombardment of H_2O:CO ices (Hudson & Moore 1999), or electron irradiation of H_2O:CO:H_2O layered ices (Yamamoto et al. 2004). Equivalent formation pathways using H_2O:CH_4 ice analogs have also been proposed for the proton bombardment (Moore & Hudson 1998) and the electron irradiation mechanisms (Wada et al. 2006), suggesting that the contribution of this mechanism for the formation of methanol was at least comparable to the H atom grain surface reactions. In Chapter 10 we have explored the photolysis of H_2O:CH_4 ice analogs. Madzunkov et al. (2010) propose a completely different formation route by collision of superthermal O atoms with CH_4 molecules in a methane ice with an overcoat of CO molecules.

No UV-photon-induced desorption of CH_3OH was observed in Cruz-Díaz et al. (2016) during irradiation of a pure methanol ice, in contrast to what was previously reported in Öberg et al. (2009) [3]. The low CH_3OH photodesorption of $\leq 1.8 \times 10^{-4}$ molecules per incident photon found in UV irradiation experiments of pure methanol ices, probably due to the likely dissociation of CH_3OH molecules upon vacuum-UV-photon absorption, cannot account for the abundances of gas-phase methanol in cold regions, and formation followed by subsequent nonthermal desorption pathways must therefore be explored as an alternative.

Formaldehyde has also been detected in both solid and gaseous phases. Solid H_2CO has not been detected yet in dense cores (Mumma & Charnley 2011), but it is present with an abundance of 1 % - 6 % relative to water in the cold envelopes around high- and low-mass protostars (Keane et al. 2001, Maret et al. 2004, Dartois 2005, Boogert et al. 2008), while its abundance is a little lower in solar system comets (0.1 - 1 %, Mumma & Charnley 2011, and references therein).

Gas-phase H_2CO is also detected in dense cores and PDRs with a similar abundance to that of methanol (see, e.g., Guzmán et al. 2011, Guzmán et al. 2013) and in hot cores, probably after thermal evaporation of ice mantles (e.g., Wootten et al. 1996, Ceccarelli et al. 2000, Maret et al. 2004, Young et al. 2004, Araya et al. 2007). Although pure gas-phase models have been able to reproduce the abundance of H_2CO in dense cores, formation of this species on dust grains and subsequent (nonthermal) desorption is still needed to account for its abundance in low UV-field, illuminated PDRs (for example, the Horsehead PDR, see Guzmán et al. 2011, Guzmán et al. 2013, and references therein).

Most of the solid-phase formation pathways proposed for H_2CO are shared with CH_3OH, since the former is usually an intermediate product in the formation of the latter. Formaldehyde can thus be produced by successive addition of H atoms to CO molecules (Tielens & Hagen1982, Hiraoka et al. 1994, Watanabe & Kouchi 2002, Fuchs et al. 2009). Madzunkov et al. (2009) report a similar formation route of H_2CO by collision of superthermal H atoms with CO molecules on a gold surface. Alternatively, photolysis (Schutte et al. 1996), proton bombardment (Hudson & Moore 1999), and electron irradiation (Yamamoto et al. 2004) of H_2O:CO ice analogs have reported the formation of H_2CO as an intermediate product in the formation of methanol. Moore & Hudson (1998) and Wada et al. (2006) studied the proton bombardment and electron irradiation of H_2O:CH_4 ice analogs, respectively. Photolysis of these binary ice samples is studied in Chapter 10, as mentioned above. Formaldehyde can also be produced from UV or soft X-ray irradiation of pure methanol ices (Öberg et al. 2009, Ciaravella et al. 2010, respectively). Collision of superthermal O atoms with CH_4 molecules also leads to the formation of H_2CO according to Madzunkov et al. (2010).

Nonthermal desorption from pure formaldehyde ices has not yet been reported [4], but a behavior similar to that of pure methanol irradiation can be expected. Nonthermal desorption of molecules in cold regions can be induced by UV photons, cosmic rays, or exothermic chemical reactions (products formed in the surface of dust grains

---

[3] Bertin et al. (2016) reported a photodesorption yield for methanol on the order of 10^{-5} ($\frac{\text{molecules}}{\text{incident photon}}$) from a pure CH_3OH ice.

[4] Bertin et al. (2017, *in prep.*)

Table 9.1. *IR feature used to calculate the column density of selected ice components. Frequencies and band strengths for pure ices at 10 K, except for C_2H_5OH (see text).*

Molecule	Frequency (cm^{-1})	Band strength (cm $molec^{-1}$)
C_2H_5OH	1044	7.3×10^{-18} [a]
CH_3OH	1025	1.8×10^{-17} [b]
H_2CO	1720	9.6×10^{-18} [c]

[a] From Moore & Hudson 1998. [b] From d'Hendecourt & Allamandola 1986. [c] From Schutte et al. 1996.

can immediately desorb due to the exothermicity of the reaction, Garrod et al. 2007, Hocuk & Cazaux 2015). A summary of the current knowledge on the photodesorption processes can be found in Chapter 7.

In the present work we have explored new UV-induced-formation pathways and subsequent desorption for CH_3OH and H_2CO. On one hand, we have followed a top-down approach, studying the UV photodissociation of a pure ethanol ice (solid C_2H_5OH has been proposed as one of the possible carriers of the 7.24 μm ice band, Schutte et al. 1999, Öberg et al. 2011). A bottom-up approach is represented by a more realistic binary H_2O:CH_4 ice analog, following the experiments already mentioned in this section, and is studied in Chapter 10.

This Chapter is organized as follows. Section 9.2 describes the experimental simulations performed. The results are presented in Sect. 9.3 . The astrophysical implications are elucidated in Sect. 9.4, and the conclusions for the two series of experiments are summarized in Chapter 10, Sect. 10.5.

9.2 Experimental setup

The experimental simulations have been performed using the InterStellar Astrochemistry Chamber (ISAC) at the Centro de Astrobiología (see Muñoz Caro et al. 2010 and Chapter 4, Sect. 4.1.1). The ISAC setup consists in an ultra-high-vacuum (UHV) chamber with a base pressure of about 4 x 10^{-11} mbar, similar to what is found in dense cloud interiors.

Pure ethanol ices were grown by deposition of C_2H_5OH vapor onto a diamond window at 8 K, achieved by means of a closed-cycle helium cryostat. At this temperature, ices are deposited as amorphous solids. We used C_2H_5OH (liquid, 99.9%) in this series of experiments.

Ice samples were UV-irradiated using an F-type microwave-discharged hydrogen flow lamp (MDHL) from Opthos Instruments with a VUV-flux of $\approx 2 \times 10^{14}$ photons cm^{-2} s^{-1} at the sample position, measured by $CO_2 \rightarrow CO$ actinometry (Muñoz Caro et al. 2010). The spectrum of the MDHL is similar to the secondary UV field of dense cloud interiors calculated by Gredel et al. (1989) and also to the diffuse interstellar UV field (Jenniskens et al. 1993, Muñoz Caro & Schutte 2003), as well as to the far-UV field of emission/reflection nebulae (France et al. 2005). It has been characterized previously by Chen et al. (2010, 2014). More information can be found in Chapter 4, Sect. 4.1.3.

The ice samples were monitored by in situ Fourier-transform infrared (FTIR) trans-

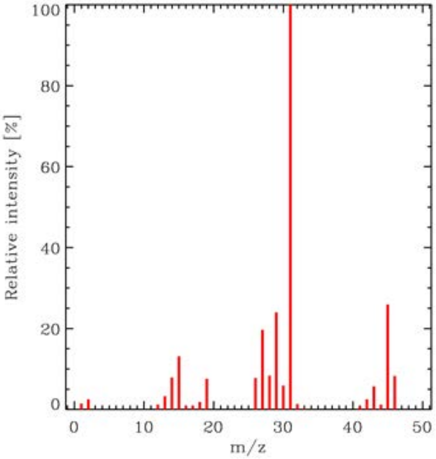

Figure 9.1. *Mass spectrum of ethanol in our setup.*

mittance spectroscopy after deposition and after every irradiation period, using a Bruker Vertex 70 spectrometer equipped with a deuterated triglycine sulfate detector (DTGS). The IR spectra were collected with a spectral resolution of 2 - 4 cm^{-1} (most spectra were subsequently smoothed). Column densities of selected species in the ice were calculated from the IR spectra using the formula

$$N = \frac{1}{A} \int_{band} \tau_\nu \, d\nu, \tag{9.1}$$

where N is the column density in molecules cm^{-2}, τ_ν the optical depth of the absorption band, a nd A the band strength in cm molecule^{-1}, as derived from laboratory experiments (Table 9.1). Band strengths in Table 11.1 were measured for pure amorphous ices, except for ethanol. The same values are usually adopted in ice mixtures, which introduces an uncertainty of about 20-30% (d'Hendecourt & Allamandola 1986). In the case of ethanol, the band strength in Table 9.1 was measured in a mixture with amorphous water ice at T <20 K (Moore & Hudson 1998). Using this value in a pure amorphous ethanol ice introduces a similar uncertainty than that mentioned above.

A Pfeiffer Prisma quadrupole mass spectrometer (QMS) of a mass spectral range from 1 to 200 amu with a Channeltron detector was used to detect molecules in the gas phase. The QMS ionizes gas-phase molecules with $\sim$ 70 eV electron bombardment, leading to fragmentation of the molecules with a given pattern. The species potentially desorbing into the phase were preferably monitored through their main mass fragment, which does not always coincide with the molecular ion. In some cases the main mass fragment of a given species was common to a mass fragment of another species (see, for example, Figs. 9.1 and 9.2 for the mass spectrum of ethanol and methanol, respectively, in our setup). When possible, alternative mass fragments were used in those cases (see Table 10.2).

Table 9.2. *Mass fragments used to monitor potentially desorbing species into the gas phase.*

Molecule	Molecular ion	Main mass fragment	Mass fragment used	Notes
C_2H_5OH	45	31	45	m/z=31 was common to CH_3OH
H_2O	18	18	18	
CH_4	16	16	15	m/z=16 was common to H_2O Contribution from CH_3OH molecules was negligible
CH_3OH	32	31	31	CH_3OH could not be unambiguously detected in the gas phase during C_2H_5OH irradiation (see text)
H_2CO	30	29	29	m/z=30 was also used (see text)
CH_3CHO	44	29	43	m/z=29 was common to H_2CO m/z=44 was common to CO_2 CH_3CHO was not detected in the gas phase during irradiation
C_2H_6	30	28	27	m/z=28 was common to CO m/z=30 was common to H_2CO
CO	28	28	28	Contribution from other species was negligible
CO_2	44	44	44	CO_2 was not detected in the gas phase during irradiation

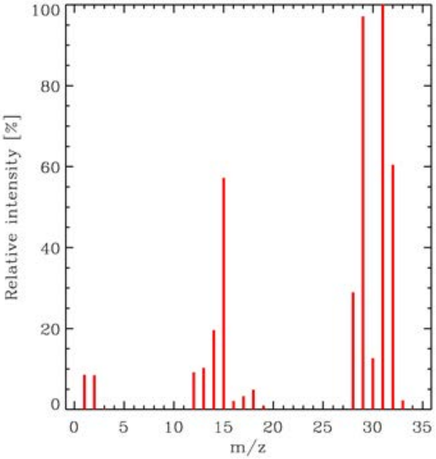

Figure 9.2. *Mass spectrum of methanol in our setup.*

The targeted molecules of this work were CH_3OH and H_2CO. The mass fragment m/z=31 was common to the main mass fragments of the ethanol and methanol molecules. The rest of methanol mass fragments with a reasonable abundance, according to Fig. 9.2 (m/z=29, m/z=32, m/z=15, m/z=28, and m/z=30), were also common to H_2CO, O_2, CH_4, CO, and H_2CO molecules, respectively. Therefore, CH_3OH could not be unambiguously detected in the gas phase in this series of experiments.

The main mass fragment of H_2CO is m/z=29, which was common to ethanol, methanol, and ethane (see below). Ethanol molecules could contribute with up to a 20% of the total m/z=29 signal, according to the mass spectrum of this molecule in Fig. 9.2, since the level of the m/z=31 signal (likely coming from ethanol, as explained below) was found to be comparable to the m/z=29 mass fragment. Contribution from methanol molecules was not likely, since the behavior of the m/z=31 signal follows that of the m/z=45 signal, and it was therefore coming from ethanol molecules. However, contribution from ethane molecules could not be completely discarded, although the second most abundant fragment (m/z=30) was used to double-check the detection formaldehyde molecules in the gas phase.

Calibration of our QMS allows conversion from integrated ion currents into photon-induced desorbed column densities, using the equation

$$N(mol) = \frac{A(m/z)}{k_{CO}} \cdot \frac{\sigma^+(CO)}{\sigma^+(mol)} \cdot \frac{I_F(CO^+)}{I_F(z)} \cdot \frac{F_F(28)}{F_F(m)} \cdot \frac{S(28)}{S(m/z)}, \tag{9.2}$$

where $N(mol)$ is the total number of photon-induced desorbed molecules cm^{-2}, $A(m/z)$ the integrated area below the QMS signal of a given mass fragment m/z during photon-induced desorption, k_{CO} is the proportionality constant between the integrated ion current and the column density of desorbed molecules in the case of a pure CO ice, as shown by

$$k_{CO} = \frac{A(28)}{N(CO)} = k_{QMS} \cdot \sigma^+(CO) \cdot I_F(CO^+) \cdot F_F(28) \cdot S(28), \tag{9.3}$$

with k_{QMS} the proportionality constant independent of the species. The constant k_{CO} is regularly calculated with pure CO ice irradiation experiments. Parameter $\sigma^+(mol)$ is the ionization cross section for the first ionization of the species of interest and the incident electron energy of the mass spectrometer; $I_F(z)$ is the ionization factor, that is, the fraction of ionized molecules with charge z; $F_F(m)$ the fragmentation factor, that is, the fraction of molecules of the isotopolog of interest leading to a fragment of mass m in the mass spectrometer; and $S(m/z)$ the sensitivity of the QMS to the mass fragment (m/z). In practice, we work with the product $k^*_{QMS} \cdot S(m/z)$ (k^*_{QMS} indicates that pressure units are used instead of column density units), since the ratio $S(m/z)/S(28)$ is the same as the ratio $k^*_{QMS} \cdot S(m/z)/k^*_{QMS} \cdot S(28)$. Sensitivity of the QMS is also probed regularly, using noble gases. Calibration of the QMS is detailed in Martín-Doménech et al. (2015) and Chapter 4, Sect. 4.1.5.

Equations 10.2 and 10.3 assume that the pumping speed in the ISAC setup is the same for all molecules, so that k_{QMS} does not depend on the species (see Martín-Doménech et al. 2015). In fact, the pumping speed depends on the molecular mass and, to a lesser extent, on the molecular structure (Kaiser et al. 1995). Constant k_{QMS} in equation 10.3 thus corresponds to the pumping speed of CO molecules. Therefore, $N(mol)$ calculated with equation 10.2 is only valid if the pumping speed of a specific species is the same as for CO. Taking the different pumping speeds into account, the real number of photon-induced desorbed molecules would be

$$N^{real}(mol) = N^{calc}(mol) \cdot S_{rel}(mol), \tag{9.4}$$

with $N^{calc}(mol)$ the column density calculated with eq. 10.2, and $S_{rel}(mol)$ the relative pumping speed with respect to the CO molecules. According to the manufacturer of the pumping devices used in the ISAC setup, the relative pumping speed with respect to CO of a species with molecular mass $M(mol)$ is

$$S_{rel}(mol) = 1.258 - 9.2 \cdot 10^{-3} \cdot M(mol). \tag{9.5}$$

Photon-induced desorption yields can be subsequently calculated by dividing $N^{real}(mol)$ by the fluence (the product of the VUV-flux and the irradiation time).

A small rise in the signal of several mass fragments was detected every time the UV lamp was switched on. This effect has been previously reported in other works(see, e.g., Loeffler et al. 2005), but it was not reproducible and difficult to quantify. When comparable to the rise produced by photon-induced desorption of molecules from the ice during the first series of experiments, calculated desorption yields were considered upper limits.

At the end of the experimental simulations, ice samples were warmed up to room temperature using a LakeShore Model 331 temperature controller, until a complete sublimation was attained. A silicon diode temperature sensor located close to the ice substrate was used, reaching a sensitivity of about 0.1 K. The IR spectra of the solid sample were collected every five minutes during warm-up. At the same time, all the desorbing species, including the components of the ice analogs and the products of the photochemical reactions, were detected by the QMS mentioned above.

Table 9.3. *UV photoprocessing experiments of pure C_2H_5OH ices.*

Experiment	$N_{initial}(C_2H_5OH)$ $\times 10^{15}$molecules cm^{-2}	Fluence $\times 10^{17}$photons cm^{-2}	$N_{final}(C_2H_5OH)$ $\times 10^{15}$molecules cm^{-2}	$N_{final}(CH_3OH)$	$N_{final}(H_2CO)^a$
1	204.7	7.2	39.8	0.0	$\leq$90.1
2	185.6	7.2	38.3	0.0	$\leq$85.5

[a] This is an upper limit since the H_2CO IR band used is blended with two more bands corresponding to acetaldehyde and water.

9.3 Experimental results and discussion

Table 9.3 presents the two experiments performed involving UV photoprocessing of a pure C_2H_5OH ice. The production of new species due to the energetic processing of the ice samples is studied in Sect. 9.3.1 by means of IR spectroscopy and mass spectrometry (during temperature-programmed desorption (TPD) of the ice sample at the end of the e xperiment). Photon-induced desorption of the photoproducts is studied in Sect. 9.3.2 by means of mass spectrometry.

9.3.1 Photon-induced chemistry of pure C_2H_5OH ice

An IR spectrum of the ice sample was collected after every irradiation interval to monitor the ice composition in the two experiments. Figure 9.3 shows the evolution of the mid-IR spectrum (between 3800 cm^{-1} and 750 cm^{-1}) of the ice sample in experiment 2. Similar results were found during experiment 1.

The IR spectrum of the ice sample is dominated by the C_2H_5OH features between 3600 cm^{-1} and 2650 cm^{-1} (Fig. 9.3a), 1580 cm^{-1} and 1230 cm^{-1} (Fig. 9.3c), and 1120 cm^{-1} and 860 cm^{-1} (Fig. 9.3d). New IR features appearing as the result of the UV photoprocessing of the ice samples were assigned to the formation of photoproducts. These assignments could be subsequently confirmed by monitoring the corresponding mass fragment during the TPD carried out at the end of the experiments. Figure 9.4 shows TPD spectra of selected mass fragments at the end of experiment 2. Results were similar during experiment 1.

The C_2H_5OH column density was best monitored with the IR band peaking at 1048 cm^{-1} shown in Fig. 9.3d. The intensity of this band gradually decreases with continuing irradiation, and ~80% of the initial ethanol was either photodissociated or, to a lesser extent, photodesorbed after a total fluence of 7.2 $\times 10^{17}$photons cm^{-2} in the two experiments (see Table 9.3). A similar behavior is seen for the other C_2H_5OH features in Figs. 9.3a, 9.3c, and 9.3d.

Photodissociation of C_2H_5OH triggered a complex photochemical network whose complete study is beyond the scope of this work.

No evidence of CH_3OH formation was found during irradiation of the ice samples. In particular, the C-O stretching mode of CH_3OH that should appear at ~1016 cm^{-1} in a relatively clean region of the spectrum is not detected in Fig. 9.3d. Formation of CH_3OH in an extent below the sensitivity limit of our FTIR spectrometer is rejected since no desorption peak is detected with the more sensitive QMS for the m/z=31 mass fragment at the desorption temperature of methanol (~145 K according to Martín-Doménech et al. 2014, see Fig. 9.4c).

On the other hand, a new IR band is clearly detected at 1715 cm^{-1} in Fig. 9.3c, due to the C=O stretching mode of a carbonyl group, reaching its maximum intensity after 31 minutes of irradiation. Both H_2CO and CH_3CHO contribute to this band, since desorption peaks at ~121 K and ~116 K were detected for the mass fragments m/z=30 (Fig. 9.4b) and m/z=43 (Fig. 9.4d), respectively, confirming the presence of these species in the processed ice (desorption temperatures of pure H_2CO and CH_3CHO ices are ~112 K and ~105 K, respectively, according to Noble et al. 2012, Öberg et al. 2009). An upper limit to the column density of H_2CO in the ice is shown in Table 9.3. Up to 45% of the initial ethanol was converted into formaldehyde at the end of the experiments.

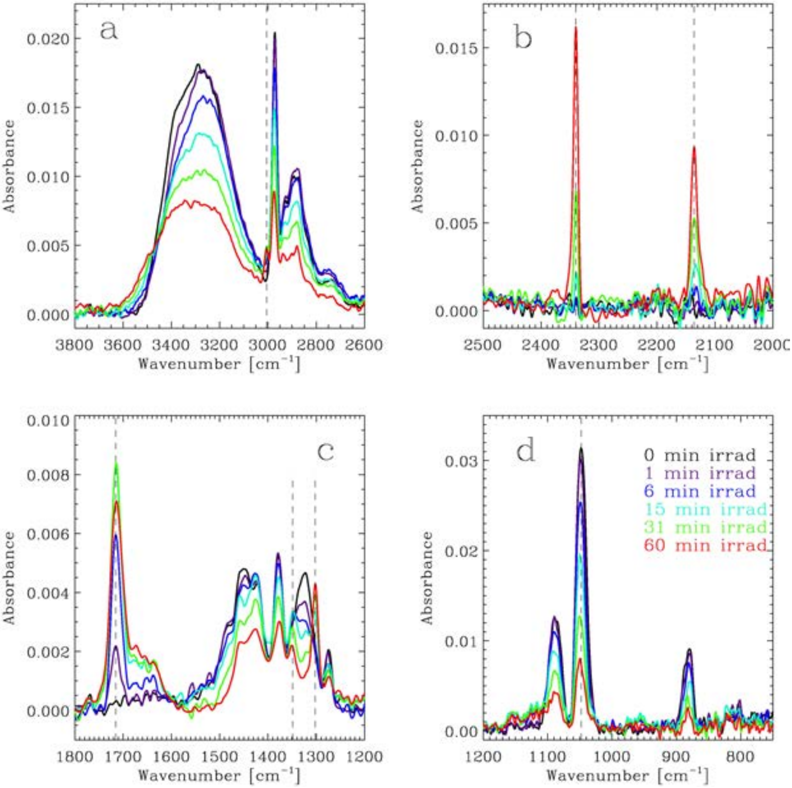

Figure 9.3. *Evolution of the IR spectrum of the ice sample during UV photoprocessing in experiment 2 (see Table 9.3) conveniently split in four regions. Results were similar in experiment 1.* ***a)*** *A new feature appears at 3005 cm^{-1} (dashed line) between the O-H and C-H stretching bands of C_2H_5OH, which is attributed to the formation of CH_4. This species also displays a more intense band near 1302 cm^{-1}, shown in panel c.* ***b)*** *Formation of CO_2 and CO leads to the appearance of two C-O stretching bands at 2340 cm^{-1} and 2136 cm^{-1} (dashed lines), respectively.* ***c)*** *Dashed lines at 1715 cm^{-1}, 1349 cm^{-1}, and 1302 cm^{-1} indicate new features due to the formation of photoproducts (probably H_2CO, CH_3CHO, C_2H_6, and CH_4; see text). A broad band on the red side of the 1715 cm^{-1} peak may indicate the presence of H_2O.* ***d)*** *The intensity of the C-O stretching band of C_2H_5OH at 1048 cm^{-1} (dashed line) decreases as the ice is processed.*

A broad band on the red side of the C=O stretching mode of carbonyl groups is due to blending with the water O-H bending mode. Other four carbon-bearing species were formed during UV photoprocessing of the pure ethanol ice. The C-H stretching and the deformation modes of CH_4 are clearly detected at 3005 cm^{-1} and 1302 cm^{-1} after 15 minutes of irradiation (see Figs. 9.3a and 9.3c, respectively). The deformation mode

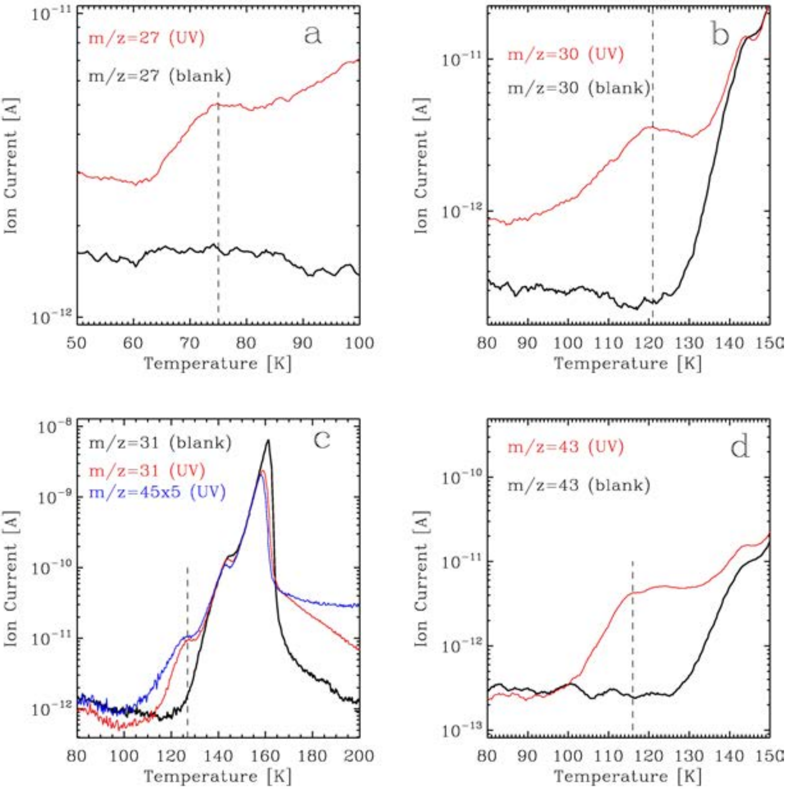

Figure 9.4. *TPD curves displaying the thermal desorption of photoproducts through selected mass fragments at the end of experiment 2 (see Table 9.3) in red, compared to the blank experiment with no irradiation (black).* ***a)*** *TPD curves of the m/z=27 mass fragment, corresponding to the $C_2H_3^+$ fragment of C_2H_6. A desorption peak at ∼75 K (dashed line) confirms the presence of ethane in the processed ethanol ice (desorption of a pure ethane ice takes place above 60 K according to Öberg et al. 2009).* ***b)*** *TPD curves of the m/z=30 mass fragment, corresponding to the molecular ion of H_2CO. The desorption peaking at ∼121 K (dashed line) confirms the formation of formaldehyde during UV photoprocessing of a pure ethanol ice (see text).* ***c)*** *TPD curves of the m/z=31 mass fragment corresponding to the CH_3O^+ fragment of CH_3OH. Since no excess in the desorption is detected at ∼145 K compared to the blank, formation of methanol during UV photoprocessing of a pure ethanol ice is negligible. Desorption at ∼127 K (dashed line) is probably due to an earlier ethanol desorption triggered by less polar and more volatile components in the ice matrix that were not present in the blank experiment (mainly formaldehyde and acetaldehyde), since it is shared with the m/z=45 mass fragment (blue).* ***d)*** *TPD curves of the m/z=43 mass fragment, corresponding to the CH_3CO^+ fragment of CH_3CHO. The desorption peaking at ∼116 K (dashed line) confirms the formation of acetaldehyde during UV photoprocessing of a pure ethanol ice (see text).*

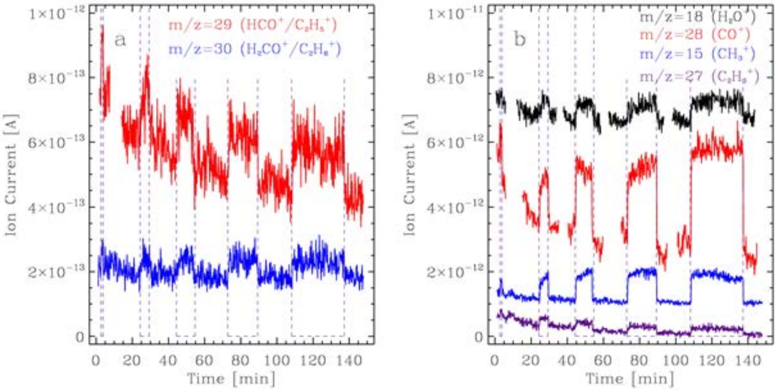

Figure 9.5. *Photon-induced desorption of several photoproducts during irradiation of a pure ethanol ice in experiment 2, see Table 9.3. Results were similar in experiment 1. Irradiation intervals are indicated with vertical dashed lines. Signal due to rotation of the sample holder between irradiation intervals was omitted.* ***a)*** *Phochemidesorption of formaldehyde/ethane (see text) observed with mass fragments m/z=29 and m/z=30.* ***b)*** *Photochemidesorption of ethane observed with mass fragment m/z=27. DIET photodesorption was detected for H_2O, CO and CH_4 (m/z=18, m/z=28 and m/z=15, respectively). Ion currents of different mass fragments are offset for clarity.*

of C_2H_6 is also detected at 1349 cm^{-1} (Fig. 9.3c) after six minutes of irradiation. The presence of ethane in the ice sample was confirmed during the TPD at the end of the experiments (see Fig. 9.4a). Finally, the C-O stretching band of CO is clearly detected at 2136 cm^{-1}, while the C-O stretching band of CO_2 molecules is observed at 2340 cm^{-1} (Fig. 9.3b).

9.3.2 Photon-induced desorption from pure C_2H_5OH ice

A QMS was used during UV photoprocessing of the ice samples to monitor the photon-induced desorption of the photoproducts detected in Sect. 9.3.1 using the mass fragments selected in Sect. 9.2. Results are shown in Fig. 9.5.

Photon-induced desorbing species presented a rise in the QMS ion current of their corresponding mass fragments during irradiation. As mentioned in Sect. 9.2, calibration of the QMS allowed us to obtain desorption yields of the photon-induced desorbing species from the integrated ion currents. Parameters used in Eq. 10.2 for the photoproducts in experiments 1 and 2 are shown in Table 9.4. Proportionality constant k_{CO} was 1.74 x 10^{-10} A min ML^{-1} for both experiments. Photon-induced desorption yields of all photoproducts in pure ethanol ice irradiation experiments (except for CH_3CHO and CO_2, whose desorption, if taking place, was negligible) are presented in Table 9.5 for experiment 2, averaged for each irradiation period. Results were similar in experiment 1.

Evolution of the photodesorption yield with fluence is related to the two main photon-

Table 9.4. *Values used in Eq. 10.2 to convert integrated QMS signals for the mass fragments into column densities of desorbing molecules.*

Factor	H_2CO	C_2H_6	H_2O	CH_4	CO
$\sigma^+(mol)$ ($\AA^2$)[a]	4.140	6.422	2.275	3.524	2.516
fragment	H_2CO^+	$C_2H_6^+$	H_2O^+	CH_3^+	CO^+
m/z	30	30	18	15	28
$I_F(z)$	1[b]	1[b]	1[b]	1[b]	1[b]
$F_F(m)$	0.319[a]	0.121[c]	0.806[c]	0.406[c]	0.949[c]
$k^*_{QMS} \cdot S(m/z)$ (A mbar^{-1} $\AA^{-2}$)[d]	1.77 x 10^{15}	1.77 x 10^{15}	3.86 x 10^{15}	4.69 x 10^{15}	2.02 x 10^{15}
$k^*_{QMS} \cdot S(m/z)$ (A mbar^{-1} $\AA^{-2}$)[e]	9.30 x 10^{14}	9.30 x 10^{14}	1.69 x 10^{15}	1.97 x 10^{15}	1.03 x 10^{15}
$k^*_{QMS} \cdot S(m/z)$ (A mbar^{-1} $\AA^{-2}$)[f]	1.29 x 10^{15}	1.29 x 10^{15}	2.50 x 10^{15}	2.94 x 10^{15}	1.44 x 10^{15}
$S_{rel}(mol)$[g]	0.982	0.982	1.092	1.111	1.000

[a] Extracted from the online database of the National Institute of Standard and Technologies (NIST).

[b] A value of 1 was adopted, assuming that no double ionization of the molecules takes place.

[c] Extracted from the mass spectral library of the QMS software.

[d] Calculated for our QMS and valid for experiments 1, 2, 6, 9, and 10 (see Sect. 9.2).

[e] For experiments 3 and 7 (see Sect. 9.2).

[f] For experiments 4, 5, and 8 (see Sect. 9.2).

[g] Calculated with Eq. 10.4.

Table 9.5. *Evolution of the photon-induced desorption yields during UV irradiation of a pure C_2H_5OH ice.*

Irradiation period (min)	Fluence[a] (photons cm^{-2})	Y_{pd} (H_2CO)^{b,c}	Y_{pd} (C_2H_6)^{b,c}	Y_{pd} (H_2O)^{b,c}	Y_{pd} (CH_4)^{b}	Y_{pd} (CO)^{b}
		(molecules/incident photon)				
0 - 1	1.2 x 10^{16}	$\leq 7.6 \times 10^{-5}$	$\leq 1.3 \times 10^{-4}$	$\leq 1.1 \times 10^{-4}$	1.8×10^{-4}	0.6×10^{-3}
1 - 6	7.2 x 10^{16}	$\leq 5.9 \times 10^{-5}$	$\leq 1.0 \times 10^{-4}$	$\leq 2.0 \times 10^{-4}$	2.3×10^{-4}	0.7×10^{-3}
6 - 15	1.8 x 10^{17}	$\leq 5.5 \times 10^{-5}$	$\leq 1.0 \times 10^{-4}$	$\leq 2.7 \times 10^{-4}$	3.1×10^{-4}	1.0×10^{-3}
15 - 31	3.7 x 10^{17}	$\leq 6.4 \times 10^{-5}$	$\leq 1.1 \times 10^{-4}$	$\leq 2.4 \times 10^{-4}$	3.4×10^{-4}	1.1×10^{-3}
31 - 60	7.2 x 10^{17}	$\leq 5.8 \times 10^{-5}$	$\leq 1.0 \times 10^{-4}$	$\leq 2.7 \times 10^{-4}$	3.2×10^{-4}	1.5×10^{-3}

[a] Total fluence at the end of the irradiation period.

[b] Averaged for each irradiation period in experiment 2. Results were similar in experiment 1. Photon-induced desorption yield values could be different by a factor 2 due to the uncertainties in all the parameters of Eq. 10.2.

[c] We consider these values upper limits due to possible contribution from other species to the signal of the selected mass fragment and/or from the small rise experienced by the ion currents when the UV lamp is switched on (see Sect. 9.2).

induced desorption mechanisms presented in Chapter. 7. Photoproducts that are able to desorb through the process called indirect desorption induced by electronic transitions (DIET) [5] increase their photodesorption yield (or in other words, their QMS ion current during irradiation) with fluence, since molecules previously formed and accumulated in the bulk of the ice are later available for desorption when a photon is absorbed by a nearby molecule [6] (indirect DIET photodesorption is also included) [7].

On the other hand, photochemidesorbing-only species do not increase their photodesorption yield (or ion current) with fluence, since only molecules formed on the surface of the ice are able to desorb right after their formation, and molecules accumulated in the bulk of the ice are not able to desorb later on during irradiation. In the case of molecules able to both photochemidesorb and desorb through the DIET mechanisms, the effect of the former will be negligible compared to the latter since the number of molecules at the surface of the ice is much lower than in the bulk (see also Fillion et al. 2014).

Photon-induced desorption of methanol was discarded since the behavior of the m/z=31 signal follows that of the m/z=45 signal, and it was therefore coming from ethanol molecules.

On the other hand, ion currents of mass fragments m/z=29 and m/z=30 in Fig. 9.5a present rather constant rises during UV irradiation of the ice sample, suggesting photochemidesorption. As explained in Sect. 9.2, either formaldehyde and/or ethane molecules could be responsible for the detected mass fragments, since a similar rise is detected for the ethane mass fragment m/z=27 in Fig. 9.5b. This means that one out of two, or even both species could be photochemidesorbing to the gas phase during irradiation of the pure ethanol ice. Therefore, we used the integrated ion currents of mass fragment m/z=30 and the parameters shown in Table 9.4 for both species to extract upper limits to their photon-induced desorption yields (see Table 9.5). The average photon-induced desorption yield would be of $\sim$6.2 x 10^{-5} molecules/incident photon if the m/z=30 signal was due only to formaldehyde molecules, and of $\sim$1.1 x 10^{-4} molecules/incident photon if only ethane molecules contributed to the signal. These values should be considered upper limits due to the possible contribution from the small rise experienced by the ion current when the UV lamp was switched on during this series of experiments (see Sect. 9.2). In both cases the photon-induced desorption yields remain almost constant with fluence, as expected for photochemidesorbing species.

Figure 9.5b shows the evolution during photoprocessing of a pure ethanol ice for the mass fragments corresponding to other photoproducts detected in Sect. 9.3.1.

Apart from the m/z=27 mass fragment corresponding to ethane molecules commented above, the ion current of mass fragments m/z=15 (CH_3^+), m/z=18 (H_2O^+), and m/z=28 (CO^+) were found to increase from one irradiation interval to the next, indicating that the photoproduced methane, water [8], and carbon monoxide, respectively, are able to desorb through the DIET mechanism [9] during irradiation of a pure ethanol ice.

---

[5] Or through any mechanism in two steps involving energy transfer to the previously photoproduced molecules (see Chapter 7).

[6] and the energy is subsequently transferred to a surface molecule

[7] When the molecule absorbing the photon and the desorbing molecule do not belong to the same species.

[8] There is a misprint in the published version of the paper, where water is claimed to photochemidesorb in the caption of Fig. 9.5.

In the case of CH_4, this behavior is different from the one experienced by the molecules photoproduced in a pure methanol ice, which were able to photochemidesorb but not to desorb through the DIET mechanism (Cruz-Díaz et al. 2016). In pure methane ice, CH_4 molecules are not able to desorb, probably because methane molecules are readily photodissociated by the VUV photons, and they cannot trigger the DIET photodesorption mechanism. Therefore, in the ethanol ice [10], the DIET photodesorption process of methane molecules would be triggered more likely by the absorbtion of the VUV photons by molecules of other species in the subsurface layers of the ice[11]. The different behavior in these two ice irradiation experiments indicates that the energy redistributed to methane molecules in the surface of the ice is enough to break the intermolecular bonds in the case of pure ethanol ice irradiation experiments, but not during irradiation of a pure methanol ice. This may be due to a higher intermolecular binding energy of methane molecules to their neighbors in the methanol ice irradiation experiments or, alternatively, to a higher energy redistributed by the absorbing molecules to the surface in the ethanol ice experiments.

The photodesorption yield of water and methane molecules reached a constant value after approximately 15 minutes of irradiation, of $\leq$2.6 x 10^{-4} molecules/incident photon, and $\sim$3.3 x 10^{-4} molecules/incident photon, respectively (see Table 9.5). The photodesorption yield of CO molecules increased with fluence (Table 9.5) during the full experiment [12].

9.4 Astrophysical implications

In cold dense interstellar and circumstellar regions, molecules form ice mantles upon freeze-out onto cold dust grains. These ice mantles are mainly observed in the near- to far-IR region of the spectrum (Boogert et al. 2015, and ref. therein). As mentioned in Sect. 9.1, C_2H_5OH has been suggested as one of the possible carriers of the 7.24 μm IR band (Schutte et al. 1999). Schriver et al. (2007) derived an upper limit to the abundance of ethanol in interstellar ices of 1.2% relative to water ice from ISO observations. In addition, the presence of solid ethanol is needed to explain gas-phase abundances in dense star-forming regions that cannot be reproduced by pure gas-phase chemical models. Pure ethanol ice samples were used for our first series of experiments (discussed in this Chapter, the second series is discussed in Chapter 10).

Ice mantles can be energetically processed by cosmic rays, UV, and X-ray photons, and also thermally in regions around protostars. Energetic processing of ices leads to several effects, including photon-induced chemistry and photon-induced desorption as studied in this work. Solid-phase chemistry has been widely proposed as a possible source of molecules in the ISM. In some cases, formation in ice mantles followed by nonthermal desorption needs to be invoked to explain the observed abundances of some species in dense cores and low UV-field illuminated PDRs. This is the case of the targeted molecules of this work, CH_3OH and H_2CO (see Sect. 9.1). Photoprocessing in particular takes place in dense cores thanks to the secondary UV field generated by the interaction of H_2 molecules in the gas phase with cosmic rays, leading to a photon flux of $\sim10^4$ photons cm^{-2} s^{-1} (Cecchi-Pestellini & Aiello 1992, Shen et al. 2004). On the other hand, PDRs are illuminated by nearby massive stars with a UV flux of $\sim10^{11}$ eV cm^{-2} s^{-1} for a low UV-field illuminated PDR as for the Horsehead PDR (Pety et al. 2012). In our experiments, we used a MDHL with a photon flux of $\sim2 \times 10^{14}$ photons cm^{-2} s^{-1} and an average photon energy of 8.6 eV (see Chapter 4, Sect. 4.1.3). Therefore, the ice samples in our experimental simulations experience the same total fluence as the ice mantles during the typical lifetime of dense cores ($\sim3 \times 10^{17}$ photons cm^{-2} for a cloud lifetime of 10^6 years) after 30 minutes of irradiation. At the same time, the UV flux experienced by the ice samples in the experiments is about four orders of magnitude higher than that present in low-illuminated PDRs.

---

[9] Or through any mechanism in two steps involving energy transfer to the previously photoproduced molecules (see Chapter 7).

[10] There is a misprint in the published version of the paper where methanol ices are also included in this sentence.

[11] This is called indirect DIET in the published version of the paper.

[12] Note that the intensity of the CO IR feature in Fig. 9.3b also increases during the whole experiment. In Chapter 8, CO photodesorption yield shares the same behavior with N_{CO}.

As mentioned in Sect. 3, gas-phase abundances of CH_3OH in dense cores and PDRs where thermal desorption is inhibited cannot be reproduced by gas-phase chemical models, and solid chemistry followed by nonthermal desorption needs to be invoked.

Methanol formation was not observed during irradiation of a pure ethanol ice sample.

On the other hand, formaldehyde was formed in this series of experiments. Photochemidesorption of this species was detected with a yield of $\leq$6 x 10^{-5} (molecules/incident photon). However, a more accurate value extracted from experimental simulations closer to the astrophysical scenario is provided in Chapter 10.

Acknowledgements

We are grateful to Javier Manzano-Santamaría for his support on the experiments. Special thanks go to Marcelino Agúndez for useful discussions. This research was financed by the Spanish MINECO under project AYA2011-29375. R.M.D. benefited from a FPI grant from Spanish MINECO.

References

Araya, E., Hofner, P., Goss, W. M., et al. 2007, ApJS, 170, 152
Bergman, P., Parise, B., Liseau, R., & Larsson, B. 2011, A&A, 527, 39
Bernstein, M. P., Dworkin, J. P., Sandford, S. A., Cooper, G. W., & Allamandola, L. J. 2002, Nature, 416, 401
Bernstein, M. P., Sandford, S. A., Allamandola, L. J., Chang, S., & Scharberg, M. A. 1995, ApJ, 454, 327
Bertin, M., Fayolle, E. C., Romanzin, C., et al. 2012, PCCP, 14, 9929
Bertin, M., Fayolle, E. C., Romanzin, C., et al. 2012, ApJ, 779, 120
Bertin et al. 2017, *in prep.*
Boogert, A. C. A., Huard, T. L., Cook, A. M., et al. 2011, ApJ, 729, 92
Boogert, A. C. A., Gerakines, P. A., & Whittet, D. C. B. 2015, ARA&A, 53, 541
Boogert, A. C. A., Pontoppidan, K. M., Knez, C., et al. 2008, ApJ, 678, 985
Bottinelli, S., Boogert, A. C. A., Bouwman, J., et al. 2010, ApJ, 718, 1100

Ceccarelli, C., Loinard, L., Castets, A., Tielens, A. G. G. M., & Caux. E. 2000, A&A, 357, L9
Cecchi-Pestellini, C. & Aiello, S. 1992, MNRAS, 258, 125
Charnley, S. B., Tielens, A. G. G. M., & Millar, T. J. 1992, ApJ, 399, L71
Chen, Y.-J., Chu, C.-C, Lin, Y.-C. et al. 2010, Advances in Geosciences, 25, 259
Chen, Y.-J., Chuang, K.-J, Muñoz Caro, G. M., et al. 2014, ApJ, 781, 15
Ciaravella, A., Muñoz Caro, G., Jiménez-Escobar, A. et al. 2010, ApJL, 722, L45
Cruz-Díaz, G. A., Martín-Doménech, R., Muñoz Caro, G. M., & Chen, Y.-J. 2016, A&A, 592, A68
Cruz-Díaz, G. A., Muñoz Caro, G. M., Chen, Y.-J., & Yih, T.-S. 2014a, A&A, 562, A119
Dartois, E. 2005, Space Sci. Rev., 119, 293
Dartois, E., Geballe, T. R., Demyk, K., Ehrenfreund, P., & dHendecourt, L. 1999, A&A, 342, L32
d'Hendecourt, L. B.,& Allamandola, L. J. 1986, A&AS, 64, 453
Ehrenfreund, P., Irvine, W., Becker, L., Blank, J, Brucato, J. R., et al. 2002, Rep. Prog. Phys., 65, 1427
Fayolle, E. C., Bertin, M., Romanzin, C., et al. 2011, ApJL, 739, L36
Fayolle, E. C., Bertin, M., Romanzin, C., et al. 2013, A&A, 556, A122
Fillion, J.-H., Fayolle, E., Michaut, X., et al. 2014, Faraday Discuss., 168, 533
France, K., Andersson, B.-G., McCandliss, S. R., & Feldman, P. D. 2005, ApJ, 682, 750
Fuchs, G. W., Cuppen, H. M., Ioppolo, S., et al. 2009, A&A, 505, 629
Garrod, R. T., Park, I. H., aselli, P., & Herbst, E. 2006, Faraday Discussions, 133, 51
Garrod, R. T., Wakelam, V., & Herbst, E. 2007, A&A, 467, 1103
Garrod, R. T., Weaver, S. L., & Herbst, E. 2008, ApJ, 682, 283
Geppert, W. D., Hamberg, M., Thomas, R. D., et al. 2006, Faraday Discussions, 133, 177
Gerakines, P. A., Moore, M. H., & Hudson, R.L. 2001, J. Geophys. Res. -Planets, 106 (E12), 33381
Gerakines, P. A., Schutte, W. A., Greenberg, J. M., & van Dischoeck, E. F. 1995, A&A, 296, 810
Gibb, E. L., Whittet, D. C. B., Boogert, A. C. A., & Tielens, A. G. G. M. 2004, ApJS, 151, 35
Gibb, E. L., Whittet, D. C. B., Schutte, W. A. 2000, ApJ, 536, 347
Gredel, R., Lepp, S., Dalgarno, A., & Herbst, E. 1989, ApJ, 347, 289
Guzman, V. V., Pety, J., Goicoechea, J. R., Gerin, M., & Roueff, E. 2011, A&A, 534, A49
Guzmán, V. V., Goicoechea, J. R., Pety, J., et al. 2013, A&A, 560, A73
Hagen, W. 1981, Chem. Phys., 56, 367
Hiraoka, K., Ohashi, N., Kihara, Y., et al. 1994, Chemp. Phys. Lett., 229, 408
Herbst, E., & van Dishoeck, E. F. 2009, Annu. Rev. Astron. Astrophys., 47, 427
Hiraoka, K., Sato, T., Sato, S., et al. 2002, ApJ, 577, 265
Hiraoka, K., Wada, A., Hidekazu, K., et al. 2005, ApJ, 620, 542
Hocuk, S., & Cazaux, S. 2015, A&A, 576, A49
Hudson, R. L., Moore, M. H. 1999, Icarus, 140, 451
Jenniskens, P., Baratta, G. A., Kouchi, A., et al. 1993, A&A, 273, 583
Kaiser, R. I., Jansen, P., Petersen, K., & Roessler, K. 1995, Rev. Sci. Instrum. 66, 5226
Keane, J. V., Tielens, A. G. G. M., Boogert, A. C. A. Schutte, W. A., & Whittet, D. C. B. 2001, A&A, 376, 254
Leurini, S., Parise, B., Schilke, P. Pety, J., & Rolffs, R. 2010, A&A, 511, A82

Loeffler, M. J., Baratta, G. A., Palumbo, M. E., Strazzulla, G., & Baragiola, R. A. 2005, A&A, 435, 587

Madzunkov, S. M., MacAskill, J. A., Chutjian, A. et al. 2009, ApJ, 697, 801

Madzunkov, S. M., MacAskill, J. A., Chutjian, A. et al. 2010, ApJ, 712, 194

Maret, S., Ceccarelli, C., Caux, E., et al. 2004, A&A, 416, 577

Martín-Doménech, R., Manzano-Santamaría, J., Muñoz Caro, G. M., et al. 2015, A&A, 584, A14

Martín-Doménech, R., Muñoz Caro, G. M., Bueno, J., & Goesmann, F. 2014, A&A, 564, A8

Moore, M. H., & Hudson, R. L. 1998, Icarus, 135, 518

Mumma, M. J., & Charnley, S.B., 2011, Annu. Rev. Astron. Astrophys., 49, 471

Muñoz Caro, G. M., Jiménez-Escobar, A., Martín-Gago, J.Á. et al. 2010, A&A, 522, A108

Muñoz Caro, G. M., Meierhenrich, U. J., Schutte, W. A., et al. 2002, Nature, 416, 403

Muñoz Caro, G. M., & Schutte, W. A. 2003, A&A, 412, 121

Muñoz Caro, G. M., & Dartois, E. 2009, A&A, 494, 109

Noble, J. A., Theule, P., Mispelaer, F., et al. 2012, A&A, 543, A5

Nuevo, M., Meierhenrich, U. J., Muñoz Caro, G. M., et al. 2006, A&A, 457, 741

Öberg, K. I., Boogert, A. C. A., Pontoppidan K. M., et al. 2011, ApJ, 740, 109

Öberg, K. I., Bottinelli, S., Jørgensen, J. K., & van Dishoeck, E. F. 2010, ApJ, 716, 825

Öberg, K. I., Fayolle, E. C., Reiter, J. B., & Cyganowski, C. 2014, Faraday Discussions, 168, 81

Öberg, K. I., Fuchs, G. W., Zainab, A., et al., 2007, ApJ, 662, L23

Öberg, K. I., Garrod, R. T., van Dishoeck, E. F., & Linnartz. H. 2009, A&A, 504, 891

Pety, J., Gratier, P., Guzmán, V., et al. 2012, A&A, 548, A68

Pontoppidan, K. M., Boogert, A. C. A., Fraser, H. J. et al. 2008, ApJ, 678, 1005

Rakhovskaia, O., Wiethoff, P., & Feulner, P. 1995, NIM B, 101, 169

Schriver, A., Schriver-Mazzuoli, L., Ehrenfreund, P., & d'Hendecourt, L. 2007, Chem. Phys. 334, 128

Schutte, W. A., Boogert, A. C. A., Tielens, A. G. G. M., et al. 1999, A&A, 343, 966

Schutte, W. A., Gerakines, P. A., Geballe, T. R., van Dishoeck, E. F., & Greenberg, J. M. 1996, A&A, 309, 633

Shen, C. J., Greenberg, J. M., Schutte, W. A., & van Dishoeck, E. F. 2004, A&A, 415, 203

Smith, I. W. M., Herbst, E., & Chang, Q. 2004, MNRAS, 350, 323

Sutton, E. C., Peng, R., Danchi, W. C., et al. 1995, ApJS, 97, 455

Tielens, A. G. G. M. & Hagen, W. 1982, A&A, 114, 245

Tielens, A. G. G. M. & Whittet, D. C. B. 1997, in Molecules in Astrophysics: Probe and Processes, ed. E. F. van Dishoeck (Dordrecht: Kluwer), 45

Wada, A., Mochizuki, N., & Hiraoka, K. 2006, ApJ, 644, 300

Watanabe, N. & Kouchi, A. 2002, ApJ, 571, L173

Watanabe, N., Mouri, O., Nagaoka, A., Chigai, T., & Kouchi, A. 2007, ApJ, 668, 1001

Watanabe, N., Shikari, T., & Kouchi, A. 2003, ApJ, 588, L121

Wootten, A., Mangnum, J., & Barsony, M. 1996, BAAS, 28, 105.08

Yamamoto, S., Beniya, A., Mukai, K., Yamashita, Y., & Yoshinobu, J. 2004, Chem. Phys. Lett., 388, 384

Young, K. E., Lee, J., Evans, II, N. J., Goldsmith, P. F., & Doty, S. D. 2004, ApJ, 614, 252

Chapter 10

UV photoprocessing of H_2O:CH_4 ice

Adapted from *Study of the photon-induced formation and subsequent desorption of CH_3OH and H_2CO in interstellar ice analogs*, Martín-Doménech, R., Muñoz Caro, G.M., & Cruz-Díaz, G.A. 2016, 589, A107 [1]

Abstract

Methanol and formaldehyde are two simple organic molecules that are ubiquitously detected in the interstellar medium, in both the solid and gaseous phases. An origin in the solid phase and a subsequent nonthermal desorption into the gas phase is often invoked to explain their abundances in some of the environments where they are found. Experimental simulations under astrophysically relevant conditions have been carried out in the past four decades in order to find a suitable mechanism for that process.

In Chapters 9 and 10 we explore the *in situ* formation and subsequent photon-induced desorption of these species, studying the UV photoprocessing of pure ethanol ice (Chapter 9), and a more realistic binary H_2O:CH_4 (3:1) ice analog (Chapter 10).

Experimental simulations were performed in an ultra-high vacuum chamber. Binary H_2O:CH_4 ice samples deposited onto an infrared transparent window at 8 K were UV-irradiated using a microwave-discharged hydrogen flow lamp. Evidence of photochemical production of these two species and subsequent UV-photon-induced desorption into the gas phase were searched for by means of a Fourier transform infrared spectrometer and a quadrupole mass spectrometer, respectively. After irradiation, ice samples were warmed up to room temperature until complete sublimation was attained for detection of volatile products.

Formation of CH_3OH was observed during photoprocessing of the H_2O:CH_4 ice analog, accounting for $\sim$4% of the initial CH_4 ice column density, but no photon-induced desorption was detected. Photochemical production of H_2CO was also observed, but it could not be quantified. Photochemidesorption of formaldehyde, i.e., photon-induced formation on the ice surface and inmediate desorption, was observed with a yield of $\sim 4.4 \times 10^{-5}$ $(\frac{\text{molecules}}{\text{incident photon}})$. Photoprocessing of the ice analogs lead to formation of other species. Some of them were also found to desorb upon UV irradiation.

While certain C-bearing species, in particular H_2CO, were found to desorb upon irradiation, nonthermal desorption of CH_3OH was not observed. So far, there is no experimental evidence of any efficient CH_3OH desorption induced by UV photons. On the other hand, the observed photon-induced desorption of H_2CO could account for the total formaldehyde abundance observed in the Horsehead PDR.

---

[1] This paper has been splitted in Chapters 9 and 10. Therefore, some parts of the Abstract, Introduction, Experimental, and Astrophysical implications sections are common to both chapters. The information on the photodesorption processes present in the Introduction of the published version of the paper has been moved to Chapter 7.

10.1 Introduction

More than 180 molecules have been detected to date in the interstellar medium (ISM). Simple organic molecules (hydrogenated species with just one carbon atom and another heavy element) are proposed as precursors of more complex organic species with prebiotic interest.

Two of the most studied simple organic molecules are CH_3OH and H_2CO. These species are found in a variety of interstellar environments, such as molecular clouds and hot cores, and in comets inside our solar system, with abundances relative to H_2 ranging from 10^{-6} to 10^{-9} (see, e.g., Sutton et al. 1995, Wootten et al. 1996, Ceccarelli et al. 2000, Ehrenfreund et al. 2002, Maret et al. 2004, Smith et al. 2004, Young et al. 2004, Araya et al. 2007, Leurini et al. 2010, Bergman et al. 2011, Guzmán et al. 2011 Guzmán et al. 2013).

The origin of CH_3OH and H_2CO is, however, not yet fully understood. Pure gas-phase chemical models cannot always reproduce their observed abundances (Garrod et al. 2006, Geppert et al. 2006, Guzmán et al. 2011, Guzmán et al. 2013), and solid-phase chemistry, either on the surface of dust grains or in the ice mantles that accrete on top of them, must therefore play a role in their formation. This scenario has been studied in the past two decades through experimental simulations under astrophysically relevant conditions. A short summary of the different formation pathways proposed for both methanol and formaldehyde can be found in Chapter 9, Sect. 9.1.

In the present work we have explored new UV-induced-formation pathways and subsequent desorption for CH_3OH and H_2CO. In Chapter 9 a top-down approach was followed, studying the UV photodissociation of a pure ethanol ice. In this Chapter, a bottom-up approach is represented by the UV photoprocessing of a more realistic binary H_2O:CH_4 ice analog.

This Chapter is organized as follows. Section 10.2 describes the experimental simulations performed. The results are presented in Sect. 10.3 . The astrophysical implications are elucidated in Sect. 10.4, and the conclusions for Chapters 9 and 10 are summarized in Sect. 10.5.

10.2 Experimental setup

The experimental simulations have been performed using the InterStellar Astrochemistry Chamber (ISAC) at the Centro de Astrobiología (see Muñoz Caro et al. 2010 and Chapter 4, Sect. 4.1.1). The ISAC setup consists in an ultra-high-vacuum (UHV) chamber with a base pressure of about 4 x 10^{-11} mbar, similar to what is found in dense cloud interiors.

Binary ice analogs with a 3:1 H_2O:CH_4 ratio were grown in the interior of the chamber by simultaneous deposition of H_2O vapor and CH_4 gas onto a KBr substrate at 8K. The isotopolog $^{13}CH_4$ was used in similar experiments to confirm the results. The chemical components used in this series of experiments were H_2O (liquid, triply distilled), CH_4 (gas, Praxair 99.95%), and $^{13}CH_4$ (gas, Cambridge Isotope Laboratories 99.9%).

Ice samples were UV-irradiated using an F-type microwave-discharged hydrogen flow lamp (MDHL) from Opthos Instruments with a VUV-flux of $\approx 2 \times 10^{14}$ photons cm^{-2} s^{-1} at the sample position, measured by $CO_2 \rightarrow CO$ actinometry (Muñoz Caro et al. 2010). More information can be found in Chapter 4, Sect. 4.1.3.

The ice samples were monitored by in situ Fourier-transform infrared (FTIR) trans-

Table 10.1. *IR feature used to calculate the column density of selected ice components. Frequencies and band strengths for pure ices at 10 K.*

Molecule	Frequency (cm^{-1})	Band strength ($cm\ molec^{-1}$)
H_2O	3280	$2.0\times10^{-16\ a}$
CH_4	1304	$6.4\times10^{-18\ b}$
CH_3OH	1025	$1.8\times10^{-17\ c}$
H_2CO	1720	$9.6\times10^{-18\ d}$

[a] From Hagen (1981). [b] From d'Hendecourt & Allamandola (1986). The same value was used as an approximation for the experiments with $^{13}CH_4$. [c] From d'Hendecourt & Allamandola (1986). [d] From Schutte et al. (1996).

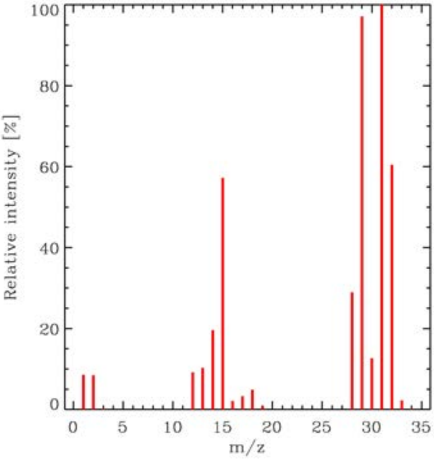

Figure 10.1. *Mass spectrum of methanol in our setup.*

mittance spectroscopy after deposition and after every irradiation period, using a Bruker Vertex 70 spectrometer equipped with a deuterated triglycine sulfate detector (DTGS). The IR spectra were collected with a spectral resolution of 2 - 4 cm^{-1} (most spectra were subsequently smoothed). Column densities of selected species in the ice were calculated from the IR spectra using the formula

$$N = \frac{1}{A}\int_{band} \tau_\nu \, d\nu, \qquad (10.1)$$

where N is the column density in molecules cm^{-2}, τ_ν the optical depth of the absorption band, a nd A the band strength in cm molecule^{-1}, as derived from laboratory experiments (Table 10.1). Band strengths in Table 11.1 were measured for pure amorphous ices. The same values are usually adopted in ice mixtures, which introduces an uncertainty of about 20-30% (d'Hendecourt & Allamandola 1986).

Pfeiffer Prisma quadrupole mass spectrometer (QMS) of a mass spectral range from 1 to 200 amu with a Channeltron detector was used to detect molecules in the gas phase. The QMS ionizes gas-phase molecules with $\sim$ 70 eV electron bombardment, leading to fragmentation of the molecules with a given pattern. The species potentially desorbing into the phase were preferably monitored through their main mass fragment, which does not always coincide with the molecular ion. In some cases the main mass fragment of a given species was common to a mass fragment of another species (see, for example, Figs. 9.1 and 9.2 in Chapter 9 for the mass spectrum of ethanol and methanol, respectively, in our setup). When possible, alternative mass fragments were used in those cases (see Table 10.2). Fragments in Table 10.2 were also used in the experiments with the isotopically labeled molecules, but mass fragments with ^{13}C were 1 amu higher. There were two exceptions: $^{13}CH_4$ was monitored through the mass fragment m/z=15, which corresponds to the $^{13}CH_2^+$ fragment, and $^{13}CH_3OH$ was monitored through the mass fragment m/z=33, which corresponds to the molecular ion.

The targeted molecules of this work were CH_3OH and H_2CO. Methanol was monitored through its main mass fragment, m/z=31.

The main mass fragment of H_2CO is m/z=29, which was common to methanol, and the second most abundant fragment (m/z=30) was used to double-check the detection formaldehyde molecules in the gas phase.

Calibration of our QMS allows conversion from integrated ion currents into photon-induced desorbed column densities, using the equation

$$N(mol) = \frac{A(m/z)}{k_{CO}} \cdot \frac{\sigma^+(CO)}{\sigma^+(mol)} \cdot \frac{I_F(CO^+)}{I_F(z)} \cdot \frac{F_F(28)}{F_F(m)} \cdot \frac{S(28)}{S(m/z)}, \tag{10.2}$$

where $N(mol)$ is the total number of photon-induced desorbed molecules cm^{-2}, $A(m/z)$ the integrated area below the QMS signal of a given mass fragment m/z during photon-induced desorption, k_{CO} is the proportionality constant between the integrated ion current and the column density of desorbed molecules in the case of a pure CO ice, as shown by

$$k_{CO} = \frac{A(28)}{N(CO)} = k_{QMS} \cdot \sigma^+(CO) \cdot I_F(CO^+) \cdot F_F(28) \cdot S(28), \tag{10.3}$$

with k_{QMS} the proportionality constant independent of the species. The constant k_{CO} is regularly calculated with pure CO ice irradiation experiments. Parameter $\sigma^+(mol)$ is the ionization cross section for the first ionization of the species of interest and the incident electron energy of the mass spectrometer; $I_F(z)$ is the ionization factor, that is, the fraction of ionized molecules with charge z; $F_F(m)$ the fragmentation factor, that is, the fraction of molecules of the isotopolog of interest leading to a fragment of mass m in the mass spectrometer; and $S(m/z)$ the sensitivity of the QMS to the mass fragment (m/z). In practice, we work with the product $k^*_{QMS} \cdot S(m/z)$ (k^*_{QMS} indicates that pressure units are used instead of column density units), since the ratio $S(m/z)/S(28)$ is the same as the ratio $k^*_{QMS} \cdot S(m/z)/k^*_{QMS} \cdot S(28)$. Sensitivity of the QMS is also probed regularly, using noble gases. Calibration of the QMS is detailed in Martín-Doménech et al. (2015) and Chapter 4, Sect. 4.1.5.

Equations 10.2 and 10.3 assume that the pumping speed in the ISAC setup is the same for all molecules, so that k_{QMS} does not depend on the species (see Martín-

Table 10.2. *Mass fragments used to monitor potentially desorbing species into the gas phase.*

Molecule	Molecular ion	Main mass fragment	Mass fragment used	Notes
H_2O	18	18	18	
CH_4	16	16	15	m/z=16 was common to H_2O Contribution from CH_3OH molecules was negligible
CH_3OH	32	31	31	
H_2CO	30	29	29	m/z=30 was also used (see text)
CO	28	28	28	Contribution from other species was negligible
CO_2	44	44	44	CO_2 was not detected in the gas phase during irradiation

Doménech et al. 2015). In fact, the pumping speed depends on the molecular mass and, to a lesser extent, on the molecular structure (Kaiser et al. 1995). Constant k_{QMS} in equation 10.3 thus corresponds to the pumping speed of CO molecules. Therefore, $N(mol)$ calculated with equation 10.2 is only valid if the pumping speed of a specific species is the same as for CO. Taking the different pumping speeds into account, the real number of photon-induced desorbed molecules would be

$$N^{real}(mol) = N^{calc}(mol) \cdot S_{rel}(mol), \tag{10.4}$$

with $N^{calc}(mol)$ the column density calculated with eq. 10.2, and $S_{rel}(mol)$ the relative pumping speed with respect to the CO molecules. According to the manufacturer of the pumping devices used in the ISAC setup, the relative pumping speed with respect to CO of a species with molecular mass $M(mol)$ is

$$S_{rel}(mol) = 1.258 - 9.2 \cdot 10^{-3} \cdot M(mol). \tag{10.5}$$

Photon-induced desorption yields can be subsequently calculated by dividing $N^{real}(mol)$ by the fluence (the product of the VUV-flux and the irradiation time).

A small rise in the signal of several mass fragments was detected every time the UV lamp was switched on. This effect has been previously reported in other works(see, e.g., Loeffler et al. 2005), but it was not reproducible and difficult to quantify. When comparable to the rise produced by photon-induced desorption of molecules from the ice during the first series of experiments, calculated desorption yields were considered upper limits.

At the end of the experimental simulations, ice samples were warmed up to room temperature using a LakeShore Model 331 temperature controller, until a complete sublimation was attained. A silicon diode temperature sensor located close to the ice substrate was used, reaching a sensitivity of about 0.1 K. The IR spectra of the solid sample were collected every five minutes during warm-up. At the same time, all the desorbing species, including the components of the ice analogs and the products of the photochemical reactions, were detected by the QMS mentioned above.

10.3 Experimental results and discussion

A binary H_2O:CH_4 ice analog was used in experiments 3 to 10 described in Table 10.3 (Experiments 1 and 2 are discussed in Chapter 9). The initial ice composition in this series of experiments was held, approximately, to 75% of water and 25% of methane. The irradiation time changed from one experiment to the next so that the total fluence was, approximately, one photon per initial molecule. In experiments 7 - 10 we used $^{13}CH_4$ instead of CH_4 to confirm the results found in experiments 3 - 6 and to reject fake positives due to contamination. As in Chapter 9, we used the FTIR spectrometer to monitor the ice composition after every irradiation interval and to detect new IR features corresponding to the formation of photoproducts. The presence of these new species could be subsequently confirmed during the TPD performed at the end of the experiments when necessary. Results for the photon-induced chemistry are shown in Sect. 10.3.1. At the same time, the QMS was used during irradiation to detect the molecules desorbing into the gas phase as a consequence of the UV photoprocessing. Photon-induced desorption is studied in Sect. 10.3.2.

Table 10.3. *UV photoprocessing experiments of H_2O:CH_4 ice analogs.*

Experiment	$N_{initial}(H_2O)$	$N_{initial}(CH_4)$	Fluence	$N_{final}(H_2O)$	$N_{final}(CH_4)$	$N_{final}(CH_3OH)^a$
	$\times 10^{15}$molecules cm^{-2}		$\times 10^{17}$photons cm^{-2}	$\times 10^{15}$molecules cm^{-2}		
3	426.7	119.2	7.2	376.0	62.0	7.2
4	586.2	229.6	7.8	520.9	173.8	7.8
5	898.2	216.3	10.8	878.2	153.7	4.9
6	560.1	161.3	7.2	500.1	101.2	4.2
7^b	506.6	150.6	7.2	462.4	89.0	0.0
8^b	721.9	263.0	10.8	665.4	165.3	0.4
9^b	372.9	160.2	7.2	335.0	90.6	1.8
10^b	523.7	146.8	6.0	...^{c}	...^{c}	...^{c}

[a] Formaldehyde was barely detected by means of IR spectroscopy, and no quantification was possible. Formation of H_2CO was confirmed during the TPD.

[b] $^{13}CH_4$ was used instead of CH_4 in these experiments.

[c] No IR spectrum was collected at the end of this experiment, since it focused only on measuring QMS signals during irradiation. (see Fig. 10.6).

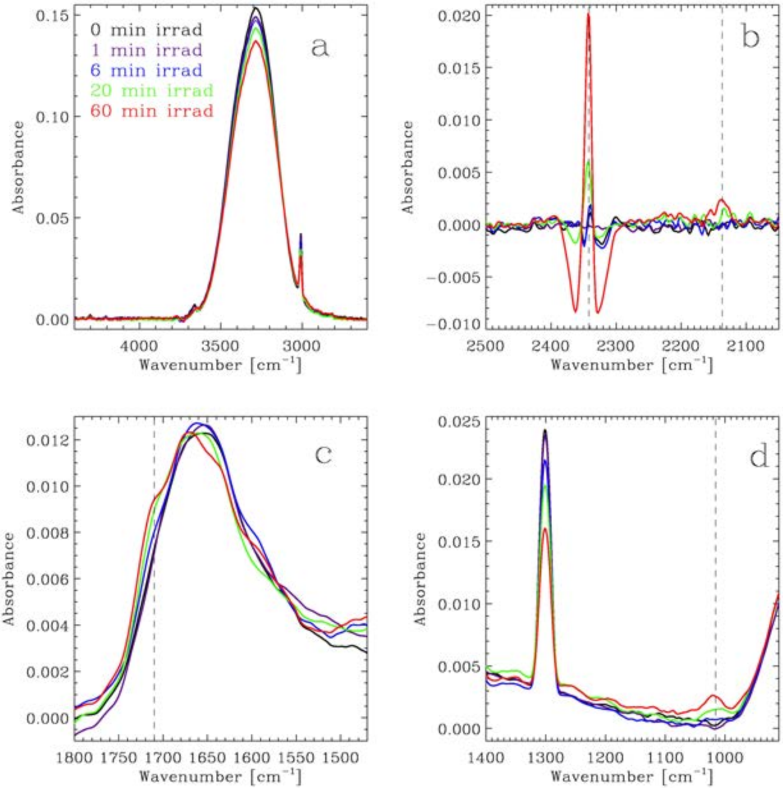

Figure 10.2. *Evolution of the IR spectrum of the H_2O:CH_4 ice mixture during UV photoprocessing in experiment 6, see Table 10.3. Results were similar in experiments 3 - 5.* ***a)*** *Evolution of the O-H stretching band of H_2O (broad band peaking at ~3280 cm^{-1}), and the C-H stretching band of CH_4 (in the red side of the former).* ***b)*** *Formation of CO_2 and CO leads to the appearence of two C-O stretching bands at 2342 cm^{-1} and 2137 cm^{-1}, respectively (dashed lines). Negative absorbances are due to the atmospheric correction applied by the FTIR software, but the band is due to solid CO_2, as the peak position indicates.* ***c)*** *Evolution of the O-H deformation band of H_2O. The apearance of a shoulder at ~1710 cm^{-1} is probably due to the formation of H_2CO.* ***d)*** *Evolution of the C-H deformation band of CH_4 at 1300 cm^{-1}. The new feature at 1016 cm^{-1} is due to the formation of methanol.*

10.3.1 Photon-induced chemistry of a H_2O:CH_4 ice analog

Figure 10.2 shows the evolution of the mid-IR spectrum of the ice sample in experiment 6 between 4400 cm^{-1} and 910 cm^{-1}, and Fig. 10.3 shows the mid-IR spectra between 2500 cm^{-1} and 910 cm^{-1} of the ice sample in experiment 9. Results were similar for the rest of the experiments. As expected, some of the IR features are shifted in the

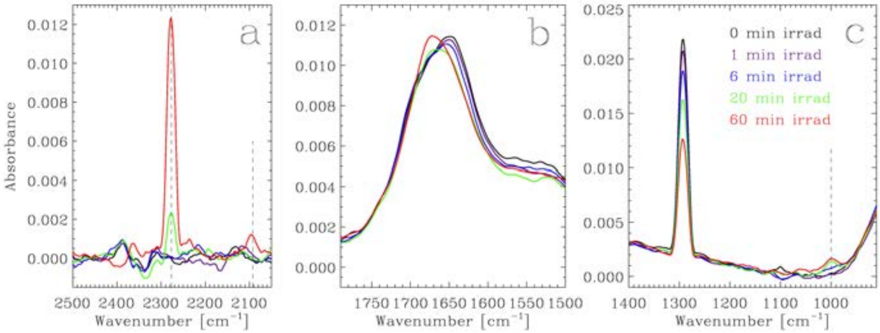

Figure 10.3. *Evolution of the IR spectrum of the H_2O:CH_4 ice mixture during UV photoprocessing in experiment 9, see Table 10.3. Results were similar in experiments 7, 8, and 10.* ***a)*** *Formation of $^{13}CO_2$ and ^{13}CO leads to the appearence of two C-O stretching bands at 2277 cm^{-1} and 2092 cm^{-1}, respectively (dashed lines).* ***b)*** *Evolution of the O-H deformation band of H_2O.* ***c)*** *Evolution of the C-H deformation band of CH_4 at 1292 cm^{-1}. The new feature at 1000 cm^{-1} is due to the formation of methanol.*

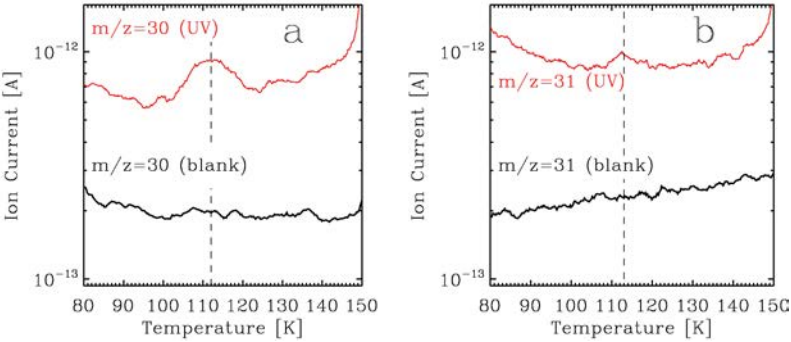

Figure 10.4. ***a)*** *TPD curve of the m/z=30 mass fragment, corresponding to the molecular ion of H_2CO, after irradiation in experiment 3 (red) compared to the blank (black). A desorption peak at ∼112 K (dashed line) confirms the formation of formaldehyde.* ***b)*** *TPD curve of the m/z=31 mass fragment, corresponding to the molecular ion of $H_2^{13}CO$, after irradiation in experiment 7 (red) compared to the blank (black). A desorption peak at ∼113 K (dashed line) confirms the formation of formaldehyde.*

experiments with $^{13}CH_4$. In particular, the C-H deformation band of CH_4 shifts from 1300 cm^{-1} in Fig. 10.2d to 1292 cm^{-1} in Fig. 10.3c. Bands of C-bearing photoproducts are also shifted in a similar way (see below).

The initial components of the ice analogs were monitored with the O-H stretching band at ∼3280 cm^{-1} corresponding to water molecules (Fig. 10.2a), and the C-H deformation band mentioned above corresponding to methane (Figures 10.2d and 10.3c). The intensity of these bands gradually decrease with continuing irradiation, leading to a loss of ∼11% of initial H_2O and ∼35% of initial CH_4 molecules at the end of experiments 3 - 6 (Table 10.3). Loss of water was similar within 10% in experiments with $^{13}CH_4$, while loss of methane was about 40% higher, with no obvious explanation.

In this series of experiments, formation of CH_3OH during UV photoprocessing of the ice analogs was observed, thanks to the detection of the C-O stretching band at 1016 cm^{-1} in Fig. 10.2d and at 1000 cm^{-1} in Fig. 10.3c. The column density of methanol in the ice at the end of irradiation in experiments 3 - 6 accounts for ∼4% of the initial CH_4 column density (Table 10.3). Formation of methanol took place to a lower extent in experiments 7 - 10. It did not reach the sensitivity limit of our FTIR in experiment 7 (see Table 10.3), but it was detected by the QMS during TPD (not shown).

On the other hand, the relatively strong O-H bending band that is due to water molecules prevented us from clearly detecting the C=O stretching mode of H_2CO in Figs. 10.2c and 10.3b. A shoulder at ∼1715 cm^{-1} is observed on the blue side of the O-H bending band in Fig. 10.2c, while a shift in the peak frequency of this band is observed in Fig. 10.3b. Formation of H_2CO was confirmed during the TPD performed at the end of the experiments. A peak near the desorption temperature of pure H_2CO (∼112 K, Noble et al. 2012) was observed for the mass fragments m/z=30, corresponding to H_2CO^+ in experiments 3 - 6 (Fig. 10.4a), and m/z=31, corresponding to $H_2^{13}CO^+$ in experiments 7 - 10 (Fig. 10.4b). However, photoproduction of formaldehyde could not be quantified using the IR spectra, since its IR band was barely detected.

Photochemistry was simpler in this series of experiments compared to those discussed in Chapter 9. In addition to CH_3OH and H_2CO, only CO and CO_2 were detected in the IR spectra. The C-O stretching mode of these molecules is observed at 2137 cm^{-1} and 2342 cm^{-1}, respectively, in Fig. 10.2b. The C-O stretching bands of ^{13}CO and $^{13}CO_2$ are redshifted to 2092 cm^{-1} and 2277 cm^{-1} in Fig. 10.3a, respectively, in fair agreement with the values reported in Gerakines et al. (1995).

10.3.2 Photon-induced desorption from a H_2O:CH_4 ice analog

As in Chapter 9, the QMS allowed us to detect desorption of the photoproducts observed in Sect. 10.3.1 during irradiation of the ice analogs, monitoring the mass ion fragments selected in Sect. 10.2. Results are shown in Figs. 10.5 and 10.6. As explained in Sect. 10.2, mass fragments in experiments 7 - 10 were 1 amu higher than in exp. 3 - 6 because of the presence of ^{13}C in the molecules. Photon-induced desorption yields were calculated for experiments 7 - 10 using the parameters shown in Table 10.4, since experiments with isotopically labeled molecules are more reliable thanks to the lack of contamination effects. Compared to the m/z=31 fragment that corresponds to the molecular ion $H_2^{13}CO^+$, the $H^{13}CO^+$ fragment (m/z=30) displayed a more intense signal with a lower noise level. Therefore, the latter was used to quantify the formaldehyde photon-induced desorption yield (the molecular ion was used in exp. 1 - 2, Chapter 9). Proportionality constant k_{CO} varied between 1.35 x 10^{-10} A min ML^{-1} and 1.90 x 10^{-10} A min ML^{-1} for experiments 7 - 10. Table 10.5 shows the photon-induced desorption yields measured in experiment 9, averaged for every irradiation interval. Results were similar in experiments 7, 8, and 10.

Table 10.4. *Values used in Eq. 10.2 to convert integrated QMS signals in experiments 7 - 10 into column densities of desorbed molecules.*

Factor	$H_2^{13}CO$	^{13}CO
$\sigma^+(mol)$ ($\AA^2$)[a]	4.140	2.516
fragment	$H^{13}CO^+$	$^{13}CO^+$
m/z	30	29
$I_F(z)$	1[b]	1[b]
$F_F(m)$	0.549[c]	0.949[d]
$k^*_{QMS} \cdot S(m/z)$ (A mbar^{-1} $\AA^{-2}$)[e]	9.30 x 10^{14}	9.77 x 10^{14}
$k^*_{QMS} \cdot S(m/z)$ (A mbar^{-1} $\AA^{-2}$)[f]	1.29 x 10^{15}	1.36 x 10^{15}
$k^*_{QMS} \cdot S(m/z)$ (A mbar^{-1} $\AA^{-2}$)[g]	1.77 x 10^{15}	1.89 x 10^{15}
$S_{rel}(mol)$[h]	0.973	0.991

[a] We used the values corresponding to $H_2^{12}CO$ and ^{12}CO, extracted from the online NIST database, as an approximation.

[b] A value of 1 was adopted, assuming that no double ionization of the molecules takes place.

[c] We used the value corresponding to the fragment $H^{12}CO^+$, extracted from the online NIST database, as an approximation.

[d] We used the value corresponding to the molecular ion $^{12}CO^+$, extracted from the mass spectra library of the QMS software, as an approximation.

[e] Calculated for our QMS and valid for experiment 7 (see Sect. 10.2)

[f] For experiment 8 (see Sect. 10.2)

[g] For experiment 9 and 10 (see Sect. 10.2)

[h] Calculated with equation 10.4.

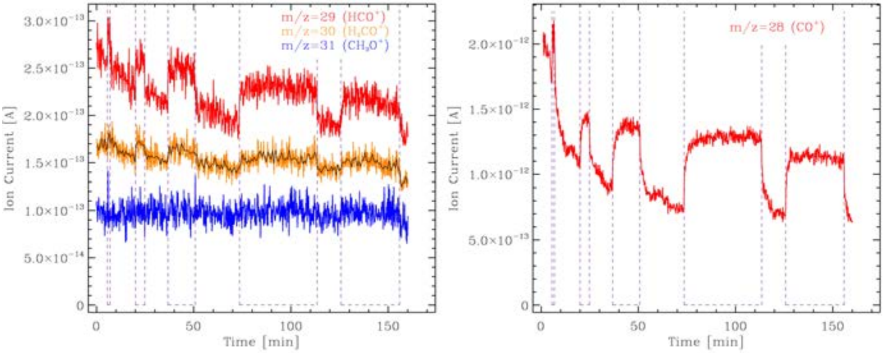

Figure 10.5. *Photon-induced desorption of formaldehyde observed with mass fragments m/z=29 and m/z=30 (left panel), and carbon monoxide (m/z=28 in right panel) during UV irradiation of a H_2O:CH_4 ice analog in experiment 5. Results were similar in exp. 3, 4, and 6. Ion currents of different mass fragments are offset for clarity. The black solid line represent an average of the corresponding ion current, shown to better evaluate the shape of the signal. Irradiation intervals are indicated with dashed vertical lines.*

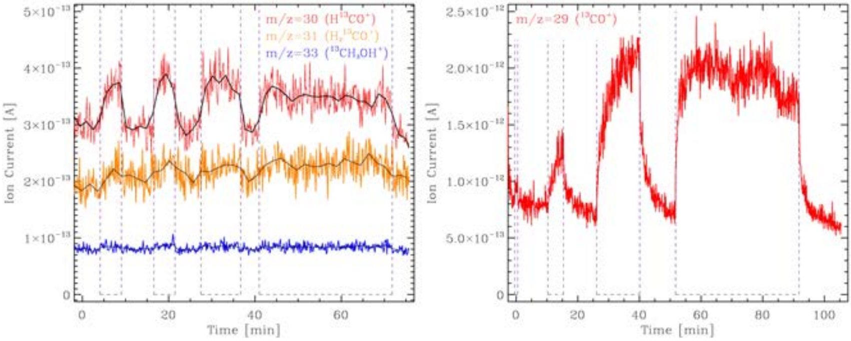

Figure 10.6. *Photon-induced desorption of $H_2^{13}CO$ (m/z=30 and m/z=31 in left panel) and ^{13}CO (m/z=29 in right panel) during UV irradiation of a H_2O:$^{13}CH_4$ ice analog in experiments 10 and 7, respectively. Results were similar for experiments 8 and 9. Ion currents of different mass fragments are offset for clarity. Black solid lines represent an average of the corresponding ion currents, as shown to better evaluate the shape of the signals. Irradiation intervals are indicated with dashed vertical lines.*

No clear photon-induced desorption was observed for the mass fragments m/z=31 (left panel of Fig. 10.5) and m/z=33 (left panel of Fig. 10.6) corresponding to methanol molecules in experiments 3 - 6 and 7 - 10, respectively. On the other hand, a constant rise was detected during irradiation in experiments 3 - 6 for mass fragments m/z=29 and m/z=30 (left panel of Fig. 10.5), suggesting photochemidesorption (see Chapters 7 and 9) of formaldehyde. The same behavior is observed in mass fragments m/z=30 and m/z=31 in experiments 7 - 10 (left panel of Fig. 10.6). This confirms photochemidesorption of formaldehyde, since the fragments of $H_2^{13}CO$ are 1 amu higher than those of H_2CO. Averaged photodesorption yields of $H_2^{13}CO$ in Table 10.5 are slightly lower than the upper limits derived in Chapter 9 for the pure C_2H_5OH ice photoprocessing experiments.

Desorption of CO molecules during irradiation is detected in the righthand panel of Fig. 10.5 with the mass fragment m/z=28. The increasing[2] behavior of the photon-induced desorption is more clearly observed with the mass fragment m/z=29 in the righthand panel of Fig. 10.6. The measured photodesorption yield of ^{13}CO in Table 10.5 is one order of magnitude lower than that found in Chapter 9. This is probably due to the much lower formation rate found for the CO molecules in this series of experiments. After a fluence of 7.2 photons cm^{-2}, only $\sim$0.5% of the initial column density had formed CO in experiments 3 - 10, while the value in experiments 1 and 2 is $\sim$13% (see the low intensity of the C-O stretching band corresponding to CO in Figs. 10.2b and 10.3a compared to Fig. 9.3b).

Photon-induced desorption of CO_2 was not observed in experiments 3 - 10 (not shown in Figures 10.5 and 10.6).

10.4 Astrophysical implications

In cold dense interstellar and circumstellar regions, molecules form ice mantles upon freeze-out onto cold dust grains. These ice mantles are mainly observed in the near- to far-IR region of the spectrum (Boogert et al. 2015, and ref. therein). Solid H_2O is the most abundant species observed in interstellar and circumstellar ices with an average abundance of $\sim 4 \times 10^{-5}$ relative to N_H (Boogert et al. 2015). Several other species have been confirmed to be present in ice mantles, in particular, CO, CO_2, CH_3OH, NH_3 and CH_4. Solid methane has been detected with abundances ranging from 0.4% to 11% relative to water ice (Boogert et al. 2015, and ref. therein). . In the second series of experiments (which are discussed in this Chapter), we used binary H_2O:CH_4 ice analogs with a methane abundance that is somehow higher ($\sim$33%).

Ice mantles can be energetically processed by cosmic rays, UV, and X-ray photons, and also thermally in regions around protostars. Energetic processing of ices leads to several effects, including photon-induced chemistry and photon-induced desorption as studied in this work. Solid-phase chemistry has been widely proposed as a possible source of molecules in the ISM. In some cases, formation in ice mantles followed by nonthermal desorption needs to be invoked to explain the observed abundances of some species in dense cores and low UV-field illuminated PDRs. This is the case of the targeted molecules of this work, CH_3OH and H_2CO (see Chapter 9, Sect. 9.1).

Photoprocessing in particular takes place in dense cores thanks to the secondary UV field generated by the interaction of H_2 molecules in the gas phase with cosmic rays, leading to a photon flux of $\sim$10^4 photons cm^{-2} s^{-1} (Cecchi-Pestellini & Aiello 1992, Shen et al. 2004). On the other hand, PDRs are illuminated by nearby massive stars with a UV flux of $\sim$10^{11} eV cm^{-2} s^{-1} for a low UV-field illuminated PDR as for the Horsehead PDR (Pety et al. 2012). In our experiments, we used a MDHL with a photon flux of $\sim 2 \times 10^{14}$ photons cm^{-2} s^{-1} and an average photon energy of 8.6 eV (see Sect.

---

[2] Called DIET-like in the published version of the paper.

Table 10.5. *Evolution of the photodesorption yields during UV irradiation of a binary H_2O:$^{13}CH_4$ ice analog in exp. 9 (results were similar in experiments 7, 8, and 10).*

Irradiation period (min)	Fluence[a] (photons cm^{-2})	Y_{pd} ($H_2^{13}CO$)[b] 10^{-5} (molecules/incident photon)	Y_{pd} (^{13}CO)[b] 10^{-4} (molecules/incident photon)
0 - 1	1.2 x 10^{16}	4.3	0.8
1 - 6	7.2 x 10^{16}	3.9	0.9
6 - 20	2.4 x 10^{17}	4.8	1.5
20 - 60	7.2 x 10^{17}	4.4	4.9

[a] Total fluence at the end of the irradiation period. [b] Averaged for each irradiation period in experiment 9. Photon-induced desorption yield values could be different by a factor 2 due to the uncertainties in all the parameters of equation 10.2.

4.1.3). Therefore, the ice samples in our experimental simulations experience the same total fluence as the ice mantles during the typical lifetime of dense cores ($\sim 3 \times 10^{17}$ photons cm^{-2} for a cloud lifetime of 10^6 years) after 30 minutes of irradiation. At the same time, the UV flux experienced by the ice samples in the experiments is about four orders of magnitude higher than that present in low-illuminated PDRs.

As mentioned in Chapter 9, Sect. 9.1, gas-phase abundances of CH_3OH in dense cores and PDRs where thermal desorption is inhibited cannot be reproduced by gas-phase chemical models, and solid chemistry followed by nonthermal desorption needs to be invoked. Methanol formation was not observed during irradiation of a pure ethanol ice sample (Chapter 9, but it was formed in the H_2O:CH_4 ice irradiation experiments, accounting for $\sim$1% of the total initial column density. However, photon-induced desorption of methanol was not observed in this second series of experiments, and therefore its abundance in these regions remains an open question in astrochemistry.

On the other hand, formaldehyde was formed in both series of experiments. Photochemidesorption of this species was detected with a yield of ≤ 6 x 10^{-5} (molecules per incident photon) in the case of the pure ethanol ice experiments, and ~ 4.4 x 10^{-5} (molecules per incident photon) when the H_2O:CH_4 ice analogs were photoprocessed. The latter value (more accurate, and closer to the astrophysical scenario) could be used in gas-grain chemical models, taking photon-induced desorption from dust grains and subsequent gas-phase reactions into account, in order to test whether photochemidesorption of formaldehyde as observed in this work is able to account for all the formaldehyde detected in low UV-field illuminated PDRs or if an additional source of formaldehyde is needed.

10.5 Conclusions for Chapters 9 and 10

We have explored two UV-induced formation pathways and subsequent desorption for CH_3OH and H_2CO, which are two simple organic molecules that are ubiquitously detected in the ISM. Photoproduction of these species was searched for with an IR spectrometer during UV irradiation of the ice samples. Photon-induced desorption of several photoproducts was observed directly in the gas phase by means of mass spectrometry. Calibration of our QMS allowed us to quantify the photon-induced desorbing molecules and calculate desorption yields.

In a first series of experiments, a top-down approach to the formation of methanol and formaldehyde was used when studying the photodissociation of a pure ethanol ice. Seven photoproducts were detected: H_2O, CO, CO_2, CH_4, C_2H_6, H_2CO, and CH_3CHO. Photon-induced desorption of four of the photoproducts was observed during photoprocessing of the ice sample. The increasing desorption yield observed for H_2O, CO, and CH_4 suggests that the DIET mechanism [3] was active for these species [4]. In particular, the photon-induced desorption yield of water and methane reached constant values of $\leq 2.6 \times 10^{-4}$ molecules/incident photon and $\sim 3.3 \times 10^{-4}$ molecules/incident photon, respectively, after a fluence of 1.8 × 10^{17} photons cm^{-2}, while that of carbon monoxide continued increasing, reaching a value of 1.5 × 10^{-3} molecules/incident photon after a total fluence of 7.2 × 10^{17} photons cm^{-2}. On the other hand, formaldehyde and/or ethane molecules were observed to photochemidesorb with a constant desorption yield of ∼6 × 10^{-5} molecules/incident photon in case the QMS m/z=29 signal was only due to H_2CO molecules.

---

[3] see Chapter 7 for more information on the photodesorption mechanisms.

[4] Or through any mechanism in two steps involving energy transfer to the previously photoproduced molecules (see Chapter 7).

In a second series of experiments, a bottom-up approach was explored, using a more realistic water-reach ice analog containing methane. Photoprocessing of H_2O:CH_4 ice samples with a 3:1 ratio led to a simpler photochemical network , and only four photoproducts were detected: CO, CO_2, CH_3OH, and H_2CO. Only CO and H_2CO were observed to desorb upon UV irradiation of the ice mixtures. The photon-induced desorption yield of carbon monoxide was found to increase during photoprocessing up to 4.9 × 10^{-4} molecules/incident photon after a total fluence of 7.2 × 10^{17} photons cm^{-2}, suggesting that the desorption was driven by the DIET mechanism. Photochemidesorption of formaldehyde was also detected, with a constant yield of ∼4.4 x 10^{-5} molecules/incident photon. These results were confirmed using H_2O:$^{13}CH_4$ ice analogs.

Methanol was only formed during the second series of experiments, but no significant photon-induced desorption was observed. So far, there has been no experimental evidence of an efficient nonthermal desorption mechanism that explained the gas-phase methanol abundances in dense cores and low UV-field illuminated PDRs, where thermal desorption from ice mantles is inhibited, and gas-phase chemical models fail to account for all the detected methanol. On the other hand, formaldehyde was photoproduced in both series of experiments. Photochemidesorption took place with a similar yield in both cases. While gas-phase chemical models are able to reproduce the formaldehyde abundances in dense cores, formation in the solid phase and subsequent desorption to the gas phase is needed in the case of low UV-field illuminated PDRs. The photon-induced desorption yield found in this work can be used in gas-grain chemical models to test that the observed column densities of formaldehyde in low UV-field illuminated PDRs can be explained by the proposed photon-induced formation and subsequent desorption process.

Acknowledgements

We are grateful to Javier Manzano-Santamaría for his support on the experiments. Special thanks go to Marcelino Agúndez for useful discussions. This research was financed by the Spanish MINECO under project AYA2011-29375. R.M.D. benefited from a FPI grant from Spanish MINECO.

References

Araya, E., Hofner, P., Goss, W. M., et al. 2007, ApJS, 170, 152

Bergman, P., Parise, B., Liseau, R., & Larsson, B. 2011, A&A, 527, 39

Bernstein, M. P., Dworkin, J. P., Sandford, S. A., Cooper, G. W., & Allamandola, L. J. 2002, Nature, 416, 401

Bernstein, M. P., Sandford, S. A., Allamandola, L. J., Chang, S., & Scharberg, M. A. 1995, ApJ, 454, 327
Bertin, M., Fayolle, E. C., Romanzin, C., et al. 2012, PCCP, 14, 9929
Bertin, M., Fayolle, E. C., Romanzin, C., et al. 2012, ApJ, 779, 120
Boogert, A. C. A., Huard, T. L., Cook, A. M., et al. 2011, ApJ, 729, 92
Boogert, A. C. A., Gerakines, P. A., & Whittet, D. C. B. 2015, ARA&A, 53, 541
Boogert, A. C. A., Pontoppidan, K. M., Knez, C., et al. 2008, ApJ, 678, 985
Bottinelli, S., Boogert, A. C. A., Bouwman, J., et al. 2010, ApJ, 718, 1100
Ceccarelli, C., Loinard, L., Castets, A., Tielens, A. G. G. M., & Caux. E. 2000, A&A, 357, L9
Cecchi-Pestellini, C. & Aiello, S. 1992, MNRAS, 258, 125
Charnley, S. B., Tielens, A. G. G. M., & Millar, T. J. 1992, ApJ, 399, L71
Chen, Y.-J., Chu, C.-C, Lin, Y.-C. et al. 2010, Advances in Geosciences, 25, 259
Chen, Y.-J., Chuang, K.-J, Muñoz Caro, G. M., et al. 2014, ApJ, 781, 15
Ciaravella, A., Muñoz Caro, G., Jiménez-Escobar, A. et al. 2010, ApJL, 722, L45
Cruz-Díaz, G. A., Martín-Doménech, R., Muñoz Caro, G. M., & Chen, Y.-J. 2016, A&A, 592, A68
Cruz-Díaz, G. A., Muñoz Caro, G. M., Chen, Y.-J., & Yih, T.-S. 2014a, A&A, 562, A119
Dartois, E. 2005, Space Sci. Rev., 119, 293
Dartois, E., Geballe, T. R., Demyk, K., Ehrenfreund, P., & dHendecourt, L. 1999, A&A, 342, L32
d'Hendecourt, L. B.,& Allamandola, L. J. 1986, A&AS, 64, 453
Ehrenfreund, P., Irvine, W., Becker, L., Blank, J, Brucato, J. R., et al. 2002, Rep. Prog. Phys., 65, 1427
Fayolle, E. C., Bertin, M., Romanzin, C., et al. 2011, ApJL, 739, L36
Fayolle, E. C., Bertin, M., Romanzin, C., et al. 2013, A&A, 556, A122
Fillion, J.-H., Fayolle, E., Michaut, X., et al. 2014, Faraday Discuss., 168, 533
France, K., Andersson, B.-G., McCandliss, S. R., & Feldman, P. D. 2005, ApJ, 682, 750
Fuchs, G. W., Cuppen, H. M., Ioppolo, S., et al. 2009, A&A, 505, 629
Garrod, R. T., Park, I. H., aselli, P., & Herbst, E. 2006, Faraday Discussions, 133, 51
Garrod, R. T., Wakelam, V., & Herbst, E. 2007, A&A, 467, 1103
Garrod, R. T., Weaver, S. L., & Herbst, E. 2008, ApJ, 682, 283
Geppert, W. D., Hamberg, M., Thomas, R. D., et al. 2006, Faraday Discussions, 133, 177
Gerakines, P. A., Moore, M. H., & Hudson, R.L. 2001, J. Geophys. Res. -Planets, 106 (E12), 33381
Gerakines, P. A., Schutte, W. A., Greenberg, J. M., & van Dischoeck, E. F. 1995, A&A, 296, 810
Gibb, E. L., Whittet, D. C. B., Boogert, A. C. A., & Tielens, A. G. G. M. 2004, ApJS, 151, 35
Gibb, E. L., Whittet, D. C. B., Schutte, W. A. 2000, ApJ, 536, 347
Gredel, R., Lepp, S., Dalgarno, A., & Herbst, E. 1989, ApJ, 347, 289
Guzman, V. V., Pety, J., Goicoechea, J. R., Gerin, M., & Roueff, E. 2011, A&A, 534, A49
Guzmán, V. V., Goicoechea, J. R., Pety, J., et al. 2013, A&A, 560, A73
Hagen, W. 1981, Chem. Phys., 56, 367
Hiraoka, K., Ohashi, N., Kihara, Y., et al. 1994, Chemp. Phys. Lett., 229, 408
Herbst, E., & van Dishoeck, E. F. 2009, Annu. Rev. Astron. Astrophys., 47, 427
Hiraoka, K., Sato, T., Sato, S., et al. 2002, ApJ, 577, 265

Hiraoka, K., Wada, A., Hidekazu, K., et al. 2005, ApJ, 620, 542
Hocuk, S., & Cazaux, S. 2015, A&A, 576, A49
Hudson, R. L., Moore, M. H. 1999, Icarus, 140, 451
Jenniskens, P., Baratta, G. A., Kouchi, A., et al. 1993, A&A, 273, 583
Kaiser, R. I., Jansen, P., Petersen, K., & Roessler, K. 1995, Rev. Sci. Instrum. 66, 5226
Keane, J. V., Tielens, A. G. G. M., Boogert, A. C. A. Schutte, W. A., & Whittet, D. C. B. 2001, A&A, 376, 254
Leurini, S., Parise, B., Schilke, P. Pety, J., & Rolffs, R. 2010, A&A, 511, A82
Loeffler, M. J., Baratta, G. A., Palumbo, M. E., Strazzulla, G., & Baragiola, R. A. 2005, A&A, 435, 587
Madzunkov, S. M., MacAskill, J. A., Chutjian, A. et al. 2009, ApJ, 697, 801
Madzunkov, S. M., MacAskill, J. A., Chutjian, A. et al. 2010, ApJ, 712, 194
Maret, S., Ceccarelli, C., Caux, E., et al. 2004, A&A, 416, 577
Martín-Doménech, R., Manzano-Santamaría, J., Muñoz Caro, G. M., et al. 2015, A&A, 584, A14
Martín-Doménech, R., Muñoz Caro, G. M., Bueno, J., & Goesmann, F. 2014, A&A, 564, A8
Moore, M. H., & Hudson, R. L. 1998, Icarus, 135, 518
Mumma, M. J., & Charnley, S.B., 2011, Annu. Rev. Astron. Astrophys., 49, 471
Muñoz Caro, G. M., Jiménez-Escobar, A., Martín-Gago, J.Á. et al. 2010, A&A, 522, A108
Muñoz Caro, G. M., Meierhenrich, U. J., Schutte, W. A., et al. 2002, Nature, 416, 403
Muñoz Caro, G. M., & Schutte, W. A. 2003, A&A, 412, 121
Muñoz Caro, G. M., & Dartois, E. 2009, A&A, 494, 109
Noble, J. A., Theule, P., Mispelaer, F., et al. 2012, A&A, 543, A5
Nuevo, M., Meierhenrich, U. J., Muñoz Caro, G. M., et al. 2006, A&A, 457, 741
Öberg, K. I., Boogert, A. C. A., Pontoppidan K. M., et al. 2011, ApJ, 740, 109
Öberg, K. I., Bottinelli, S., Jørgensen, J. K., & van Dishoeck, E. F. 2010, ApJ, 716, 825
Öberg, K. I., Fayolle, E. C., Reiter, J. B., & Cyganowski, C. 2014, Faraday Discussions, 168, 81
Öberg, K. I., Fuchs, G. W., Zainab, A., et al., 2007, ApJ, 662, L23
Öberg, K. I., Garrod, R. T., van Dishoeck, E. F., & Linnartz. H. 2009, A&A, 504, 891
Pety, J., Gratier, P., Guzmán, V., et al. 2012, A&A, 548, A68
Pontoppidan, K. M., Boogert, A. C. A., Fraser, H. J. et al. 2008, ApJ, 678, 1005
Rakhovskaia, O., Wiethoff, P., & Feulner, P. 1995, NIM B, 101, 169
Schriver, A., Schriver-Mazzuoli, L., Ehrenfreund, P., & d'Hendecourt, L. 2007, Chem. Phys. 334, 128
Schutte, W. A., Boogert, A. C. A., Tielens, A. G. G. M., et al. 1999, A&A, 343, 966
Schutte, W. A., Gerakines, P. A., Geballe, T. R., van Dishoeck, E. F., & Greenberg, J. M. 1996, A&A, 309, 633
Shen, C. J., Greenberg, J. M., Schutte, W. A., & van Dishoeck, E. F. 2004, A&A, 415, 203
Smith, I. W. M., Herbst, E., & Chang, Q. 2004, MNRAS, 350, 323
Sutton, E. C., Peng, R., Danchi, W. C., et al. 1995, ApJS, 97, 455
Tielens, A. G. G. M. & Hagen, W. 1982, A&A, 114, 245
Tielens, A. G. G. M. & Whittet, D. C. B. 1997, in Molecules in Astrophysics: Probe and Processes, ed. E. F. van Dishoeck (Dordrecht: Kluwer), 45
Wada, A., Mochizuki, N., & Hiraoka, K. 2006, ApJ, 644, 300
Watanabe, N. & Kouchi, A. 2002, ApJ, 571, L173

Watanabe, N., Mouri, O., Nagaoka, A., Chigai, T., & Kouchi, A. 2007, ApJ, 668, 1001
Watanabe, N., Shikari, T., & Kouchi, A. 2003, ApJ, 588, L121
Wootten, A., Mangnum, J., & Barsony, M. 1996, BAAS, 28, 105.08
Yamamoto, S., Beniya, A., Mukai, K., Yamashita, Y., & Yoshinobu, J. 2004, Chem. Phys. Lett., 388, 384
Young, K. E., Lee, J., Evans, II, N. J., Goldsmith, P. F., & Doty, S. D. 2004, ApJ, 614, 252

Chapter 11

Thermal processing of circumstellar and cometary ice analogs

Adapted from *Thermal desorption of circumstellar and cometary ice analogs*. Martín-Doménech, R., Muñoz Caro, G.M., Bueno, J., and Goesmann, F. 2014, A&A, 564, A8.

Abstract

Thermal annealing of interstellar ices takes place in several stages of star formation. Knowledge of this process comes from a combination of astronomical observations and laboratory simulations under astrophysically relevant conditions.

We present the results of temperature programmed desorption (TPD) experiments with pre-cometary ice analogs composed of up to five molecular components: H_2O, CO, CO_2, CH_3OH, and NH_3.

The experiments were performed with an ultra-high vacuum chamber. A gas line with a novel design allows the controlled preparation of mixtures with up to five molecular components. Volatiles desorbing to the gas phase were monitored using a quadrupole mass spectrometer, while changes in the ice structure and composition were studied by means of infrared spectroscopy.

The TPD curves of water ice containing CO, CO_2, CH_3OH, and NH_3 present desorption peaks at temperatures near those observed in pure ice experiments, volcano desorption peaks after water ice crystallization, and co-desorption peaks with water. Desorption peaks of CH_3OH and NH_3 at temperatures similar to the pure ices are observed when their abundance relative to water is above ~ 3 % in the ice matrix. We found that CO, CO_2, and NH_3 also present co-desorption peaks with CH_3OH, which cannot be reproduced in experiments with binary water-rich ice mixtures (extensively used in the study of thermal desorption of interstellar ices).

These results reproduce the heating of circumstellar ices in hot cores and can be also applied to the late thermal evolution of comets. In particular, TPD curves represent a benchmark for the analysis of the measurements that mass spectrometers on board the ESA-Rosetta cometary mission performed on the coma of comet 67P/Churyumov-Gerasimenko, which was active before the arrival of Rosetta in line with our predictions[1].

11.1 Introduction

Dense molecular clouds have typical densities of 10^4-10^6 particles cm^{-3} and temperatures down to 10 K in their interiors (see Chapter 3). These low temperatures are reached thanks to the screening from the interstellar ultraviolet (UV) radiation field provided by the gas, dust particles and, presumably, polycyclic aromatic hydrocarbons (PAHs) at the edge of the cloud that absorb most of the radiation. Under these conditions, molecules are able to condense onto the surface of dust grains, forming ice mantles (Chapter 3, Sect. 3.2 and 6). The size of interstellar dust grains is usually given by dust models as a power-law distribution, and they are covered by a ~ 0.01 μm ice mantle in dense cloud interiors (Zubko et al. 2004).

---

[1] The measurements were made public after publication of the paper.

When a dense core collapses to form a star, grain agglomeration can take place during the cold core phase, leading to cluster particles composed of sub-micron grains. Later on, during the warm-up phase, the protostar heats its environment, leading to thermal processing of ice mantles. This thermal annealing takes place in two different ways. On the one hand, grains at a certain distance are heated (approximately 1 K/century; Viti & Williams 1999) as the temperature of the protostar increases. On the other hand, grains are also able to undergo periodic radial excursions to distances less than 0.1 AU from the central protostar on short timescales (from a few to hundreds of hours), according to the fluctuating X-wind model for the formation of Ca-Al-rich inclusions (CAIs) and chondrules (Shu et al. 1996, 1997, 2001).

The main effect of thermal annealing is the sublimation of ice mantles explaining the excess gas-phase abundances of some species in the inner regions of protostellar envelopes (e.g., Pauls et al. 1983; Herbst & van Dischoeck 2009 and ref. therein). Models predict that thermal desorption of ice governs the gas-phase chemistry during star formation (e.g., Viti et al. 2004).

The remaining ice mantles in protoplanetary disks are incorporated in comets and other minor bodies. Cometary ice composition is thought to be similar to that of the interstellar ice mantles (Mumma & Charnley 2011 and ref. therein), although it can vary between comets. Molecules present on ices, both originally or created afterwards by means of energetic processing, are thus transported by these bodies, which may be responsible for the delivery of organic material to habitable planets, and, ultimately, the origin of life.

Cometary ices are also exposed to thermal processing, which is the main responsible for the activity observed in comets. When a comet passes within r $\sim$ 3 AU of the Sun during its orbit, icy volatiles form an expanding atmosphere of gas and dust called the coma (Wyckof 1982).

Most of our current knowledge on interstellar, circumstellar, and cometary ices comes from a combination of infrared observations and laboratory experiments that simulate their energetic processing under astrophysically relevant conditions.

Heating of ice mixtures leads to structural changes in the ice, involving diffusion of molecules, phase changes, and ice segregation. Segregation is expected to occur whenever ice diffusion of molecules is possible, and it is energetically favorable for molecules of the same kind to group together. Ice diffusion barriers are proportional to the binding energy of the species (i.e., their volatility). Thermal annealing of ice samples also leads to sequential desorption of ice molecules that are able to diffuse through the structure of the ice toward the surface, which starts with the most volatile species (Öberg et al. 2009).

The experiments presented here contribute to a better understanding on the thermal processing of circumstellar and cometary ices. The majority of published results of temperature programmed desorption (TPD) experiments of astrophysical ice analogs deal with pure ices or binary mixtures with H_2O as the primary component (e.g., Collings et al. 2004). Some ternary mixtures have been treated as well (e.g., Fayolle et al. 2011).
This work represents the first attempt to study the thermal processing of a more realistic

astrophysical ice with up to five molecular components (H_2O, CO, CO_2, CH_3OH, and NH_3) using both mass spectrometry and infrared spectroscopy.

Our results can be also used to predict and analyze the data collected by mass spectrometers on board cometary missions like Rosetta. The International Rosetta Mission was approved in 1993 and has been developed by the European Space Agency (ESA). Since its approval, several works were published studying the target of this cometary mission using both ground and space-based observations with special interest on the evolution of the activity during its orbit (e.g., Kelley et al. 2009; de Almeida et al. 2009; Snodgrass et al. 2013). Rosetta was launched in March 2004 and was expected to arrive at comet 67P/Churyumov-Gerasimenko (a short-period comet with P = 6.45 yrs) in July 2014 at $\sim$ 3.8 AU from the Sun[2]. The Rosetta orbiter remained in close proximity to the comet nucleus, and a small lander was released onto its surface.

Previous cometary missions have provided in situ measurements of cometary gas composition (e.g., for comet Halley; Eberhardt 1999). Ground-based observations have been also used to detect coma components (Mumma & Charnley 2011 and ref. therein). However, no direct measurements of cometary ice composition are avaliable so far. The NASA-Deep Impact cometary mission studied the nucleus of comet 9P/Temple 1 but from a more geological point of view (e.g., Thomas et al. 2007).

Rosetta instruments were meant to provide for the first time simultaneous measurements of both the nucleus and the coma of a comet. Our experiments, using realistic astrophysical ice analogs, can be used to understand the relation between the nucleus and the coma compositions and also the cometary ice conditions. However, as we discuss in Sect. 10.4, caution is needed to extrapolate these experimental results to a real cometary scenario.

The layout of this Chapter is as follows. In Sect. 10.2, we describe the experimental protocol. Section 10.3 presents the experimental results. Their astrophysical implications are discussed in Sect. 10.4. Section 10.5 summarizes the main conclusions.

11.2 Experimental setup

The results presented here have been obtained using the novel InterStellar Astrochemistry Chamber (ISAC) at the Centro de Astrobiología (Muñoz Caro et al. 2010, Chapter 4, Sect. 4.1.1). The ISAC set-up is an ultra-high vacuum (UHV) chamber with a pressure about 4 x 10^{-11} mbar, which corresponds to a density of 10^6 cm^{-3} (Muñoz Caro et al. 2010), similar to that found in dense cloud interiors. Ice samples made by deposition of a gas mixture onto a KBr window at 8 K (achieved by means of a closed-cycle helium cyostat) were warmed up until a complete sublimation was attained. A silicon diode temperature sensor and a LakeShore Model 331 temperature controller were used, reaching a sensitivity of about 0.1 K. Complex gas mixtures were prepared in the gas line system, using a Pfeiffer Prisma quadrupole mass spectrometer (QMS) of mass spectral range from 1 to 100 amu with a Faraday detector, and electrovalves were used to control the flow of the components, thus allowing co-deposition of gas mixtures with the desired composition.

The chemical components used in the experiments were H_2O (liquid), triply distilled, CH_3OH (liquid, Panreac 99.9%), CO (gas, Praxair 99.998%), CO_2 (gas, Praxair

---

[2] It arrived actually in August 2014.

Table 11.1. *IR feature used to calculate the column density of each component (frequencies and band strengths for pure ices at 8 K).*

Molecule	Vibrational mode	Frequency (cm^{-1})	Band strength (cm $molec^{-1}$)
H_2O	stretching O-H	3280	2.0×10^{-16} [a]
CO	stretching C=O	2138	1.1×10^{-17} [b]
CO_2	stretching C=O	2344	7.6×10^{-17} [c]
CH_3OH	stretching C-O	1025	1.8×10^{-17} [d]
NH_3	umbrella mode	1070	1.7×10^{-17} [e]

[a] From Hagen 1981. [b] From Jiang et al. 1975. [c] From Yamada & Person 1964. [d] From d'Hendecourt & Allamandola 1986. [e] From Sandford & Allamandola 1993.

99.996%), and NH_3 (gas, Praxair 99.999%), which was deposited through the second deposition tube.

The evolution of the solid sample was monitored by in situ Fourier transform infrared (FTIR) transmittance spectroscopy (see also Chapter 4, Sect. 4.1.4), using a Bruker Vertex 70 spectrometer equipped with a deuterated triglycine sulfate detector (DTGS). The IR spectra were collected after ice deposition at 8 K, or every five minutes during warm-up, with a spectral resolution of 2 cm^{-1}. Column densities of each species in the ice were calculated from the IR spectra using the formula

$$N = \frac{1}{A} \int_{band} \tau_\nu \, d\nu, \tag{11.1}$$

where N is the column density in molecules cm^{-2}, τ_ν the optical depth of the absorption band, and A the band strength in cm $molecule^{-1}$, as derived from laboratory experiments (Table 11.1). Band strengths were measured for pure ices made of one molecular component. The same values are usually adopted in ice mixtures, which introduce an uncertainty of about 20-30% (d'Hendecourt & Allamandola 1986).

The desorbing molecules were detected by a second Pfeiffer Prisma QMS of mass spectral range from 1 to 200 amu with a Channeltron detector, which is situated $\sim$ 17 cm apart from the sample (see also Chapter 4, Sect. 4.1.5). Gas-phase molecules were ionized by low energy ($\sim$ 70 eV) electron bombardment. Every species was monitored through its main mass fragment (except for NH_3), namely: m/z=18 (H_2O), m/z=28 (CO, with a small contribution of CO_2 fragmentation into CO^+ of, approximately, 10% of the m/z=44 signal), m/z=31 (CH_3OH; in addition, the ion molecule with m/z=32 coincides with O_2), and m/z=44 (CO_2). Ammonia, NH_3, was monitored through the mass fragment m/z=15 to avoid confusion with the mass fragment m/z=17 of H_2O. The m/z=17 signal was, nonetheless, used to confirm that the m/z=15 signal was not produced by contaminants present in small amounts.

An overview of all the experiments is shown in Table 11.2. All ice analogs have column densities above one hundred monolayers (1 ML is commonly defined as 10^{15} molecules cm^{-2}), which are well above the canonical thickness of a thin interstellar ice

Table 11.2. *Composition of the ice mixture measured with FTIR spectroscopy at 8 K. For each experiment, the first row indicates the abundance (by number of molecules) in percent relative to water, while the second row shows the absolute abundance (also in percent).*

Exp	H_2O (%)	CO (%)	CO_2 (%)	CH_3OH (%)	NH_3 (%)	$N/10^{15}$ mol/cm^2
E1 [a]	100.0	0.0	0.0	0.0	0.0	1554.61
	100.0	0.0	0.0	0.0	0.0	
E2 [a]	0	100.0	0.0	0.0	0.0	104.97
	0.0	100.0	0.0	0.0	0.0	
E3 [a]	0.0	0.0	100.0	0.0	0.0	134.88
	0.0	0.0	100.0	0.0	0.0	
E4 [a]	0.0	0.0	0.0	100.0	0.0	190.81
	0.0	0.0	0.0	100.0	0.0	
E5 [a]	0.0	0.0	0.0	0.0	100.0	154.60
	0.0	0.0	0.0	0.0	100.0	
E6 [b]	100.0	7.8	6.8	1.6	0.0	308.69
	86.1	6.7	5.8	1.3	0.0	
E7 [b]	100.0	6.6	27.9	3.1	3.4	1395.54
	70.9	4.7	19.8	2.2	2.4	
E8 [b]	100.0	0.0	0.0	9.3	0.0	109.52
	91.5	0.0	0.0	8.5	0.0	
E9 [b]	100.0	0.0	0.0	68.6	0.0	385.58
	59.3	0.0	0.0	40.7	0.0	
E10 [b]	100.0	8.7	20.2	5.7	5.7	749.50
	71.2	6.2	14.4	4.1	4.1	
E11 [a]	100.0	15.0	10.3	7.2	8.0	912.43
	71.2	10.7	7.3	5.7	5.1	

[a]Heating rate = 1 K/min. [b]Heating rate = 2 K/min

mantle (~ 40 ML; Bisschop et al. 2006). Therefore, these experiments more faithfully reproduce the thermal annealing of thicker ice mantles formed in cold circumstellar regions by grain agglomeration (and even cometary ices, see Sect. 11.4). Pre-cometary ice analog composition in experiments E10 and E11 is similar to that found in most interstellar and pre-cometary icy environments (Mumma & Charnley 2011 and ref. therein). We also performed additional experiments (E6-E9) involving ices with a different composition to study in depth some particular effects. Experiments with pure ices of each component were performed as references to study mixture effects (E1-E5).

11.3 Experimental results and discussion

11.3.1 Mixture effects on TPD of a pre-cometary ice analog

Figure 11.1a shows the TPD curves of the pure ices (E1-E5), which are measured with the QMS of ISAC. The ices were deposited at 8 K and subsequently warmed up with a heating rate of 1 K/min. All curves are similar to those reported in previous works (e.g., Collings et al. 2004) with a broad feature that peaks at a different temperature according to the sublimation energy or the volatility of the species. The bumps that appear in these broad features are due to phase changes occurring in the ice between different amorphous structures, or from an amorphous to a crystalline phase. In all cases the previous structure has a higher vapor pressure. Therefore, the desorption rate first increases with temperature, then decreases as the phase change occurs, and increases again after it is completed. These bumps are more easily observed for thick ices (Brown et al. 2006).

Unlike the rest of the studied molecules, CO molecules bind more strongly to the KBr substrate than to themselves. Therefore, its curve presents two peaks: the first peak at T = 29.9 K corresponds to the bulk (multilayer) desorption, while the second peak at T = 56.1 K[3] corresponds to molecules desorbing directly from the substrate (monolayer desorption) [3].

Figure 11.1b shows the TPD curve of each ice component in a pre-cometary ice mixture co-deposited at 8 K and warmed up with a heating rate of 2 K/min (experiment E10). All species show desorption peaks at temperatures near the ones corresponding to pure ices. Desorption of NH_3 and CH_3OH at temperatures compatible with pure desorption was not previously documented for co-deposited mixtures (Collings et al. 2004; Brown et al. 2006). Desorption of molecules from a pure ice environment is considered evidence of segregation occuring in the ice mixture, at least to some extent (Bisschop et al. 2006). Segregation of species during thermal annealing is studied in more depth in Sect. 11.3.5.

We detect the two desorption peaks of CO between 30 K and 50 K[3], as reported in Collings et al. (2004) for a co-deposited binary mixture, and also a third peak at a temperature below 30 K thanks to a better sensitivity of the QMS and a slower heating rate. The peak detected at 29.0 K and the peak at 49.8 K[3] correspond to the multilayer and monolayer[3] desorption of CO ice, respectively, which are also observed in the pure ice experiment (E2, Fig. 11.1a). The origin of the peak at 35.9 K, attributed by Collings et al. (2004) to monolayer desorption, is not fully understood.

In addition, CO molecules in the ice keep desorbing continuously at temperatures higher than those corresponding to multilayer and monolayer desorptions, according to the QMS data, see Fig. 11.1a. This was confirmed by means of IR spectroscopy. Figure 11.4 shows the evolution of the C=O stretching band at 2139 cm^{-1} during warm-up of the pre-cometary ice mixture in experiment E10. The absorbance decreases between the monolayer desorption at $T \sim 50$ K and the next desorption peak at $T \sim 146$ K. Assuming that the band strength does not change very significantly with temperature, as it is the case for pure CO ices, the column density drops from ~ 81 % of its initial value at $T \sim 63$ K to ~ 48 % at $T \sim 133$ K.

All the species except H_2O present desorption peaks at temperatures higher than the corresponding temperature for pure ices. This indicates that these molecules are retained in the water ice structure (Bar-Nun et al. 1985; Collings et al. 2004; Fayolle et al. 2011). A fraction of the trapped molecules is released in the "volcano" desorption (Smith et al. 1997) when the change from amorphous to cubic crystalline water ice occurs at $T \sim 160$ K. Volcano desorption of NH_3 molecules in co-deposited mixtures with water was not reported in Collings et al. (2004) , while volcano desorption of CH_3OH had already been detected by Brown et al. (2006). Another fraction of the trapped molecules co-desorbs later with water, which peaks at T $\sim$ 171 K.

---

[3] After publication of this paper, it was found that the second desorption peak is actually an artifact (see Chapter 6 for more information).

A second volcano desorption in the 160 - 170 K temperature range, corresponding to the release of molecules during the phase change from cubic to hexagonal water ice, is probably responsible for the shift between the co-desorption peaks temperature (T $\sim$ 166 K) and the water desorption peak temperature. This transformation takes place at 213 K in pure ices (Dowell & Rinfret, 1960), but the presence of large quantities of trapped molecules eases the phase change at a lower temperature range (Notesco & Bar-Nun, 2000). Therefore, we found that

- No shift is detected when the concentration of H_2O is above 85% (E6, Fig. 11.2a; E8, Fig. 11.2d).
- A shift of $\sim$ 5 K is observed when the concentration is $\sim$ 70% (E7, Fig. 11.2b; E10, Fig 11.1b; E11 Fig. 11.1c).
- A shift of $\sim$ 10 K is observed when the concentration is below 60% (E9, Fig. 11.2e).

The three types of desorption described so far (desorption as for the pure ice, volcano desorption and co-desorption with water) are common to most of the binary mixtures with H_2O. In a first approximation, the thermal desorption behavior of interstellar and cometary ices is dominated by interactions with the water ice matrix (diffusion and entrapment of molecules within the water ice structure). However, co-desorption of the three most volatile species (CO, CO_2, and NH_3) with CH_3OH at T $\sim$ 146 K is also observed in three of the studied multicomponent mixtures, where desorption of methanol at a temperature near the one corresponding to the pure ice is detected (E10, Fig 11.1b; E11, Fig. 11.1c; and E7, Fig. 11.2b). These co-desorption peaks cannot be reproduced in binary ice mixtures with water.

Effects of the heating rate

Figure 11.1c shows the TPD curves of a pre-cometary ice mixture with a heating rate of 1 K/min (E11). The curves are rather similar to those observed in experiment E10 (Fig. 11.1b) with a similar ice composition and thickness and a heating rate two times faster (2 K/min). All desorption peaks observed in Fig. 11.1b are detected in Fig. 11.1c with the addition of a second co-desorption bump at T $\sim$ 174 K. Temperatures of most of the desorption peaks are cooler in experiment E11 (see Table 10.3), as it is expected for a slower heating rate (see Sect. 10.3). It is unclear, though, why monolayer desorption of CO takes place at higher temperatures[3].

11.3.2 Binding energies of pure ices

The desorption rate of pure ices can be modeled by the Polanyi-Wigner equation[4],

---

[4] This section has been sligthly changed compared to the published version of the paper

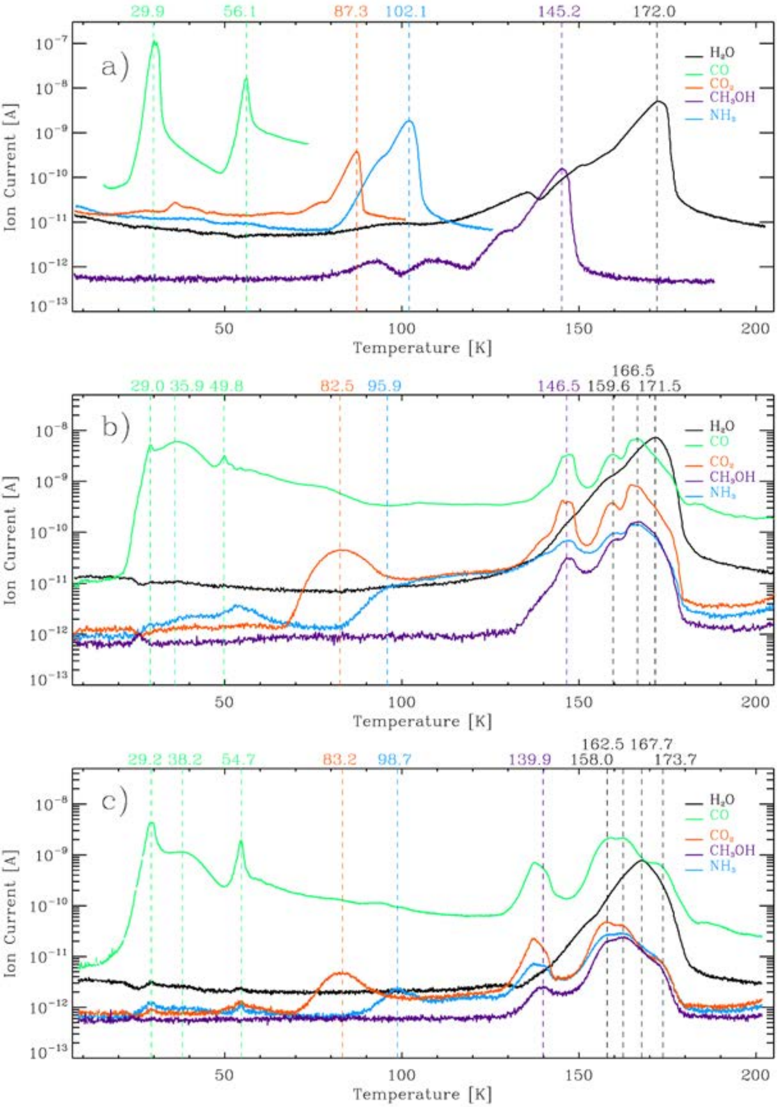

Figure 11.1. *The TPD curves of each component in experiments* ***a)*** *E1-E5 (pure ices),* ***b)*** *E10 (pre-cometary ice mixture with heating rate = 2 K/min). Desorption of a molecule with mass fragment m/z=15 at $T < 60$ K does not correspond to NH_3, since that feature is not shared with the m/z=17 fragment (not shown for clarity), and it may be due to a contaminant,* ***c)*** *E11 (pre-cometary ice mixture with heating rate = 1K/min). Temperatures of desorption peaks are indicated. Ion current in the y-axis corresponds approximately to the partial pressure (mbar) in the main chamber. Note that the y-axis is on a logarithmic scale.*

Desorption peak	Temperature (K) E11	E10
CO multilayer	29.2	29.0
CO monolayer	38.2	35.9
	54.7	49.8
CO_2	83.2	82.5
NH_3	98.7	~95.9
CH_3OH	140.0	146.5
volcano	158.0	159.6
co-desorption w/ H_2O	162.5	166.5
H_2O	167.7	171.5

Table 11.3. *Temperature of desorption peaks in experiments E11 (Fig. 11.1c, heating rate = 1 K/min) and E10 (Fig. 11.1b, heating rate = 2 K/min). Temperature of the ammonia desorption peak in E10 (Fig. 11.1b) is not well constrained due to the shape of the curve. Temperatures of volcano and co-desorption peaks are approximate, since they do not coincide exactly for all the species.*

$$\frac{dN_g}{dt} = \nu_i N_s^i exp(-E_{des}/T), \tag{11.2}$$

where dN_g/dt is the desorption rate in molecules cm^{-2} s^{-1}, ν_i a pre-exponential constant[5] for order i in molecules^{1-i} cm$^{-2(1-i)}$ s^{-1}, N_s the column density of the desorbing ice at time t in molecules cm^{-2}, E_{des} the binding energy in K, and T the ice temperature in K at time t.

A zeroth order (i = 0) kinetics is a reasonable approximation for multilayer desorption (Noble et al. 2012). The derived binding energy does not vary significantly, though, when a zeroth or a first order kinetics is assumed for a particular desorption process (Luna et al. 2014).

For desorption processes following a zeroth order kinetics, the desorption peak temperature depends (in addition to the binding energy and the pre-exponential factor) on the deposited ice thickness, and the heating rate applied. In particular, a change in the initial ice thickness of an order of magnitude leads to a variation of ~10% in the ratio $\frac{E_{des}}{RT_{peak}}$ (Luna et al. 2017); while slower heating rates lead in general to lower desorption peak temperatures.

Desorption of pure ices can thus be fitted using the Polanyi-Wigner expression and the relation,

$$\frac{dN_g}{dt} = \frac{dN_g}{dT}\frac{dT}{dt}, \tag{11.3}$$

where dT/dt is the heating rate.

Table 10.4 presents an estimate of the pre-exponential factor (assuming a constant pre-exponential factor) and the binding energy for the five pure ices, assuming zeroth

---

[5] After publication of this paper, Luna et al. (2015) reported that the pre-exponential factor depends on the temperature.

Table 11.4. *Desorption rate parameters for the five pure ices.*

Species	$\nu_0/10^{27}$ (mol cm^{-2}s^{-1})	E_{des} (K)	Estimated E_{des} (K)
CO	$6.5^{+15.3}_{-4.6}$	890±35	899
CO_2	$5.2^{+4.3}_{-1.6}$	2605^{+50}_{-30}	2625
NH_3	$2.1^{+2.7}_{-1.2}$	2965±80	3070
CH_3OH	$5.3^{+16.0}_{-2.7}$	4355^{+200}_{-100}	4366
H_2O	$32.1^{+12.8}_{-8.5}$	5165±55	5172

Columns 2 and 3: Pre-exponential factor and binding energies assuming the Polanyi-Wigner desorption rate equation, a constant pre- exponential factor, and zeroth order kinetics. Errors arise from the range of values leading to a similar χ^2. Column 4: estimated binding energy from equation 4.

order kinetics. We used the binding energy estimated by the TPD peak position with equation 4 (Attard & Barnes 1998, Luna et al. 2017) as the initial E_{des} for the fit.

$$E_{des} = T_{des} \times 30.068, \tag{11.4}$$

and a χ^2 parameter to manually find the best fit to the experimental desorption curves. Therefore, errors indicated in Table 10.4 arise from the range of values leading to a similar χ^2. In Luna et al. (2015) a more accurate, linear regression of the logartihm of the desorption rate *versus* 1/T is used to obtain E_{des} and $\nu(T)$.

The pre-exponential constant for the CO desorption peak is one order of magnitude larger than the values previously reported[5], while the binding energy coincides within errors (Muñoz Caro et al. 2010; Noble et al. 2012). The binding energy obtained for the CO_2 desorption peak also coincides within errors with the value reported by Sandford & Allamandola (1990), although it is $\sim$ 10 % larger than that reported by Noble et al. (2012) while the pre-exponential constant is a factor $\sim$ 5 larger in our case. Bolina et al. (2005b) used a desorption order of 0.25±0.05 for the NH_3 desorption peak leading to a binding energy close to the one reported here, but a pre-exponential constant two orders of magnitude lower. In the case of CH_3OH, the binding energy in Table 10.4 is within the range of values reported by Bolina et al. (2005a), where a desorption order of 0.35±0.21 is used. Pre-exponential constant for H_2O desorption coincides within errors with that reported in Fraser et al. (2001), although the binding energy we obtained is $\sim$ 10 % lower.

11.3.3 Entrapment of molecules in multicomponent ices

Since ice diffusion barriers are proportional to the volatility of the species (Öberg et al. 2009), volatile molecules like CO or, to a lesser extent, CO_2, are able to diffuse more easily through the amorphous solid water. Therefore, multilayer and/or monolayer desorption peaks are usually detected for these two species. In exchange, less volatile components, like NH_3 and CH_3OH, do not diffuse so easily, and are retained to a larger extent within the water ice structure. Desorption of NH_3 and CH_3OH prior to the volcano desorption had not been previously detected in co-deposited mixtures (Collings et al. 2004; Brown et al. 2006). This might be due to a lower sensitivity of the mass spectrometers used in previous works and the faster heating rate applied, which hinders the detection of these desorptions. These peaks have been detected in our pre-cometary ice mixtures (Figures 11.1b and c) with similar mixture ratios and thicker ices.

We have studied the effect of the concentration on the entrapment of NH_3 and CH_3OH molecules (experiments E6-E10, Fig. 11.2a-e) using ice analogs with a different composition than that of the pre-cometary ice mixtures. The fraction of trapped molecules can be inferred from the relative intensities of the peaks corresponding to pure desorption and the volcano and co-desorption peaks, which correspond to desorption of trapped molecules. As it has been reported for other species, this fraction decreases with an increase of the species concentration relative to water:

- Below a concentration of $\sim$ 2% relative to water, desorption of CH_3OH, expected at T $\sim$ 145 K according to Fig. 11.1a, was not detected (E6, Fig. 11.2a), and only volcano and co-desorption peaks were observed. Therefore, all CH_3OH molecules were trapped in the water ice structure.
- With a concentration of $\sim$ 3%, desorption of CH_3OH at T $\sim$ 149 K, prior to the volcano and co-desorption peaks, was clearly detected thanks to the co-desorption of CO and CO_2 (E7, Fig. 11.2b)). The partial pressure of NH_3 in the chamber also increases slightly in the temperature range at which pure desorption of this species is expected.
- Above a concentration of $\sim$ 5%, desorption peaks equivalent to those of pure NH_3 and CH_3OH, respectively, at 95.9 K and 146.5 K are clearly identified (E10, Fig. 11.2c).
- The intensity of the desorption peak equivalent to pure CH_3OH increases with its concentration in the water-dominated ice matrix (E8, Fig. 11.2d; E9, Fig. 11.2e).

Clear trends are observed regardless of the total column density deposited in each experiment, which indicates that the total thickness of the ice is not as relevant for ices of a few hundred monolayers as it is for thin ices.

11.3.4 Mixture effects on IR spectra of a pre-cometary ice analog

The IR spectra collected during the heating of the ice analogs compliment the analysis of the TPD data. Figure 11.3 shows the infrared spectrum at 8 K of the pre-cometary ice mixture in experiment E11, along with a spectral fit consisting of the sum of the individual pure ice spectra (E1-E5) that are also registered at 8 K, after scaling with a factor to reproduce the composition of the ice mixture.

The IR spectrum of the pre-cometary ice mixture appears to be fairly well reproduced by the sum of individual spectra of pure ices, although some significant differences are observed, which are discussed below in order of decreasing wavenumber. Most of these differences are due to interactions between water molecules and the rest of ice components and have been previously reported for binary mixtures. This is in line with the similarity between TPD curves in pre-cometary ice mixtures and in binary mixtures with the exception for the co-desorption of CO, CO_2, and NH_3 with CH_3OH, as mentioned in Sect. 10.3.1.

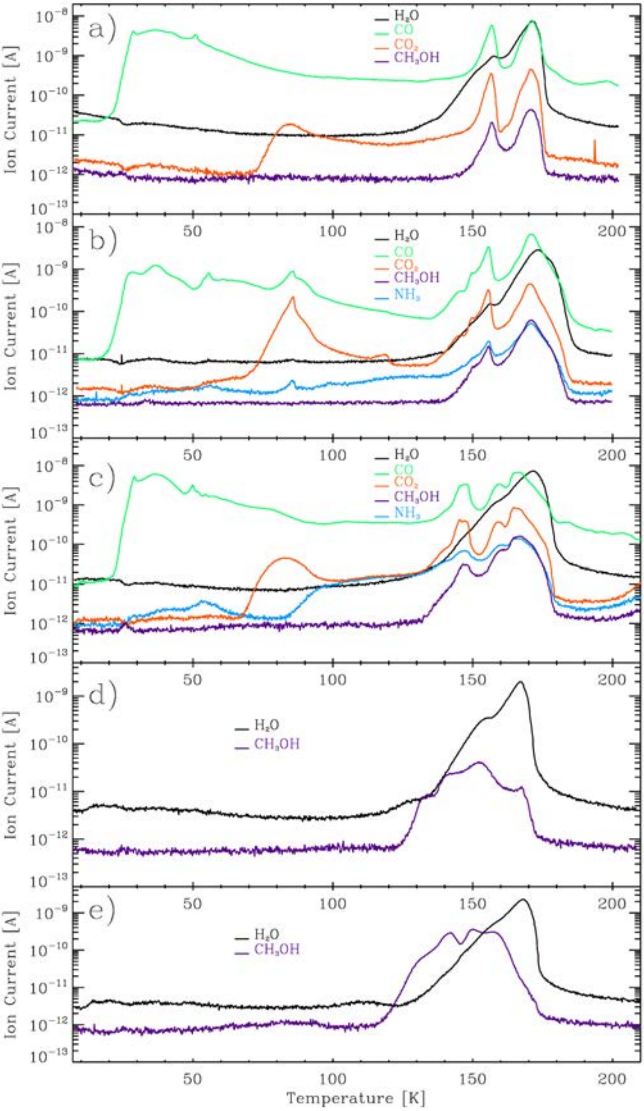

Figure 11.2. *The TPD curves of each component in experiments* ***a)*** *E6,* ***b)*** *E7,* ***c)*** *E10,* ***d)*** *E8, and* ***e)*** *E9. The concentration of CH_3OH in the mixture increases from* ***a)*** *to* ***e)****. Ion current in the y-axis corresponds approximately to the partial pressure (mbar) in the main chamber. Note that the y-axis is on a logarithmic scale.*

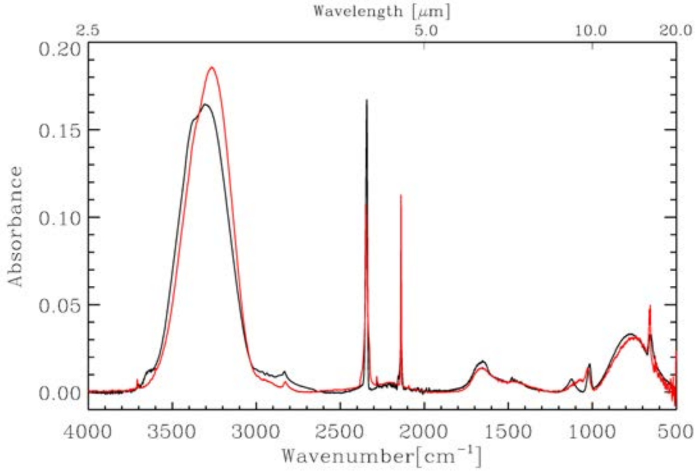

Figure 11.3. *Black: IR spectra of a pre-cometary ice mixture (E11) registered at 8 K. Red: Sum of the IR spectra of individual pure ice components (E1-E5) registered at 8 K; they were multiplied by a factor to reproduce the composition of the pre-cometary ice mixture.*

There is a new feature at ~ 3650 cm^{-1} which is not reproduced by the sum of pure ice spectra. This feature arises from the interactions of CO and CO_2 molecules with the amorphous solid water (Hagen et al. 1983). Hydrogen bonds formed between CO_2 and H_2O molecules are weaker than those formed between water molecules. The molecule CO is not even able to form these bonds. Therefore, there are some water OH-groups, who are not connected to the hydrogen bonded network and whose O-H stretching mode has a higher frequency, leading to the appearance of this feature in the blue side of the O-H stretching band.

Moreover, the extent of intermolecular coupling in the water ice structure becomes smaller and the hydrogen bonds that do form become weaker, which explains the blueshift of the O-H stretching band of H_2O, from 3262 cm^{-1} to 3307 cm^{-1} due to the presence of CO and CO_2. In addition, this band has a lower intensity than expected, since the induced polarization is reduced, but has a more intense low-frequency wing due to the presence of CH_3OH and NH_3 in the ice mixture (Hagen et al. 1983).

The band strength of the N-H stretching mode of NH_3 seems to be also enhanced in the mixture, since the shoulder at ~ 3370 cm^{-1} is more intense than expected. Due to the overlap with the O-H stretching mode of H_2O, this mixture effect is very difficult to quantify (d'Hendecourt & Allamandola 1986).

The C=O stretching band of CO_2 at 2344 cm^{-1} is slightly redshifted to 2342 cm^{-1} (see left panel of Fig. 11.5), and it is sharper in the mixture. The behavior of this band in mixtures with H_2O depends on the concentration of CO_2 and also on the presence of other polar molecules, such as CH_3OH (Sandford & Allamandola 1990; Ehrenfreund et al. 1999).

The C=O stretching band of CO at 2139 cm^{-1} has a shoulder on its blue side, peaking at $\sim$ 2152 cm^{-1} (see Fig. 11.4). This shoulder is believed to originate from the interaction of CO molecules with dangling O-H bonds of water molecules at a surface or discontinuity that cannot complete a tetrahedrally hydrogen bonded network (Collings et al. 2003a). Surprisingly, this peak is not observed in astronomical spectra, which can be reproduced with a mixture of solid CO and CH_3OH without the presence of H_2O (Cuppen et al. 2011).

The band strength of the O-H bending mode at $\sim$ 1650 cm^{-1} is increased in the mixture due to the presence of CO and CO_2 (Hagen et al. 1983).

The umbrella mode of NH_3 at 1067 cm^{-1} is blueshifted to 1124 cm^{-1} in the mixture. This is observed in binary mixtures with H_2O (Hagen et al. 1983; d'Hendecourt & Allamandola 1986). The relatively strong shift of this band manifests the intermolecular bond strength between NH_3 and H_2O molecules.

On the other hand, the C-O stretching band of CH_3OH is redshifted from 1025 cm^{-1} to 1016 cm^{-1}. This effect has been also observed in binary mixtures (d'Hendecourt & Allamandola 1986). This relatively small shift indicates that the hydrogen bond strength between CH_3OH and H_2O molecules in the ice, and the CH_3OH - CH_3OH bonds are only slightly different. This observation is confirmed by the similar binding energies inferred from the desorption temperatures.

The degenerate bending modes of CO_2 at $\sim$ 655 cm^{-1} lose the double-peak structure in the mixture, as previously reported for binary mixtures with water (Sandford & Allamandola 1990).

11.3.5 Evolution of IR spectra during thermal annealing

Figure 11.4 shows the gradual disappearance of the shoulder in the blue side of the C=O stretching band of CO during the warm-up. It is negligible at $\sim$ 63 K and has completely disappeared at $\sim$ 83 K. This phenomenon is thought to be an effect of the decrease in the number of dangling O-H bonds in the water ice structure during the transition from the highly porous to the less porous amorphous solid water (Sandford et al. 1988; Collings et al. 2003b). Öberg et al. (2009) observed an increase in the intensity of the main peak at 2138 cm^{-1} relative to the shoulder at T $\sim$ 25 K (before the onset of the phase transition), suggesting that the change in the IR band is due to segregation of CO in the ice. Since the loss of the shoulder in Fig. 11.4 takes place along with a redshift of the main peak, which is characteristic of binary mixtures with water (Sandford et al. 1988) in our experiment these effects are most likely due to structural changes in the ice. Therefore, no strong evidence of CO segregation is found in the IR spectra, despite the detection of desorption peaks at temperatures corresponding to pure CO ice in the TPD curves. This probably means that CO segregation takes place only to a small extent (to a small spatial extent within the ice and/or in a short time span before multilayer desorption occurs) and its effects cannot be detected with the FTIR spectrometer because it is less sensitive than the QMS.

The evolution of the CO_2 stretching and bending bands is shown in the left and right panel of Fig. 11.5, respectively. The C=O stretching band at 2342 cm^{-1} slightly increases its intensity between 65 K and 125 K at the same temperature range in which pure CO_2 desorption takes place. This behavior is shared with the C=O stretching band of pure

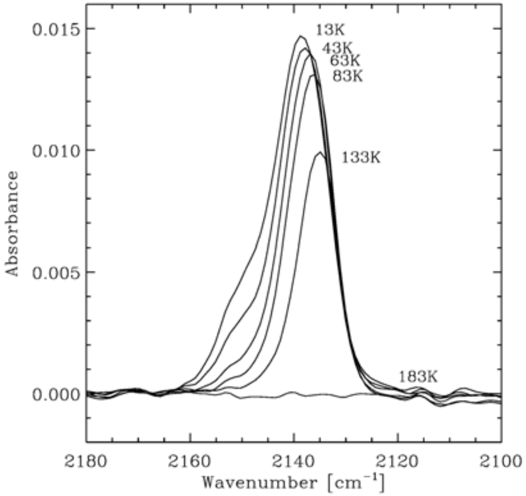

Figure 11.4. *Evolution of the C=O stretching band of CO during the warm-up of a pre-cometary ice mixture (experiment E10).*

CO_2 ice, but we do not observe other effects of ice segregation, as reported by Öberg at al. (2009) for a binary mixture of CO_2 and H_2O, such as the blueshift or the appearance of a new feature in the blue side of this band (Instead, the redshift increases to 2339 cm^{-1} at higher temperatures in our ice mixture.), or the double peak structure of the degenerate bending modes. Again, there is no strong evidence of CO_2 segregation in our IR spectra, probably because it takes place only to a small extent, as it does in the case of CO molecules.

The feature at ~3650 cm^{-1}, which corresponds to the O-H stretching mode of water molecules that are not completely connected to the hydrogen bonded network due to interactions with CO and CO_2 molecules, gradually disappears during the warm-up (left panel of Fig. 11.6). This is most likely an effect of transition to a more compact ice structure (Isokoski 2013), since there is no reliable evidence of CO and CO_2 segregation (see above). The intensity of the bending mode of H_2O decreases in the same temperature range (right panel of Fig. 11.6), which can also be explained by compaction.

Figure 11.7 shows the evolution of the umbrella mode of NH_3 at 1124 cm^{-1} and the C-O stretching mode of C H_3OH at 1016 cm^{-1}. No substantial changes are observed in the former, but the latter changes its band profile and peak frequency during the warm-up. Above a temperature of T ~ 110 K before the onset of the desorption of CH_3OH, the peak shifts toward shorter wavelengths. At T ~ 145 K, the band is broader and peaks at a frequency close to that of pure CH_3OH ice. At higher temperatures, the red component of the band gradually disappears and the peak is shifted to ~ 1034 cm^{-1}. This indicates that a fraction of the CH_3OH molecules segregates in the ice at

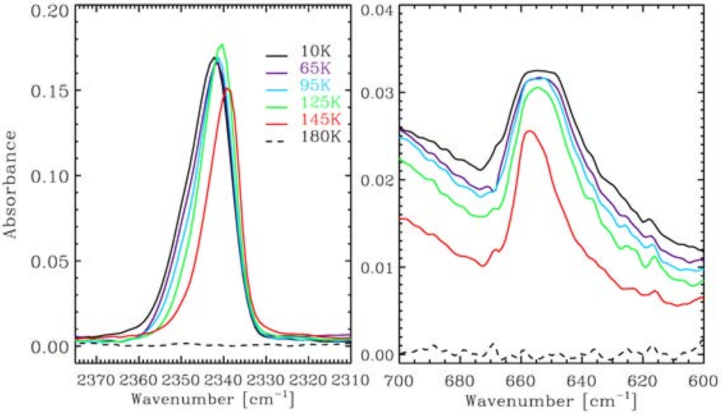

Figure 11.5. *Evolution of the IR bands of CO_2 during the warm-up of a pre-cometary ice mixture (experiment E11). Left: C=O stretching mode at $\sim$ 2342 cm^{-1}. Right: bending mode at $\sim$ 655 cm^{-1}.*

temperatures above T $\sim$ 110 K, while other CH_3OH molecules form a type II clathrate hydrate (Blake et al. 1991). Segregated molecules are able to desorb more easily than molecules in the clathrate hydrates, which mainly desorb at higher temperatures.

CH_3OH segregation

The CH_3OH molecules segregate enough to an extent to be detected by the FTIR spectrometer. We have fitted the C-O stretching band of CH_3OH in the IR spectra collected above T $\sim$ 110 K by using three Gaussians to estimate the contribution of the three types of methanol that can be found in the ice sample, namely: mixed methanol (centered at 1016 cm^{-1}), segregated methanol (centered at 1025 cm^{-1}), and methanol forming a type II clathrate hydrate with water molecules (centered at 1034 cm^{-1}). A fourth Gaussian was used to take into account the contribution of the blue wing of the H_2O librational band.

Figure 11.8 shows the fit for three spectra at T $\sim$ 110 K, 150 K, and 160 K, respectively. We used a χ^2 parameter to find the best fit in each case. The evolution of the contribution of each Gaussian to the total area of the C-O stretching band is shown in Fig. 11.9. Above T $\sim$ 110 K, the contribution of segregated methanol and methanol in a type II clathrate hydrate to a lesser extent increases, while that of the mixed methanol decreases. At T $\sim$ 150 K, before the volcano desorption occurs, segregated methanol dominates in the ice mixture and above that temperature methanol in a type II clathrate hydrate becomes the major contributor to the IR band until it is completely desorbed.

A final confirmation of the methanol segregation can be found in the C-H stretching region of the spectrum. At these high temperatures, pure (segregated) CH_3OH should be in its crystalline form. When pure CH_3OH ice changes from the amorphous to the crystalline α structure, the asymmetric C-H stretching mode (which at 8 K is a wide

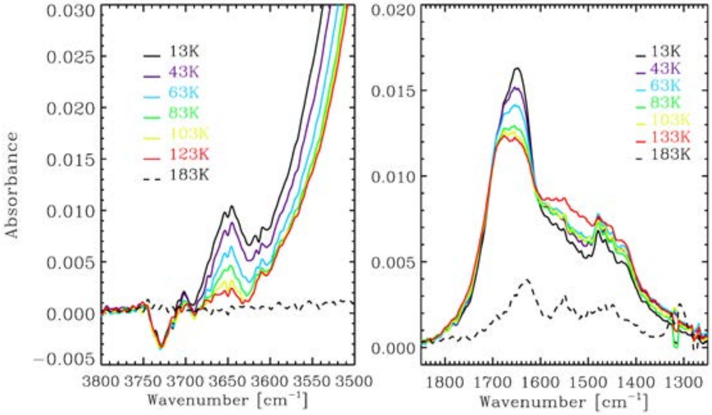

Figure 11.6. *Evolution of the IR bands of H_2O during the warm-up of a pre-cometary ice mixture (experiment E10). Left: O-H stretching mode at $\sim$ 3650 cm^{-1}. Negative absorbances are due to the atmospheric compensation applied by the spectrometer software. Right: O-H bending mode at $\sim$ 1654 cm^{-1}.*

band peaking at 2930 cm^{-1} with a shoulder at $\sim$ 2984 cm^{-1}) is perfectly resolved into the a′ (ν_2) and a″ (ν_9) modes at 2984 cm^{-1} and 2856 cm^{-1}, respectively, while the symmetric mode (ν_3) at 2827 cm^{-1} remains basically unchanged (Falk & Whalley 1961). Unfortunately, the ν_9 mode is barely detected in the pre-cometary ice mixture (Fig. 11.3), and it is not possible to confirm this process, but it is observed in a binary mixture with a higher concentration of methanol (experiment E9, Fig. 11.10). In this mixture, we observe three peaks at 2989 cm^{-1}, 2960 cm^{-1}, and 2933 cm^{-1} at 8 K, instead of the wide band peaking at 2930 cm^{-1}. These peaks may arise from the interaction between CH_3OH and H_2O. When the temperature raises to T $\sim$ 113 K, these three peaks begin to change, and at T $\sim$ 143 K, two peaks are clearly identified at frequencies near those of the a′ and a″ asymmetric stretching modes (2988 cm^{-1} and 2948 cm^{-1}). This proves that a fraction of CH_3OH molecules is actually segregating into its crystalline form.

It has been pointed out previously that segregation takes place if diffusion of molecules in the ice is possible and it is energetically favorable for molecules of the same species to group together, being ice diffusion barriers proportional to their volatility (Öberg et al. 2009). Therefore, the most volatile ice species, like CO, can diffuse easily within the water ice structure and, eventually, meet other CO molecules. However, since the CO - CO interaction is the weakest among the species studied here, only small groups of segregated CO molecules can be formed before they reach the ice surface and desorb or, alternatively, the segregated-CO seed is torn apart by stronger interactions with other species (mainly H_2O, since it is the major constituent in our pre-cometary ice analogs). On the other hand, less volatile species like CH_3OH can form larger groups of segregated molecules when the ice temperature is sufficiently high, despite the fact that they do not diffuse so easily through the ice structure. Once methanol molecules meet, the

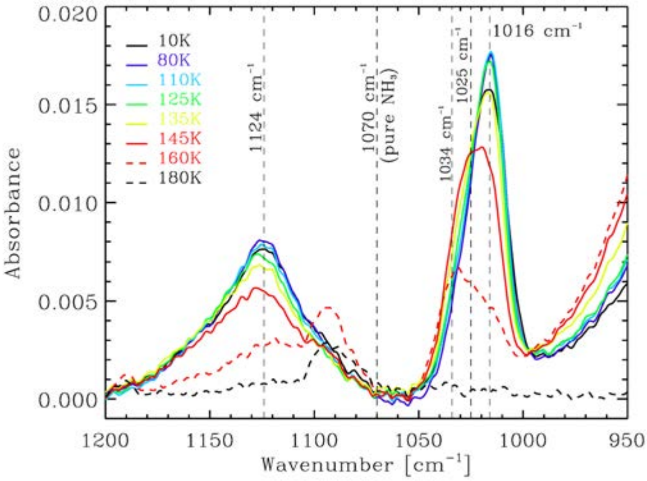

Figure 11.7. *Evolution of the umbrella mode of NH_3 and the C-O stretching mode of CH_3OH during the warm-up of a pre-cometary ice mixture (experiment E11).*

CH_3OH - CH_3OH interactions are stronger, since these molecules form hydrogen bonds with a similar strength to those formed by H_2O molecules (Bakkas et al. 1993; note that, unlike CO, CO_2, and NH_3, water and methanol are both liquids at standard conditions) In addition, methanol desorbs at higher temperatures compared to CO, CO_2, and NH_3. Therefore, segregated-CH_3OH seeds can grow without desorbing or being disrupted, forming larger regions of segregated CH_3OH which can be detected by the FTIR spectrometer.

11.4 Astrophysical implications

The heating rate used in our experiments is fast compared to most astrophysical scenarios, as it is generally the case in experimental simulations of astrophysical processes. The desorption behavior of an ice mixture does not strongly depend on the heating rate (see above), but differences in the desorption temperatures are usually found (e.g., Collings et al. 2004).

Using the kinetic parameters for pure H_2O ice desorption, Collings et al. (2004) performed a series of theoretical simulations of water ice desorption with different heating rates. The desorption peak reaches its maximum at $T \sim 160$ K for a heating rate of 4.8 K/min, similar to the value used in our experiments and at $T \sim 105$ K for a heating rate of 1 K/century, close to the heating rate in hot cores.

Thermal annealing of interstellar, circumstellar, and cometary ices takes place in three different stages of stellar evolution:

- Interstellar ice mantles covering dust grains are formed in dense molecular clouds ($T \sim 10$ K). These dust grains cycle between the dense and the diffuse interstellar

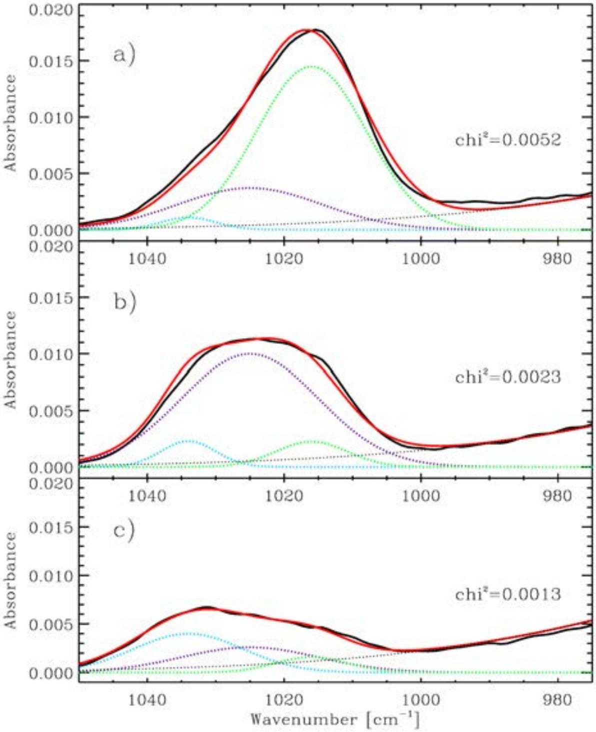

Figure 11.8. *The C-O stretching band of CH_3OH (black) fitted with the sum of three Gaussians (red), which account for: mixed methanol (green dotted, centered at 1016 cm^{-1}), segregated methanol (purple dotted, centered at 1025 cm^{-1}), and methanol forming a type II clathrate hydrate with water molecules (blue dotted, centered at 1034 cm^{-1}). A fourth Gaussian has been used to take into account the contribution of the blue wing of the H_2O librational band (black dotted). The IR spectra correspond to a pre-cometary ice analog (E11) at a) T = 110 K, b) T = 150 K, and c) T = 160 K. The χ^2 parameter is indicated for each fit.*

medium. Ice mantles do not survive the harsh radiation conditions of the diffuse medium. These cycles proceed until dust grains are incorporated in star-forming regions.

- Circumstellar ices are heated during the star formation, as the temperature of the central object increases. Some grains undergo transient episodes of ”flash-heating” lasting up to hundreds of hours according to the fluctuating X-wind model for CAIs and chondrules formation (Shu et al. 1996, 1997, 2001).

- Cometary ices are heated during late thermal evolution of comets around already formed stars, as the comet comes closer to the star during its orbit.

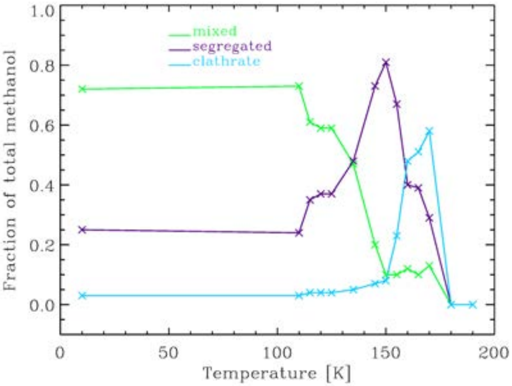

Figure 11.9. *Evolution of the contribution of mixed methanol (green), segregated methanol (purple), and methanol forming a type II clathrate hydrate (blue) to the total area of the C-O stretching band of CH_3OH during warm-up of a pre-cometary ice mixture (E11), according to fit with three Gaussians of the IR band. Temperatures for which the fit was done are indicated. Figure 11.8 shows three selected fits as an example.*

As it was mentioned in Section 10.2, thermal annealing of thick ice mantles, which are formed in outer regions of disks around high and low-mass protostars by grain agglomeration, is mimicked more faithfully in the TPD experiments presented in this work , due to the thickness of our ice analogs. We explain in Section 11.4.2 that our results can be also applied with some limitations to cometary ices.

11.4.1 Circumstellar ices

Chemical models of hot cores use the experimental data on TPD of ice analogs in the study of their astrochemical network (e.g., Viti et al. 2004; Wakelam et al. 2004). It was suggested that binary mixtures can be used as templates for more complex ice mixtures to model the desorption of interstellar and circumstellar ices (Fayolle et al. 2011). In our experiments, we have observed co-desorption of CO, CO_2, and NH_3 with CH_3OH in all the studied mixtures with an abundance of these species relative to water above $\sim 3\%$ (which falls in the range of typical abundances found in most astrophysical environments; see Mumma & Charnley 2011 and ref. therein). Appropiate TPD experiments with complex (at least tertiary) mixtures are thus needed to incorporate this co-desorption into the models.

The TPD curves and IR spectral evolution of our pre-cometary ice analogs allowed us to build a schematic representation of the thermal annealing process of ice mantles in circumstellar regions (Fig. 11.11). The heating rate applied to the pre-cometary ice mixtures in experiments E10 and E11 is of the same order of magnitude than that applied to ice mantles during the "flash-heating", as explained by the fluctuating X-wind model for CAIs and chondrules formation. Therefore, similar desorption temperatures

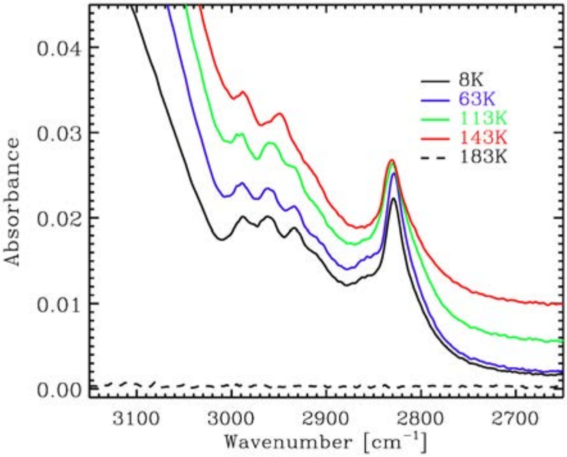

Figure 11.10. *Evolution of the C-H stretching modes of* CH_3OH *during the warm-up of a binary mixture (experiment E9). Spectra are offset for clarity.*

are expected in this case. We have scaled all laboratory temperatures to the scenario in which grains at a certain distance are heated as the temperature of the central object increases by multiplying them by a factor of 0.62. This factor corresponds to the relation between the desorption peak temperature of water ice in our experiments ($\sim$ 170 K) and the one expected for a slower heating rate (1 K/century; Collings et al. 2004)[6].

The temperature gradient generated in the circumstellar envelope by the central protostar leads to chemical segregation in the gas phase. High-angular resolution observations of protostellar envelopes represent the best chance to observe this phenomenon in space.

11.4.2 Cometary ices

The large size of a comet nucleus (up to 40 km in diameter) establishes several important differences between the simulations we have performed and the real processes that take place during the thermal annealing of a comet:

- Comet nuclei have a temperature gradient in their interiors and the temperature profile is not symmetric (Prialnik et al. 2008). The whole ice sample in TPD experiments is kept at the same temperature.

- The Deep Impact mission revealed that comet 9P/Temple 1 has an inhomogeneous composition at least at the surface layers (Thomas et al. 2007), while our ice analogs are expected to be homogeneously mixed.

---

[6] This is an approximation. Similar tehoretical simulations as those presented in Collings et al. (2004) for H_2O should be performed in order to correctly scale the laboratory temperatures to the astrophysical scenario.

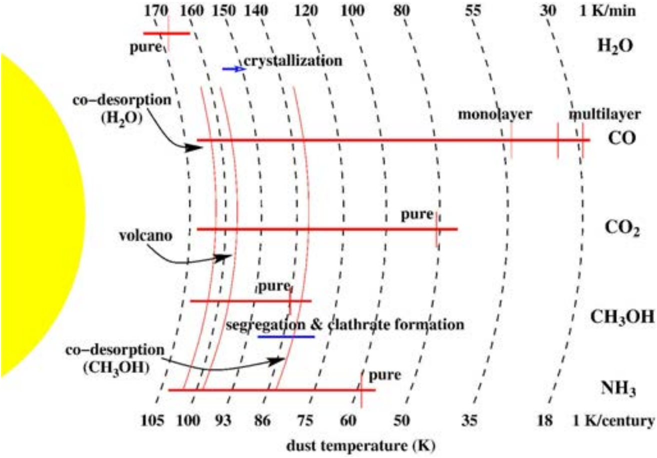

Figure 11.11. *Schematic representation of thermal annealing process of ice mantles in circumstellar regions based on our experimental results for the warm-up of a pre-cometary ice mixture (H_2O:CO:CO_2:CH_3OH:NH_3 = 100:10-20:10-20:5:5). Red lines represent the temperature ranges at which the species used in our pre-cometary ice analogs desorb. Approximate positions of desorption peaks are indicated with vertical red lines. Desorption of NH_3 and CH_3OH prior to volcano desorption takes place when their abundance relative to water is above ~ 3 % in the ice. Blue lines represent the temperature ranges at which structural changes in the ice occur. The top temperature scale corresponds to a heating rate of 1-2 K/min (used in experiments E10 and E11 with our pre-cometary ice mixtures and also suited to the "flash-heating" of dust grains during the periodic radial excursions considered in the fluctuating X-wind model for CAIs and chondrules formation). The bottom temperature scale corresponds to a first approximation to grains at a certain distance heated with a heating rate of 1 K/century, see text for details.*

- Molecules released from the ice can flow both outward (toward the cometary surface and the coma), or inward, due to the dynamic percolation through the comet nucleus (Notesco & Bar-Nun 2000).

- The energy balance in a comet, dominated by the solar energy during the late thermal evolution of these objects, could be more complex than that of our experimental set-up with a small substrate and a controlled warm-up process.

In any case, this work should contribute to a better understanding of the late thermal cometary evolution, particularly, of the formation of the coma, as volatiles begin to sublime when the comet approaches the Sun during its orbit. Assuming a symmetrical temperature profile and a homogeneous ice composition in the nucleus, our simulations would correspond to the warm-up process suffered by a finite cometary slice, which is not at the same temperature than the rest of the comet nucleus during the heating process. The thermal annealing of a comet could thus be seen in a first approximation, as the sum of the warm-up of every cometary slice with a missmatch between the temperature of each slice in a certain moment. Molecules flowing inward instead of outward could alter the composition of the coma compared to that of the nucleus.

From our results, we can infer that when a comet is at a distance to the Sun close enough to heat the cometary surface to a temperature of around 20 K, CO ice starts to desorb along with other volatile species that possess a similar desorption temperature, such as N_2 and O_2 (Collings et al. 2004), and the coma begins to form. As we have observed in our experiments, once the desorption of CO has begun, it desorbs continuously during the warm-up.

As the comet gets closer to the Sun, less volatile species like CO_2 desorb successively, although in small amounts. Desorption of NH_3 and CH_3OH will take place if their abundance relative to water is above ~ 3 % in the cometary ice. When the temperature in the most external layer is high enough to allow desorption of, for instance, CO_2, desorption of more volatile species like CO should be taking place in inner layers due to the temperature gradient of the comet nucleus. Similarly, if desorption of NH_3 begins in the most external ice layer, CO_2 and CO should be desorbing from inner layers. Therefore, the possible co-desorption of several species with CH_3OH should have no strong consequences on the composition of the coma because the same species that would co-desorb with CH_3OH should be also desorbing from inner layers.

The initially (small) CO-rich coma thus becomes more chemically complex as it is enriched with other less volatile molecules during the orbit of the comet. The contribution of the inner ice layers makes it difficult to predict the proportion in which volatiles are present in the coma at any time and also how this proportion varies as volatiles desorb from deeper inner layers simultaneously to the desorption of less volatile species from the outer layers. In any case, CO is expected to be the main component in the early stages of activity.

Once the temperature has reached the value at which phase transition between amorphous and crystalline water ice takes place, volcano desorption of all volatiles would increase the activity of the comet. After this event, desorption of water begins to be quite important, becoming the main component in the coma, as it is observed in infrared and radio spectroscopic surveys (Mumma & Charnley 2011 and ref. therein). We note that the detection of species in the coma also includes the "daughters" of parent ice molecules in the nucleus, making the interpretation of cometary data even more complex than outlined above.

11.4.3 The ESA-Rosetta cometary mission

Rosetta was scheduled to arrive at comet 67P/Churyumov-Gerasimenko in July 2014[7]. After that, the Rosetta orbiter remained in close proximity to the comet nucleus and a small lander was released onto its surface.

The Rosetta orbiter included eleven scientific instruments. The instrument ROSINA (Rosetta Orbiter Spectrometer for Ion and Neutral Analysis) was used to determine the composition of the comet atmosphere, playing a similar role to the QMS in our experiments. The Rosetta lander is known as Philae. There are two evolved gas analyzers (EGAs) among the ten instruments on board Philae: Ptolomey and COSAC (COmetary SAmpling and Composition experiment). The instrument COSAC is a combined gas chromatograph - mass spectrometer that was meant to analyze the volatile fraction of

---

[7] It arrived actually in August 2014.

Date	r_h (UA)	T (K)[7]	Heating rate (K/min)
01-07-2014	3.80	141.0	6.7×10^{-5}
01-08-2014	3.63	144.0	($\sim$ 3.0 K/month)
01-07-2015	1.35	236.7	2.0×10^{-4}
01-08-2015	1.25	245.7	($\sim$ 0.3 K/day)

Table 11.5. *Estimation of heliocentric distance, temperature, and heating rate of comet 67P/Churyumov-Gerasimenko during its orbit, as calculated using orbital parameters provided online by the Jet Propulsion Laboratory (NASA) and equation 5.*

surface and subsurface samples with special attention to the detection and identification of complex organic molecules. Alternatively, it could be operated in sniffing mode where only the mass spectrometer is used, analyzing the gas present in the ionization chamber (this gas is mainly composed of external gas in the case of high pressures; otherwise internal contamination dominates. Goesmann et al. 2012). While the Rosetta orbiter will probably survive perihelion passage, Philae may suffer overheating and cease functioning once the comet approaches its closest distance to the Sun[8].

Using a simple planetary energy balance equation, it was possible to estimate a mean temperature of the comet on its surface by knowing its heliocentric distance by the time Rosetta started the measurements and to make bold predictions of what the mass spectrometers were going to detect based on our laboratory results. Assuming that the comet is in radiative equilibrium, meaning that the incoming radiative energy emitted by the Sun and absorbed by the comet is equal to the radiation emitted by the comet, the temperature of its surface can be calculated as

$$T = (\frac{L_{sun}(1-a)}{16\pi\sigma r^2})^{1/4}, \tag{11.5}$$

where L_{sun} is the Sun luminosity, a the albedo of the comet, σ the Boltzmann constant, and r the heliocentric distance of the comet.

On July 1, 2014, the distance from the comet to the Sun was of about 3.80 AU. Assuming a cometary albedo of $a = 0.054$ (Kelley et al. 2009)[9], the mean temperature at the surface of the comet was T $\sim$ 141.0 K[9]. In our experiments with a heating rate of 1 K/min, water does not desorb substantially at this temperature. The coma should be thus composed of small amounts of more volatile species (mostly CO, with the presence of less volatile species like CO_2 and, maybe, NH_3 and CH_3OH). However, the heating rate applied to the comet during its orbit around the Sun is much slower than the one applied to the ice analogs in our simulations. Data from Table 11.5 allows us to make a rough estimate of the heating rate during the Rosetta approach and near the perihelion, after a year. As the comet got closer to the perihelion of its orbit, its velocity, and therefore, also the heating rate, increased. Combining the theoretical simulations performed by Collings et al. (2004) of water ice desorption with different heating rates and the cometary heating rate estimated in Table 11.5 by the time of arrival scheduled for Rosetta, we found that the desorption peak temperature for water ice in comet 67P/Churyumov-Gerasimenko should fall between 115 K and 130 K, approximately, This temperatures correspond to a heliocentric distance between 5.75 AU and 4.50 AU, according to equation (5)[10]. Therefore, superficial water ice should be detected already during the first measurements with an increasing activity in the next months[11]. It was difficult, though, to predict how the composition of the coma would be affected by desorption from different layers as the comet was heated by the Sun.

---

[8] Its fate was, however, even worse.

[9] The albedo of the comet was found to be lower than expected. Therefore, the cometary temperatures in this section are underestimated. Fortunately, this does not change the reported predictions.

Observations carried out with the Spitzer Space Telescope during the last passage of comet 67P/Churyumov-Gerasimenko did not detect signs of activity before r_h = 4.30 AU (Kelley et al. 2009). The authors thus expected to find an inactive or weakly active nucleus at the arrival of Rosetta. However, ground-based observations carried out at the VLT have recently revealed that the comet presented detectable activity at a heliocentric distance of r_h = 4.30 AU, which is based on the excess flux in the R-band assigned to dust brightness. Therefore, the comet was expected to be active again in March 2014 before the arrival of Rosetta (Snodgrass et al. 2013), which was in line with our predictions presented above. Analysis of previous observations also indicates that the peak of activity takes place about two months after perihelion (de Almeida et al. 2009).

11.5 Conclusions

We studied the temperature programmed desorption (TPD) of pre-cometary ice analogs with up to five components (H_2O, CO, CO_2, CH_3OH, and NH_3) using mass spectrometry to detect molecules desorbing to the gas phase and complementary infrared spectroscopy to study the composition, structure, and evolution of the ice during warm-up. Comparison with pure ice experiments, which are made of a single molecular component, revealed several effects on both the TPD curves and the IR spectra arising mainly from the interaction between H_2O, the major constituent of our pre-cometary ice analogs, and the rest of the species, and also between CH_3OH and the most volatile components.

All species presented desorption peaks at temperatures near the ones corresponding to pure ices. For NH_3 and CH_3OH, these desorption peaks were observed for the first time in water-rich ice analogs at T $\sim$ 97 K and T between 140 -147 K, respectively. Both species were previously classified as "water-like", since only peaks at temperatures close to water desorption were reported for co-deposited binary mixtures. Thermal desorption of ice mixture analogs with different abundances of NH_3 and CH_3OH have revealed that desorption in our experiments as in the pure ices is detected for ices with an abundance above $\sim$ 3 % relative to water.

Desorption of molecules from a pure ice environment suggest segregation of the species in the ice mixture to some extent. Only segregation of CH_3OH molecules was confirmed by means of IR spectroscopy. The C-O stretching band of CH_3OH at $\sim$ 1025 cm^{-1} is redshifted in the pre-cometary ice mixture at 8K, but a blueshift is observed at temperatures above $\sim$ 110 K, indicating segregation of this species and formation of a type II clathrate hydrate. Segregation of CO, CO_2, and NH_3 molecules may occur only to a small extent due to their weaker interactions.

---

[10] This estimated distance would be higher if a lower albedo was used.

[11] Water and carbon dioxide were indeed detected at the arrival of Rosetta (Migliorini et al. 2016).

Desorption peaks at temperatures higher than the corresponding temperature for pure ices are also observed for all the species, except for H_2O, which indicates entrapment of molecules within the water ice structure. The desorption peaks at T $\sim$ 159 K correspond to volcano desorption after crystallization of the water ice structure, while the peaks at T $\sim$ 165 K result from co-desorption with water. The shift between the water desorption peak at T $\sim$ 170 K and the co-desorption peaks temperature can be explained by the contribution of a second volcano desorption peak in the 160 - 170 K temperature range due to the phase change from cubic to hexagonal water ice. This phase change is eased by the presence of large quantities of trapped molecules (Notesco & Bar-Nun, 2000).

Prior to the volcano desorption, co-desorption of the more volatile species (CO, CO_2, and NH_3) with CH_3OH has been detected at T between 140 -147 K.

During thermal annealing of the ice analogs, CO, CO_2, and NH_3 molecules can find themselves in ice regions where segregated methanol is the dominant component due to the further segregation of CH_3OH. Methanol behaves similarly to water, forming hydrogen bonds with a similar strength. Therefore, the three most volatile species co-desorb with methanol and later with water. Peaks corresponding to co-desorption of CO, CO_2, and NH_3 with methanol cannot be reproduced in experiments with binary mixtures, which are extensively used in the study of thermal desorption of interstellar ices. In addition, IR spectra confirmed that CO is continuously desorbing between the desorption peaks corresponding to monolayer [12] desorption and co-desorption with methanol.

The experiments reported here help to understand the thermal annealing process of circumstellar ices inside hot cores. The heating rate applied to our ice analogs is on the same order of magnitude than the one dust grains experience during the periodic radial excursions considered in the fluctuating X-wind model for CAIs and chondrules formation (Shu et al. 1996, 1997, 2001). A similar behavior is expected for ice mantles at a given distance from the central object, as they are heated with an approximate heating rate of 1 K/century. However, differences in desorption peak temperatures are expected. Observations with sufficient spatial resolution will serve to test the model sketched in Fig. 4.2.

With some limitations, these results can be also applied to cometary ices. A possible scenario of ice evaporation during comet approach to the Sun is provided in Section 4.2. The TPD curves of a pre-cometary ice analog indicated that water could be already detected in the coma of comet 67P/Churyumov-Gerasimenko during the first approach of the ESA-Rosetta cometary mission.

Acknowledgements

We are grateful to Gustavo A. Cruz Díaz, Barbara Michela Giuliano, and Antonio Jiménez Escobar for their support on the experiments. This research was financed by

---

[12] After publication of this paper, it was found that the monolayer desorption peak is actually an artifact (see Chapter 6 for more information).

the Spanish MINECO under projects AYA2011-29375 and CONSOLIDER grant CSD2009-00038. R. M. D. benefited from a FPI grant from Spanish MINECO.

References

Attard, G. & Barnes, C. 1998, Surfaces (Oxford Science Publications), 72

Bar-Nun, A., Herman, G., & Laufer, D. 1985, Icarus, 63, 317

Bakkas, N., Bouteiller, Y., Louteiller, A., Perchard, J.P., & Racine, S. 1993, J. Chem. Phys. 99, 3335

Bisschop, S.E., Fraser, H.J., Öberg, K.I., van Dishoeck, E.F., & Schlemmer, S. 2006, A&A, 449, 1297

Blake, D., Allamandola, L., Sandford, S., Hudgins, D., & Freund, F. 1991, Science, 254, 548

Bolina, A.S., Wolf, A.J., & Brown, W.A. 2005a, J. Chem. Phys., 122, 4713

Bolina, A.S., Wolf, A.J., & Brown, W.A. 2005b,, Sur. Sci. 598, 45

Brown, W.A., Viti., S., Wolff, A.J., & Bolina, A.S. 2006, Faraday Discussions, 133, 113

Collings, M.P., Dever, J.W., Fraser, H.J., & McCoustra, M.R. 2003a, ApJ, 583, 1058

Collings, M.P., Dever, J.W., Fraser, H.J., & McCoustra, M.R. 2003b, Ap&SS, 385, 633

Collings, M.P., Anderson, M.A., Chen, R., et al. 2004, MNRAS, 354, 1133

Cuppen, H.M., Penteado, E.M., Isokoski, K., van der Marel, N., & Linnartz, H. 2011, MNRAS, 417, 2809

de Almeida, A.A., Sanzovo, D.T., Sanzovo, G.C., Boczko, R., & Torres, R.M. 2009, Adv. Space Res. 43, 1993

d'Hendecourt, L.B. & Allamandola, L.J. 1986, A&ASS, 64, 453

Dowell, L.G. & Rinfert, A.P. 1960, Nature, 188, 1144

Eberhardt, P. 1999, Space Sci. Rev., 90, 45

Ehrenfreund, P., Kerkhof, O., Schutte, W.A., et al. 1999, A&A, 350, 240

Falk, M. & Whalley, E. 1961, J. Chem. Phys. 34, 1554

Fayolle, E.C., Öberg, K.I., Cuppen, H.M., Visser, R., & Linnartz, H. 2011, ApJ, 529, A74

Fraser, H.J., Collings, M.P., McCoustra, M.R.S., & Williams, D.A. 2001, MNRAS, 327, 1165

Goesmann, F., McKenna-Lawlor, S., Roll, R., et al. 2012, Planet. Space Sci., 66, 187

Hagen, W. 1981, Chem. Phys., 56, 367

Hagen, W., Tielens, A.G.G.M., & Greenberg, J.M. 1983, A&ASS, 51, 389

Herbst, E. & van Dischoeck, E.F. 2009, Annu. Rev. Astron. Astrophys., 47, 427

Isokoski, K. 2013, PhD Thesis

Jiang, G.J., Person, W.B., & Brown, K.G. 1975, J. Chem. Phys., 62, 1201

Kelley, M.S., Wooden, D.H., Tubiana, C., et al. 2009, AJ, 137, 4633

Luna, R., Luna-Ferrándiz, R., Satorre, M.Á., Domigo, M., Millán, & Santonja, C. 2017, *in prep.*

Luna, R., Millán, C. Domigo, M., Santonja, C., & Satorre, M.Á. 2015, Vacuum, 122, 154

Luna, R., Satorre, M.Á., Santonja, C., & Domigo, M. 2014, A&A, 2014, 566, A27

Migliorini, A., Piccioni, G., Capaccioni, F., et al. 2016 A&A, 589, A45

Mumma, M.J. & Charnley, S.B. 2011, Annu. Rev. Astron. Astrophys., 49, 471

Muñoz Caro, G.M., Jiménez-Escobar, A., Martín-Gago, J.A., et al. 2010, A&A, 522, A108

Noble, J.A., Congiu, E., Dulieu, F., & Fraser, H.J. 2012, MNRAS, 421, 768

Notesco, G. & Bar-Nun, A. 2000, Icarus, 148, 456

Öberg, K.I. 2009, PhD Thesis, Universiteit Leiden
Öberg, K.I., Fayolle, E. C., Cuppen, H.C., van Dishoeck, E.F., Linnartz, H. 2009, A&A, 505, 183
Pauls, T.A., Wilson, T.L., Bieging, J.H., & Martin, R.N. 1983, A&A, 124, 123
Prialnik, D., Sarid, G., Rosenberg, E.D., & Merk, R. 2008, Space Sci. Rev., 138, 147
Sandford, S.A. & Allamandola, L.J. 1990, ApJ, 355, 357
Sandford, S.A. & Allamandola, L.J. 1993, ApJ, 417, 815
Sandford, S.A., Allamandola, L.J., Tielens, A.G.G.M., & Valero, G.J. 1988, ApJ, 329, 498
Shu, F.H., Shang, H., & Lee, T. 1996, Science, 271, 1545
Shu, F.H., Shang, H., Glassgold, A.E., & Lee, T. 1997, Science, 277, 1475
Shu, F.H., Shang, H., Gounelle, M., Glassgold, A.E., & Lee, T. 2001, ApJ, 548, 1029
Smith, R.S., Huang, C., Wong, E.K.L., & Kay B.D. 1997, Phys. Rev. Lett., 79, 909
Snodgrass, C., Tubiana, C., Bramich, D.M., et al. 2013, A&A, 557, A33
Thomas, P.C., Veverka, J., Belton, M.J.S., et al. 2007, Icarus, 187, 4
Viti, S. & Williams, D.A. 1999, MNRAS, 310, 517
Viti, S., Collings, M.P., Dever, J.W., & McCoustra, M.R.S. 2004, MNRAS, 354, 1141
Wakelam, V., Caselli, P., Ceccarelli, C., Herbs, E., & Castets, A. 2004, A&A, 422, 159
Wyckof, S. 1982, Comets, ed. L.L. Wilkening, (The University of Arizona Press, Tucson), 20
Yamada, H. & Person, W.B. 1964, J. Chem. Phys., 41, 2478
Zubko, V., Dwek, E., & Arendt, R.G. 2004, ApJSS, 152, 211

Part V
Results - Gas

Chapter 12

Upper limits on the H_2S_2, $HS_{\dot{2}}$, and S_2 abundances toward the low-mass warm core IRAS 16293-2422

Adapted from *The sulfur depletion problem: upper limits on the H_2S_2, $HS_{\dot{2}}$, and S_2 abundances toward the low-mass warm core IRAS 16293-2422*. Martín-Doménech, R., Jiménez-Serra, I., Muñoz Caro, G.M., Müller, H.S.P., Occhiogrosso, A., Testi, L., Woods, P.M., & Viti, S. 2016, A&A, 585, A112.

Abstract

A fraction of the missing sulfur in dense clouds and circumstellar regions could be in the form of three species not yet detected in the interstellar medium: H_2S_2, $HS_{\dot{2}}$, and S_2 according to experimental simulations performed under astrophysically relevant conditions. These S-S bonded molecules can be formed by the energetic processing of H_2S-bearing ice mantles on dust grains, and subsequently desorb to the gas phase.

The detection of these species could partially solve the sulfur depletion problem, and would help to improve our knowledge of the poorly known chemistry of sulfur in the interstellar medium. To this purpose we calculated the frequencies and expected intensities of the rotational transitions not previously reported, and performed dedicated ground-based observations toward the low-mass warm core IRAS16293-2422, a region with one of the highest measured gas-phase H_2S abundances.

Observations in the submillimeter regime were obtained with the APEX 12 m telescope during 15 hours of observation. A total of $\sim$16 GHz were covered in a range of about 100 GHz, targeting a wide selection of the predicted rotational transitions of the three molecules.

The 1σ noise rms values were extracted in the spectral regions where the targeted species should have been detected. These values were a factor of 2 - 7 lower than those reached by previous observations toward the same source, and allowed us to estimate a 1σ upper limit to their molecular abundances of $\leq 8.1\times10^{-9}$, $\leq 1.1\times10^{-8}$, and $\leq 2.9\times10^{-7}$ relative to H_2, for H_2S_2, $HS_{\dot{2}}$, and S_2, respectively.

The upper limit abundances of the three molecules containing the S_2 unit are up to two orders of magnitude lower than the H_2S abundance in the source, and one order of magnitude lower than the expected abundances from the experimental simulations using ice analogs. Subsequent gas-phase chemistry after desorption could lower the abundances of the three species to undetectable levels in our observations.

12.1 Introduction

Sulfur, the tenth most abundant element in the Galaxy, is of particular interest from an astrochemical point of view. On the one hand it has been suggested that sulfur-bearing species can act as chemical clocks in star forming regions (Charnley 1997, Hatchell et al. 1998, Viti et al. 2001, Wakelam et al. 2004a, Wakelam et al. 2011). On the other hand, along with carbon, hydrogen, nitrogen, oxygen and phosphorus, it is one of the elements commonly present in molecules of biotic interest.

Previous observations have shown that sulfur is depleted in dense clouds and circumstellar regions around young stellar objects (YSOs) The S-bearing species already detected in these regions account for only $\sim$ 0.1% of its estimated cosmic abundance (1.23 x 10^{-5} N_H; Tieftrunk et al. 1994). It has been proposed that the missing sulfur is locked onto the icy mantles of dust grains (e.g., Millar & Herbst 1990, Jansen et al. 1995, Ruffle et al. 1999). Until now, only OCS (Geballe et al. 1985, Palumbo et al. 1995) and SO_2 (Boogert et al. 1997) have been firmly detected in icy grain mantles toward high-mass protostars, but their estimated abundances are on the order of $\sim$ 0.5%, and $\sim$ 0.8 - 4.0%, respectively, of the total cosmic S abundance (Boogert et al. 1997).

In cometary ices H_2S is the most abundant S-bearing molecule, with an abundance of up to 1.5% relative to water (Bockelée-Morvan et al. 2000)), or 1.5$\times$ 10^{-6} relative to H_2. The presence of H_2S in interstellar ices was inferred from IR observations toward the high-mass protostar W33A (Geballe et al. 1985). However, a robust detection of this molecule in interstellar ices has not been reported yet, probably because of the overlapping of the 3.92 μm IR band of H_2S with a strong IR feature of methanol. The upper limits found for these species toward dense clouds and circumstellar regions (0.6 - 1.6 $\times$ 10^{-6}, and 0.04 - 0.12 $\times$ 10^{-6} relative to H_2, respectively; Smith 199)) account for only 10% of the cosmic S abundance.

A fraction of the H_2S present in interstellar ices could be energetically processed by UV-photons, X-rays, or cosmic rays in dense cloud interiors and regions around YSOs, leading to the formation of other S-bearing species. These new molecules would subsequently be released to the gas phase by means of photon or ion-induced desorption, and also thermal desorption in the hot regions of the circumstellar envelopes around YSOs, harboring part of the missing sulfur. This is indeed a very plausible scenario, since several of the gas-phase S-containing molecules already observed in hot cores, such as H_2S, SO_2, OCS, SO, H_2CS, HCS^+, and NS (van der Tak et al. 2003, Jiménez-Serra et al. 2012), have abundances that cannot be explained with gas-phase-only chemical models (Doty et al. 2004, Viti et al. 2004, Wakelam et al. 2004a).

This scenario has been tested in the laboratory for the past thirty years. Experimental simulations of the irradiation of interstellar ices containing H_2S under astrophysically relevant conditions have been performed using UV photons (Grim & Greenberg 1987, Jiménez-Escobar & Muñoz Caro 2011, Jiménez-Escobar et al. 2014), X-rays (Jiménez-Escobar et al. 2012), or ions (Moore et al. 2007, Ferrante et al. 2008, Garozzo et al. 2010). Energetic processing of H_2S-bearing ices readily generates sulfur-sulfur bonds, and the main S-bearing products in these experiments are usually H_2S_2 and $HS_2^{\cdot}$. The molecule H_2S_2 can subsequently photodissociate forming S_2 and S_3, which have recently been detected by Jiménez-Escobar & Muñoz Caro (2011). These molecules with two S atoms could thus contain a significant fraction of the missing sulfur in dense clouds and circumstellar regions, but their observation in the solid or gas phase have not yet been reported.

Dense circumstellar envelopes around YSOs such as high-mass hot cores and low-mass warm cores (or hot corinos) are prime candidates for the detection of these S-bearing molecules in the gas phase, since ice mantles are largely affected by intense UV and/or X-ray irradiation from their central protostars before their thermal desorption.

The low-mass warm core IRAS16293-2422 (or hot corino) is known to show an active chemistry as demonstrated by its rich molecular line spectrum (Caux et al. 2011, Jørgensen et al. 2011). The derived gas-phase H_2S abundance toward this object is one of the highest measured in low-mass warm cores (5 x 10^{-7}; Wakelam et al. 2004b) and is therefore a good candidate to test whether an important fraction of the missing sulfur is contained in the form of any of these S-bearing species coming from H_2S. IRAS16293-2422 is a binary system whose sources A and B are spatially separated by 5″ (Mundy et al. 1992). Among the two sources, IRAS16293-2422 A shows a very rich sulfur chemistry with several sulfur-bearing molecules detected, such as H_2S, SO, SO_2, HCS^+, H_2CS, CS, and OCS (Wakelam et al. 2004b, Caux et al. 2011, Jørgensen et al. 2011). The measured rotational temperature of the hot corino is T_{rot} = 100 K (Ceccarelli et al. 2000).

We present the first single-dish observations targeting a wide selection of the predicted rotational transitions for three of the products detected in the experimental simulations (H_2S_2, $HS_2^{\cdot}$, and S_2) toward IRAS16293-2422. Although none of the three species was firmly detected, our observations provide stringent upper limits to their molecular abundances, constraining the efficiency of UV-photoformation of H_2S_2, $HS_2^{\cdot}$, and S_2 in interstellar ices. This paper is organized as follows. Section 12.2 describes the observations that have been performed, while the results are shown in Section 12.3. In particular, Section 12.2.1 presents spectroscopic information of the three targeted molecules, and the upper limits derived from our observations are discussed in Section 12.3.3. In Section 12.4.1 these upper limits are compared to the expected abundances from the experimental simulations with ice analogs, and in Section 12.4.2 to the estimated abundances from theoretical simulations taking into account the subsequent gas-phase chemistry. The conclusions are summarized in Section 12.5.

12.2 Observations

The observations were carried out with the APEX 12 m telescope located at the high altitude site of Llano Chajnantor (Chile) in 2013, between August 30 and September 10, under good (PWV = 1.1 - 2.2 mm) weather conditions. We used the Swedish Heterodyne Facility Instruments (SHeFI; Vassilev et al. 2008) APEX-1 and APEX-2 as frontends with four different frequency setups of 4 GHz bandwidth each, covering a total of ~16 GHz in a range of about 100 GHz. The eXtended bandwith Fast Fourier Transform Spectrometer (XFFTS; Klein et al. 2012) was used as backend. The XFFTS yields a spectral resolution of 76 KHz, which corresponds to ~ 0.07 - 0.10 km s^{-1} in the spectral range observed.

The position-switching mode was chosen to perform the on/off observations[1]. The on position was centered toward IRAS16293-2422 A, α_{J2000} = $16^h32^{min}22.9^s$, δ_{J2000} = -24°28′37.0″, while the off position was located at α_{J2000} = $16^h32^{min}09.4^s$, δ_{J2000} = -24°28′33.0″, which is free of any $C^{18}O$ and ^{13}CO emission (Wakelam et al. 2004b). The half-power beamwidth of the telescope is ~ 30″ - 25″ for the APEX-1 receiver, and ~ 23″ - 17″ for the APEX-2 receiver. Therefore, emission from sources A and B of the binary protostellar system IRAS16293-2422 could not be spatially resolved. The receivers were tuned to single sideband, and the intensities were measured in units of T_{A}^*. The conversion to T_{mb} was done by using main beam efficiencies ($\eta_m b$) of 0.75 and 0.73 for APEX-1 and APEX-2, respectively. Calibration and reduction of the data was previously performed with the software CLASS of the GILDAS package.

---

[1] This is done to substract the contribution of the sky and the instrument to the proper emission from the source.

Our observations covered a total of 17 H_2S_2 transitions, 96 $HS^{\cdot}_2$ transitions, and 6 S_2 transitions. For H_2S_2, we selected the transitions with low upper level energy (a total of three transitions per frequency setup). The central frequency of the four observational setups corresponds to the frequencies of the selected H_2S_2 transitions expected to be the most intense in each setup, and are boldfaced in Table 12.1. For $HS^{\cdot}_2$ and S_2, we selected only those transitions with low upper level energy that fell in a clean region of the spectrum. The selected lines for H_2S_2, $HS^{\cdot}_2$, and S_2 are listed in Table 12.1.

12.2.1 Laboratory spectroscopy of sulfur-containing molecules in the gas phase

Disulfane, H_2S_2, also known as hydrogen disulfide, is a heavy homologue of hydrogen peroxide, H_2O_2. Whereas H_2O_2 displays large torsional splitting in the ground vibrational state, this splitting is hard to resolve for H_2S_2 even in the laboratory. It is an asymmetric top rotor very close to the prolate limit, i.e., its A rotational constant of almost 147 GHz is much larger than B and C, which are almost equal and slightly smaller than 6.97 GHz. Its dipole moment of about 1.1 D (Woon & Herbst 2009) is along the c-axis. The two equivalent H nuclei result in a 3 : 1 spin-statistical ratio between *ortho* and *para* levels which are described by K_c being odd and even, respectively. A large body of transition frequencies up to 421 GHz were taken from Behrend et al. (1990) with additional terahertz data from Belov et al. (1994) and Yamada et al. (1996). The precision of the data appeared to be 20 or 30 kHz for the most part. The $K = 3 - 2$ data in Belov et al. (1994) is too low compared with the data reported in Behrend et al. (1990) by about 300 kHz with rather small scatter. The absence of a reference signal in, e.g., Belov et al. (1994) could be an explanation, see SO data in Klaus et al. (1994) and Klaus et al. (1996). Therefore, the $K = 3-2$ data from Belov et al. (1994) were omitted from the fit. As a consequence, predicted transition frequencies should be viewed with some caution. As the result of this work, a catalog entry was created for the Cologne Database for Molecular Spectroscopy, CDMS, (Müller et al. 2001, Müller et al. 2005) with the spectroscopic information of this species, including predicted frequencies and intensities for its rotational transitions.

Elimination of one H atom from disulfane leads to the $2A''$ thiosulfeno radical, $HS^{\cdot}_2$. The A rotational constant is roughly twice that of H_2S_2, while B and C are about 1 GHz larger. The dipole moment components were calculated as $\mu_a = 1.16$ D and $\mu_b = 0.83$ D (Peterson et al. 2008). Predictions of the $HS^{\cdot}_2$ rotational spectrum were also taken from the CDMS. They were based on the analysis of Tanimoto et al. (2000) which included lower frequency data from Yamamoto & Saito (1994). ^1H hyperfine structure is usually small and was often not resolved in the laboratory. Electron spin-rotation splitting is small for a-type transitions, e.g., on the order of 200 MHz and 1 GHz for $K_a = 0 - 0$ and $1 - 1$, respectively. It is several tens of gigahertz for b-type transitions.

Elimination of the second H atom yields S_2, the smallest molecule containing only sulfur. It is a heavy homologue of O_2, the ground electronic state is $^3\Sigma_g^-$. Because of its symmetry, it does not have an electric dipole moment, but it has a magnetic dipole moment which gives rise to a weak rotational spectrum. The selection rules are $\Delta N = 0, \pm2$ and $\Delta J = 0, \pm1$. The predictions were taken from the JPL catalog catalog

(Pickett et al. 1998). They are based on rotational data from Pickett & Boyd (1979) with additional ground state combination differences taken from the $b - X$ electronic spectrum (Fink et al. 1986). The magnetic g-factors were redetermined by Pickett & Boyd (1979). The rotational spectrum of O_2 is quite close to Hund's case (b), in which the three $\Delta N = 2$ transitions occur quite close in frequency. The rotational splitting in S_2 is considerably smaller than in O_2 whereas the splitting caused mainly by the spin-spin coupling is much larger. As a consequence, the rotational spectrum is much more complex in its structure, closer to Hund's case (a) at low rotational quantum numbers N and closer to Hund's case (b) at higher N. Relatively strong transitions are those with $\Delta J = 0$, those with $\Delta N = 0$ are also comparatively strong.

12.3 Results

Our observations toward the IRAS16293-2422 hot corino reached rms values which are a factor 2 - 7 better than those reached by the TIMASS survey (Caux et al. 2011) in the 197 GHz - 280 GHz frequency range, while they are comparable in the 328 GHz - 366 GHz range. For the analysis of the spectra, we resampled the observations to a resolution of 0.5 km s^{-1}, and assumed a central radial velocity of v_{lsr} = 3.2 km s^{-1} for IRAS16293 A (Jørgensen et al. 2011).

Lines detected at frequencies near those of the targeted transitions in Table 12.1 were assigned to previously detected species. The observed lines were then fitted with Gaussians (when possible, more than one Gaussian was used in the case of blended lines). For every putative assigned line, we used the integrated intensity extracted from the fit, and a simple model[2] assuming Local Thermodinamical Equilibrium (LTE) to readily extract column densities that were compared with the column densities derived in previous works for the same species. This way, we could confirm the quality of our observations, and even assign lines corresponding to previously detected species that were not documented in previous works (see Section 12.3.1).

Putative assignments of transitions corresponding to the targeted species were, however, ruled out because of missing lines (see Section 12.3.2).

12.3.1 Detection of species not containing sulfur

As mentioned above, we detected transitions from a collection of molecular species previously observed in other works such as $C^{17}O$, SO_2, HDCO, CH_3OH, CH_3CHO, CH_3OCHO, CH_3OCH_3, and others. Estimated column densities extracted from these emission lines are consistent with the column densities previously reported for these species (see, e.g., Cazaux et al. 2003, Caux et al. 2011). Some of these transitions are present in the spectral windows of Figures 12.1 and 12.2 near the frequencies where the targeted transitions should be detected, and shortly described below.

Fig. 12.1 shows one transition corresponding to CH_3CHO ($13_{2,12}$-$14_{1,14}$ panel) with E_u = 92.6 K, and one transition corresponding to HDCO ($14_{1,13}$-$13_{0,13}$ panel) with E_u = 56.3 K. The linewidth of the latter may indicate that HDCO is probing outflow material

---

[2] In particular, the total column densities of the species were calculated from the integrated intensity I in K km s^{-1} of a given transition between levels u and l with frequency ν (in GHz) using eq. 4.10 in Chapter 4, Sect. 4.2. N_u was calculated as $N_u = I \times 1.94\times10^3 \times \nu^2 / A_{ul}$, and a temperature of T_{ex}=100 K was assumed.

Table 12.1. *Targeted transitions and observational results*

Molecule	Transition	Frequency (MHz)	E_u (K)	g_u	A_{ul} (s^{-1})	beam size ($''$)	rms $^{(1)}$ (K)	N (cm^{-2})
H_2S_2	$6_{1,5}$-$5_{0,5}$	**223535.85**	20.8	39	4.23 x 10 $^{-5}$	28	...	...$^{(2)}$
H_2S_2	$13_{2,11}$-$14_{1,13}$	224367.15	87.8	81	1.64 x 10 $^{-5}$	28	0.0018	$\leq$ 1.7 x 10^{15}
H_2S_2	$13_{2,12}$-$14_{1,14}$	224657.47	87.8	27	1.65 x 10 $^{-5}$	28	...	...$^{(2)}$
H_2S_2	$8_{1,7}$-$7_{0,7}$	**251423.70**	30.8	51	5.92 x 10 $^{-5}$	25	0.0026	$\leq$ 6.1 x 10^{14}
H_2S_2	$11_{2,9}$-$12_{1,11}$	252271.50	71.0	69	2.25 x 10 $^{-5}$	25	0.0025	$\leq$ 1.7 x 10^{15}
H_2S_2	$11_{2,10}$-$12_{1,12}$	252486.63	71.0	23	2.25 x 10 $^{-5}$	25	...	...$^{(2)}$
H_2S_2	$10_{1,9}$-$9_{0,9}$	**279312.25**	43.5	63	8.04 x 10 $^{-5}$	22	...	...$^{(2)}$
H_2S_2	$9_{2,7}$-$10_{1,9}$	280174.30	57.0	57	2.94 x 10 $^{-5}$	22	...	...$^{(2)}$
H_2S_2	$9_{2,8}$-$10_{1,10}$	280325.68	57.0	19	2.94 x 10 $^{-5}$	22	0.0022	$\leq$ 3.7 x 10^{15}
H_2S_2	$14_{1,13}$-$13_{0,13}$	**335087.32**	77.0	87	1.37 x 10 $^{-4}$	19	...	...$^{(2)}$
H_2S_2	$5_{2,3}$-$6_{1,5}$	335971.39	36.9	33	4.05 x 10 $^{-5}$	19	0.0036	$\leq$ 2.1 x 10^{15}
H_2S_2	$5_{2,4}$-$6_{1,6}$	336029.02	36.9	11	4.05 x 10 $^{-5}$	19	...	...$^{(2)}$
$HS_2^{\cdot}$	$16_{0,16,16,15}$-$15_{0,15,15,14}$	252270.66	103.1	31	1.22 x 10 $^{-4}$	25	0.0028	$\leq$ 8.0 x 10^{14}
$HS_2^{\cdot}$	$16_{0,16,16,16}$-$15_{0,15,15,15}$	252270.71	103.1	33	1.22 x 10 $^{-4}$			
$HS_2^{\cdot}$	$4_{1,3,5,4}$-$4_{0,4,5,4}$	280022.63	21.0	9	7.45 x 10 $^{-5}$	22	0.0027	$\leq$ 1.6 x 10^{15}
$HS_2^{\cdot}$	$4_{1,3,5,5}$-$4_{0,4,5,5}$	280023.28	21.0	11	7.49 x 10 $^{-5}$			
$HS_2^{\cdot}$	$21_{1,20,22,22}$-$20_{1,19,21,21}$	333247.58	189.7	45	2.84 x 10 $^{-4}$	19	0.0052	$\leq$ 1.3 x 10^{15}
$HS_2^{\cdot}$	$21_{1,20,22,21}$-$20_{1,19,21,20}$	333247.67	189.7	43	2.84 x 10 $^{-4}$			
S_2	11_{10}-9_9	224301.13	82.1	21	3.02 x 10 $^{-7}$	28	0.0017	$\leq$ 2.2 x 10^{16}
S_2	15_{14}-13_{13}	333685.77	126.3	29	7.78 x 10 $^{-7}$	19	0.0039	$\leq$ 2.3 x 10^{16}

(1)rms is given in 5 km s^{-1} bins. (2)Since these spectral regions present line contributions from other species near the frequency of the H_2S_2 transition, we have not used the corresponding noise rms value to compute the 1σ upper limits to the column density.

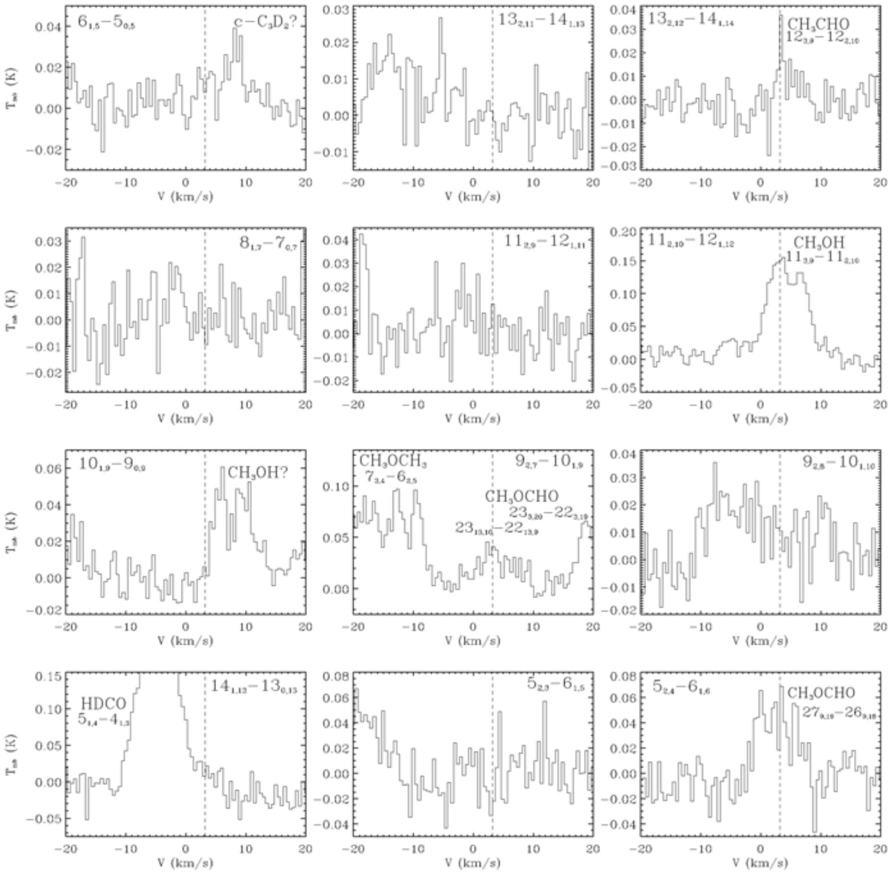

Figure 12.1. *Spectral windows where the H_2S_2 transitions listed in Table 12.1 should be detected. Vertical dashed lines mark a central radial velocity of $v_{\rm lsr}$ = 3.2 km s^{-1}, assumed for IRAS16293 A (Jørgensen et al. 2011).*

(IRAS16293-2422 is embedded in the molecular cloud L1689N, which harbors multiple outflows; Wakelam et al. 2004b).

In the case of CH_3OH, one transition with E_u = 203 K is detected in the $11_{2,10}$-$12_{1,12}$ panel of Fig. 12.1. The double-peaked structure of the line may indicate that the emission is also originated in outflowing gas. The double-peaked line detected in the $10_{1,9}$-$9_{0,9}$ panel of Fig. 12.1 may correspond to the 27_3-27_2 CH_3OH transition. However, the energy of this transition may be too high, even for an outflow (E_u = 926.1 K).

Four blended CH_3OCH_3 transitions with E_u = 38.2 K lead to three emission peaks in the $9_{2,7}$-$10_{1,9}$ panel of Fig. 12.1. They are possibly also blended with the $14_{11,4}$-$13_{11,3}$

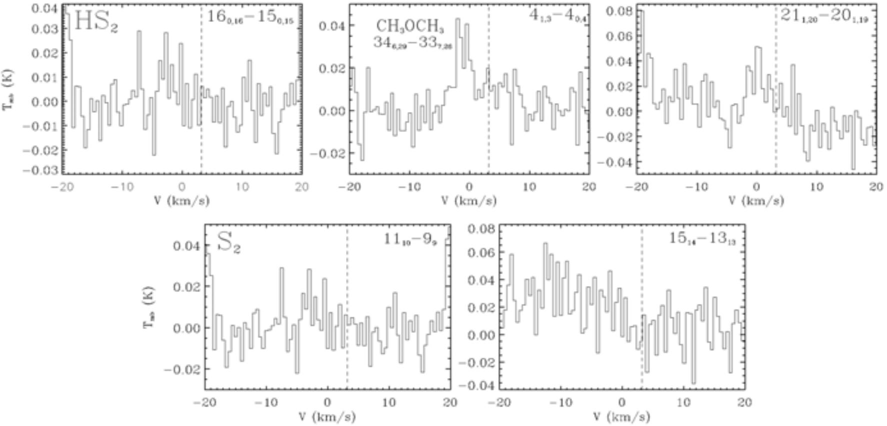

Figure 12.2. *Spectral windows where the* $HS^{\cdot}_2$ *(top panels) and* S_2 *(bottom panels) transitions listed in Table 12.1 should be detected. Vertical dashed lines mark a central radial velocity of* $v_{\rm lsr}$ *=* 3.2 *km* s^{-1}*, assumed for IRAS16293 A (Jørgensen et al. 2011).*

H_2CCO transition (E_u = 113.9 K) that should appear at a slightly higher frequency and therefore at more blue-shifted velocities. The weaker $30_{4,26}$-$30_{3,27}$ CH_3OCH_3 transition is probably blended with the $23_{13,10}$-$22_{13,9}$ CH_3OCHO transition in that spectral window (E_u = 433.7 K and 462.6 K, respectively). Other four blended transitions with high upper level energy (E_u = 593.9 K) corresponding to dimethyl ether are detected in the $4_{1,3}$-$4_{0,4}$ panel of Fig. 12.2.

Three more CH_3OCHO transitions are shown in Fig. 12.1, one in the $9_{2,7}$-$10_{1,9}$ panel (E_u = 173.2 K), and two blended transitions in the $5_{2,4}$-$6_{1,6}$ panel (E_u = 277.8 K for both transitions).

12.3.2 Non-detection of H_2S_2, $HS^{\cdot}_2$ or S_2

In Figures 12.1 and 12.2, we show the spectral windows where the transitions listed in Table 12.1 should have been detected. The $6_{1,5}$-$5_{0,5}$ panel of Fig. 12.1 presents some emission centered at $v_{\rm lsr} \sim 3.2$ km s^{-1}, which may correspond to the $6_{1,5}$-$5_{0,5}$ transition of H_2S_2. However, the lack of detection of other transitions of this molecule prevents us from claiming this identification. In addition, the observed feature may present some contribution from the $18_{5,14}$-$17_{5,13}$ CH_3OCHO transition (E_u = 305.1 K).

Other possible lines of HCOCN and NCHCCO could be overlapping with this emission. However, their frequencies are typically shifted by $\sim$ 0.5 MHz with respect to that of the H_2S_2 transition, which would imply an offset of $\sim$ 0.6 km s^{-1} in the $v_{\rm lsr}$. The $14_{11,4}$-$14_{10,5}$ transition of c-C_3D_2 (an isotopologue not reported in Cazaux et al. (2003) and Caux et al. (2011)) with E_u = 271.0 K could also contribute to the observed emission, since the uncertainty of the expected frequency is larger than 5 MHz.

For $HS^{\cdot}_2$ and S_2 (see Figure 12.2), there are no clear emission features arising at the

Table 12.2. *Upper limits to the column densities and molecular abundances of H_2S_2, $HS^{\cdot}_2$, and S_2 estimated from the observations, and abundances calculated in laboratory experiments.*

Molecule	N_{mol} (cm^{-2})	$N_{\mathrm{mol}}/N(H_2)$	$[N_{\mathrm{mol}}/N(H_2S)]_{\mathrm{obs}}$ (%)	$[N_{mol}/N(H_2S)_i]_{\mathrm{lab}}$ (1) (%)
H_2S_2	$\leq 6.1 \times 10^{14}$	$\leq 8.1 \times 10^{-9}$	≤ 1.5	≤ 25.0 (2)
$HS^{\cdot}_2$	$\leq 8.0 \times 10^{14}$	$\leq 1.1 \times 10^{-8}$	≤ 2.0	15.0
S_2	$\leq 2.2 \times 10^{16}$	$\leq 2.9 \times 10^{-7}$	≤ 55.0	...(3)

(1)After irradiation of pure H_2S ices with a total fluence of $\sim 1.5 \times 10^{18}$ photons cm^{-2}. Abundances are relative to the initial H_2S in the experiments. Derived from Jiménez-Escobar et al. (2012). (2)This upper limit is estimated considering that all the sulfur atoms not contained in H_2S or $HS^{\cdot}_2$ molecules at the end of the experiments reported in Jiménez-Escobar et al. (2012) are forming H_2S_2. (3)S_2 was not quantified since it was detected by mass spectrometry during warm-up of the UV-processed ice analogs in Jiménez-Escobar et al. (2012), but not by infrared spectroscopy.

v_{lsr} of the source, except for the $4_{1,3}$-$4_{0,4}$ panel. However, as mentioned in Section 12.3.1, the detected feature is likely associated with four blended transitions of dimethyl ether.

From all this, we conclude that none of the transitions of H_2S_2, $HS^{\cdot}_2$ or S_2 observed toward IRAS16293-2422 are detected. In Table 12.1, we provide the noise rms values over a linewidth of 5 km s^{-1} in the spectral region around the frequency of each transition. The measured rms values range from $\sim$1.8 to 5.2 mK, which provide stringent constraints on the upper limits to the molecular column densities and abundances of these species toward this low-mass warm core (see Section 12.3.3).

12.3.3 Upper limits to the abundances of H_2S_2, $HS^{\cdot}_2$ and S_2

From the 1σ rms values shown in Table 12.1, we have estimated the 1σ upper limits to the column densities and abundances of H_2S_2, $HS^{\cdot}_2$ and S_2 measured toward IRAS16293-2422. To this purpose, we have used the simple model mentioned in Section 12.3.1, assuming that the emission of these molecules is optically thin, that their line profiles have linewidths of 5 km s^{-1}, and that the excitation temperature of the gas is 100 K. The column densities of the three species were subsequently corrected from beam dilution using the beam filling factor (Maret et al. 2011)

$$\eta = \frac{\theta^2_{source} + \theta^2_{beam}}{\theta^2_{source}} \tag{12.1}$$

and considering a source extension of 2″ in diameter[3] (Wakelam et al. 2004b). In addition, the 1σ upper limits for $HS^{\cdot}_2$ are computed taken into account that the three pairs of lines cannot be resolved in our observations.

The upper limits to the column densities of H_2S_2, $HS^{\cdot}_2$ and S_2 are shown in the last column of Table 12.1. The most stringent values are $\leq 6.1\times10^{14}$ cm^{-2}, $\leq 8.0\times10^{14}$ cm^{-2}, and $\leq 2.2\times10^{16}$ cm^{-2} respectively (see also Table 12.2, column 2).

---

[3] This is the size of the region where these species are assumed to be present.

The upper limits to the abundance of these molecules with respect to H_2 are derived by using an H_2 column density of $N(H_2) = 7.5 \times 10^{22}$ cm^{-2} Ceccarelli et al. 2000 These upper limits are shown in column 3 of Table 12.2 and are $\leq 8.1\times10^{-9}$ for H_2S_2, $\leq 1.1\times10^{-8}$ for $HS_2^{\cdot}$, and $\leq 2.9\times10^{-7}$ for S_2.

Since no molecule with a sulfur-sulfur bond has been detected so far in the interstellar medium, the estimated upper limits can be compared only to the abundances of species with just one sulfur atom. In this case, we have calculated the upper limits to the abundance of these species with respect to H_2S in the same source, which is thought to be the parent molecule of the targeted species. We have considered an H_2S column density of $N(H_2S)=4\times10^{16}$ cm^{-2} as reported in Wakelam et al. (2004b). The relative upper limits are shown in column 4 of Table 12.2 and are $\leq$1.5%, $\leq$2.0% and $\leq$55.0% for H_2S_2, $HS_2^{\cdot}$ and S_2, respectively, which leads to a rough upper limit of about 1% of S-S bonded species with respect to those with only one S atom.

12.4 Discussion

12.4.1 Comparison with laboratory H_2S-bearing ice irradiation experiments

The upper limits to the abundances relative to H_2S are compared to the values expected from the laboratory experiments peformed by Jiménez-Escobar & Muñoz Caro (2012), also shown in Table 12.2 (column 5). The measured upper limits are factors of 7-17 lower than the abundances measured in the experiments.

Differences between experimental and observed abundances could arise, on one hand, from the differences between the experimental simulations performed in the laboratory and the real processes taking place in the interstellar and circumstellar medium, leading to an overestimation of the expected abundances, as it is explained below.

The laboratory simulations reported in Jiménez-Escobar & Muñoz Caro (2011) used to derive the abundances shown in the fifth column of Table 12.2 were carried out with pure H_2S ices. However, solid H_2S is expected to be found in a water-rich environment in the interstellar and circumstellar medium, along with other hydrogenated species (Allamandola et al. 1999, Jiménez-Escobar & Muñoz Caro 2011). Since H_2S has not been firmly detected in interstellar or circumstellar ices, this scenario remains to be confirmed, but processing of solid H_2S could take place to a limited extent in multicomponent ices.

In the dense interstellar medium, solid H_2S can be processed in dense cloud interiors by the secondary UV-field produced by excitation of H_2 molecules by cosmic rays, and/or by the radiation emitted by the central object in hot cores and hot corinos. During the experiments in Jiménez-Escobar et al. (2012), pure H_2S ice analogs experienced a total fluence of $\sim 1.5 \times 10^{18}$ UV-photons cm^{-2}, which is higher than the fluence of $\sim 3.2 \times 10^{17}$ photons cm^{-2} that ice mantles are expected to experience in dense cloud interiors after 10^6 yr, assuming a flux value of 10^4 photons cm^{-2} s^{-1} for the secondary UV-field (Shen et al. 2004, and ref. therein).

On the other hand, the region affected by the X-ray radiation emitted by a protostar like IRAS16293 A, with a typical extension of $\sim$ 10 AU (Ciaravella et al. 2011), is smaller

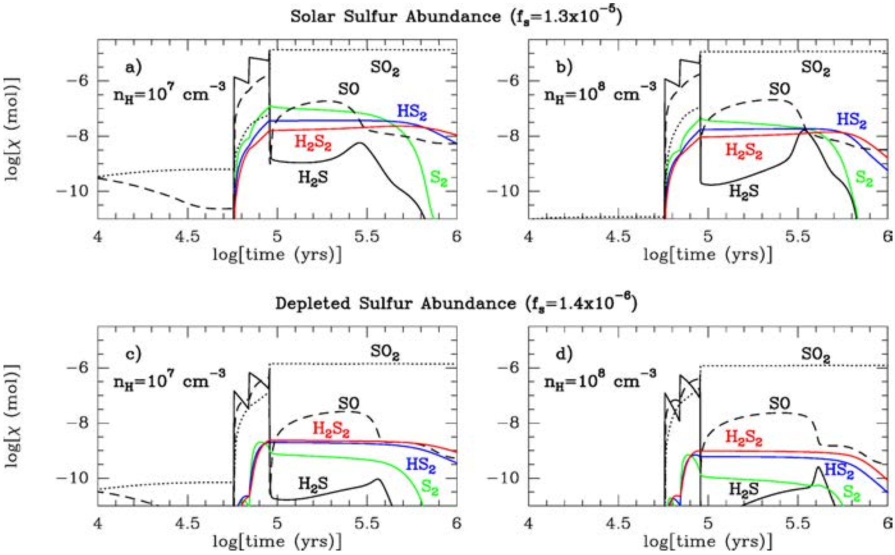

Figure 12.3. *Time-dependent evolution of abundances of selected sulfur-bearing species in IRAS16293 according to the UCL_CHEM code for models (a), (b), (c), and (d), whose most important parameters are shown in Table 12.3. Colored lines correspond to the targeted species. Black solid line is for H_2S. Black dashed and dotted lines correspond to SO and SO_2, respectively.*

than the region where the sulfur-containing species are expected to be detected in these observations (with an extension of ∼ 230 AU for an assumed source size of 2″ in diameter; Wakelam et al. 2004b). Therefore, the upper limits shown in the third and fourth columns of Table 12.2 could be affected by beam dilution, (and, therefore, be underestimated) if the sulfur-bearing molecules were confined to the region affected by the X-ray emitted by the protostars in IRAS16293-2422.

Finally, H_2S_2 and HS_2, although efficiently produced in ices, may undergo an active gas-phase chemistry once desorbed from dust grains. This could lower the gas-phase abundances of these species to undetectable levels. This possibility is further explored in Section 12.4.2.

12.4.2 A chemical model of H_2S_2, HS_2 and S_2 in IRAS16293-2422

In a recent paper, Woods et al. (2015) have incorporated the experimental data of Garozzo et al. (2010) on the production of the S-bearing species H_2S_2, HS_2 and S_2 in ices, into the UCL_CHEM chemical code (Viti & Williams 1999, Viti et al. 2004). In these experiments, Garozzo et al. (2010) bombarded a CO:H_2S = 10:1 mixture sample with 200 keV protons simulating the impact of cosmic rays on interstellar ice analogs. Although the irradiation source is different from the ones used in Jiménez-Escobar & Muñoz Caro (2011) and Jiménez-Escobar et al. (2014), we note that the measured production of H_2S_2

in the ices at low fluences is about 30%, i.e., similar within 5% to the one obtained in the experiments with UV-photon and X-ray irradiation (see Table 12.2). Since we are interested in the chemistry of these sulfur-bearing species in the gas phase after thermal desorption, a small difference in the H_2S_2 production by 5% is not expected to have a noticeable effect in the final results. We therefore made use of this new chemical network to test whether gas-phase chemistry is responsible for the lack of detection of H_2S_2, $HS_2^{\cdot}$ and S_2 toward IRAS16293.

The UCL_CHEM gas-grain chemical code is a two-phase model.

In Phase 1, this code simulates the free-fall gravitational collapse of a cloud where the mantles of dust grains form self-consistently via freeze-out reactions. In our modeling, we have considered two groups of freeze-out reactions for the sulfur species: one group where molecules can either freeze onto grains as themselves, or undergo hydrogenation/dehydrogenation reactions in the ices; and a second group where species freeze onto grains only as themselves (see Table 12.3 for the freeze-out reactions considered in the models). The formation of the initial core occurs from a diffuse medium with H_2 densities of $\sim$100 cm^{-3} and the collapse stops when the final density is reached in the model. The UCL_CHEM is run for two final densities of 10^7 cm^{-3} and 10^8 cm^{-3}, covering the range of H_2 gas densities typically assumed for low-mass warm cores (see, e.g., Awad et al. 2010). Finally, in order to test the effects of the presence of a sulfur residue in dust grains in the form of S_8 or of any other type of aggregate (see Jiménez-Escobar & Muñoz Caro 2011), we also considered two models with different initial sulfur abundances (see Table 12.3): one assuming the solar sulfur abundance (f_s=1.318×10^{-5}; Asplund et al. 2009) and a second model considering a depleted abundance of sulfur (f_s=1.4×10^{-6}; Sofia et al. 1994).

In Phase 2, UCL_CHEM calculates the time-dependent evolution of the chemistry of gas and dust once stellar activity is present. As explained in Viti et al. (2004), molecular species are thermally evaporated after the turning on of the protostar in different temperature bands. Here, we follow the classification proposed by Woods et al. (2015) where H_2S, HS and H_2S_2 are considered as *intermediate* species evaporating at temperatures between 80 K - 90 K, and where $HS_2^{\cdot}$ is a *reactive* molecule that co-desorbs with water at around 100 K. The maximum temperature assumed for IRAS16293 in Phase 2 is 100 K (Ceccarelli et al. 2000). In our models the temperature increases monotonically following the prescription of Viti et al. (2004). We also assume a standard cosmic ray ionisation rate (ζ=1.3×10^{-17} s^{-1}) for all models.

In Figure 12.3, we report the abundances of all major species involved in the sulfur chemistry toward IRAS16293. Consistently with the results of Woods et al. (2015), the level of hydrogenation of the ice species in Phase 1 does not significantly affect the abundances of these species in Phase 2. Gas phase reactions after ice desorption clearly dominate the chemistry of S-bearing species. The abundances of H_2S_2, $HS_2^{\cdot}$ and S_2 in the mantles at the end of Phase 1 indeed differ by only factors of a few between the two freeze-out cases considered in our models. Therefore, in Figure 12.3 we only show the modeling results for the cases where molecules freeze out both as themselves or undergoing hydrogenation/dehydrogenation in the ices (see Group 1 reactions in Table 12.3).

Differences are found between models with different H_2 gas densities (see, e.g., models (a) and (b)). In particular, the abundances of H_2S_2, $HS_2^{\cdot}$ and S_2 are factors 1.7 - 6.7

Table 12.3. *Models run for the chemistry of H_2S_2, $HS_2^{\cdot}$ and S_2 toward IRAS16293*

Model	n_{H_2} (cm^{-3})	f_s	Freeze-out reactions group	Reactions$^{(1)}$
				50% $HS_2 \rightarrow mHS_2$
				50% $HS_2 \rightarrow mH_2S_2$
a)	1×10^7	1.3×10^{-5}	1	50% $H_2S_2 \rightarrow mH_2S_2$
				50% $H_2S_2 \rightarrow mHS_2$
b)	1×10^8	1.3×10^{-5}	1	50% $S \rightarrow mHS$
				50% $S \rightarrow mH_2S$
				0% $S \rightarrow mS$
				50% $HS_2 \rightarrow mHS_2$
				50% $HS_2 \rightarrow mH_2S_2$
c)	1×10^7	1.4×10^{-6}	1	50% $H_2S_2 \rightarrow mH_2S_2$
				50% $H_2S_2 \rightarrow mHS_2$
d)	1×10^8	1.4×10^{-6}	1	50% $S \rightarrow mHS$
				50% $S \rightarrow mH_2S$
				0% $S \rightarrow mS$
				100% $HS_2 \rightarrow mHS_2$
				0% $HS_2 \rightarrow mH_2S_2$
e)	1×10^7	1.3×10^{-5}	2	100% $H_2S_2 \rightarrow mH_2S_2$
				0% $H_2S_2 \rightarrow mHS_2$
f)	1×10^8	1.3×10^{-5}	2	0% $S \rightarrow mHS$
				0% $S \rightarrow mH_2S$
				100% $S \rightarrow mS$

$^{(1)}$$mH_2S_2$, mHS_2, mH_2S, and mS refers to species frozen onto the mantles of dust grains.

higher in the models with n_{H_2}=10^7 cm^{-3} than for H_2 gas densities of 10^8 cm^{-3}. One explanation is that more H_2S is formed on grain surfaces at higher densities, which in turn is converted into SO_2 via the surface reaction $H_2S + 2O \rightarrow SO_2 + H_2$ (see Table 3 in Woods et al. 2015). Since H_2S preferentially goes into SO_2 at high densities, there is a smaller amount of this molecule available in the ices for the production of H_2S_2, $HS_2^{\cdot}$ and S_2, leading to lower abundances of the latter species. As expected, Figure 12.3 also shows that a depleted initial abundance of atomic sulfur yields lower abundances in Phase 2 for all S-bearing species considered in our modeling.

In order to compare the model results with our upper limits of Section 12.3.3, we need to inspect the abundances of H_2S_2, $HS_2^{\cdot}$ and S_2 at time-scales $\sim10^5$ yrs inferred for the IRAS16293 low-mass warm core (see André et al. 1993). The predicted abundances of these species for models (a), (b), (c), and (d) are shown in Table 12.4 along with the upper limits derived from our observations. For the models with a sulfur solar abundance (models (a) and (b)), higher H_2 densities of 10^8 cm^{-3} fit better the observations (see Table 12.4). However, for models (c) and (d) where the initial sulfur abundance is depleted, we find that the predicted abundances of H_2S_2, $HS_2^{\cdot}$ and S_2 lie within the upper limits measured toward IRAS16293. Therefore, even in the absence of a sulfur residue, our modeling shows that gas-phase chemistry can explain the lack of detection of H_2S_2, $HS_2^{\cdot}$ and S_2 toward this source.

Table 12.4. *Comparison of the modelled H_2S_2, $HS_2^{\cdot}$ and S_2 abundances with the upper limits derived from the observations.*

	X_{mol}				
Molecule	Model (a)	Model (b)	Model (c)	Model (d)	Observations
H_2S_2	1.6×10^{-8}	9.3×10^{-9}	2.3×10^{-9}	1.0×10^{-9}	$\leq8.1\times10^{-9}$
$HS_2^{\cdot}$	3.6×10^{-8}	1.7×10^{-8}	2.0×10^{-9}	6.2×10^{-10}	$\leq1.1\times10^{-8}$
S_2	1.1×10^{-7}	3.7×10^{-8}	7.4×10^{-10}	1.1×10^{-10}	$\leq2.9\times10^{-7}$

12.5 Conclusions

A fraction of the missing sulfur in the interstellar medium is thought to be locked in the ice mantles on dust grains. Interstellar ice mantles are energetically processed, leading to chemical and structural changes. Previous laboratory experiments simulating the irradiation of H_2S-containing ice analogs under astrophysically relevant conditions lead to the production of H_2S_2, $HS_2^{\cdot}$, and S_2 among other species. These molecules would be subsequently released to the gas phase by non-thermal desorption in dense clouds, and also by thermal desorption in regions around YSOs.

We have presented the first single-dish observations targeting a wide selection of rotational transitions predicted for the S-S bonded molecules H_2S_2, $HS_2^{\cdot}$, and S_2 toward the low-mass warm core IRAS16293-2422, a region with an active chemistry and a high H_2S gas-phase abundance.

As a result of this work, the predicted rotational spectrum of H_2S_2 was made available as a new entry in the CDMS catalog. Although none of the species were firmly detected, we have estimated an upper limit to their molecular abundances of $\leq$8.1 x 10^{-9}, $\leq$1.1 x 10^{-8}, and $\leq$2.9 x 10^{-7} relative to H_2 or $\leq$1.5 x 10^{-2}, $\leq$2.0 x 10^{-2}, and $\leq$5.5 x 10^{-1} relative to H_2S, respectively. These abundances are therefore up to two orders of magnitude lower than the observed abundance of H_2S in the same source, which is thought to be the parent molecule of species with a disulfide (S-S) bond.

The estimated upper limits are one order of magnitude lower than the abundances found in the experimental simulations. This could be the result of an underestimation of the measured upper limits caused by beam dilution of their emitting regions, or an overestimation of the expected abundances from the laboratory experiments. Although experimental simulations try to mimick interstellar conditions, differences between the ice analogs and the interstellar ice mantles, the densities in the UHV chamber and the interstellar and circumstellar regions, and the processing time of the samples are inevitable.

On the other hand, subsequent gas-phase chemistry after desorption could have reduced the gas-phase abundances of these species to undetectable levels in our observations.

Future high-angular resolution observations will establish whether these species are truly depleted in the gas phase or whether their emitting regions are largely diluted in our single-dish observations.

Acknowledgements

This research was financed by the Spanish MINECO under project AYA2011-29375. R.M.-D. benefited from a FPI grant from Spanish MINECO. I.J.-S. acknowledges the funding received from the People Programme (Marie Curie Actions) of the European Unions Seventh Framework Programme (FP7/2007-2013) under REA grant agreement PIIF-GA-2011-301538, and from the STFC through an Ernest Rutherford Fellowship (proposal number ST/L004801/1).

References

Allamandola, L. J., Bernstein, M. P., Sandford, S. A., & Walker, R. L. 1999, Space Sci. Rev., 90, 219

André, P., Ward-Thompson, D., & Barsony, M. 1993, ApJ, 406, 122

Asplund, M., Grevesse, N., Sauval, A. J., & Scott, P. 2009, ARA&A, 47, 481

Awad, Z., Viti, S., Collings, M. P., & Williams, D. A. 2010, MNRAS, 407, 2511

Behrend, J., Mittler, P., Winnewisser, G., Yamada, K. M. T., & Winnewisser, M. 1990, J. Mol. Spectrosc., 141, 265

Belov, S. P., Liedtke, M., Klaus, T., et al. 1994, J. Mol. Spectrosc., 166, 489

Bockelée-Morvan, D., Lis, D. C., Wink, J. E., et al. 2000, A&A, 353, 1101

Boogert, A. C. A., Schutte, W. A., Helmich, F. P., Tielens, A. G. G. M.,& Wooden, D.H. 1997, A&A, 317, 929

Caux, E., Kahane, C., Castets, A., et al. 2011, A&A, 532, A23

Cazaux, S., Tielens, A. G. G. M., Ceccarelli, C., et al. 2003, ApJL, 593, L51

Ceccarelli, C., Castets, A., Caux, E., Hollenbach, D., Loinard, L., Molinari, S., & Tielens, A. G. G. M. 2000, A&A, 355, 1129

Charnley, S. B. 1997, ApJ, 481, 396

Ciaravella, A., Jiménez-Escobar, A., Muñoz Caro, G. M., et al. 2011, ApJ, 746, L1

Doty, S. D., van Dishoeck, E. F., & Tan, J. 2004, BAAS, 36, 1505

Ferrante, R. F., Moore, M. H., Spiliotis, M. M., & Hudson, R. L. 2008, ApJ, 684, 1210

Fink, E. H., Kruse, H., & Ramsay, D. A. 1986, J. Mol. Spectrosc., 119, 377

Garozzo, M., Fulvio, D., Kanuchova, Z., Palumbo, M. E., & Strazzulla, G. 2010, A&A, 509, A67

Geballe, T. R., Baas, F., Greenberg, J. M., & Schutte, W. 1985, A&A, 146, L6

Grim, R. J. A., & Greenberg, J. M. 1987, A&A, 181, 155

Hatchell, J., Thompson, M. A., Millar, . J., MacDonald, G. H. 1998, A&A, 338, 713

Jansen D. J., Spaans M., Hogerheijde M. R., & van Dishoeck E. F. 1995, A&A, 303, 541

Jiménez-Escobar, A. & Muñoz Caro, G. M. 2011, A&A, 536, A91

Jiménez-Escobar, A., Muñoz Caro, G. M., & Chen, Y.-J. 2014, MNRAS, 443, 343

Jiménez-Escobar, A., Muñoz Caro, G. M., Cicarelli, A., Cecchi-Pestellini, C., Candia, R., & Micela, G. 2012, ApJL, 751, L40

Jiménez-Serra, I., Zhang, Q., Viti, S., Martín-Pintado, J., & de Wit, W.-J. 2012, ApJ, 753, id.34

Jørgensen, J. K, Bourke, T. L., Nguyen Luong, Q., & Takakuwa, S. 2011, A&A, 534, A100

Klaus, T., Belov, S. P., Saleck, A. H., Winnewisser, G., & Herbst, E. 1994, J. Mol. Spectrosc., 168, 235

Klaus, T., Saleck, A. H., Belov, S. P., et al. 1996, J. Mol. Spectrosc., 180, 197

Klein, B., Hochgürtel, S., Krämer, I., Bell, A., Meyer, K., & Güsten, R. 2012, A&A, 542, L6

Maret, S., Hily-Blant, P., Pety, J., Bardeau, S., & Reynier, E. 2011, A&A, 526, A47

Millar, T. J., & Herbst E. 1990, A&A, 231, 466

Moore, M. H., Hudson, R. L., & Carlson, R. W. 2007, Icarus, 189, 409

Müller, H. S. P., Thorwirth, S., Roth, D. A., & Winnewisser, G. 2001, A&A, 370, L49

Müller, H. S. P., Schlöder, F., Stutzki, J., & Winnewisser, G. 2005, J. Mol. Struct., 742, 215

Mundy. L. G., Wootten, A., Wilking, B. A., Blake, G. A., & Sargent, A. I. 1992, ApJ, 385, 306

Muñoz Caro, G. M., Jiménez-Escobar, A., Martín-Gago, J.Á., Rogero, C., Atienza, C., Puertas, S., Sobrado, J. M., & Torres-Redondo, J. 2010, A&A, 522, A108

Palumbo, M. E., Tielens, A. G. G. M., Tokunaga, A. T. 1995, ApJ, 449, 674

Peterson, K. A., Mitrushchenkov, A., & Francisco, J. S. 2008, Chem. Phys., 346, 34

Pickett, H. M., & Boyd, T. L. 1979, J. Mol. Spectrosc., 75, 53

Pickett, H. M., Poynter, R. L., Cohen, E. A., et al. 1998, JQSRT, 60, 883

Ruffle D. P., Hartquist T. W., Caselli P., & Williams D. A. 1999, MNRAS, 306, 691

Smith, R. G. 1991, MNRAS, 249, 172

Tanimoto, M., Klaus, T., Müller, H. S. P., & Winnewisser, G. 2000, J. Mol. Spectrosc., 199, 73

Tieftrunk, A., Pineau des Forets, G., Schilke, P., & Walmsley, C. M. 1994, A&A 289, 579

Shen, C. J., Greenberg, J. M., Schutte, W. A., & van Dishoeck, E. F. 2004, A&A, 415, 203

Sofia, U. J., Cardelli, J. A., & Savage, B. D. 1994, ApJ, 430, 650

van der Tak, F. F. S, Boonman, A. M. S., Braakman, R., & van Dishoeck, E. F. 2003, A&A, 412, 133

Vassilev, V., Meledin, D., Lapkin, I., et al. 2008, A&A, 490, 1157

Viti, S., Caselli, P., Hartquist, t. W., Williams, D. A. 2001, A&A, 370, 1017

Viti, S., Collings, M. P., Dever, J. W., McCoustra, M. R. S., & Williams, D. A., 2004, MNRAS, 354, 1141

Viti, S., & Williams, D. A. 1999, MNRAS, 305, 4, 755

Wakelam, V., Caselli, P., Ceccarelli, C., Herbst, E., & Castets, A., 2004a, A&A, 422, 159

Wakelam, V., Castets, A., Ceccarelli, C., Lefloch, B., Caux. E., & Pagani, L., 2004b, A&A, 413, 609

Wakelam, V., Hersant, F., Herpin, F. 2011, A&A, 529, A1112

Woods, P. M., Occhiogrosso, A., Viti, S., et al. 2015, MNRAS, 450, 1256

Woon, D. E., & Herbst, E. 2009, ApJSS, 185, 273

Yamada, K. M. T., Behrend, J., Belov, S. P., & Winnewisser, G. 1996, J. Mol. Spectrosc., 176, 397

Yamamoto, S., & Saito, S. 1994, Can. J. Phys., 72, 954

Chapter 13

Detection of CH_3NCO toward the low mass warm core IRAS16293-2422

Adapted from *Detection of methyl isocyanate (CH_3NCO) in a solar-type protostar*, Martín-Doménech, R., Rivilla, V.M., Jiménez-Serra, I., Quenard, D., Testi, L. & Martín-Pintado, J. 2017, submitted to MNRASL[1]

Abstract

We report the detection of the prebiotic molecule CH_3NCO in IRAS16293-2422 B. A significant abundance of this species on the surface of the comet 67P/Churyumov-Gerasimenko has been proposed, and it has recently been detected in a couple of hot cores around high-mass protostars. We observed IRAS16293-2422 B with ALMA covering a total bandwidth of $\sim$6 GHz in the 90 GHz to 265 GHz range with Bands 3, 4, and 6, and detected 8 unblended transitions of CH_3NCO. From our Local Thermodynamic Equilibrium analysis we derived an excitation temperature of 110 ± 19 K and a column density of $(4.0\pm0.3)\times10^{15}$ cm^{-2}, which results in an abundance of $(1.4\pm0.1)\times10^{-10}$ with respect to molecular hydrogen. This implies a $CH_3NCO/HNCO$ and CH_3NCO/NH_2CHO column density ratios of $\sim$0.08, calculated from the abundance of these species derived from the same data.

13.1 Introduction

Understanding the origin of life is one of the main challenges of modern science. It is believed that some basic prebiotic chemistry could have developed in space, likely transferring prebiotic molecules to the solar nebula and later on to Earth (see, e.g., Oró 1961; and more recently, Muñoz Caro & Dartois 2013 and references therein).

Studies of the chemical composition of comets have indeed reported that these objects exhibit a wide variety of complex organic molecules (or COMs) that are commonly detected in the ISM (see, e.g., Biver et al. 2014). Recently, the spacecraft Rosetta studied the chemical composition of the comet 67P/Churyumov-Gerasimenko and found evidences for the presence of 16 different COMs of prebiotic interest on the cometary surface using the Cometary Sampling and Composition (COSAC; Goesmann et al. 2012) mass spectrometer (as, e.g., glycoladehyde, CH_2OHCHO, or formamide, NH_2CHO; Goesmann et al. 2015), and in the coma of the comet using the Rosetta Orbiter Spectrometer for Ion and Neutral Analysis (ROSINA; Balsiger et al. 2007) instrument (with the detection of the amino acid glycine; Altwegg et al. 2015).

Among these species, the COSAC mass spectrometer suggested the presence of methyl isocyanate (CH_3NCO) in the surface of comet 67P/Churyumov-Gerasimenko, with an abundance relatively high compared to other COMs (Goesmann et al. 2015). CH_3NCO is the simplest isocyanate, which along NH_2CHO contains C, N, and O atoms.

---

[1] The submitted version includes a chemical model that required major changes. It was therefore not included in this thesis.

Isocyanates are a family of complex organics that could play a key role in the synthesis of amino acid chains known as peptides (Pascal et al. 2005).

After COSAC's tentative detection, CH_3NCO was searched for, and detected, in massive hot molecular cores such as SgrB2 N (Halfen et al. 2015, Belloche et al. 2017) and Orion KL (Cernicharo et al. 2016). However, CH_3NCO remained to be reported around solar-type protostars.

IRAS 16293−2422 (hereafter IRAS16293) is located in the ρ Ophiuchi cloud complex at a distance of 120 pc (Loinard et al. 2008), and it is considered an excellent template for astrochemical studies in solar-type protostars (e.g., Jørgensen et al. 2011, Jørgensen et al. 2016, Lykke et al. 2017). IRAS16293 is composed by sources A[2] and B, separated in the plane of the sky by $\sim5''$ ($\sim$600 AU), and whose masses are $\sim$0.5 $M_\odot$ (Looney et al. 2000). Their emission exhibits line profiles with linewidths of up to 8 km s^{-1} for IRAS 16293 A and < 2 km s^{-1} for IRAS 16293 B. The narrow emission of IRAS 16293 B, along with its rich COM chemistry, makes this object the perfect target to search for new COMs (see, e.g., Jørgensen et al. 2011, Jaber et al. 2014, Jørgensen et al. 2016).

In this work, we report the detection of CH_3NCO toward the source IRAS 16293−2422 B carried out with the Atacama Large Millimeter Array (ALMA). The observations are described in Sect. 13.2, while the detection is reported in Sect. 13.3, and the conclusions are summarized in Sect. 13.4.

13.2 Observations

The analysis was carried out using the ALMA data from our own project (#2013.1.00352.S), and all other public datasets in Bands 3, 4, and 6 available in the ALMA archive as of January 2017 (#2011.0.00007.SV, #2012.1.00712.S, and #2013.1.00061.S). We note that we have excluded from our analysis other ALMA public datasets in Bands 7 and 8, i) to prevent any dust optical depth problems (the dust continuum emission of IRAS16293 B is known to be very optically thick at frequencies >300 GHz, which severely affects the line intensities of the molecular emission; see Zapata et al. 2013, Jørgensen et al. 2016); and ii) to limit the level of line confusion, which allows the correct subtraction of the continuum emission by selecting a suitable number of line-free channels in the observed spectra.

All data matching our criteria were downloaded and re-calibrated using standard ALMA calibration scripts and the Common Astronomy Software Applications package[3]. The angular resolution of all datasets was sufficient to resolve source B from source A (with angular resolutions below 1.5"), and therefore the emission lines arising from source B are narrow with linewidths $\leq$2 km s^{-1} (see, e.g., Pineda et al. 2012, Oya et al. 2016. Continuum subtraction was performed in the uv-plane before imaging using line-free channels.

Our dataset covers a total bandwidth of $\sim$6 GHz split in 26 spectral windows spread between 89.5 and 266.5 GHz, with synthesised beam sizes ranging from $0.57''\times0.28''$ to $1.42''\times1.23''$. The velocity resolution falls between 0.14 and 0.30 km s^{-1}. For the

---

[2] Source A is probably a binary system formed by components Aa and Ab (Chandler et al. 2005).

[3] https://casa.nrao.edu

Table 13.1. *Detected CH_3NCO unblended lines in IRAS16293 B.*

Frequency (GHz)	Transition	$\log A_{ul}$ (s^{-1})	E_u (K)	Integrated flux Jy km s^{-1}
157.258419	18,2,0,3−17,2,0,3	-3.75	210	0.028 ± 0.009
157.259087	18,2,0,-3−17,2,0,-3	-3.75	210	0.028 ± 0.009
232.342227	27,2,0,2−26,2,0,2	-3.22	234	0.12 ± 0.04
232.411044	27,1,0,1−26,1,0,1	-3.22	175	0.16 ± 0.06
240.302835	28,0,0,1−27,0,0,1	-3.17	181	0.18 ± 0.06
250.313498	29,3,27,0−28,3,26,0	-3.13	235	0.16 ± 0.05
250.323521	29,3,26,0−28,3,25,0	-3.13	235	0.16 ± 0.05
250.676140	29,0,29,0−28,0,28,0	-3.13	181	0.21 ± 0.07

analysis, a spectrum was extracted from each datacube using a circular support with size ∼1.6″ centered at the position of IRAS16293 B ($RA_{\rm J2000}$ = $16h\,32m\,22.61s$, $DEC_{\rm J2000}$ = -24° 28′ 32.44″). We note that the molecular emission from IRAS16293 B for the species considered in this study (e.g. CH_3NCO, NH_2CHO and $HN^{13}CO$), is compact and lies below 1.5" (see Figure 13.2 below and Coutens et al. 2016).

13.3 Results

13.3.1 Detection of CH_3NCO

The rotational spectrum of CH_3NCO, with the A and E torsional states, has been studied by Koput et al. (1986, from 8 to 40 GHz), and more recently by Halfen et al. (2015, from 68 to 105 GHz) and Cernicharo et al. (2016, from 40 to 363 GHz).

The identification of the lines was performed using the software MADCUBAIJ[4], using the information from the Jet Propulsion Laboratory (JPL, Pickett et al. 1998) and the Cologne Database for Molecular Spectroscopy spectral catalogs (CDMS, Müller et al. 2005).

We identified a total of 22 transitions of CH_3NCO, 8 out of which were unblended with upper energy levels ranging from 175 to 233 K (see Table 13.1), using MADCUBAIJ. The remaining 14 lines appear contaminated by emission from other species.
The CH_3NCO lines peak at a radial velocity of v_{LSR} = 2.7 km s^{-1} and have linewidths of ∼1.1 km s^{-1} (Fig. 13.1), similar to those from other molecules in IRAS16293 B (see, e.g., Jørgensen et al. 2011).

MADCUBAIJ produces synthetic spectra assuming Local Thermodinamical Equilibrium (LTE) conditions. The comparison between the observed and the synthetic spectrum for the unblended transitions can be used to derive the excitation temperature and total column density that best match the observations. We assumed a linewidth of 1.1 km s^{-1}, and the source size was constrained by the continuum emission to 0.5″ (see Figure 13.2), which agrees with the source size assumed in previous works Jørgensen et al. 2016, Coutens et al. 2016, Lykke et al. 2017. .

---

[4] Madrid Data Cube Analysis on ImageJ is a software developed in the Center of Astrobiology (Madrid, INTA-CSIC) to visualize and analyze single spectra and datacubes (Rivilla et al. 2016, Rivilla et al. 2017).

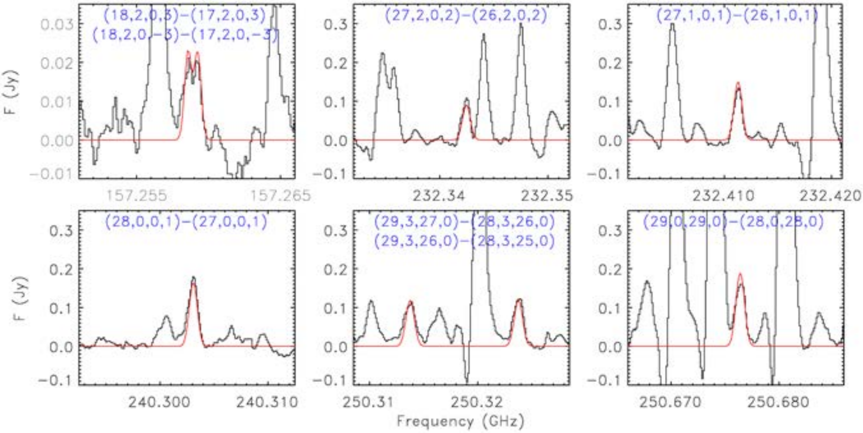

Figure 13.1. *CH_3NCO unblended lines measured toward IRAS16293 B with ALMA (solid black). Transitions are shown in every panel, while their rest frequencies are reported in Table 13.1. The synthetic LTE spectrum generated by MADCUBAIJ is overplotted in red.*

The observed spectra and the corresponding LTE fitted synthetic spectrum for the 8 unblended lines detected, are shown in Fig 13.1. All CH_3NCO transitions were found to be optically thin ($\tau < 0.08$), and thus our analysis is not affected by optical depth effects.

The detected CH_3NCO transitions are well reproduced by an excitation temperature of T_{ex}=110±19 K. This T_{ex} is similar to that found for other COMs such as acetaldehyde or propanal in IRAS16293 B (Lykke et al. 2017). The derived column density is $N(CH_3NCO)=(4.0\pm0.3)\times10^{15}$ cm^{-2}, which agrees with the column density reported in Ligterink et al. (2017)[5] assuming the same source size and excitation temperature for 43 unblended transitions with $E_u > 300$ K, detected at frequencies higher than 320 GHz using a different dataset.

Transitions corresponding to two isomers of methyl isocyanate, CH_3CNO and CH_3OCN, were not detected in our dataset, and 3σ upper limits of 2.7×10^{13} cm^{-2}, and 5.1×10^{14} cm^{-2} (respectively) were extracted assuming the same linewidth and excitation temperature. This upper limits lead to column density ratios of $CH_3NCO/CH_3CNO\geq148$ and $CH_3NCO/CH_3OCN\geq8$.

In order to estimate the CH_3NCO abundance, we have derived the H_2 column density by using the continuum flux measured at 232 GHz (1.4±0.05 Jy) within a deconvolved size of $0.55''\times0.47''$, and by assuming optically thin dust, a dust opacity of 0.009 cm^2 g^{-1} (thin ices in a H_2 density of 10^6 cm^{-3}; see Ossenkopf & Henning 1994) and a gas-to-dust mass ratio of 100. The estimated H_2 column density for $T_{dust}=T_{ex}=110$ K[6] is $N(H_2)=2.8\times10^{25}$ cm^{-2}, consistent with that estimated by Jørgensen et al. (2016) at

---

[5] This work was developed in parallel.

[6] At the high H_2 volume densities of IRAS16293 B, dust and gas are thermally coupled.

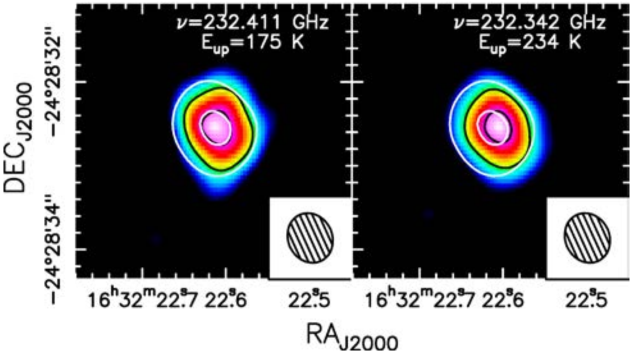

Figure 13.2. *Integrated intensity maps of two representative CH_3NCO unblended lines observed toward IRAS16293 B. Black contours indicate 50% and 90% of the peak line emission, while white contours indicate 20%, and 80% of the continuum peak emission at 232 GHz. The rest frequency and E_u of the transitions are shown in every panel (see also Table 13.1). Beam sizes are shown in the bottom right corner.*

higher frequencies. We however caution that this value should be considered as a lower limit since dust may be optically thick even at these low frequencies. The derived abundance of CH_3NCO is χ(CH_3NCO)=(1.4±0.1)×10^{-10} and it should be considered as an upper limit.

The spatial distribution of CH_3NCO is shown in Fig. 13.2 and it is coincident with the continuum emission. The measured deconvolved size is ∼0.5", consistent with the source size assumed in our LTE analysis. The CH_3NCO emission is thus originated in an unresolved compact region around the protostar in IRAS16293 B.

13.3.2 Chemically-related species: HNCO and NH_2CHO

In Orion KL, CH_3NCO shows the same spatial distribution as HNCO and NH_2CHO (Cernicharo et al. 2016) and therefore they are thought to be chemically related. Several transitions of HNCO and NH_2CHO, and of some of their isotopologs, are also covered and detected in our dataset. The HNCO and NH_2CHO lines are optically thick (Coutens et al. 2016) and therefore, their column densities have been inferred using the $HNC^{18}O$ and $NH_2^{13}CHO$ isotopologues.

Five unresolved transitions of $HNC^{18}O$ are found at 250 GHz with E_u=122 K. Assuming LTE conditions and a fixed excitation temperature of T_{ex}=110 K (the T_{ex} derived for CH_3NCO), we obtain a column density of N($HNC^{18}O$)=(9.7±3.8)×10^{13} cm^{-2}. By assuming an isotopic ratio $^{16}O/^{18}O$ = 500 (Wilson & Rood 1994), the derived total column density of HNCO is N(HNCO)=(4.9±1.9)×10^{16} cm^{-2}, which yields an abundance of (1.8±0.7)×10^{-9}.

For $NH_2^{13}CHO$, three lines are detected at 156.957 GHz, 157.097 GHz, and 239.628 GHz, with E_u = 58−98 K. Their emission is fitted in MADCUBAIJ by using an excitation temperature of T_{ex}=75 K, and a column density of N($NH_2^{13}CHO$)=(7.6±3.7)×10^{14}

Table 13.2. *Comparison of the CH_3NCO/HNCO and CH_3NCO/NH_2CHO ratios measured in IRAS16293 B, SgrB2(N), Orion KL and comet 67P.*

Molecular ratio	Protostars				Comet
	Low-mass	High-mass			
	IRAS16293 B	SgrB2(N)	Orion KL		67P
			A	B	
CH_3NCO/HNCO	0.08	0.11	0.02	0.06	4.33
CH_3NCO/NH_2CHO	0.08	0.06	1.75	5.71	0.72

cm^{-2}. The derived T_{ex} is slightly lower than that obtained for CH_3NCO. This may be a result of the lower values of E_u covered by the $NH_2^{13}CHO$ lines as compared to those of CH_3NCO. We note however, that both species show the same spatial extent (see Figure 13.2 and Coutens et al. 2016) and therefore, they likely trace the same gas. By assuming an isotopic ratio $^{12}C/^{13}C$=68 (Milam et al. 2005), the derived total column density is $N(NH_2CHO)=(5.2\pm2.5)\times10^{16}$ cm^{-2}, which gives an abundance of $(1.9\pm0.9)\times10^{-9}$. As for CH_3NCO, these abundances should be considered as upper limits.

13.3.3 Comparison with other sources

The abundance of $(1.4\pm0.1)\times10^{-10}$ measured for CH_3NCO toward IRAS16293 B is similar to that found in SgrB2(N) (1.7×10^{-9} and 1.0×10^{-9} for the two V_{LSR} components; see Cernicharo et al. 2016). In Table 13.3.3, we present the comparison between the abundance ratios CH_3NCO/HNCO and CH_3NCO/NH_2CHO measured in IRAS16293 B with those from the four sources where CH_3NCO has also been detected (i.e., SgrB2(N), Orion KL, and 67P/Churyumov-Gerasimenko; Goesmann et al. 2015, Halfen et al. 2015, Belloche et al. 2017, Cernicharo et al. 2016). Since we have estimated the column densities of CH_3NCO, HNCO and NH_2CHO considering the same emitting region, the derived CH_3NCO/HNCO and CH_3NCO/NH_2CHO ratios are likely independent on the assumed source size and the derived H_2 column density toward IRAS16293 B.

From Table 13.3.3, we find that the CH_3NCO/HNCO column density ratio in IRAS16293 B is of the same order as those measured in SgrB2(N) and Orion KL. However, it is a factor of ~50 lower than in comet 67P/Churyumov-Gerasimenko [7]. We note however that the COSAC detections are tentative and therefore the abundance ratios in column 7 of Table 13.3.3 should be taken with caution.

The CH_3NCO/NH_2CHO column density ratio in IRAS16293 B is similar to that observed in SgrB2(N), while it is factors 20-70 lower than those measured in Orion KL, and a factor of 10 lower than that in comet 67P/Churyumov-Gerasimenko.

---

[7] Ligterink et al. 2017 state that CH_3NCO could be formed by photoprocessing of ice mantles containing CH_4 and HNCO. Therefore, subsequent gas-phase destruction of CH_3NCO after thermal desorption from the ice mantles in IRAS16293 B could explain the lower ratio found in this source.

13.4 Conclusions

In summary, we present the first detection of CH_3NCO toward a solar-type protostar. The derived abundance of 1.4×10^{-10} is similar to that measured in hot cores, and the observed CH_3NCO/HNCO ratio is similar to that inferred in SgrB2(N) and Orion KL. The ratio with other chemically related N-, C-, O-bearing species suchs as NH_2CHO shows larger discrepancies across different objects, although it agrees well with that derived in SgrB2(N).

Acknowledgements

This Letter makes use of the following ALMA data:
ADS/JAO.ALMA#2011.0.00007.SV,
ADS/JAO.ALMA#2012.1.00712.S,
ADS/JAO.ALMA#2013.1.00061.S,
ADS/JAO.ALMA#2013.1.00352.S.

ALMA is a partnership of ESO (representing its member states), NSF (USA) and NINS (Japan), together with NRC (Canada), NSC and ASIAA (Taiwan), and KASI (Republic of Korea), in co-operation with the Republic of Chile. The Joint ALMA Observatory is operated by ESO, AUI/NRAO and NAOJ This research was partially financed by the Spanish MINECO under project AYA2014-60585-P, by the Italian Ministero dell Istruzione, Universit e Ricerca, through the grant Progetti Premiali 2012 iALMA (CUP C52I13000140001), and by the Gothenburg Centre for Advanced Studies in Science and Technology, where the re-calibration and re-imaging of all the ALMA Archive data on IRAS16293-2422 was carried out as part of the GoCAS program Origins of Habitable Planets. R.M.-D. benefited from a FPI grant from Spanish MINECO. I.J.-S. acknowledges the financial support from an STFC Ernest Rutherford Fellowship and Grant (projects ST/L004801/2 and ST/M004139/2). J.M.-P. acknowledges partial support by the MINECO under grants FIS2012-39162-C06-01, ESP2013-47809-C03-01, and ESP2015-65597-C4-1. We also acknowledge Dr. Wing-Fai Thi for the valuable feedback on the manuscript.

References

Altwegg, K., Balsiger, H., Bar-Nun, A., et al. 2015, Science, 347, 6220, id.1261952
Balsiger, H., Altwegg, K., Bochsler, P., et al. 2007, Space Sci. Rev. 128, 745
Belloche, A., Meshcheryakov, A.A., Garrod, R.T., et al. 2017, A&A, *accepted*
Biver, N., Bockelée-Morvan, D., Debout, V., et al. 2014, A&A, 516, A109
Cernicharo, J., Kisiel, Z., Tercero, B., et al. 2016, A&A, 587, L4
Chandler, C.J., Brogan, C.L., Shirley, Y.L., & Loinard, L. 2005, ApJ, 632, 371
Coutens, A., Jørgensen, J., van der Wiel, M.H.D., et al. 2016, A&A, 590, L6
Coutens, A., Vastel, C., Caux, E., et al. 2012, A&A, 539, A132
Goesmann, F., McKenna-Lawlor, S., Roll, R., et al. 2012, Planet. Space Sci., 66, 187
Goesmann, F., Rosenbauer, H., Bredehöft, J.H., et al. 2015, Science, 346, 6247, id.0689
Halfen, D.T., Ilyushin, V.V., & Ziurys, L.M. 2015, ApJL, 8212, L5

Hasegawa, T. I., Herbst, E., & Leung, C. M. 1992, ApJ Suppl., 82, 167

Jaber, A.A., Ceccarelli, C., Kahane, C., & Caux, E. 2014, ApJ, 791, 29

Jørgensen, J.K., Bourke, T.L., Nguyen Luong, Q., & Takakuwa, S. 2011, A&A, 534, A100

Jørgensen, J.K., Favre, C., Bisschop, S.E., Bourke, T.L., et al. 2012, ApJL, 757, 1, L4

Jørgensen, J.K., van der Wiel, M.H.D., Coutens, A., et al. 2016, A&A, 595, A117

Kasten, W., & Dreizler, H. 1986, Z. Natur. 41a, 637

Koput, J. 1986, JMoSp, 115, 131

Ligterink, N.F.W., Coutens, A., Kofman, V., et al. 2017, MNRAS, *submitted*

Loinard, L., Torres, R.M., Mioduszewski, A.J., &Rodríguez, L.F. 2008, ApJL, 675, 1, L29

Looney, L.W., Mundy, L.G., & Welch, W.J. 2000, ApJ, 529, 1, 477

Lykke, J.M., Coutens, A., Jørgensen, J., et al. 2017, A&A, 597, A53

Milam, S.N., Savage, C., Brewster, M.A., Ziurys, L.M., & Wyckoff, S. 2005, ApJ, 634, 1126

Minissale, M., Dulieu, F., Cazaux, S., & Hocuk, S. 2016, A&A, 585, A24

Müller, H. S. P., Schlöder, F., Stutzki, J., & Winnewisser, G. 2005, J. Mol. Struct. 742, 215

Muñoz Caro, G.M., & Dartois, E. 2013, Chem. Soc. Rev., 42, 2173

Oró, J., 1961, Nature, 190, 389

Ossenkopf, V. & Henning, Th. 1994, A&A, 291, 3, 943

Oya, Y., Sakai, N., López-Sepulcre, A., et al. 2016, ApJ, 824, 2, 88

R. Pascal, L. Boiteau, A. Commeyras, 2005, Top. Curr. Chem., 259, 69

Pickett, H. M., Poynter, R. L., Cohen, E. A., Delitsky, M. L., Pearson, J. C., & Müller, H. S. P. 1998, J. Quant. Spectrosc. & Rad. Transfer, 60, 883

Pineda, J. E., et al. 2012, A&A, 544, L7P

Rivilla, V.M., Fontani, F., Beltrán, M.T., et al. 2016, ApJ, 826, 2

Rivilla, V. M. and Beltrán, M. T., Cesaroni, R., et al., 2017, A&A, 598, A59

Wakelam, V., & Herbst, E. 2008, ApJ, 680, 371-383

Zapata L., et al., 2013, ApJ, 764, L14Z

Part VI

Appendix

Agradecimientos

Quisiera agradecer en primer lugar todo el esfuerzo y comprensión dedicado por parte del Dr. Guillermo M. Muñoz Caro, mi director de tesis, que ha hecho que este trabajo fuera muchísimo más fácil. Esto es extensible a todas aquellas personas que durante estos años también me han dedicado un poco de su tiempo, especialmente al Dr. Emmanuel Dartois y la Dra. Izaskun Jiménez-Serra, que me acogieron durante más o menos tiempo en sus centros para que pudiera ampliar mis conocimientos, así como al Dr. Gustavo A. Cruz Díaz y la Dra. B. Michela Giuliano, que me ayudaron con mucha paciencia durante mis primeros pasos en el Centro de Astrobiología.

I would also like to thank Dr. Y.-J. Chen and Dr. W.-F. Thi for reviewing this thesis and providing useful comments.

Esta tesis ha sido financiada por el Ministerio de Economía y Competitividad a través de una ayuda para la Formación de Personal Investigador (FPI) dentro del Subprograma Estatal de Formación, que se extendió desde diciembre de 2012 hasta diciembre de 2016. A partir de enero de 2017, el trabajo ha sido financiado por el Proyecto I+D AYA2014-60585-P dentro del Subprograma Estatal de Generación del Conocimiento del Ministerio de Economía y Competitividad.

Curriculum Vitae

Rafael Martín Doménech (rafamd86@gmail.com).

Education

- B.Sc. in Chemical Engineering, Universidad de Málaga, Spain, 2010.
- M.Sc. in Astrophysics, Universidad Complutense y Universidad Autónoma de Madrid, Spain, 2013.
- PhD. in Astrophysics, Universidad Complutense de Madrid, Spain, 2017.

Grants and Fellowships

- PhD. Grant at the Centro de Astrobiología (CAB, INTA-CSIC), Torrejón de Ardoz, Spain, 2012-2016.

  Funded by the Subprograma de Ayudas de Formación de Personal Investigador (FPI) of the Spanish Ministry of Economy & Competitivity (MINECO).

  Ref: BES-2012-05-6303

- 90 days internship at the Institute d'Astrophysique Spatial (IAS, U-PSUD-CNRS), Orsay, France, 2015.

  Funded by the Subprograma Estatal de Movilidad para Estancias Breves (EEBB) of the Spanish MINECO.

  Ref: EEBB-I-2015-10333

- Contract for work and services at the Centro de Astrobiología (CAB, INTA-CSIC), Torrejón de Ardoz, Spain, January 2017 - August 2017.

Publications

- *Thermal desorption of circumstellar and cometary ice analogs*. **Rafael Martín-Doménech**; Guillermo M. Muñoz Caro; Juan Bueno; & Fred Goesmann. Astronomy & Astrophysics. 564, pp. A8. edp sciences, 04/2014.

- *Interstellar ice analogs: band strengths of H2O, CO2, CH3OH, and NH3 in the far-infrared region*. Barbara Michela Giuliano; Rafael Escribano; **Rafael Martín-Doménech**; Emmanuel Dartois; & Guillermo M. Muñoz Caro. Astronomy & Astrophysics. 565, pp. A108. edp sciences, 05/2014.

- *UV photoprocessing of CO2 ice: a complete quantification of photochemistry and photon-induced desorption processes*. **Rafael Martín-Domnech**; Javier Manzano-Santamaría; Guillermo M. Muñoz Caro; Gustavo Adolfo Cruz-Díaz; Y.-J. Chen; Víctor J. Herrero; & Isabel Tanarro. Astronomy & Astrophysics. 584, pp. A14. edp sciences, 12/2015.

- *The sulfur depletion problem: upper limits on the H2S2, HS2, and S2 gas-phase abundances toward the low-mass warm core IRAS 16293-2422*. **Rafael Martín-Doménech**; Izaskun Jiménez-Serra; Guillermo Muñoz Caro; Holger S.P. Müller; Angela Occhiogrosso; Leonardo Testi; Paul M. Woods; & Serena Viti. Astronomy & Astrophysics. 585, pp. A112. edp sciences, 01/2016.

- *Study of the photon-induced formation and subsequent desorption of CH_3OH and H_2CO in interstellar ice analogs*. **Rafael Martín-Doménech**; Guillermo M. Muñoz Caro; & Gustavo Adolfo Cruz-Díaz. Astronomy & Astrophysics. 589, pp. A107. edp sciences, 04/2016.

- *Vacuum ultraviolet photolysis of hydrogenated amorphous carbons. III. Diffusion of photo-produced H_2 as a function of temperature*. **Rafael Martín-Doménech**; Emmanuel Dartois; & Guillermo M. Muñoz Caro. Astronomy & Astrophysics. 591, pp. A107. edp sciences, 06/2016.

- *Negligible photodesorption of methanol ice and active photon-induced desorption of its irradiation products*. Gustavo Adolfo Cruz-Díaz; **Rafael Martín-Doménech**; Guillermo M. Muñoz Caro; & Y.-J. Chen. Astronomy & Astrophysics. 592, pp. A68. edp sciences, 08/2016.

- *Interstellar ice analogs: H_2O ice mixtures with CH_3OH and NH_3 in the far-IR region*. Barbara Michela Giuliano; **Rafael Martín-Doménech**; Rafael Escribano; Javier Manzano-Santamaría; & Guillermo M. Muñoz Caro. Astronomy & Astrophysics. 592, pp. A81. edp sciences, 08/2016.

- *CO depletion: A microscopic perspective*. Stephanie Cazaux, **Rafael Martín-Doménech**; Y.-J. Chen.; & Guillermo M. Muñoz Caro. The Astrophysical Journal. *submitted*

- *Measurements on water ice photodesorption and product formation under ultraviolet irradiation*. Gustavo Adolfo Cruz-Díaz; **Rafael Martín-Doménech**; Elena Moreno-Atahonero, Guillermo M. Muñoz Caro; & Y.-J. Chen. The Astrophysical Journal. *submitted*

- *First detection of methyl isocyanate (CH_3NCO) in a solar-type protostar*. **Rafael Martín-Doménech**; Víctor Manuel Rivilla; Izaskun Jiménez-Serra; David Quenard; Leonardo Testi; & Jesús Martín-Pintado. Monthly Notices of the Royal Astronomical Society Letters. *submitted*

Selected contributions

- *Thermal desorption of circumstellar and cometary ice analogs* (Poster). Rafael Martín-Doménech; Guillermo M. Muñoz Caro; & Fred Goesmann. Astrochemistry of Dust, Ice and Gas. Faraday Discussions 168. Leiden, The Netherlands. 07-09/04/2014.
- *Photodesorption and photoprocessing of interstellar ice analogues using the InterStellar Astrochemistry Chamber* (Oral). Rafael Martín-Doménech; Gustavo Adolfo Cruz-Díaz; & Guillermo M. Muñoz Caro. Experimental Astrochemistry: from ground-based to space-borne laboratories. Liège, Belgium. 02-03/07/2014.
- *Thermal processing of astrophysical ice analogues using the InterStellar Astrochemistry Chamber* (Poster). Rafael Martín-Doménech; & Guillermo M. Muñoz Caro. Experimental Astrochemistry: from ground-based to space-borne laboratories. Liège, Belgium. 02-03/07/2014.
- *Astrophysical ice analogs: recent experimental results using the Interstellar Astrochemistry Chamber (ISAC)* (Oral). Rafael Martín-Doménech; & Guillermo M. Muñoz Caro. USM+MPE Workshop. Garching, Germany. 25/11/2014.
- *Introduction to astrophysical observations* (Oral). Rafael Martín-Doménech; & Guillermo M. Muñoz Caro. A laboratory spectroscopy workshop for astrophysics. Jaca, Spain. 27-30/06/2016.
- *IR spectroscopy and thermal programmed desorption of ices* (Oral). Rafael Martín-Doménech; & Guillermo M. Muñoz Caro. A laboratory spectroscopy workshop for astrophysics. Jaca, Spain. 27-30/06/2016.
- *Photon-induced desorption processes in astrophysical ice analogs: two observed patterns in the desorption of photoproducts* (Oral). Rafael Martín-Doménech; Guillermo M. Muñoz Caro; & Gustavo Adolfo Cruz-Díaz. European Conference on Laboratory Astrophysics. Madrid, Spain. 21-25/11/2016.
- *Chemistry of hydride-containing ices: UV photoprocessing of a H_2O:CH_4 ice analog* (Oral). Rafael Martín-Doménech; Guillermo M. Muñoz Caro. Gustavo Adolfo Cruz-Díaz; & Elena Moreno-Atahonero. The Hydride Toolbox. Paris, France. 12-16/12/2016.
- *UV photoprocessing of an H_2O:CH_4 ice analog: two observed patterns in the desorption of photoproducts* (Poster). Rafael Martín-Doménech; Guillermo M. Muñoz Caro; & Gustavo Adolfo Cruz-Díaz. The Astrochemical Week. WG3 Workshop - Non thermal desorption from cold surfaces. Olhão, Portugal. 20/01/2017.